Hydrogenated amorphous silicon: Impact of process conditions on material properties and solar cell efficiency

THÈSE N^{O} 6393 (2014)

PRÉSENTÉE LE 3 NOVEMBRE 2014
À LA FACULTÉ DES SCIENCES ET TECHNIQUES DE L'INGÉNIEUR
LABORATOIRE DE PHOTOVOLTAÏQUE ET COUCHES MINCES ÉLECTRONIQUES
PROGRAMME DOCTORAL EN SCIENCE ET GÉNIE DES MATÉRIAUX

ÉCOLE POLYTECHNIQUE FÉDÉRALE DE LAUSANNE

POUR L'OBTENTION DU GRADE DE DOCTEUR ÈS SCIENCES

PAR

Michael Elias STÜCKELBERGER

acceptée sur proposition du jury:

Prof. N. Marzari, président du jury
Prof. C. Ballif, Dr F.-J. Haug, directeurs de thèse
Dr M. Despeisse, rapporteur
Dr A. Howling, rapporteur
Dr T. Matsui, rapporteur
Prof. P. Roca i Cabarrocas, rapporteur

ÉCOLE POLYTECHNIQUE
FÉDÉRALE DE LAUSANNE

Suisse
2014

Abstract

Thin-film silicon solar cells are one possible answer to the increasing energy demand of today. Hydrogenated amorphous silicon (a-Si:H) plays a crucial role therein—as absorber layers, but also as doped layers to build p-i-n junctions. This thesis is devoted to a-Si:H, with the main focus on thin-film silicon solar cells, but also with applications for opto-electronic devices, detectors, and other types of solar cells such as heterojunction solar cells.

We discuss models of a-Si:H and develop further the representation of defects by amphoteric states. Using a simple model, we show—in agreement with layer-by-layer simulations and experimental results—that trapped electrons tend to dominate the electric field deformation in the initial state, whereas positively charged defects dominate in the degraded state.

Experimentally, we define the deposition parameter space accessible by plasma-enhanced chemical vapor deposition (PECVD) and explore that space by varying the deposition temperature, pressure, excitation frequency, power, and H_2/SiH_4 ratio for intrinsic absorber layers. This leads to a catalog of a-Si:H absorber layers with tunable properties and we incorporate these materials into solar cells. For every pressure, we find an optimum hydrogen dilution where the light-induced degradation of solar cells is minimal and comparable for all pressures.

Using narrow-bandgap absorbers, we demonstrate short-circuit current densities of $J_{\text{sc}} = 18.2\,\frac{\text{mA}}{\text{cm}^2}$ with a 300-nm-thick absorber layer and extract more than $20\,\frac{\text{mA}}{\text{cm}^2}$ from a cell with a 1000-nm-thick absorber layer. Using wide-bandgap absorbers, we achieve open-circuit voltages (V_{oc}) of 1.04 V and V_{oc}–fill factor products of 739 mV. For such materials, we find an increased V_{oc} dependence on substrate roughness. This is investigated by transmission electron microscopy and is attributed to porous a-Si:H material grown above peaks on the textured substrates. Depositing absorber layers in a triode reactor, we achieve efficiencies of 10.0% after light soaking.

Further, we describe observations of a reversible, light-induced V_{oc} increase of solar cells with thin p-type layers, and decrease with thick p-type layers, with a magnified effect on rough substrates. Based on layer measurements and simulations, we attribute the V_{oc} increase to the degradation of the p-layer and the V_{oc} decrease to the degradation of the absorber layer.

Key words: Solar energy, photovoltaics, thin-film, silicon, solar cell, amorphous, a-Si:H, protocrystalline, pc-Si:H, polymorphous, pm-Si:H, microcrystalline, μc-Si:H, micromorph, efficiency, open-circuit voltage, light-induced degradation, LID, Staebler-Wronski effect, SWE, Paschen, plasma, silane, hydrogen, ASA, simulation, amphoteric, defect, PECVD, triode, TEM, LPCVD, ellipsometry, FTIR, p-i-n.

Résumé

Les cellules solaires à couches minces de silicium offrent une réponse à la demande croissante d'énergie. Dans ces dispositifs, le silicium amorphe hydrogéné (*a*-Si:H) joue un rôle important : comme matériau absorbeur, mais également pour les couches dopées afin de réaliser des structures p-i-n. Cette thèse est dédiée à l'étude du *a*-Si:H et se focalise sur des cellules solaires à couches minces de silicium.

Dans cette thèse, le *a*-Si:H est modélisé et une représentation des défauts par des états amphotères est developpée. Il est montré que des électrons piégés dans la bande de conduction peuvent dominer le champ électrique dans l'état initial de la cellule, mais que des défauts chargés positivement deviennent dominants après dégradation.

Expérimentalement, l'espace des paramètres de dépôt accessible par le dépôt chimique en phase vapeur assisté par plasma est défini en variant les paramètres de dépôt tels que la température, la pression, la fréquence d'excitation, la puissance, et le ratio H_2/SiH_4 pour des dépôts d'absorbeurs intrinsèques. Cette étude mène à l'établissement d'un catalogue de couches de *a*-Si:H. Ces couches sont évaluées dans des cellules solaires. Pour chaque pression, nous trouvons une dilution d'hydrogène pour laquelle la dégradation causée par la lumière est minimale et comparable pour toutes les pressions.

Avec des absorbeurs ayant une bande d'énergie interdite étroite, il est démontré que des densités de courant de court-circuit de $J_{sc} = 18.2\,\frac{\mathrm{mA}}{\mathrm{cm}^2}$ avec un absorbeur de 300 nm d'épaisseur peuvent être atteintes et que plus de $20\,\frac{\mathrm{mA}}{\mathrm{cm}^2}$ dans le cas d'une cellule avec un absorbeur de 1000 nm peuvent être extraits. Avec des absorbeurs ayant une bande d'énergie interdite large, il est montré que des tensions de circuit ouvert (V_{co}) de 1.04 V, et que des produits de la V_{co} et du facteur de forme de 739 mV peuvent être atteints. Il est observé pour ces matériaux que la V_{co} dépend de la rugosité du substrat. Cette dépendence est attribuée à la présence de porosités aux sommets des rugosités. Avec des absorbeurs déposés dans un réacteur du type triode, des efficacités de 10.0 % après dégradation lumineuse sont démontrées.

Une augmentation réversible de la V_{co} induite par la lumière est observée pour des couches dopées p fines. A l'inverse, une réduction de la V_{co} est mesurée pour des couches dopées p épaisses. Ces effets sont plus prononcés sur des substrats rugueux. D'après des expériences et des simulations, l'augmentation de la V_{co} est attribuée à la dégradation de la couche p alors que la réduction de la V_{co} est liée à la dégradation de l'absorbeur.

Mots clefs : Energie solaire, photovoltaïque, couche mince, silicium, cellule solaire, amorphe, micromorphe, efficacité, tension de circuit ouvert, dégradation, effet Staebler-Wronski, hydrogène, amphotère, défaut, ellipsométrie.

Zusammenfassung

Dünnschichtsolarzellen aus Silizium sind eine mögliche Antwort auf die steigende Energienachfrage. Amorphes Silizium (a-Si:H) spielt dabei eine grosse Rolle, sowohl als Absorberschicht wie in dotierter Form. Diese Doktorarbeit ist amorphem Silizium gewidmet. Das Hauptaugenmerk richtet sich dabei auf Anwendungen in Dünnschichtsolarzellen, aber auch andere Anwendungen profitieren davon.

Wir diskutieren a-Si:H Modelle, insbesondere die Beschreibung von amphoteren Defektzuständen, die wir weiterentwickeln. Mittels eines einfaches Modells zeigen wir, in Übereinstimmung mit Schicht-basierten Simulationen und experimentellen Daten, dass im Leitungsband-Ausläufer gefangene Elektronen im Anfangs- und positiv geladene Defekte im degradierten Zustand die Deformation des elektrischen Feldes dominieren.

Experimentell bestimmen wir den über plasmaunterstützte Gasphasenabscheidung (PECVD) zugänglichen Depositionsparameterraum und loten ihn bezüglich Absorberschichten durch Variation von Temperatur, Druck, Frequenz, Leistung und H_2/SiH_4 Verhältnis aus. Daraus resultiert ein Katalog von Absorberschichten, die wir in Solarzellen einbauen. Für jeden Druck finden wir eine optimale Wasserstoffverdünnung mit vergleichbarer photoinduzierter Solarzellendegradation.

Mit einer 300 nm dicken Absorberschicht mit schmaler Bandlücke erreichen wir Kurzschlussstromdichten von $18.2\,\frac{\mathrm{mA}}{\mathrm{cm}^2}$. Mit einer zusätzlichen Vorspannung können wir über $20\,\frac{\mathrm{mA}}{\mathrm{cm}^2}$ aus einer Zelle mit einer 1000 nm dicken Absorberschicht herausholen. Absorberschichten mit weiter Bandlücke hingegen führen zu Leerlaufspannungen (V_{oc}) von 1.04 V und einem Produkt aus V_{oc} und Füllfaktor von 739 mV. Der V_{oc} solcher Materialien hängt verstärkt von der Substratrauigkeit ab. Wir untersuchen diese Abhängigkeit mittels Transmissions-Elektronenmikroskopie und können sie auf eine erhöhte a-Si:H-Porosität über Substratspitzen zurückführen. Mit Absorberschichten, die wir in einem Triodenreaktor abscheiden, erreichen wir Effizienzen von 10.0 % nach Photodegradation.

Schliesslich beobachten wir einen reversiblen, photoinduzierten V_{oc}-Anstieg für dünne, und eine V_{oc}-Reduktion für dicke p-Schichten, wobei der Effekt auf rauhen Substraten verstärkt ist. Basierend auf Schichtmessungen und Simulationen, führen wir den V_{oc}-Anstieg auf die Degradation der p-Schicht, die V_{oc}-Reduktion hingegen auf die Degradation der Absorberschicht zurück.

Stichwörter: Solarenergie, Photovoltaik, Dünnschicht, Silizium, Solarzelle, amorph, protokristallin, mikrokristallin, Leerlaufspannung, Effizienz, photoinduziert, Degradation, Staebler-Wronski Effekt, Silan, Wasserstoff, amphoter, Defekt, Ellipsometrie.

Contents

1 Introduction

Let us consider an average human being who needs to ingest a daily equivalent of about 2000 kcal of energy with food to maintain bodily functions and to exert mild work. This is 2.4 kWh per day. The same amount of energy in the form of electricity costs about 55 cents for private households.[1]

We correlate these 2.4 kWh of personal energy consumption per day with the consumption of external energy. Let our human being be an average Swiss. In that case, he consumes about 6300 W of power continuously (this corresponds to as much as four vacuum cleaners running day and night), adding up to 150 kWh per day.[2] This is more than three times more than suggested for the 2000-Watt Society [Bundesrat 02], and over 60 times more than what the average human being burns.[3]

To a large extent, the consumed energy is not sustainable, i.e. it will not be possible for everybody at anytime to consume the same amount of energy, because of a lack of materials (e.g. oil) or an overdose of waste (e.g. CO_2). One way to change this is for the average human being to become a responsible citizen of planet earth and reduce his energy consumption—another way is for the consumed energy to be renewable. There exist different possibilities to explore renewable energies: hydro-electric power, wind, biomass, geothermal energy, and others.[4] Most of these energy forms are converted solar energy, transmitted to the earth in the form of electromagnetic waves called sunlight. This thesis is about one technique of exploiting solar energy directly, by converting it into electricity.

---

[1] Calculated with the standard daytime electricity price for households in Zurich, 0.229 $\frac{\text{CHF}}{\text{kWh}}$ [EWZ 14].

[2] The total energy consumption in Switzerland in 2013 (897,000 TJ [SFOE 13]) divided by the total population in Switzerland at the end of 2012 (8,039,060 people [BFS 13]) gives 3500 W of continuous power consumption per person. This does not account for all consumed primary energy (used e.g. for the production of imported products). If all primary energy is included as detailed in [www.2000watt.ch 14], this gives 6300 W of continuous power consumption per person.

[3] Often, the quality of life is correlated with an increase of energy consumption, saturating, however, around 2000 W [Goldemberg 85]. Whether this correlation is fixed shall not be answered here, but our average human being does not want to reduce significantly his energy consumption that he hardly pays for—but others will pay for it, elsewhere or later.

[4] Strictly speaking, the primary energy of these energies are radioactive decays or fusion reactions, mostly in the sun, and in case of geothermal energy in the earth. Such nuclear reactions are not renewable. But comparing the lifetime of stars with that of human beings this energy source is unlimited in time.
The use of radioactive decays in nuclear power plants is of different nature: There, a chain reaction accelerates the natural decay tremendously, using the remaining radioactive elements so fast that they become rare, and leaving behind radioactive wastes that are not sustainable, either.

1.1 Solar energy in context

1.1.1 Technical context

Solar energy arrives with a continuous intensity of 1367 $\mathrm{W/m^2}$ on the outer atmosphere of the earth (see details in section 1.2). Multiplied with the earth's surface seen by the solar light, πr^2, where $r = 6371\,\mathrm{km}$ is the earth's radius, this gives 1.7×10^{17} W (170,000,000,000,000,000 W) of continuous solar power (see [Würfel 05] for a detailed discussion). This corresponds to about 100 million nuclear power plants, or 1000 times more than the primary power consumption of all human beings on earth.[5]

These back-of-the-envelope calculations show that it is technically feasible from an energy-flow point-of-view to provide for the worlds' energy consumption by solar energy. For large-scale applications, the abundance of different materials used for solar energy converters can be critical and should be addressed in research early on. In the worst case, technologies requiring rare materials will need to be replaced by other technologies (tellurium and indium, e.g., are rare materials limiting large-scale applications of certain solar cell types).

The distribution of solar irradiation around the whole world favors decentralized energy production, in most cases in form of electric energy. This can have a large impact on the electric grid—opportunities, but also difficulties. A whole branch of research deals with integration of solar into the grid.

---

[5] World consumption was 519 BTU per year in 2011 [EIA 13].

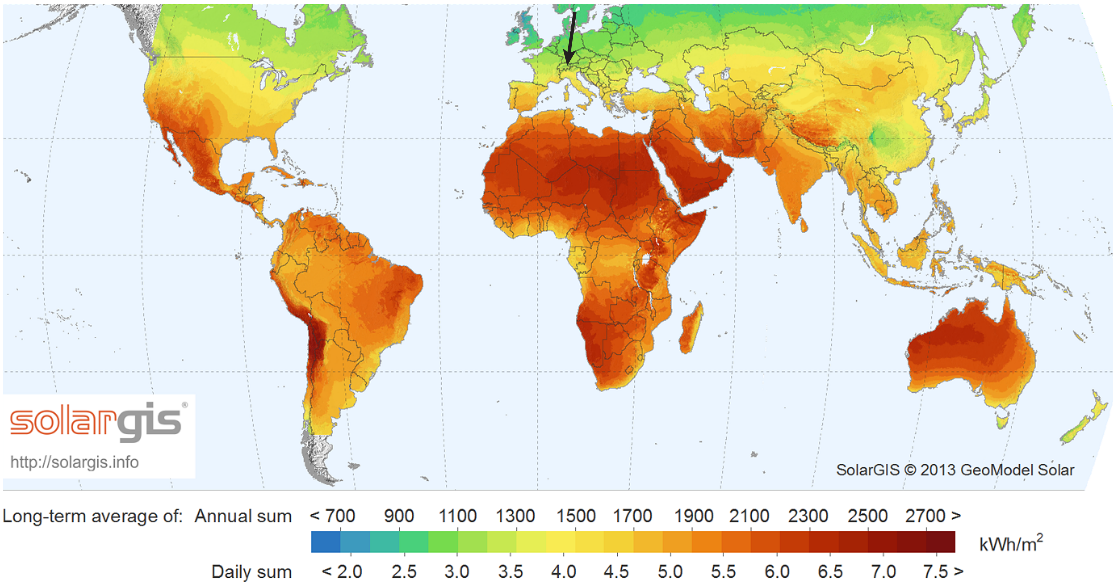

Figure 1.1: World map of the horizontal solar irradiance, integrated over one year. The arrow shows the location of the solar installation shown in Fig. 1.3a. This figure is reproduced with permission of SolarGIS © 2014 GeoModel Solar.

Although technically feasible, it is not reasonable to rely solely on solar energy; other renewable energies should be considered too. First of all, temporal fluctuations (daily and seasonal) of solar irradiation would lead to high costs for storage and grid extension. Second, solar energy is geographically not the best choice for every location: there are places where other energy sources such as wind can perform better or complement solar. Figure 1.1 shows a world map of the horizontal solar irradiance integrated over one year. Although the energy outcome can easily vary by a factor of two between an installation in central Europe and equatorial deserts, solar energy is highly interesting also in suboptimal places as proven by the large growth rates as shown in Fig. 1.2.

1.1.2 Economical context

While ecological conviction was the driving force behind civil solar installations in the beginning, only incentive schemes of solar energy led to a breakthrough of these technologies, particularly in Europe; these incentives are considered as a support to reach maturity, but can also be seen as compensation for the costs of conventional power plants based on non-renewable energies, where the external costs caused by pollution and the use of finite materials are transferred to society in any case. However, large incentives that are paid via the electricity price by end users such as in Germany or Czech Republic can also turn people's opinion from pro- to anti-solar.

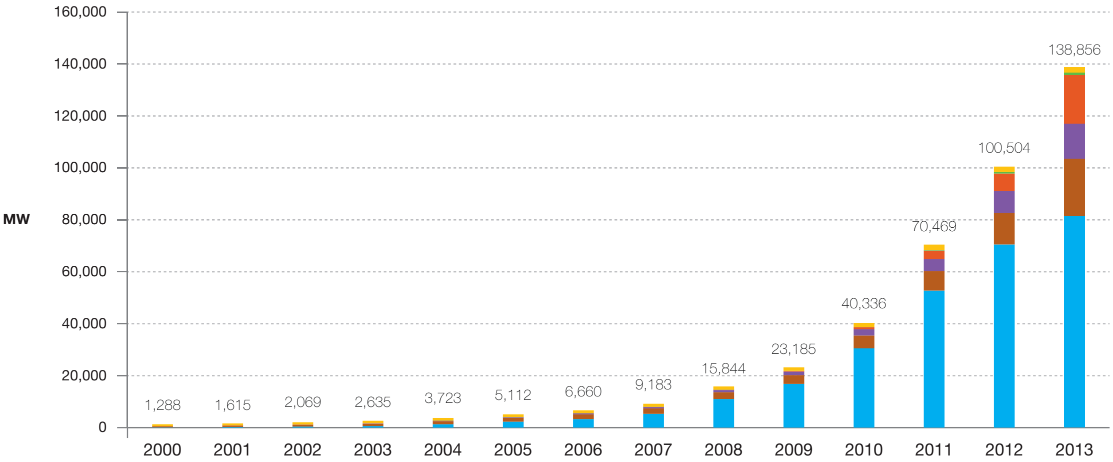

	2000	2001	2002	2003	2004	2005	2006	2007	2008	2009	2010	2011	2012	2013
🟨 RoW	751	807	887	964	993	1,003	1,108	1,150	1,226	1,306	1,590	2,098	2,098	2,098
🟩 MEA	n/a	n/a	n/a	n/a	1	1	1	2	3	25	80	205	570	953
🟥 China	19	24	42	52	62	70	80	100	140	300	800	3,300	6,800	18,600
🟪 Americas	21	24	54	102	163	246	355	522	828	1,328	2,410	4,590	8,365	13,727
🟫 APAC	368	496	686	916	1,198	1,502	1,827	2,098	2,628	3,373	4,951	7,513	12,159	21,992
🟦 Europe	129	265	399	601	1,306	2,291	3,289	5,312	11,020	16,854	30,505	52,764	70,513	81,488
Total	1,288	1,615	2,069	2,635	3,723	5,112	6,660	9,183	15,844	23,185	40,336	70,469	100,504	138,856

Figure 1.2: Global photovoltaic cumulative capacity from 2000 to 2013. Abbreviations: RoW—Rest of the world, MEA—Middle East and Africa, APAC—Asia Pacific. This figure is reproduced from [EPIA 14] with permission of EPIA.

Figure 1.3: (a): A photovoltaic installation integrated into the roof of a barn in the Swiss Alps, installed by the author. At the moment this picture was taken, it was snowing, but the modules were still injecting power into the electricity grid. (b): Modules mounted at PVLAB for the demonstration of the color tunability of thin-film silicon solar cells from black to terracotta for beautiful integration into different roofs, in particular into clay tile roofs. This figure is reproduced with permission of P. Heinstein.

Nowadays, retail grid parity has already been reached in many countries, which means it is cheaper for end users to produce their own solar energy than to buy electricity from an external company.[6] This has induced a large reorganization of the energy market that is still ongoing, leading to decentralization not only of power but also of money generation.

1.1.3 Ecological context

From the ecological point of view, solar energy is in most cases preferred to other technologies. However, its environmental impact is not negligible; in particular, energy use during solar cell production and land use are to be mentioned. The former is expressed by the energy payback time, the time after which a source of renewable energy has produced the same amount of energy that was necessary for its own production; for commercial photovoltaic systems installed in southern Europe, this is around one to two years [Raugei 12]. However, niche applications of photovoltaics such as mobile-phone chargers will hardly ever produce as much energy as was used for their production and are ecologically reasonable only when replacing other equipment or consumables.

Land use becomes significant with large-scale applications of solar power plants. Power plants using land formerly used for agriculture in rural areas is viewed unfavorably; at a minimum, double use—e.g. with sheep in the meadow below power plants—should be considered. Further, building-integrated photovoltaics—the double use of photovoltaic modules generating electricity and serving as architectural elements [Heinstein 13]—becomes more important. An example of an integration of black photovoltaic modules into the roof of a barn is shown in Fig. 1.3a. Further, techniques have been developed to adapt the solar-module color to different roof types [Perret-Aebi 14] such as shown in Fig. 1.3b.

---

[6] Different options are currently discussed, who pays the costs of the electric grid, energy storage, blind power, etc.. Traditionally, these costs were paid by the end user via a supplement to the energy price, which is no longer cost-effective for the grid operator, if an end user uses the grid only as a backup and energy storage solution.

1.1.4 Social context

The decentralization of power generation has a social impact on several levels: it is more difficult for large companies to sustain a monopoly on power distribution, and more people are aware of their energy consumption as they become power plant owners.

The highest solar irradiation around the equator, which decreases towards the poles, is clearly visible in Fig. 1.1. The distributions of wealth and technical development show opposite trends; hence, solar energy can contribute towards equalization.

1.2 Different solar energy technologies

The spectrum of solar irradiation is shown in Fig. 1.4. Different standards are used [ASTM 14b]: AM0 denotes the solar spectrum outside the atmosphere as seen by satellites with an integrated power density of 1367 W/m^2; solar cells used for space applications are optimized for this spectrum. AM1.5 denotes the spectrum of direct sunlight on the earth, if the sun passes through the atmosphere 1.5 times; this corresponds to a zenith angle of 48.19°.[7] This spectrum, including light from a cone of 2.5° totaling 900 W/m^2, is used for concentrating solar power plants. For most applications such as flat photovoltaic or thermal modules, the AM1.5g

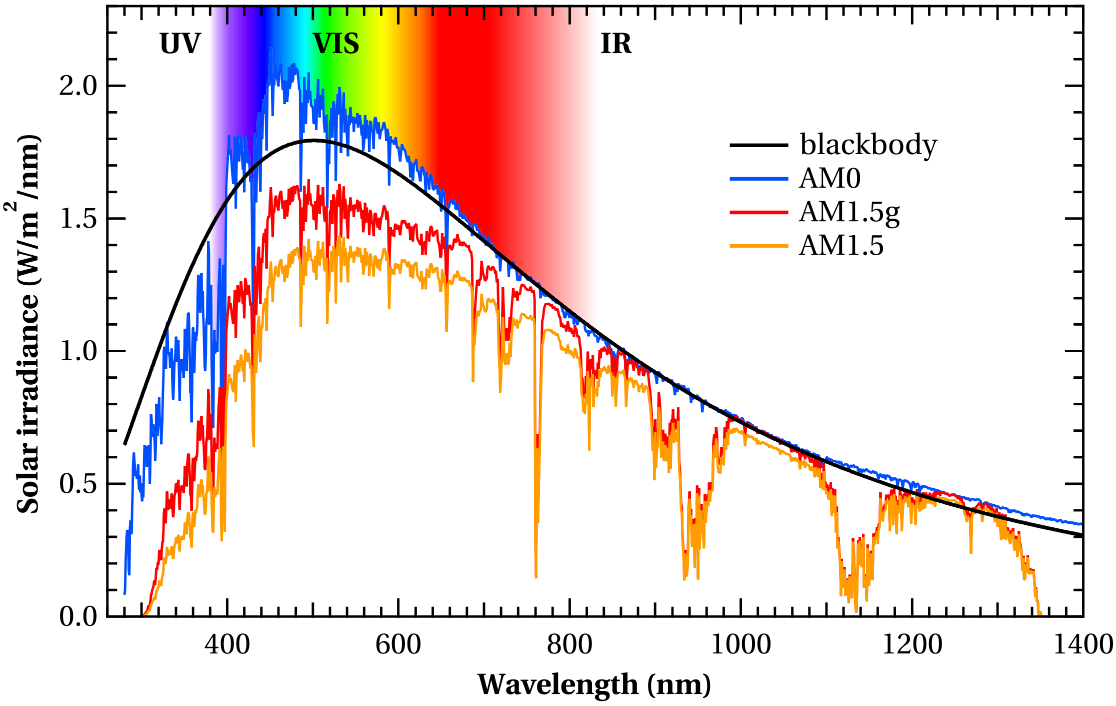

Figure 1.4: Different solar spectra and the blackbody radiation at a temperature of 5778 °C, with the color scale as seen by the human eye.

---

[7] At places of this latitude, e.g. Paris or Seattle, the sun is seen at this angle in summer at noon.

spectrum totaling 1000 $\frac{\mathrm{W}}{\mathrm{m}^2}$ is used which adds to the direct light of the AM1.5 spectrum diffuse light from scattering and multiple reflections, increasing in particular the blue component.

There are different ways of converting solar energy to energy forms that are of direct use to people. One of them is the conversion of solar energy to heat (see section 1.2.1) with the advantage of high efficiencies. A wider range of applications is possible if the solar energy is converted to electricity. This can be done either by conversion of heat into electricity (e.g. with steam turbines), or by direct conversion of solar energy into electricity, which is called photovoltaics (see section 1.2.2). The direct conversion of solar energy into other energy forms that are transportable and storable, such as hydrogen, is also possible [Abdi 13, Calvet 14]. However, it is questionable whether such a combined system, being more complex than individually optimized solar cells and hydrolysis reactors, is industrially feasible.

1.2.1 Solar-to-heat concepts

Solar energy converters can use sunlight to heat a medium. The easiest way is a flat panel with water circulating inside as often used on rooftops for tap-water heating (“solar collector”). Such a system can use the full solar spectrum, direct and diffuse solar light. It uses the full energy of each photon,[8] and has therefore a high conversion efficiency. However, the maximum temperature is rather low, limiting applications in particular for further conversion of heat into electricity.

The use of parabolic mirrors, concentrating the light onto a tube with a heat-transfer medium inside, allows a working fluid to reach higher temperatures which facilitates the conversion into electricity, e.g. via steam-engines. Even higher temperatures are used in towers onto which mirrors direct the sunlight. Both applications are industrially approved but use only direct sunlight, hence they are less suited to places where blue sky is rare or where dust is an issue.

1.2.2 Photovoltaic technologies

With the dramatic cost decrease of photovoltaic (PV) technologies that convert solar irradiation directly into electricity, these technologies gained importance during the last years relative to solar-to-heat concepts. The PV technology that is by far the most-widely used is based on crystalline silicon wafers (*c*-Si). Other solar cell technologies available on the market are based on thin-film silicon, copper-indium-gallium-selenide (CIGS), cadmium-telluride (CdTe), or III–V materials. At the research level, organic, dye-sensitized, or perovskite solar cells are investigated.

The general working principle in PV solar cells is the same: A photon creates an electron–hole pair in a semiconductor absorber material. This means that an electron gets the energy from a

---

[8] A photon is the smallest energy unit of light.

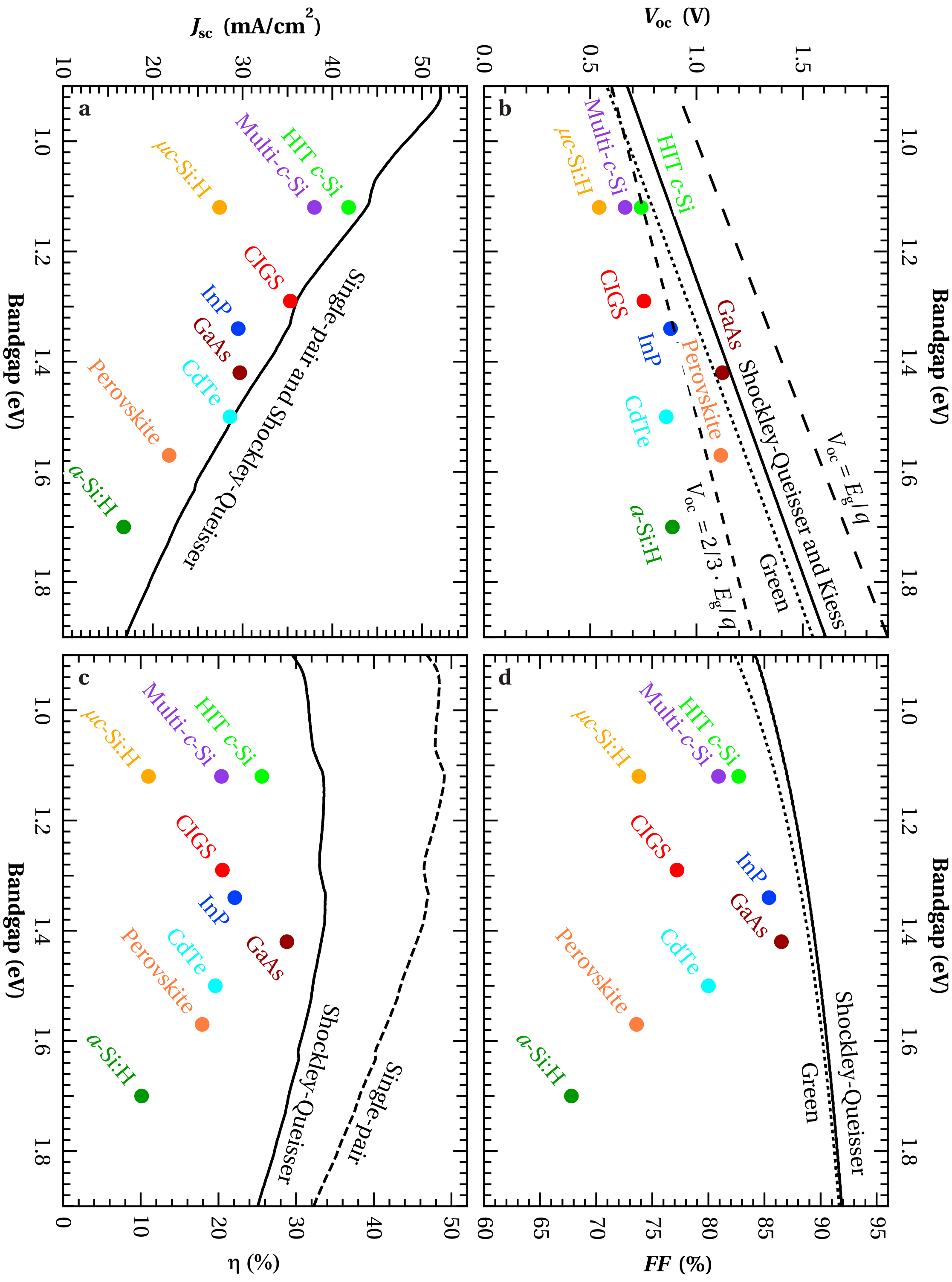

Figure 1.5: Theoretical limits and record-efficiency cells of different solar cell classes in terms of short-circuit current density (a), open-circuit voltage (b), conversion efficiency (c), and fill factor (d). We published these figures in modified form in [Shah 10], *Thin-film silicon solar cells* by Arvind Shah, ed., copyright 2010 CRC Press. The values here are updated.

photon, which allows it to move to a higher energy level. This process requires a minimum photon energy which corresponds to the bandgap of the semiconductor. For photons with a lower energy, the semiconductor is transparent. If a photon has a higher energy than the bandgap, the excess energy is lost in thermalization. Hence, one has the choice either to use an absorber material with a wide bandgap that utilizes a small fraction of the solar spectrum with a lot of energy per photon, or to use a narrow-bandgap absorber layer that utilizes a large fraction of the solar spectrum but with little energy per photon. This conceptual limitation reduces the maximum conversion efficiency of photovoltaic solar converters dramatically, in contrast to thermal solar converters. There, however, large efficiency losses occur in converting heat to electricity.

Figure 1.5 shows the main characteristics of record solar cells as a function of the bandgap. The values of open-circuit voltage (V_{oc}), fill factor (FF), short-circuit current density (J_{sc}), and conversion efficiency (η) are from [Green 14]. Definitions of these parameters and an example of a current-density–voltage ($J(V)$) curve are given in section 2.4.2. The bandgap values are from [Palik 98] (CdTe, GaAs, InP), [De Wolf 14] (perovskite), [Heath 02] (CIGS), and from our own measurements of hydrogenated amorphous silicon (a-Si:H). The lines represent the physical limits of these parameters; these calculations are detailed in appendix A.

In Fig. 1.5, we considered only single-junction solar cells without concentration. Stacking PV solar cells of different bandgaps on top of each other is one way to enhance the maximum solar efficiency. This concept is applied in concentrator solar cells or in multiple-junction thin-film silicon solar cells as detailed in section 1.2.4. Another application could be the combination of parabolic mirrors coated with solar cells—e.g. of a-Si:H or heterojunction solar cells—where the solar cells convert high-energy photons directly into electricity, and low-energy photons heat a transfer medium.

1.2.3 Thin-film silicon solar cells

Hydrogenated amorphous silicon

This thesis focuses on a-Si:H, which is a class of thin-film silicon (TF-Si) materials. To understand its nature, we first consider c-Si. Figure 1.6a shows the crystallographic unit cell of c-Si, which has the diamond cubic structure (two face-centered cubic lattices combined in zincblende structure), where each silicon forms four bonds to other silicon atoms. The lattice constant is $a = 5.43\,\text{Å}$, which means the Si–Si distance between nearest neighbors is $2.35\,\text{Å}$ and the density is $4.99 \times 10^{22}\,\text{atoms/cm}^3$ or $2.33\,\text{g/cm}^3$. The two-dimensional representation of this structure is shown in Fig. 1.6b with substitutional boron and phosphorus doping. Ideally (i.e. at 0 K), all bonds have the same length, the angles between two Si–Si bonds is always the tetrahedral angle 109.5°, and there are hardly any defects.

In contrast, Fig. 1.6c shows the two-dimensional representation of a-Si:H which is a disordered semiconductor—but the atoms are by no means randomly distributed: the average

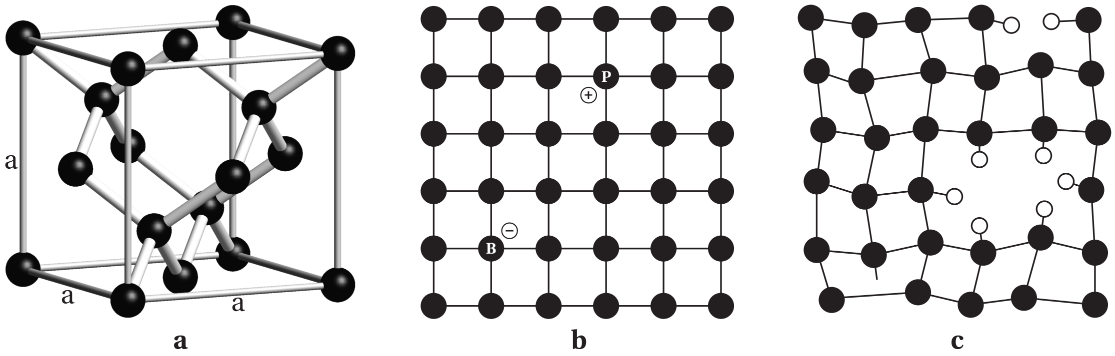

Figure 1.6: Three-dimensional structure of crystalline silicon (a) and its two-dimensional representation (b) with substitutional boron and phosphorus doping. (c): Two-dimensional representation of hydrogenated amorphous silicon with silicon atoms (filled circles), hydrogen atoms passivating dangling bonds (empty circles), an unpassivated dangling bond, and a void due to a divacancy.

bond length is the same as in crystalline silicon, also the distance between second and third nearest neighbors is the same, as X-ray and neutron scattering measurements show [Street 91, Schülke 81].

As shown by N. F. Mott et al. [Mott 69, Davis 70], amorphous materials can have a bandgap and conduct electricity similarly to crystalline semiconductors. The principle for *a*-Si:H is similar to that for *c*-Si (see Fig. 1.7): the sp^3-hybridisation of the four s and p valence electrons forms two bands with decreasing interatomic distance, separated by a forbidden energy gap. One could think that the bandgap difference between *c*-Si and *a*-Si:H (1.12 eV for *c*-Si and about 1.7 eV for *a*-Si:H) comes from a lower interatomic distance in the case of *a*-Si:H. Instead, the distances are the same, but the stress causes the higher bandgap—induced by different bonding angles, incorporated hydrogen,[9] and vacancies (the average coordination in *a*-Si:H is smaller than four) [Smets 12].

Another significant difference between *c*-Si and *a*-Si:H is the stronger absorption of *a*-Si:H at photon energies higher than the bandgap. Figure 1.8b shows a schematic band diagram in the reciprocal space of an indirect semiconductor such as *c*-Si. In this case, the minimum energy of the conduction band (CB) is not at the same crystal momentum k as the maximum energy of the valence band (VB) as is the case for direct semiconductors (Fig. 1.8a). Hence, a transition with the energy $E_g = 1.12\,\text{eV}$ is possible only if a phonon[10] is involved that compensates for the momentum, which reduces the transition (hence, absorption) probability. A direct transition without phonons is possible only above $E_g' \approx 3.4\,\text{eV}$. Like *c*-Si, *a*-Si:H is in principle an indirect semiconductor but with less sharply defined bands in the reciprocal space as shown in Fig. 1.8c. Therefore, direct transitions between the VB and CB are possible at energies that are close to

---

[9] Strictly speaking, the abbreviation of amorphous silicon is *a*-Si. However, this material contains so many defects in the form of unsaturated dangling bonds that it is technically of no use. For this thesis, we always investigated hydrogenated amorphous silicon, *a*-Si:H, that is called sometimes amorphous silicon for simplicity.

[10] A phonon is the smallest energy unit of vibration.

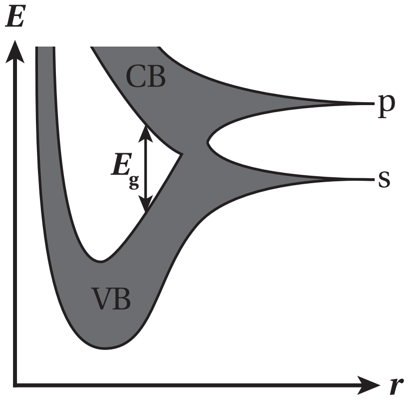

Figure 1.7: Schematic energy diagram of the bandgap splitting with decreasing interatomic distance r.

the CB-minimum and VB-maximum difference, without necessitating phonons, which leads to stronger light absorption in *a*-Si:H as compared to *c*-Si. This allows for much thinner *a*-Si:H absorber layers (on the order of 200 nm with adequate light trapping) as compared to *c*-Si absorber layers, which are 1000 times thicker.

p-*i*-*n* junctions

The discovery that *a*-Si:H as a disordered material could be doped [Spear 75] was surprising, and led soon to the first solar cells [Carlson 76] and thin-film transistors [Comber 79], and to the commercialization of solar cells with monolithic interconnection of single solar cells into small modules for applications such as calculators.

The heart of TF-Si solar cells are junctions made of *p*-type, intrinsic (*i*), and *n*-type silicon. In contrast to *c*-Si solar cells, where thin slices of silicon are cut out of large silicon crystals, TF-Si solar cells can be grown directly from silicon in the gas phase by plasma-enhanced chemical vapor deposition (see chapter 5). They can be deposited either in the *p*-*i*-*n* or in the

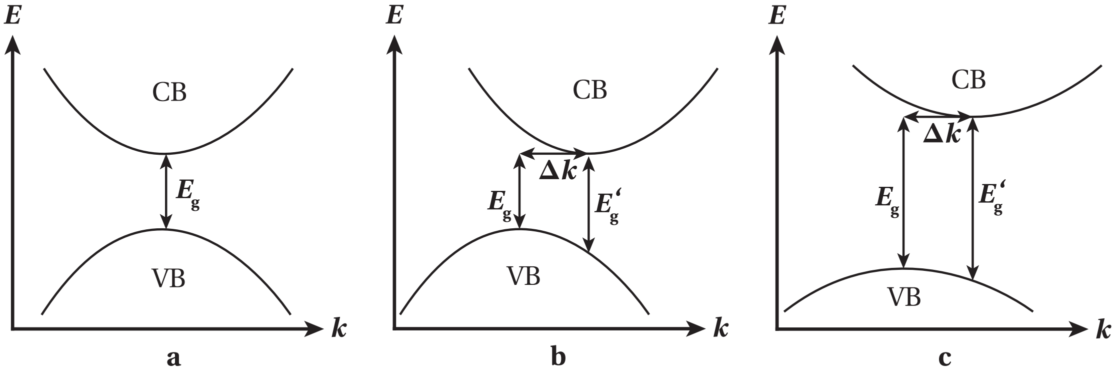

Figure 1.8: Schematic band diagrams in the reciprocal space for direct (a, e.g. CdTe), indirect (b, e.g. *c*-Si), and non-direct (c, e.g. *a*-Si:H) semiconductors.

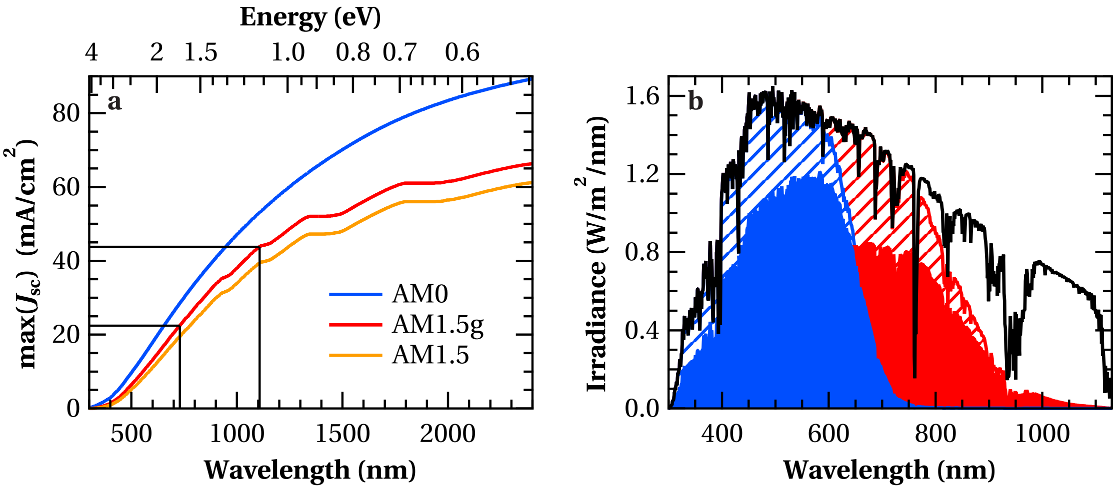

Figure 1.9: (a): Maximum current density that can be obtained for absorber materials with a given bandgap energy (top axis) and the corresponding wavelength (bottom axis) for three spectra introduced in Fig. 1.4. The black lines mark the bandgaps of 1.7 for *a*-Si:H and 1.12 eV for *μc*-Si:H. (b): Spectral splitting in micromorph solar cells, calculated from typical absorption coefficients of *a*-Si:H (the same as in Fig. 2.8) and *μc*-Si:H. Due to the wider bandgap of *a*-Si:H (blue), the amount of energy per absorbed photon is higher than in *μc*-Si:H (red).

n-*i*-*p* sequence with transparent conductive oxides (TCOs) on both sides of the junction; the processing is described in chapter 2 and a typical layer stack is shown in Fig. 8.1.

The electrons and holes, generated in the *i*-layer, are separated by the electric field that is spanned by the *p*-*i*-*n* junction (for details see chapter 4). Holes are collected in the *p*-layer, electrons in the *n*-layer. As holes are slower and tend to get lost in recombination more easily than electrons, the light always enters through the *p*-layer so that most holes are generated close to the *p*-layer, which facilitates their collection. Consequently, *p*-*i*-*n* solar cells need to be deposited in the superstrate configuration on transparent substrates (usually glass), while *n*-*i*-*p* solar cells are deposited in the substrate configuration on any, also opaque, substrate, which allows, in particular, deposition on flexible substrates such as stainless steel.

Spectral use of thin-film silicon solar cells

As seen in section 1.2.2, the current density that can be provided by a solar cell depends strongly on the bandgap of the absorber material. Figure 1.9a shows the maximum current density that can be obtained for materials with a given bandgap for the three spectra introduced in section 1.2. As in Fig. 1.5a, this upper current-density limit assumes that all photons with an energy higher than the bandgap contribute to J_{sc}, and that all photons with a lower energy are lost. Multiple electron-hole pair generation from a single photon is not considered. This gives an absolute upper limit—without any reflection or parasitic absorption—of 22.4 mA/cm^2 for a bandgap of 1.7 eV as is typical for *a*-Si:H, and of 43.8 mA /cm^2 for a bandgap of 1.12 eV, corresponding to microcrystalline silicon (*μc*-Si:H) or *c*-Si.

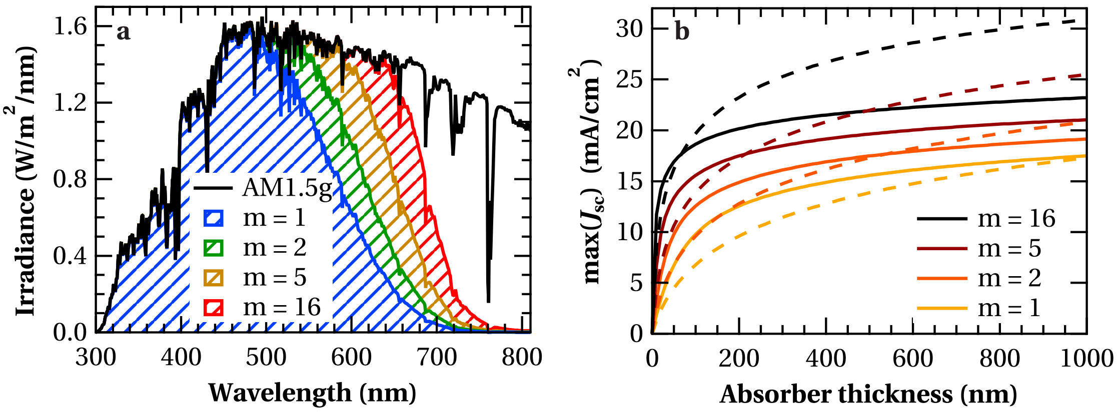

Figure 1.10: (a): Absorbed spectral power in *a*-Si:H solar cells, calculated with different effective light-path enhancement factors *m*. (b): Theoretical current-density maximum of solar cells with *a*-Si:H (lines) and *µc*-Si:H absorbers materials (dashed) as a function of the absorber thickness. We published these figures in modified form in [Shah 10], *Thin-film silicon solar cells* by Arvind Shah, ed., copyright 2010 CRC Press.

While solar cells with narrow-bandgap absorber layers provide high current densities, their voltage is low, and vice versa for wide-bandgap absorber layers. Solar cells combining subcells with different absorber-layer bandgaps profit from both advantages simultaneously, allowing for generally higher conversion efficiencies. The combination of a top cell with an *a*-Si:H absorber and a bottom cell with a *µc*-Si:H absorber layer is called a micromorph solar cell. The spectral distribution between top and bottom cells is shown in Fig. 1.9b. Here, typical absorption coefficients for *a*-Si:H and *µc*-Si:H were assumed, with a light-path enhancement factor of 5 for the 200-nm-thick top cell and 10 for the 2000-nm-thick bottom cell.

In Figure 1.10a, we compare the absorbed spectral power I_A for different light-path enhancement factors *m* for 200-nm-thick single-junction *a*-Si:H solar cells with an absorber bandgap of 1.7 eV. These curves are calculated from the irradiance *I* as

$$I_\mathrm{A} = I \times \left(1 - e^{-\alpha \cdot d \cdot m}\right), \tag{1.1}$$

where α is the absorption coefficient of *a*-Si:H as shown in Fig. 2.8, and *d* is the absorber thickness. Light trapping for TF-Si solar cells is discussed e.g. in [Söderström 13, Boccard 12b] and references therein. Effective light-path enhancement can be obtained by growing TF-Si solar cells on rough substrates and back reflectors. $m = 1$ corresponds to a single pass of incident light through a solar cell (flat substrate, no back reflector), $m = 2$ to a double pass (flat substrate with an ideal specular back reflector), $m = 5$ to multiple passes (rather smooth substrate with a scattering back reflector), and $m = 16$ closer to the Yablonovitch limit [Yablonovitch 87] considering scattering from a typical TCO into silicon as the absorber layer (for scattering from air into silicon, it is 50).

Figure 1.10b shows the maximum current density that can be obtained with a-Si:H and μc-Si:H absorbers under the conditions of no reflection, collection, or parasitic absorption loss, i.e. if every incident photon creates exactly one collected electron-hole pair. We note:

- The factor m and the absorber layer thickness have the same influence on the maximum current according to equation (1.1).
- Thicker absorbers/better light trapping are more important for μc-Si:H than for a-Si:H because the indirect bandgap is more pronounced.
- The impact of m on the current density, both absolutely and relative, is larger for thin than for thick absorbers. This means that it is more important to use rough substrates for thin solar cells, and one can accept smoother substrates for thick cells.

Unfortunately, the use of rough substrates can induce zones of poor material quality. This tradeoff between good optical/poor electrical properties of solar cells on strongly scattering (rough) substrates, and good electrical/poor optical properties on smooth substrates, is addressed at several places in this thesis.

For the deposition of multiple-junction solar cells, we worked closely together with S. Hänni and G. Bugnon, who developed μc-Si:H solar cells [Hänni 14, Bugnon 13], with M. Boccard, who combined a-Si:H, μc-Si:H, and intermediate reflectors in high-efficiency micromorph solar cells [Boccard 12b], and with J.-W. Schüttauf, who developed amorphous silicon-germanium alloys (a-SiGe:H) for applications in triple- and quadruple-junction solar cells. For solar cells in the n-i-p configuration, we collaborated with K. Söderström and R. Biron [Söderström 13, Biron 13].

1.2.4 Pros and cons of thin-film silicon solar cells

Compared to other PV technologies, TF-Si solar cells deposited by plasma-enhanced chemical vapor deposition (PECVD) have great advantages:

- *Abundant materials:* The materials used are non-toxic in production and for disposal after end-of-life, and abundant in amounts that allow for upscaling to the production of modules in the range of terawatt peak power.
- *Low energy payback time:* The energy payback time is lower than for other types of solar cells.
- *Low temperature:* All steps in the production chain of TF-Si solar cells can be performed at temperatures below 200 °C.[11] Hence, they are compatible with a wide variety of substrates such as glass and low-cost flexible substrates like plastic foils that are destinated for industrially advantageous roll-to-roll processes.
- *Automated cell interconnections:* Laser scribing interconnections between solar cells allow for low production costs on large areas, in contrast to individually soldered connections for c-Si-wafer-based solar cells.

---

[11] If the substrates allow, higher temperatures are common e.g. for SnO_2 or Ag deposition; however, low-temperature alternatives to these processes exist.

- *Mature deposition techniques:* For upscaling from laboratory cells to large modules on glass substrates, one can profit from the experience of flat-panel display production for which production has been intensively developed in recent decades.
- *High energy yield:* The energy yield (produced energy per installed power) is superior to that of standard c-Si thanks to a lower temperature coefficient and self-annealing of a-Si:H at high temperatures.
- *Variable appearance:* With little efficiency loss, the optical appearance (e.g. color) of TF-Si modules can be varied, allowing for visually pleasing integration in buildings.

However, there are important drawbacks of TF-Si:

- *Low efficiencies:* The conversion efficiencies of TF-Si solar cells are low compared to other technologies and theoretical limits. The main reason is the poor material quality of the absorber layers—the mobility and lifetime of charge carriers in a-Si:H materials will never be comparable to that of c-Si due to its amorphous nature. This trend is weaker for μc-Si:H (being a mixed material including a crystalline and an amorphous phase) and stronger for amorphous silicon alloys with carbon, oxygen, or germanium.
- *Degradation:* TF-Si solar cells degrade substantially at the beginning of operation until they reach the degraded state (Staebler-Wronski effect), which depends on the cell environment and history. This is accounted for in the advertised peak power, but buying TF-Si modules is psychologically difficult if the modules degrade in the first months of operation.
- *Demanding encapsulation:* Proper encapsulation of TF-Si solar cells is highly important, mainly because of the humidity sensitivity of the ZnO that is often used as the TCO for the front and back contacts. One way to deal with this is the use of a second glass at the back side instead of a back sheet. However, this increases the weight, and hence, the installation costs.

Very recently, several new certified world records of TF-Si solar cell conversion efficiency were presented: 10.1% [Matsui 13b] for a-Si:H single-junction solar cells, 10.7% [Hänni 13, Hänni 14] and 11.0% [Sai 13, Green 14] for μc-Si:H single-junction solar cells, 12.2% [TEL solar 14a] for micromorph tandem silicon solar modules (G5 size, 1.43 m^2) and 12.6% [Boccard 14] for micromorph tandem silicon solar cells, and 13.4% [Kim 13b] for triple-junction silicon solar cells. These are remarkable results for thin-film solar cells, and the small difference between laboratory scale and module-size efficiencies shows the maturity of this technology.

In the last years, solar module producers encountered a difficult economic environment with a stronger and faster drop of module prices than expected. However, they can not hide the fact that TF-Si solar cells have lost the efficiency race; with generally decreasing solar module prices, low production costs—which was a major argument for TF-Si solar cells—become less important because the relative importance of surface- and hence efficiency-related costs (glass, installation, etc.) increases.

1.3 Objectives and structure of this thesis

1.3.1 Motivation

The personal motivation for the research on photovoltaics is the conviction that it can contribute to a cleaner, safer, and more peaceful environment—be it TF-Si or another technology. The scientific motivation of this thesis is to understand properties of a-Si:H materials: fundamental properties, specific properties for application in solar cells, and the limitations of this material class.

1.3.2 Approach

A tremendous amount of research has been conducted for decades in the field of a-Si:H. To answer a few of the remaining open questions, we chose a fourfold approach:

- *Deposition conditions:* In the past, different names were given to a-Si:H materials produced in different institutes, each of which claimed their material to be best while sometimes lacking a systematic method to characterize and classify the materials. This thesis describes a wide variety of plasma-enhanced chemical vapor deposition conditions, and correlates them with growth models and material properties of the resulting layers and solar cells.

- *Material structure:* Many limitations of TF-Si solar cells are linked to structural properties of a-Si:H. For instance, the low diffusion length is a direct consequence of band tail and defect states that are inevitable in non-crystalline semiconductors. Therefore, high priority is given to the study of state-of-the-art a-Si:H materials within solar cells (including doping). These and newly synthesized materials, typically materials that are at the transition between a-Si:H and μc-Si:H which show very interesting and sometimes unexpected properties, were investigated and compared. In this, solar cells played a double role: on one hand they were the object to be optimized, on the other hand they are extremely sensitive tools to investigate materials incorporated therein. The leading question throughout this work was: which material is best for which application?

- *Electrical performance:* To understand the material properties of complex structures like TF-Si solar cells, we investigated the fundamental electrical aspects of the bulk materials as well as of the functional devices, namely how the electric field is built up between the p and n layers, how it is deformed as a function of the material properties, and how it can be tuned. For that reason, models of solar cells on the macro-scale as integrated circuits, and on the micro-scale as a stack of different layers were developed and tested against real devices.

- *Degradation:* Different effects lead to degradation of solar cells, among them the Staebler-Wronski effect (SWE). As it is not trivial to separate SWE-degradation from other kinds of degradation, we developed experimental techniques to distinguish them. We worked on the understanding of these effects (mainly of SWE) and on possibilities to overcome or to compensate for them.

Gathering the puzzle pieces of these four subjects together, a consistent picture of a-Si:H evolved from different plasma deposition conditions to layer properties and structure, to the performance of these layers in solar cells and the effect of material properties on light-induced degradation (LID) of high-efficiency solar cells.

A strong substrate roughness dependence, known from μc-Si:H materials, was observed for a-Si:H materials during these studies. Dedicated experiments with advanced transmission electron microscopy (TEM) methods followed, and models were developed to understand these effects.

This work was performed in close collaboration with other researchers focusing on other aspects of TF-Si solar cells, e.g. μc-Si:H, light trapping, the combination of different elements for multi-junction devices, or characterization.

1.3.3 Structure of this thesis

After this introductory chapter, this thesis contains the following chapters:

Chapter 2 details experimental processes of solar cell fabrication and characterization methods with a focus on setups that have not been described in other theses. Experimental details that are significant in other chapters are included in those chapters for convenience.

Chapter 3 describes a solar simulator that was developed during this thesis, fully based on light-emitting diodes (LEDs). It was designed specifically to study LID with in-situ measurement of solar cell performance under different conditions.

Chapter 4 derives different models for thin-film solar cells, with a focus on amphoteric-defect models that are refined, tested against real a-Si:H solar cells and other models, and used to understand observed solar cell performance trends.

Chapter 5 gives an overview of PECVD conditions. Plasmas of different gases are analyzed with basic tools available in industrial reactors, and simple models are used to correlate them with deposition rates and layer properties.

Chapter 6 is the heart of this thesis. It includes a description and comparison of intrinsic absorber layers and solar cells resulting from systematic scanning of the multidimensional PECVD parameter space spanned by excitation frequency, substrate temperature, H_2/SiH_4 ratio, and deposition pressure. These experimental layer and solar cell results are put into relation with plasma conditions and solar cell modeling of chapters 4 and 5.

Chapter 7 investigates the LID kinetics of solar cell series varying different deposition condition parameters. The solar simulator presented in chapter 3 was used for these studies.

Chapter 8 describes under which conditions V_{oc} decreases or increases during light soaking, combined with p-layer thickness and substrate roughness series. A model is developed, supported by layer measurements, that can explain the V_{oc} changes we observed and others reported in literature.

Chapter 9 pushes the range of deposition conditions for a-Si:H to the limits for application in TF-Si solar cells. We show solar cells with very narrow bandgaps (hence high currents) on one hand, and with very wide bandgaps (hence high voltages) on the other. Further, we present high-efficiency solar cells obtained with absorber layers deposited in a triode reactor.

Chapter 10 presents conclusions and an outlook.

1.4 Contribution of this thesis to the research field

This thesis contributes with many respects to the fields of a-Si:H and TF-Si solar cells:

- We established a catalog of intrinsic a-Si:H layers, covering the deposition conditions of low-pressure, high-pressure, protocrystalline and polymorphous silicon. From plasma conditions to layer properties, to solar cell properties and their degradation behavior, a consistent picture of a-Si:H evolved. In particular, we could not confirm specific deposition conditions leading to outstanding performance as stated in the literature, but found continuous trends.
- For different pressure regimes of a-Si:H absorber layers, we found an optimum H_2 dilution in terms of minimum LID: it increases with pressure. Solar cells with such optimized intrinsic absorber layers degrade similarly by about 15% under standard light-soaking conditions. Subtracting the degradation of ZnO, we believe that a LID of about 10% marks the lower limit for a-Si:H solar cells with 220-nm-thick intrinsic layers, if the bulk is limiting conversion efficiency. This is in agreement with lowest reported LID in the literature.
- Pushing the bandgaps of a-Si:H absorber layers to the limits, still providing device-grade material quality, led to a-Si:H single-junction solar cells with very high V_{oc} of 1.04 V with wide-bandgap absorbers, and to J_{sc} of 18.2 $\mathrm{mA/cm^2}$ for a 300-nm-thick narrow-bandgap absorber. From the same absorber layer, but grown 1000 nm thick in a standard solar cell, we could extract more than 20 $\mathrm{mA/cm^2}$ applying -2 V reverse bias voltage, showing its large potential for multi-junction devices.
- A reversible, light-induced V_{oc} increase for thin, and decrease for thick, p-type hydrogenated amorphous silicon carbide (p-(a-SiC:H)) layers was observed, with an enhanced effect on rough substrates. Based on layer and solar cell characterization, we simulated these solar cells with ASA and concluded that the V_{oc} increase is caused by LID of the p-(a-SiC:H) layer (enhancing the space-charge concentration at the p-i interface), but the V_{oc} decrease is caused by i-layer degradation. This is good news for

solar cell optimization, as the optimum p-(a-SiC:H) layer thickness after light soaking is lower than in the as-deposited state.

- A V_{oc} decrease with increasing substrate roughness, stronger for high than for low H_2 dilutions, was observed. With TEM images, we correlated this V_{oc} dependence with chains of microvoids, in the form of platelets, in the bulk absorber material above peaks of the underlaying ZnO. These structural effects could be explained by a growth model of a-Si:H.
- The systematic studies of a-Si:H materials are an important building block for multi-junction devices, allowing us to fine-tune the optical and electrical properties of subcells according to the needs in tandem-, triple-, or quadruple-junction solar cells developed by collaborators.
- The advantage of heterojunction solar cells over standard c-Si solar cells is the passivation by a-Si:H and the built-in electric field by doped a-Si:H layers. This thesis contributes to the understanding and specific optimization of these solar cells with the knowledge obtained on processing and properties of intrinsic and doped a-Si:H materials.
- In addition to energy generation, the findings of this thesis are also of direct use for applications of a-Si:H in other fields:
  - Solar cells for indoor applications with excellent low-illumination performance.
  - Position and illumination detectors on earth and in space.
  - Irradiation detectors for particle physics experiments and medical applications.
  - Waveguides for opto-electronic applications. Within this thesis, a-Si:H layers were provided to three institutes that successfully made waveguides out of them.

This thesis led to several publications: six publications as first author (of which five are peer-reviewed), and 13 publications as co-author; further articles are under review or in preparation. A list of all publications is given on page 241.

We attended four international conferences in Japan, Canada, the USA, and the Netherlands, giving five oral presentations and presenting two posters.

A patent evolved from industrial collaborations for TF-Si module optimizations with respect to building integration. This technology combines high efficiency and consumer-friendly module appearance.

2 Experimental processes and equipment

This chapter explains the processes and equipment that were used for our studies. Many processes and systems were described earlier in great detail and we refer to the literature for them. This gives room for more detailed descriptions of equipment that we used extensively and that had not been discussed previously by members of our institute. These are the Octopus deposition system (section 2.2.1), the ellipsometer (section 2.3.1), the photothermal deflection spectroscopy setup, and the dark conductivity measurements setup (section 2.3.4).

The equipment and techniques that we used during the thesis but from which no results are shown here (large plasma-enhanced chemical vapor deposition (PECVD) systems, sputter deposition tools, Fourier transform photocurrent spectroscopy (FTPS), etc.) are not described; this is the case also for techniques we used as customers only (atomic force microscopy (AFM), secondary-ion mass spectroscopy (SIMS), transmission electron microscopy (TEM), glow discharge optical emission spectroscopy (GDOES), charge extraction by linearly increasing voltage (CELIV), etc.).

During the thesis, we were accommodated twice (for three weeks in 2011, and for three months in 2012) at AIST[1] in Tsukuba, Japan; a short description of their processes and equipment is included in the following sections.

2.1 Process flows

2.1.1 Substrate preparation

For solar cells and layer depositions, we used mainly 0.5-mm-thick alkali-free aluminoborosilicate glass substrates from Schott, called AF 45 and later AF 32 [Schott 14], 82 mm × 41 mm. The manual cleaning of the substrates is detailed in [Cuony 11]. Both for solar cells and layer depositions, cleaned substrates were used; substrates without cleaning were used only for depositions for reactor conditioning or as dummy substrates to fill the substrate holder.

---

[1] Advanced Industrial Science and Technology

At AIST, 1.1-mm-thick glass substrates from Asahi Glass Company [AGC 14] were provided by AIST and cleaned by T. Matsui.

For specific analysis methods, single layers were by default co-deposited on double-side polished intrinsic crystalline silicon (c-Si) wafers ($> 1000\,\Omega\,\text{cm}$, 3 inch diameter, float zone, (100) orientation) from CrysTec [CrysTec 14]. These layers, cut into small pieces of about $1\,\text{cm} \times 2\,\text{cm}$ by laser or manually with a diamond tip, were taped with two strips of Kapton tape on dummy glass substrates. We did not observe any contamination originating from the Kapton tape in any deposition system. Nevertheless, we kept the quantities small, using two strips of about $2\,\text{mm} \times 8\,\text{mm}$ per wafer piece.

2.1.2 Layer processing

After layer depositions, the layers were stored in N_2, protected from light until characterization. In the case of hydrogenated amorphous silicon (a-Si:H), storage in air leads to oxidation of a few nanometers at the top. For layers that are thick enough, this is not a problem for optical measurements such as ellipsometry or photospectroscopy (in the model, it can be considered easily), but can cause misinterpretation of more precise measurements such as in photothermal deflection spectroscopy [Holovský 12].

The standard characterization of thin-film silicon (TF-Si) layers consisted of three-angle spectroscopic ellipsometry as described in section 2.3.1 and transmittance measurement (section 2.3.5). Sometimes, the thickness was determined by profilometer (section 2.3.7); in this case, part of the layer was marked either with permanent black felt pen or P-70 followed by a dry-etch of the silicon around by an SF_6 plasma (see section 2.2.4) and wet-etch of the black pen/P-70 by acetone. Finally, the layer was rinsed by isopropanol and a substrate–layer edge was accessible.

To determine the thickness of the ZnO layers, the ZnO was deposited on a mark of permanent black felt pen; the ZnO on top of it could be lifted off with acetone afterward to get a sustrate–ZnO edge. Alternatively, a P-70 mark was applied on the ZnO and masked the underlying layer during a wet-etch of ZnO in HNO_3.

2.1.3 Solar cell processing

In vacuum or N_2, ZnO substrates can be stored for weeks; after deposition of the p-i-n junction by PECVD, even storage in N_2 was not necessary, but storage of the cells in ambient air for a few days (protected against light and dust) reduced the probability of shunting. Prior to the low-pressure chemical vapor deposition (LPCVD) of the ZnO back contact, a mask was used for structuring the cells by painting the full area except the solar cells with permanent black felt pen. After deposition of the back contact, the felt pen layer was resolved in acetone and the ZnO peeled off there. The underlying silicon layers were removed by dry-etch as described in section 2.2.4.

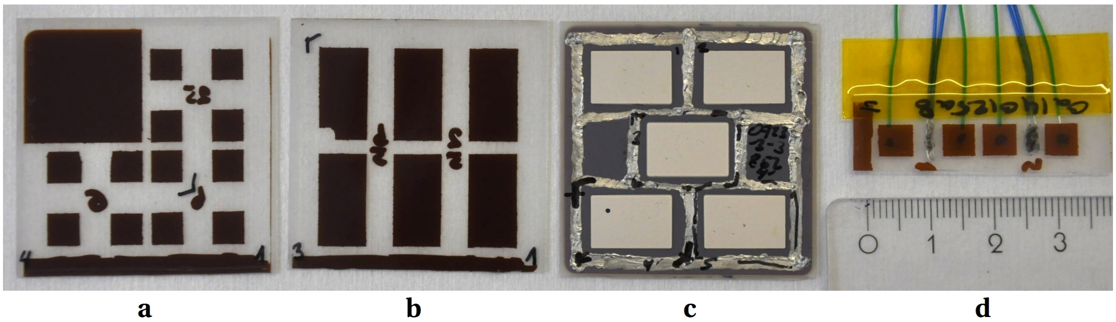

Figure 2.1: Pictures of solar cells on 41 mm × 41 mm glass substrates with often-used designs in this thesis. (a): Twelve cells of 5 mm × 5 mm with one cell of 18 mm × 18 mm for transmittance and reflectance measurements. (b): Six cells of 1.06 cm^2. (c): Backside of silver-back-contacted 1-cm^2 cells deposited at AIST. Instead of dry-etching of the silicon, an ultrasonic soldering on a scratch between the cells provided access to the front contact. Shunting of the cells via the silicon is not an issue; these layers are too resistive. (d): Four cells of 5 mm × 5 mm for degradation kinetics measurements. Only one wire was connected to the front and back contacts for simplicity. After about 10 cm, just before the connector, each wire was split in two for proper four-point measurements from there.

For smooth substrates, the back contact tended to peel off all over the substrate in acetone. In this case, P-70 marks were applied to the solar cells followed by a wet-etch of the ZnO in HNO_3 and a dry-etch of the silicon.

In most cases, the substrates were cut into half to 41 mm × 41 mm with space for six cells of 1 cm^2 or sixteen cells of 0.25 cm^2. Often, the structuring included only twelve cells of 0.25 cm^2, combining four cells to a larger area allowing the measurement of optical solar cell properties in the photospectrometer. Examples of different solar cell designs used in this thesis are given in Fig. 2.1.

For solar cells with metallic back contacts (standard at most institutes including Ecole Polytechnique (France), TU Delft, FZ Jülich, AIST), the back contact serves as the back reflector. This is not the case for our LPCVD ZnO back contact, where mostly a quasi-Lambertian, 3-mm-thick back reflector from GORE [GORE 14] based on polytetrafluoroethylene (PTFE) is used. A comparison of different back reflectors is presented in section 9.3.2.

2.2 Deposition systems and process tools

2.2.1 Octopus (plasma-enhanced chemical vapor deposition)

Figure 2.2 shows a picture of the Octopus[2] deposition tool from INDEOtec [INDEOtec 14]. Its main characteristics are:

---

[2] As this is the only Octopus system used for this thesis, we call it simply Octopus. It is the model Octopus I from INDEOtec, which also produces larger PECVD systems including Octopus II.

- *Modularity:* The central transfer chamber offers eight access ports for load locks or chamber units. These can be fully mounted and tested prior to connection to the system, as done with chamber F, which was added later for depositions of germanium-containing layers.
- *Easy adaptation:* The chamber units are designed such that they can easily be adapted for different applications. For instance, the gas and frequency distributions mentioned in the caption of Fig. 2.2 show only the typical configuration during this thesis, but others were used as well.
- *Software:* The software is written in LabVIEW and follows the concept of modularity. It allows fully automated processes and manual operation.
- *Secure:* Several security levels are implemented in both hardware and software and can be user-defined (e.g. preventing insertion of doping gases into chambers that are used only for intrinsic layers).
- *High vacuum:* The dual-pump system (primary pump and turbo-molecular pump) for deposition chambers provides a base pressure better than 1×10^{-7} mbar. The transfer chamber and load lock are pumped only by primary pumps, reaching a base pressure of 1×10^{-5} mbar.
- *IRFE closed-reactor principle:* Similar to the plasma box of TEL solar, the integrated radio frequency electrode (IRFE) is a closed reactor. In Octopus I, the substrate holder closes the reactor chamber from the top, and deposition occurs from the bottom.[3] The outer chamber is connected directly to the turbo-molecular pump, bypassing the pressure-regulating butterfly valve. Hence, the outer chamber is at a lower pressure than the deposition chamber, reducing contamination and "chemical memory".

  The IRFE reactor is built symmetrically for homogeneous depositions, with a showerhead for gas distribution. It is isothermal with both top and bottom electrodes heated. The inter-electrode distance is by default 15 mm and the substrate size is up to 125 mm × 125 mm (both electrodes have an area of 15 cm × 16 cm). For processes at high pressures, we developed dedicated substrate holders ("leak-free"). Most substrate holders are designed for co-deposition on four substrates of 41 mm × 41 mm.
- *Shared MFCs and power units:* The mass flow controllers (MFCs) and amplifiers are shared between all chambers. This has the drawback that only one process is possible at once, but the advantage of lower costs and faster modification.
- *Reactor cleaning:* The reactor cleaning is performed by a NF_3-Ar plasma in the IRFE reactor, with an overpressure of N_2 in the outer chamber (contrary to deposition processes) to reduce contamination during cleaning. A separate gas line is used for the NF_3 and Ar cleaning gases.

We discuss PECVD in further detail and compare the Octopus reactor design with others in section 5.1.

---

[3] In Octopus II, the IRFE is a closed box with the substrate holder being put on pins on the lower electrode by the robot. Deposition occurs there from the top.

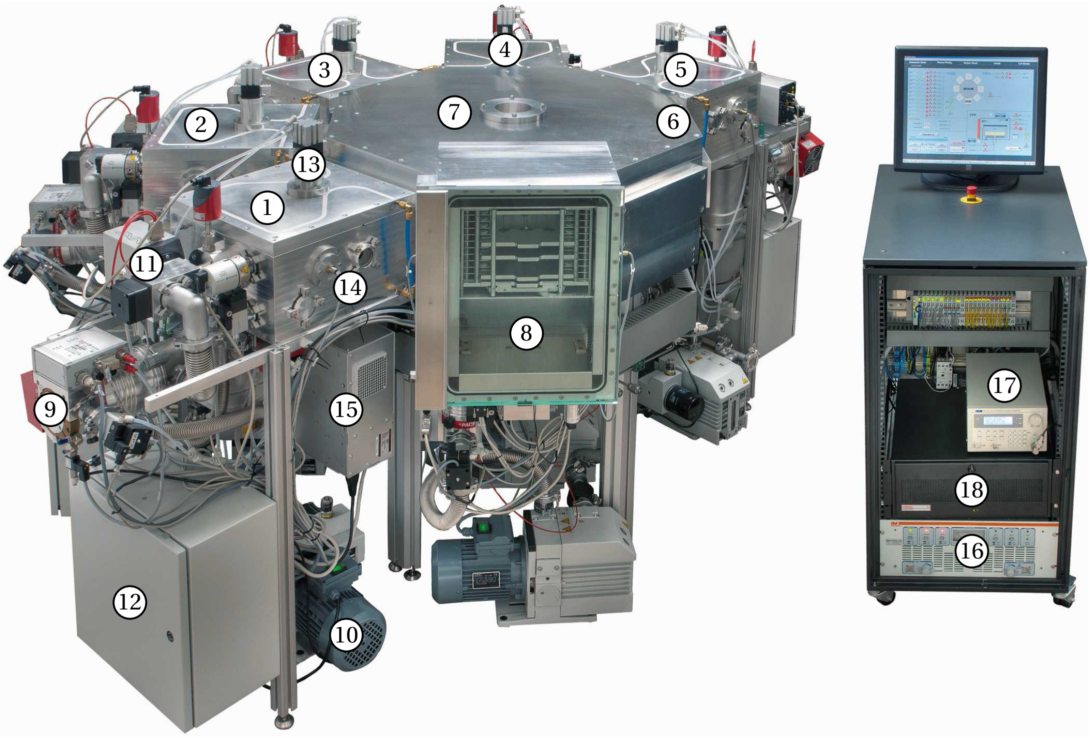

Figure 2.2: Octopus cluster tool for PECVD depositions with the following elements:
1) Chamber A: 13.56 MHz for intrinsic *a*-Si:H deposition (SiH_4, H_2, Ar, NF_3)
2) Chamber B: 81.36 MHz for intrinsic μc-Si:H deposition (SiH_4, H_2, Ar, NF_3)
3) Chamber C: 40.68 MHz for *p*-type material deposition
(SiH_4, H_2, $B(CH_3)_3$, CH_4, CO_2, Ar, NF_3)
4) Chamber D: 40.68 MHz for *n*-type material and intrinsic *a*-Si:H deposition
(SiH_4, H_2, PH_3, CH_4, CO_2, Ar, NF_3)
5) Chamber E: 13.56 MHz for intrinsic *a*-Si:H deposition (SiH_4, H_2, Ar, NF_3)
6) Chamber F: 40.68 MHz for intrinsic *a*-SiGe:H deposition (SiH_4, H_2, GeH_4, Ar, NF_3)
This chamber was added after the photograph was taken.
7) Transfer chamber with robot
8) Load lock for 10 sample holders
9) Turbo-molecular pump
10) Primary pump
11) Butterfly valve for pressure regulation
12) Electric circuits box serving as the interface between the computer and
chamber unit A
13) Pneumatic system to open/close the IRFE plasma reactor
14) Windows for diagnostics: plasma ignition detector, optical emission spectroscopy of plasma, visual access
15) Matching box with automated capacitors C_{load} and C_{tune}
16) Signal amplifier for different frequencies (later used only for very high frequencies)
A second amplifier for 13.56 MHz only was added later
17) Frequency generator providing the input signal for the VHF amplifier
18) Computer to control the deposition tool

2.2.2 System B (plasma-enhanced chemical vapor deposition)

System B is the fully manually operated PECVD deposition tool with two chambers—one for intrinsic, one for doped layers—which was used as much as Octopus for this thesis; it is described in [Cuony 11].

2.2.3 Chamber B and XL (low-pressure chemical vapor deposition)

We used different standards of LPCVD ZnO for front and back electrodes, mostly Z2 (about 2-µm-thick, strongly doped) and Z2.3 (about 2.3-µm-thick, less doped, but slightly rougher). Often, the front electrode surface was treated with an Ar plasma as described in section 2.2.4; the plasma treatment time is indicated behind the ZnO-type, Z2.3 7' indicates e.g. Z2.3, treated for seven minutes by an Ar plasma.

If nothing else is indicated, Z2.3 or, rarely, Z2 was used as the back contact (for *a*-Si:H single-junction devices, the higher transparency and light scattering with Z2.3 compensates for the higher resistivity as compared to Z2). Both front and back contacts were deposited in the small chamber B or the larger XL LPCVD system with similar properties. The reactors are described in [Faÿ 03, Ding 13]. The sheet resistances are around $9\,\Omega_\square$ for Z2 and $25\,\Omega_\square$ for Z2.3, respectively; the root-mean-square roughnesses are 80 (Z2) and 100 nm (Z2.3), and the haze, defined as the ratio between diffuse and total transmittance, are 37 (Z2) and 55% (Z2.3), respectively. Figure 2.3 shows the refractive index n and the extinction coefficient k for Z2. For further properties of the ZnO layers we refer to [Ding 13, Fanni 14] and section 8.3.5; an overview of different transparent conductive oxides (TCOs) used for single- and multi-junction TF-Si solar cells is given in [Hänni 14].

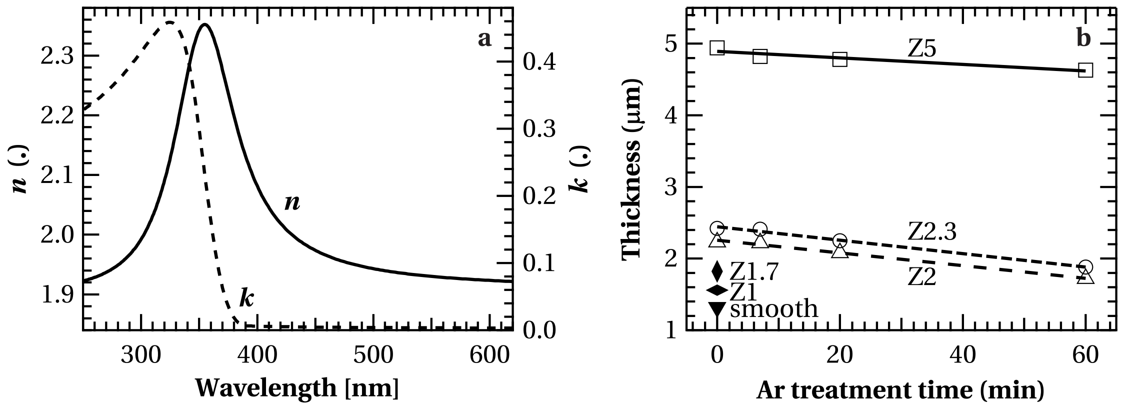

Figure 2.3: (a): (n, k) of Z2, determined from ellipsometry measurement after polishing (sample preparation: L. Fanni). (b): Thicknesses of LPCVD ZnO substrates for different Ar plasma treatment times (sample preparation: A. Billet). The lines are linear fits.

2.2.4 Integrated Plasma Limited & Oxford (Ar treatment and dry-etch)

The Ar plasma treatment modifies the surface texture from its initial V-shape into a smoother U-shape [Bailat 06, Cuony 11]. This reduces the shunt probability (hence, provides higher open-circuit voltage (V_{oc}) and fill factor (FF)), but also reduces the light scattering, leading to lower short-circuit current density (J_{sc}) [Python 09, Boccard 12b, Boccard 12a].

The smoothening is accompanied with a sputtering, hence a thickness decrease as shown in Fig. 2.3b for various ZnO standard substrates and Ar plasma treatment times. These treatments were made in the IPL (Integrated Plasma Limited) reactive-ion etching (RIE) tool using the low-pressure standard (see below); the thickness measurements were performed using a profilometer. The fits reveal sputtering rates of about 9 nm/min for Z2 and Z2.3, and about 5 nm/min for Z5. These sputtering rates—considering the average ZnO thickness—is lower than the sputtering rate reported in [Cuony 11] (15 nm/min), which was obtained from AFM measurements of completely sputtered samples (same Ar treatment conditions as here).

Until the end of 2011, the Ar plasma treatment of ZnO was performed in the IPL, later in the Oxford RIE. With a quartz plate on the electrode, the treatment recipes were optimized such that the resulting treatments were similar in both systems; the direct comparison of solar cells co-deposited on substrates treated once in Oxford and once in IPL revealed no significant difference. There was only a slightly increased shunt probability on Oxford-treated substrates, which we attributed to the less clean environment (the Oxford was not in the “clean” room, whereas the IPL was).

There were two Ar treatment standards, “low pressure” and “high pressure”. The treatment conditions are detailed in Tab. 2.1. The low-pressure standard was replaced by the high-pressure standard due to more stable plasma conditions—however, even the high-pressure standard was limited to 100 mTorr to avoid cauliflower-like structures observed at higher pressures [Cuony 11]. The comparison of low-pressure and high-pressure standards revealed no significant difference on solar cell performance.

Table 2.1: Reactive-ion-etching parameters for Ar treatment and SF_6-etching in the IPL and Oxford for the low- (LP) and high-pressure (HP) standards.

RIE	Pressure	RF power	Ar flow	O_2 flow	SF_6 flow
IPL (Ar LP)	30 mTorr	200 W	15 sccm	-	-
IPL (Ar HP)	100 mTorr	200 W	15 sccm	-	-
Oxford (Ar LP)	30 mTorr	325 W	90 sccm	2 sccm	-
Oxford (Ar HP)	100 mTorr	325 W	90 sccm	2 sccm	-
IPL (SF_6)	120 mTorr	60 W	-	12.1 sccm	92.3 sccm

2.3 Layer characterization techniques

Standard characterization methods of all deposited silicon layers for this thesis include ellipsometry (section 2.3.1) and photospectroscopy (section 2.3.5) for optical characterization and thickness determination. In the beginning of the thesis, the layer thicknesses were determined additionally by a profilometer (section 2.3.7); this step was skipped later because ellipsometry was more precise.

2.3.1 Spectroscopic ellipsometry

Ellipsometry is based on the principle that the polarization of light can change when it is reflected at an interface. Hence, by comparing the polarization of incident and reflected light, one can deduce the optical parameters of the interface. A detailed discussion of ellipsometry is given e.g. in [Fujiwara 07] and [Tompkins 05].

The UVISEL measurement setup

There are different technological implementations of ellipsometry; at PVLAB (UVISEL from Horiba Jubin Yvon), it is done as shown in Fig. 2.4 with the elements described in the caption.

The working principle is as follows: Via an optical fibre, the white, unpolarized light from the xenon arc lamp is transmitted to the excitation head with a beam-splitting polarizer made of birefringent MgF_2. Two beams merge: a linearly polarized beam, and a beam with different polarization states that is focused aside and is of no further interest (indicated in Fig. 2.4 by a thinner arrow). The electric field of the incident beam (seen from the sample), E^{i}, can be represented by $E^{\mathrm{i}}_{\mathrm{p}}$ and $E^{\mathrm{i}}_{\mathrm{s}}$ that are parallel (German "*parallel*") and perpendicular (German "*senkrecht*"), respectively, to the plane of incidence. It includes the angle A with the plane of incidence. [4] A schema with the relevant angles and polarizations is shown in Fig. 2.5.

The beam hits the sample under an angle Φ_2, which is in most cases equal to the angle of the reflected beam, Φ_1. However, the parallel and perpendicular components are reflected differently, according to the material-dependent reflection or Fresnel coefficients r_{p} and r_{s}. Therefore, the reflected beam is in general not linearly, but elliptically polarized. The electric field of the reflected beam, E^{r}, is now represented by its components $E^{\mathrm{r}}_{\mathrm{p}}$ and $E^{\mathrm{r}}_{\mathrm{s}}$. To measure the polarization, the beam is polarized by a photoelastic modulator (PEM). It consists of a fused silica bar on which monoaxial stress is applied by a piezo electric transducer at a frequency of 50 kHz. With this modulation, the beam is polarized via the photoelastic effect of fused silica, under the angle M to the incident plane. Finally, a second polarizer under the angle P

---

[4] The terminology of angles can be misleading: P stands for polarizer and is the polarizer with mechanically fixed polarization, M for modulator, and A for analyzer with variable polarization. These names are taken from ellipsometers, where a fixed polarizer is in the excitation head, and a variable polarizer, hence the analyzer, in the detection head. Technically, the polarizer P and the analyzer A are the same but differ only in their function. The modulator (or a rotating polarizer) can be either in the excitation or in the detection head, but is always located between the two polarizers.

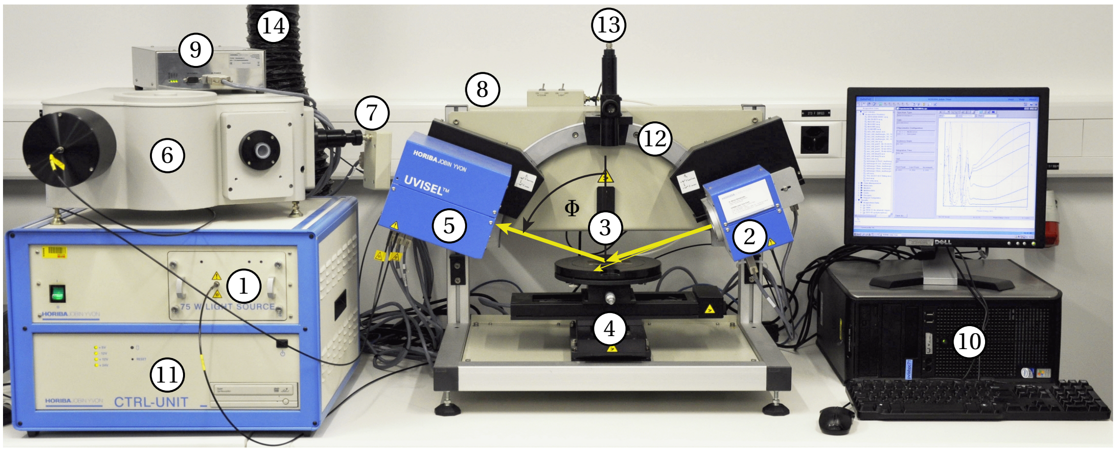

Figure 2.4: Picture of the UVISEL ellipsometer with the following elements:
1) Light source (xenon arc lamp)
2) Excitation head with analyzer
3) Sample with layer of interest face up
4) Sample holder on x-y stage with vacuum chuck
5) Detection head with modulator
6) IR monochromator
7) IR detector (InGaAs photodiode)
8) Monochromator for UV/VIS with detector (photomultiplier)
9) Power supply
10) Computer for measurement control and analysis
11) Computer for hardware control
12) Goniometer (polarizer and analyzer)
13) Autocollimator
14) Exhaust of hot air and ozone

filters the polarization of interest that is detected as a function of wavelength in one of the two monochromators. The time (t)-dependent signal measured there is $S(t) = S_0 + S_1 \cdot e^{\mathrm{i}\omega t} + S_2 \cdot e^{2\mathrm{i}\omega t}$, with S_0 the direct current (DC), S_1 and S_2 the first and second harmonic level measurements, and ω the modulator frequency.

In most cases, we measured in configuration II, i.e. $M = 0$, $A = +45°$, and $P - M = +45°$. Details are found in [Horiba 08].

Ellipsometry: (Δ, Ψ) vs. (I_s, I_c)

The ellipsometry measurement data consist of the complex ratios of the wavelength-dependent polarization changes of the parallel and perpendicular components, r_p and r_s, which are expressed by the fundamental equation of ellipsometry:

$$\rho = \frac{\frac{E_p^r}{E_p^i}}{\frac{E_s^r}{E_s^i}} \doteq \frac{r_p}{r_s} = \frac{|r_p|}{|r_s|} \cdot e^{\mathrm{i}(\delta_p - \delta_s)} = \tan(\Psi) \cdot e^{\mathrm{i}\Delta}. \tag{2.1}$$

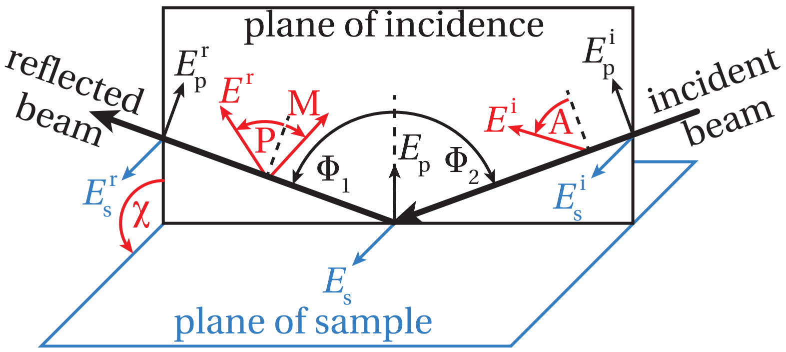

Figure 2.5: Schema of the light path and polarizations for ellipsometer measurements. Everything in the plane of incidence is black, the plane of sample is blue, and out of these planes is red. The variables are explained in the text.

Parameterizing ρ with (Δ, Ψ) gives the intuitive amplitude $\tan(\Psi) = \frac{|r_p|}{|r_s|}$ with $0° \le \Psi \le 90°$ and the phase shift difference $\Delta = \delta_p - \delta_s$ with $0° \le \Delta \le 360°$. While ellipsometry software such as WVASE from J.A. Woollam [Woollam 14] analyzes (Δ, Ψ) by default, the software DeltaPsi2 from Horiba [Horiba 14] works by default with another parameterization of the fundamental equation of ellipsometry that is closer to the actual measurement of $S(t)$. In configuration II, which is especially sensitive to Δ, this is

$$I_s = \sin(2\Psi)\cdot\sin(\Delta) \quad \text{and} \quad I_c = \sin(2\Psi)\cdot\cos(\Delta)\,. \tag{2.2}$$

Modeling of ellipsometry measurements with a Tauc-Lorentz oscillator

Modeling—like the measurements—was performed with the software DeltaPsi2 (DP2) from Horiba [Horiba 11]. Figure 2.6 shows a simple but adequate model for most *a*-Si:H layers that can be used also for doped *a*-Si:H and silicon alloys, as long as the *a*-Si:H structure is dominating. It includes the glass substrate, which had already been characterized, and reflection at the back surface is taken into account by the “void” layer.[5] It is followed by the *a*-Si:H layer, modelled by a Tauc-Lorentz oscillator. This oscillator defines the complex dielectric function $\varepsilon = \varepsilon_1 + i\varepsilon_2$ as described in [Jellison 96b] and corrected in [Jellison 96a]. Helpful comments are given in [Horiba 06].

The fitting parameters of the Tauc-Lorentz oscillator are:

- E_g^{TL}: Tauc-Lorentz bandgap below which $\varepsilon_2 \equiv 0$
- E_0: Peak central energy
- A: Amplitude of ε_2
- C: Broadening term of the oscillator
- ε_∞: High-frequency limit of the dielectric constant

---

[5] We investigated three alternatives: First to roughen the back surface by sand paper, second to paint it black, and third to roughen it and then paint it black. While the combined method is probably the best method for a single sample investigation, the reproducibility was better if a “void” layer was included at the back surface. Further arguments for this method are that it is less time-consuming and non-destructive, hence, this method was used for the analysis of layer series deposited on glass.

In most cases, the first four parameters were free fitting parameters, while ε_∞ was fixed. This parameter is correlated with others (seen in the correlation matrix) which leads to stronger scattering in series without physical background. The layer thickness was a free parameter too, as well as the thickness of a thin mixed-phase layer at the surface (taken into account using an effective-medium-approach (EMA) following the formalism developed by Bruggeman [Bruggeman 35]). This mixed-phase layer considers surface roughness originating from deposition [Aspnes 79], but also post-deposition oxidation of the surface; the surface layer thickness grows from less than 1 nm for typical *a*-Si:H depositions to several nanometers within days. The thickness of the surface layer is strongly correlated with the ratio of *a*-Si:H to void. For consistent results, we fixed this ratio at 50% but fitted on the thickness.

In addition to the Tauc-Lorentz fit parameters that allow direct comparison of different layers, the main interests of ellipsometry measurements are the layer thicknesses and the optical parameters of the bulk layer, (n,k) or $(\varepsilon_1,\varepsilon_2)$. For the use of other oscillator models such as Drude, Lorentz, and others, we refer to specific literature.

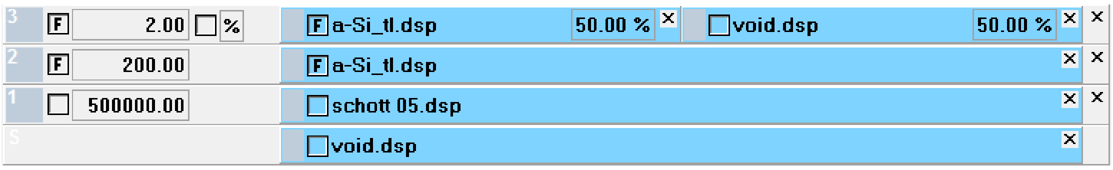
3 F 2.00 ☐ % F a-Si_tl.dsp 50.00 % ☐ void.dsp 50.00 %
2 F 200.00 F a-Si_tl.dsp
1 ☐ 500000.00 ☐ schott 05.dsp
S ☐ void.dsp

Figure 2.6: Model to fit a spectroscopic ellipsometry measurement of a hydrogenated amorphous silicon layer grown on glass with a Tauc-Lorentz oscillator.

Optimum measurement angles

Ellipsometry measurements are most sensitive on material properties, if the difference between r_p and r_s is largest, which is the case at the Brewster angle

$$\theta_\mathrm{B} \doteq \arctan\left(\frac{n_2}{n_1}\right) \tag{2.3}$$

for an interface between two materials with the refractive indices n_1 and n_2. Considering an interface with air, glass has a Brewster angle of about 56° and *c*-Si of 74°. Therefore, a measurement angle of 70° is a good compromise for most substrates, if one measures under a single angle, and we used (50°/60°/70°) for glass substrates and (60°/70°/80°) for *c*-Si substrates for variable-angle spectroscopic ellipsometry (VASE).[6]

Measurement precision and uniqueness of fitting

As shown in [Hilfiker 12] and confirmed by our own measurements, it is worthwile not only to analyze simultaneously data from VASE measurements instead of single-angle measurements,

---

[6] The abbreviation VASE is used both for variable-angle spectroscopic ellipsometry and the proprietary ellipsometry analysis software from J.A. Woollam. Later software versions are called WVASE.

but also to include transmittance measurements; this dramatically improves the uniqueness of fitting—which is even more important when analyzing unknown materials. Therefore, we performed simultaneous fitting of three-angle measurements combined with transmittance measurements from the photospectrometer in a so-called multi-model whenever this was possible.

For most applications, we measured (and considered in fitting) the whole accessible energy range from 0.6 to 6 eV equidistant in energy with a monochromator change at 880 nm (1.41 eV).

During the stay at AIST, we used an ellipsometer from J.A. Woollam (model EC-400) that uses a different technology and a diode array instead of monochromators. This makes the measurements much faster, but less precise. At AIST, ellipsometry data are analyzed by default with the VASE software. To get an estimate of absolute errors, we performed a cross check analyzing five-angle ellipsometry measurements taken with EC-400 (from 0.73 to 5 eV) and with UVISEL (from 0.6 to 6 eV) on the same samples. These measurements were analyzed once with VASE, once with DP2. This analysis revealed significant differences both in layer thickness (±2%) and bandgap (±0.01 eV), which is largely above the relative precision of each ellipsometer. This means that smaller effects can be investigated in layer series if they are analyzed using the same ellipsometer and software, but that the direct comparison of reported values needs careful interpretation. In our series, the observed trends were always the same, although with less scattering if measured with UVISEL.

For the most consistent data, layers deposited at AIST were measured with EC-400 but analyzed with DP2.

In-situ application of spectroscopic ellipsometry for thin-film silicon

Significant progress in the understanding of the growth process of TF-Si was obtained from in-situ ellipsometry measurements during layer growth such as performed by R.W. Collins et al. [Collins 02, Collins 03], P. Roca i Cabarrocas et al. [Roca i Cabarrocas 00, Roca i Cabarrocas 02], or H. Fujiwara et al. [Fujiwara 03, Fujiwara 04]. In recent studies, a new model for the dielectric function, replacing Tauc-Lorentz and based on two parameters only, was suggested [Kageyama 11, Kageyama 12].

2.3.2 Photothermal deflection spectroscopy (PDS)

The PDS measurement method was first presented in [Boccara 80] and since then has been widely used for absorption measurements over several orders of magnitude down to sub-bandgap absorption with resolution comparable to FTPS [Holovský 12] and the constant photocurrent method (CPM) [Vaněček 83], although using different measurement principles. A previous version of the PDS setup at IMT is described in [Wyrsch 92].

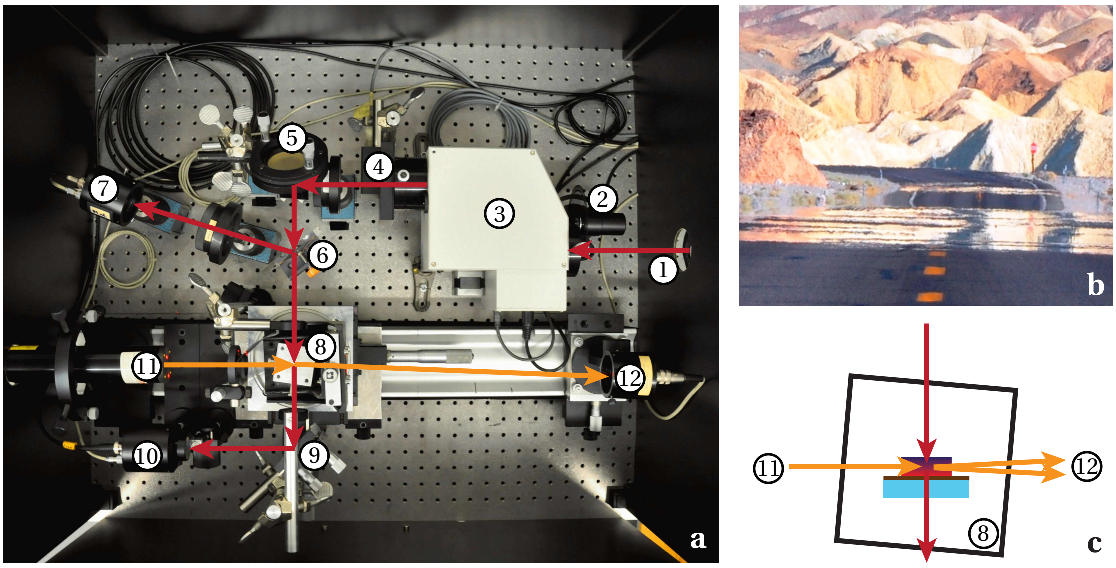

Figure 2.7: (a): The PDS setup with light paths (red: probe beam; orange: laser beam). The numbers are explained in the text. (b): The mirage-effect on a street in Death Valley (USA). (c): Schema of the light paths in the PDS measurement cuvette.

The current PDS setup at IMT is shown in Fig. 2.7a with a detailed schematic of the light paths around the sample in Fig. 2.7c. The white beam from a halogen lamp (1) enters the PDS setup on an optical table. The measurement precision is greatly improved by using the lock-in technique with a chopper wheel placed at (2) before the monochromator (3). Several optical filters (4) cut off higher harmonics of the monochromatic beam, before an optical system of several mirrors and lenses directs the beam towards the sample. A beam splitter (6) deflects a part of the beam towards a beam-intensity detector (7). The rest hits the sample (first layer, second substrate) mounted vertically in a quadratic quartz cuvette (8). The transmitted fraction of the light is reflected in (9) and detected in (10). A critical part of the PDS measurement is the alignment of the sample: a He-Ne laser beam coming from (11) should pass parallel to the layer of interest, as close as possible, though not hitting the sample. This is guaranteed by three microscrews on the sample stage allowing adjustment in vertical, horizontal, and azimuthal (around vertical) directions.

The measurement principle is based on the mirage effect [Murphy 80]: light being transmitted through a medium with a refractive-index gradient perpendicular to the light path induces bending of the light. A well-known example of the mirage effect is a hot street that seems to be wet, reflecting under small angles (cf. Fig. 2.7b). In the PDS setup, the cuvette is filled with a liquid whose refractive index is strongly temperature dependent (in the beginning of the thesis, we used carbon tetracloride (CCl_4), later the less carcinogenic Fluorinert FC-72 from 3M [3M 14]). Absorption of the probe beam, modulated by the chopper frequency, heats the sample and causes the temperature gradient. This causes a deflection of the laser beam;

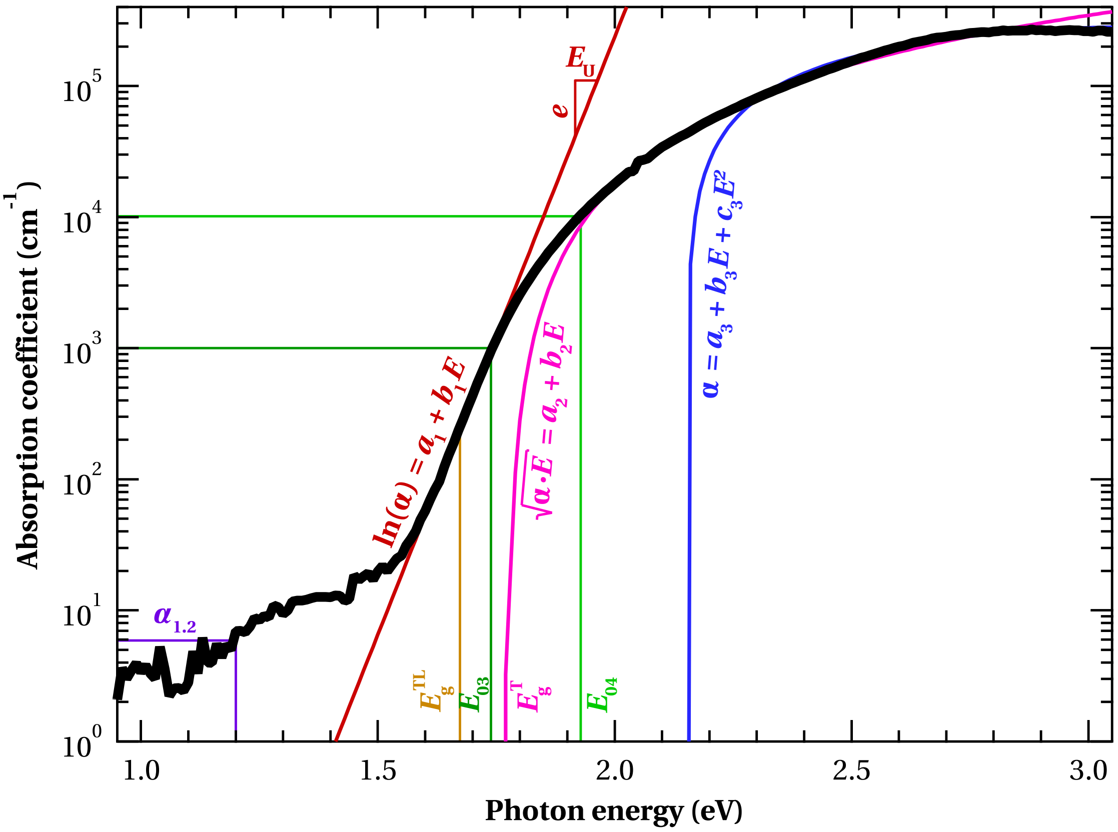

Figure 2.8: PDS measurement with indications of different bandgap measurement methods that are explained in the text.

from the position of the laser beam, being measured in (12), the absorptance in the sample is calculated assuming a linear relationship between the absorptance and the laser-beam deflection. [7]

The PDS measurement of a typical *a*-Si:H layer—the standard intrinsic absorber layer from system B (for deposition conditions, see the caption of Tab. 2.2)—in the initial state, 250 nm thick, grown on Schott AF 45 glass (hence, with glass absorption probably screening *a*-Si:H absorption) is shown in Fig. 2.8. We differentiate three regions: sub-bandgap absorption (below about 1.5 eV), bandtail-to-band absorption (between about 1.5 and 2.0 eV) and band-to-band absorption (above about 2.0 eV).

The measurement precision in the sub-bandgap region is often limited by the thickness of the layer: *a*-Si:H close to the amorphous-to-microcrystalline transition tends to have large internal stress leading to peeling of layers that are thicker than 100 to 200 nm, while layers more than 1000 nm thick would be ideal. For thinner layers, one can still determine the Urbach energy, but not sub-bandgap absorption. Further, low-absorbing substrates are needed (typically

---

[7] Often, it is thought that the refractive-index change in the PDS setup itself would cause the beam deflection. However, looking at Fig. 2.7c, one can see that in this case the laser beam would experience only a minimal parallel shift, but no deflection; for deflection, a refractive-index *gradient* is necessary.

fused silica), as the absorption of Schott AF 32 glass below 1.5 eV is on the same order as that of a few hundred nanometers of high-quality *a*-Si:H.

From sub-bandgap absorption, one can determine the defect concentration N_D; a common standard is to calculate it via $N_\mathrm{D} = c_{1.2} \cdot \alpha_{1.2}$ from the absorption coefficient α at 1.2 eV and the calibration constant $c_{1.2} \approx 2.4 \times 10^{16}\,\mathrm{cm/cm^3}$ obtained from calibrations with electron spin resonance (ESR) defect concentration measurements [Wyrsch 91, Wyrsch 92]. Defect concentrations are discussed in greater detail in section 4.3.2.

The linear (in semi-log scale) part of $\alpha(E)$ comes from the absorption in electron transitions between a band and the opposite band tail (cf. Fig. 4.3a). The linear fit around the point where the slope is steepest yields its slope denoted as Urbach energy E_U [Urbach 56] that is defined as the energy for which α increases by a factor e:

$$\alpha \propto e^{\frac{E}{E_\mathrm{U}}}. \tag{2.4}$$

The band-to-band absorption of *a*-Si:H materials can be represented by a parabolic curve; the blue line in Fig. 2.8 is a parabolic fit from 2.2 to 3 eV.

Several bandgap definitions that differ significantly are common for *a*-Si:H materials, as summarized for this example in Tab. 2.2. The Tauc-Lorentz bandgap was introduced in section 2.3.1. The Tauc [Tauc 66] or Cody bandgap $\left(E_\mathrm{g}^\mathrm{T}\right)$ [Cody 81] is determined from the so-called Tauc plot via $\sqrt{\alpha \cdot E} = a + bE$, where E_g^T is the energy of the crossing point between $\sqrt{\alpha \cdot E}$ and the energy axis. Similar bandgap definitions use other exponents x plotting $(\alpha \cdot E)^x$. These fitting-based bandgap definitions have the advantage that they can be related to physical explanations via band models. At the same time, this is a drawback, as these definitions are model dependent and the bandgap determination may not be possible for materials with different $\alpha(E)$ dependencies. For example, it does not make sense to determine a Tauc-Lorentz bandgap for biphase materials such as microcrystalline silicon where the absorption coefficient often shows two shoulders with two slopes.

The bandgap definitions E_{03} and E_{04} do not rely on models, but simply denote the energies at which α equals 1×10^3 or $1 \times 10^4\,\mathrm{cm^{-1}}$, respectively.

Table 2.2: Defect absorption, Urbach energy, and bandgap values obtained from the same absorption measurement by PDS (except E_g^TL for which ellipsometry combined with transmittance was used), but determined using different bandgap definitions. The deposition conditions of this layer were 32 sccm H_2 flow, 31 sccm SiH_4 flow, 0.5 mbar pressure, 3 W power, 70 MHz plasma excitation frequency, and 200 °C deposition temperature; the deposition rate was 2.6 Å/s.

$\alpha_{1.2}$	E_U	E_g^TL	E_g^T	E_{03}	E_{04}
5.9 cm^{-1}	47.6 meV	1.674 eV	1.773 eV	1.742 eV	1.927 eV

2.3.3 Fourier transform infrared spectroscopy (FTIR)

FTIR measurements were regularly used for intrinsic a-Si:H layer measurements, with the main focus on the microstructure factor

$$R^* = \frac{\text{HSM}}{\text{HSM}+\text{LSM}}, \tag{2.5}$$

where LSM and HSM are the integrals of the Gaussian fits of the low and high hydrogen stretching modes around 2000 cm^{-1} and 2090 cm^{-1}, respectively, of the transmittance curve.[8]

Technically, the transmittance T of the layer of interest was determined by $T = \frac{I_\text{sample}}{I_\text{reference}}$ with the light intensity I_x measured after passing through the sample or reference, respectively. A linear baseline fit T_baseline below the absorption peak was considered, and the fitting of the Gaussians was performed on the normalized transmittance $T_\text{norm} = \frac{T}{T_\text{baseline}}$. For this analysis, it was not necessary to consider the thickness of the layers.

More sophisticated methods of FTIR analysis of TF-Si materials are presented in [Smets 02, Smets 08, Bronneberg 11, Bronneberg 12].

In the literature, the interpretation of the LSM as a SiH stretching mode is generally accepted. However, there is no agreement on the HSM which is attributed to stretching modes of SiH_2, of SiH_3, or chainlike $(SiH_2)_n$ [Kageyama 11, Brodsky 77, Knights 78, Lucovsky 79, Shanks 80, Pollard 6, Ouwens 24, Smets 07b, Smets 09]. In the framework of this thesis, we do not have the experimental means to distinguish between these interpretations; hence, we use the name convention of A. H. M. Smets for the peaks that describes just their position, LSM and HSM. However, it is experimentally clear that the a-Si:H material quality is better for lower HSM hence lower R^* (see the discussion in chapter 6). Unfortunately, the measurement error for R^* was on the order of a few percent absolute.[9] This is good enough to differentiate very poor from very good materials, but not enough to optimize absorber layers based on FTIR measurements, because the solar cell performance—in particular its light-soaking behavior—is more sensitive.

The measurements presented here were taken at AIST with a Spectrum 2000 spectrometer from Perkin Elmer (with a dual sample holder for automated alternating measurements of the reference and sample). At IMT we used a Nicolet 8700 FTIR spectrometer from Thermo (with a manual change between the reference wafer and the sample), with a beam splitter made of KBr and a DTGS detector. The comparison of different wafer substrates revealed that the signal-to-noise ratio was best using intrinsic, double-side polished, 250-μm-thick wafers. However, the use of such thin wafers limited the resolution to 6 cm^{-1} (see the discussion in

---

[8] The inclusion of a third Gaussian (corresponding to the medium hydrogen stretching mode MSM) as suggested repeatedly [Fujiwara 02, Vignoli 03, Lebib 05, Smets 07b] would have provided a better fit in some cases (especially for layers deposited at high pressures), however, a direct comparison of R^* would have been more difficult.

[9] Members of other laboratories confirmed such errors, induced not only by measurement but also by fitting and baseline correction.

[Cuony 11]). For typical measurements, we averaged over 32 scans and purged the setup with N_2 for one hour between inserting the sample and measuring to reduce artifacts from H_2O and CO_2. The setup is permanently purged with N_2.

2.3.4 Dark conductivity measurement

Dark conductivity (σ_{dark}) measurements were used mainly for doped layers, especially for the development of boron- and gallium-doped hydrogenated amorphous silicon carbide (p-(a-SiC:H)) layers (see section 8.3.2) to determine the conductivity and activation energy E_{act}. For intrinsic layers, we performed such measurements as well, however, with less impact on solar cell development as dark conductivity is hardly ever a limiting factor, and solar cells are more sensitive than E_{act} measurements to n-type or p-type defects or impurities.

Prior to σ_{dark} measurements, we deposited two 100-nm-thick aluminum layers, 8 mm long and spaced 0.5 mm from each other, as electrical contacts by thermal evaporation in the Balzers setup. Given the highly conductive aluminum contacts and very thin (maximum thickness of a few hundred nanometers) layers as compared to the inter-contact distance which is small compared to the contact length, we assume a one-dimensional current flow between the contacts through the outlined layer block in Fig. 2.9a. With the layer thickness d, the contact length l, the contact distance x, and the definition of conductivity by the current density J and the electric field E, this gives

$$\sigma \doteq \frac{J}{E} = \frac{I}{V} \cdot \frac{x}{d \cdot l} = \frac{1}{R} \cdot \frac{x}{d \cdot l}. \tag{2.6}$$

The setup can be operated either in the "doped" mode with direct measurement of $\sigma(R)$ or in the "intrinsic" mode where the current I is measured for an applied voltage V. For better reproducibility and lower measurement errors, we always measured doped layers in the intrinsic mode with $V = 7\,\text{V}$.

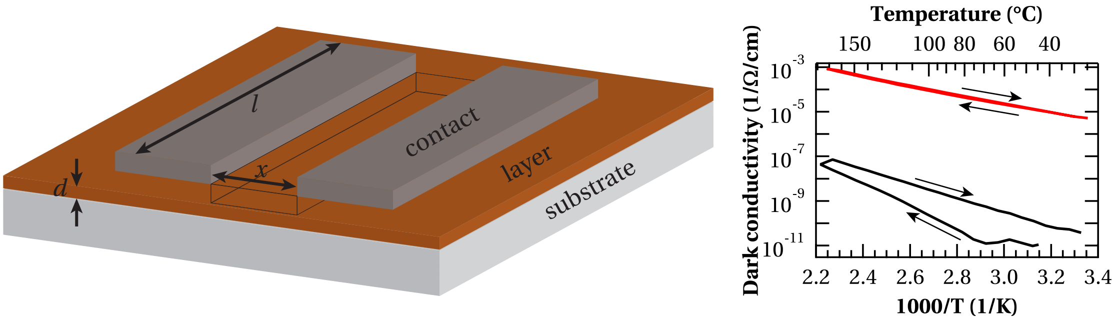

a **b**

Figure 2.9: (a): Contacting schema for σ_{dark} measurements. (b): Example of $\sigma_{\text{dark}}(T)$ measurements with arrows indicating the temperature ramps up and down.

The use of two Keithley 617 electrometers and a Keithley 705 scanner allowed for the measurement of up to four samples simultaneously. Due to the very low currents, the measurements of R were conducted as two-point probes.

The samples are positioned in a vacuum chamber on a heating stage. To determine E_{act}, σ_{dark} is measured as a function of the temperature T: a linear heating ramp brings the sample to 180 °C within 15 min. This temperature is kept for 1.5 h before cooling to nominally 25 °C within 2.5 h. This cooling ramp is linear, but the actual temperature can be higher at the end due to a lack of an active cooling. Two measurements of $\sigma_{\mathrm{dark}}(T)$ for p-(a-SiC:H) layers are shown in Fig. 2.9b in an Arrhenius plot. While good layers (high conductivity, low activation energy) systematically show only a small difference between the two temperature ramps, poor layers perform very differently in the two cases. We assume that the annealing irreversibly improves the poor p-(a-SiC:H) layers and the aluminum–p-(a-SiC:H) contact in a sample-dependent manner. Therefore, we always considered the cooling ramp to determine E_{act} from a fit of

$$\sigma_{\mathrm{dark}}(T) = \sigma_0 \cdot e^{-\frac{E_{\mathrm{act}}}{k_{\mathrm{B}} T}}. \tag{2.7}$$

In fact, a linear fit is applied to the linearized form, $\ln(\sigma_{\mathrm{dark}}) = \ln(\sigma_0) - \frac{E_{\mathrm{act}}}{1000 k_{\mathrm{B}}} \cdot \frac{1000}{T}$; fitting of the exponential function with square error minimization leads to very different weighting of the measurement data.

2.3.5 Photospectroscopy

For most transmission and reflection measurements presented in this thesis, we used a Lambda 900 photospectrometer with an integrating sphere, measuring from 320 to 2000 nm with 10-nm increments. Details can be found in [Ding 13, Steinhauser 08]. A Lambda 950 photospectrometer was used at AIST and also at IMT since January 2014 for measurements of series that were not correlated with older series.

2.3.6 Sheet resistance measurement

The sheet resistance of the front and back electrodes was determined by four-point probe measurements with four equidistant, in-line contacts. For a current I applied through the outer contacts and the voltage V measured between the inner two, the sheet resistance (measured in $\Omega_{\square}$) is

$$R_{\square} = \frac{\pi}{\ln(2)} \cdot \frac{V}{I} \cong 4.5324 \cdot \frac{V}{I}, \tag{2.8}$$

as derived in [Valdes 54] and numerically calculated in [Smits 58].

2.3.7 Profilometry

For layer thickness measurements of ZnO and, rarely, other layers, we used an Ambrios XP-2 profilometer with a diamond tip, performing a one-dimensional height scan on the decreasing step from the layer onto the substrate.

2.3.8 Raman spectroscopy

Raman measurements were used to determine the Raman crystallinity

$$\phi_\mathrm{c} = \frac{I_{510} + I_{520}}{I_{480} + I_{510} + I_{520}} \tag{2.9}$$

of TF-Si materials at the amorphous–microcrystalline transition; here I_x denotes the integrated Raman intensities below the peaks with central positions around x, fitted with Gaussians. These peaks correspond to amorphous (480 cm^{-1}), microcrystalline (490 cm^{-1}), and crystalline (520 cm^{-1}) silicon [Droz 04]. For standard analysis, the setup at IMT was used (Renishaw System 2000, described in [Hänni 14, Droz 03]); for more precise measurements, we used the Invia Raman microscope from Renishaw at AIST [AIST 14] or the Senterra Raman microscope from Bruker at TEL solar [TEL solar 14b]. For our studies, we always used green lasers.

2.3.9 Hall effect measurement

Hall effect measurements were used to determine the majority-charge-carrier concentration and mobility of LPCVD-grown ZnO. The method and settings are described in [Faÿ 03, Steinhauser 08, Ding 14].

2.4 Solar cell characterization techniques

2.4.1 External quantum efficiency (*EQE*) measurement

We used the EQE—the ratio between collected electron–hole pairs to incident photons at a given wavelength (λ)—not only for wavelength-resolved analysis of solar-cell performance, but also to determine current densities. This method is more precise than determining J_sc from $J(V)$ measurements due to the smaller probe spot size (about 1 mm × 2 mm in the focal) as compared to the solar cell dimensions (typically 5 mm × 5 mm), and hence less loss due to scattering of light outside of the active cell area occurs. Further, the spectral difference between the solar simulator spectrum and the AM1.5g spectrum, and the large measurement error of the light-intensity calibration in the case of the $J(V)$-current density favor the EQE-current density measurement (see the discussion in section B.1). In the EQE setup at AIST, the probe spot size was larger than the cell, and a mask was used for the measurements.

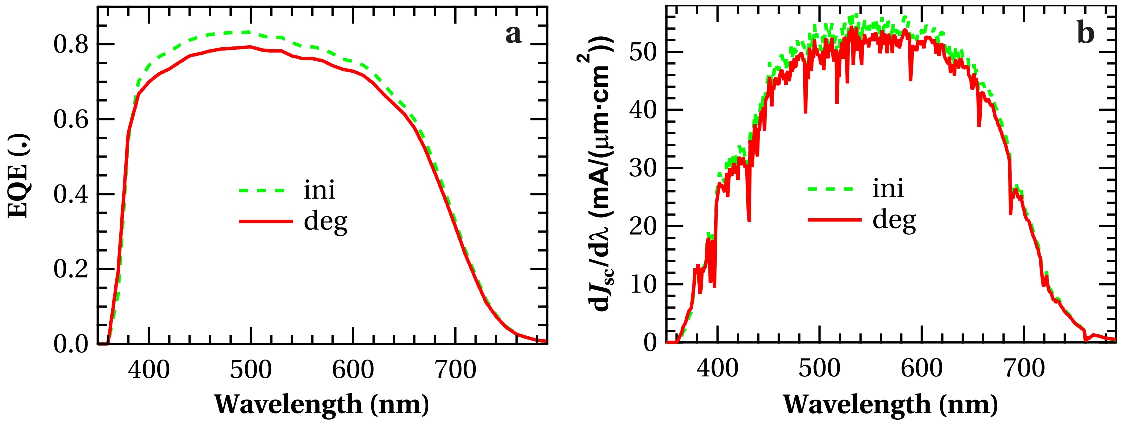

Figure 2.10: External quantum efficiency (a) and the spectral response multiplied with the AM1.5g spectrum (b) for a typical *a*-Si:H solar cell before (ini) and after (deg) light soaking. We measured these curves without an anti-reflective coating on the 0.25-cm^2 solar cell with the highest efficiency after light soaking (not optimized) of all solar cells presented in chapter 6 and [Stuckelberger 13]. The corresponding short-circuit current densities are 14.87 in the initial and 14.24 $\frac{\text{mA}}{\text{cm}^2}$ in the degraded state, respectively.

Figure 2.10a shows a typical EQE measurement of an *a*-Si:H solar cell before and after light soaking. We calculated J_{sc} from there via the spectral response SR (in $\frac{A}{W}$) by

$$J_{\text{sc}} = \int_0^\infty SR(\lambda)\cdot\Phi_{\text{AM1.5g}}(\lambda)\,\mathrm{d}\lambda \quad \text{with} \quad SR(\lambda) = \frac{q}{hc}\cdot EQE(\lambda)\cdot\lambda. \tag{2.10}$$

Here $\Phi_{\text{AM1.5g}}$ denotes the irradiance of the AM1.5g spectrum (in $\frac{\text{W}}{\text{m}^2\text{nm}}$), q the elemental charge, h the Planck constant, and c the velocity of light in vacuum.

Figure 2.10b shows the $SR(\lambda)$ weighted with the spectral distribution of AM1.5g. From this type of figure it is more easily visible than from EQE how much current is gained or lost in a given wavelength range.

The measurement setup is described in [Dominé 09], and a dedicated section in [Boccard 12b] discusses the case of EQE measurements of micromorph tandem solar cells. By default, we measured EQE with white bias light at 0 and −1 V reverse bias voltage with 10-nm step sizes. Back reflectors were mechanically pressed onto the LPCVD ZnO back contact.

2.4.2 Current–voltage (*I*(*V*)) measurement

Current–voltage ($I(V)$) measurements (or, normalized to the solar cell surface, current-density–voltage ($J(V)$) measurements) were performed under Wacom solar simulators of class AAA: either the model WXS-220S-L2 (denoted here “Wacom II”, four lamps (three halogen, one xenon), 220 mm × 220 mm illuminated area), or the model WXS-90S-L2 (“Wacom Malibu”, two lamps (one halogen, one xenon), 90 mm × 90 mm). The spectra of these and another solar simulators described in [Lo 10] are shown in Fig. 2.11.

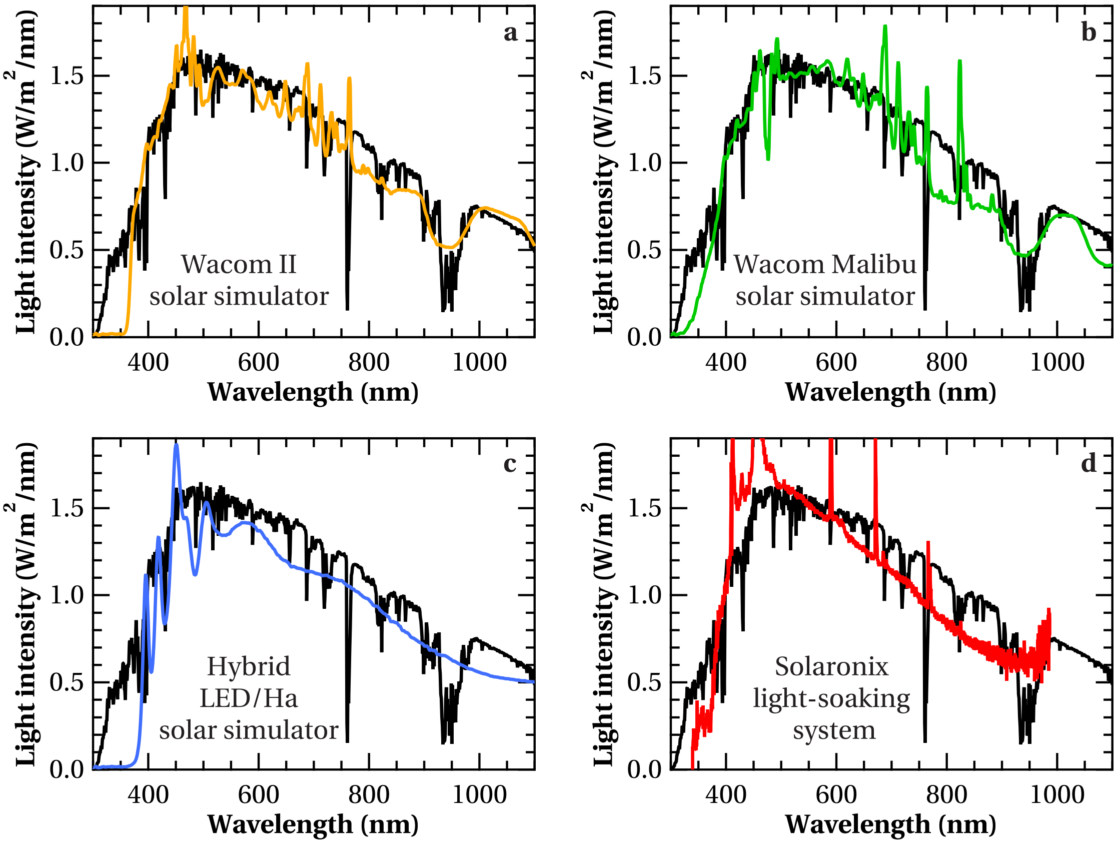

Figure 2.11: Spectra of four different solar simulators in comparison with the AM1.5g spectrum as defined in [IEC 06] in black. The spectra (a–c) were taken with the calibrated spectrometer AVS-DESKTOP-USB2 as described in section 3.3. The intensity and spectral distribution of the solar simulators were calibrated prior to these measurements with our reference cells. The spectrum (d) is a relative measurement, taken with a USB2000 spectrometer from Ocean Optics Inc. and scaled by eye.

For electrical measurements, a Keithley 2601A sourcemeter was used with a Keithley 2700 multimeter acting as a multiplexer to measure all 16 cells of a substrate consecutively. When the software was updated (see appendix D), a Keithley multimeter 2000 was added. This allowed us to measure in short time—before the cells heat up—the V_{oc} of all cells, to which the $I(V)$ curve is scaled afterwards.

Figure 2.12a shows a typical $J(V)$ curve of an a-Si:H single-junction solar cell. Three points are of special importance, indicated by black dots in the figure:

- Under *short-circuit* (sc) conditions, the voltage is 0 and the current density is J_{sc}.
- Under *open-circuit* (oc) conditions, the current density is 0 and the voltage is V_{oc}. At this point, the electric field is maximum within the productive quadrant and all generated charge carriers recombine. Note that the V_{oc} is always of the opposite sign as the current density—otherwise the device would not generate power, but consume power.
- At the *maximum power point* (mpp), the power density $p = V \cdot J$ reaches its maximum value. At this point, one defines the fill factor as $FF = \frac{V_{\mathrm{mpp}} \cdot J_{\mathrm{mpp}}}{V_{\mathrm{oc}} \cdot J_{\mathrm{sc}}}$, which is the ratio of the two squares in Fig. 2.12a.

The inverse slopes at sc and oc are the short-circuit and open-circuit resistances (R_{sc} and R_{oc}, respectively). R_{sc} is related to the parallel or shunt resistance, R_{oc} to the series resistance. However, they are not the same—their relation will be discussed in chapter 4.

The same $J(V)$ curve as in Fig. 2.12a is shown in Fig. 2.12b; it was measured on the same cell for which the EQE measurements are shown in Fig. 2.10, again in the initial and the degraded states, and scaled to the current densities obtained from EQE measurements. The drop in J_{sc} and FF upon light soaking is clearly visible; in this case, V_{oc} is not affected dramatically by light soaking—different cases in which it can be affected are discussed in chapter 8.

The conversion efficiency η is defined as the ratio between the power density of the solar cell (p_{cell}) and the power density of the solar irradiance $p_{\mathrm{solar}} = 1000\,\frac{\mathrm{W}}{\mathrm{m}^2}$. We calculate it from the V_{oc} and FF from $J(V)$ measurements, and from the J_{sc} from EQE measurements:

$$\eta = \frac{p_{\mathrm{cell}}}{p_{\mathrm{solar}}} = \frac{V_{\mathrm{oc}} \cdot FF \cdot J_{\mathrm{sc}}}{1000\,\frac{\mathrm{W}}{\mathrm{m}^2}} \quad \text{and} \quad \eta[\%] = V_{\mathrm{oc}}[\mathrm{V}] \cdot FF[.] \cdot J_{\mathrm{sc}}\left[\frac{\mathrm{mA}}{\mathrm{cm}^2}\right]. \tag{2.11}$$

For the correct measurement of the FF of multi-junction solar cells with the current-matching-machine (CMM) setup, we refer to [Boccard 12b, Bonnet-Eymard 13].

For $J(V)$ measurements, we used in most cases no back reflector for cells with LPCVD ZnO back contacts, hence underestimating the current density and, to less extent, V_{oc}. The error on the FF is small and can be positive or negative, depending on what is limiting the FF.

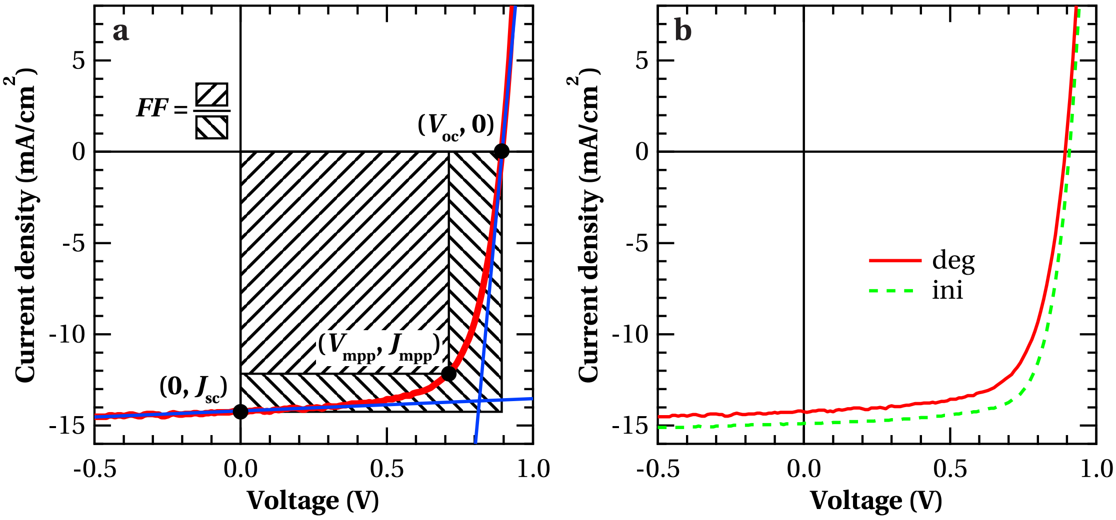

Figure 2.12: (a): Example of an $J(V)$ curve from which the solar cell parameters J_{sc}, V_{oc}, and FF are determined as described in the text. (b): The same $J(V)$ curve as in (a)—it is the $I(V)$ curve of the same solar cell for which the EQE measurements are shown in Fig. 2.10—in the initial state (continuous line) and after light soaking (dashed line).

2.5 Light-soaking tools

The combination of the experimental need for a solar simulator for light soaking with tunable properties (spectrum, temperature, intensity), and the non-existence of such a system on the market, resulted in the construction of a light-soaking system by ourselves. It is described in detail in chapter 3. In that system, light soaking was typically performed for 24 h at 50 °C under three sun-equivalent light intensity; standard light soaking was performed for 1000 h at 50 °C under 1000 $\frac{\mathrm{W}}{\mathrm{m}^2}$ light intensity (one sun) with the AM1.5g spectrum [IEC 06] in a solar simulator of class AAA [IEC 07].[10]

2.5.1 Light-soaking unit (unclassified)

In the beginning of the thesis, a prototype solar simulator with metal-halide light sources and air-cooled substrate holders was used; it was not classified according to [IEC 07].

2.5.2 Light-soaking unit (class AAA)

From 2011, we used a solar simulator from Solaronix [Solaronix 14]. The two light sources used microwave-excited plasmas, providing class AAA solar simulator characteristics [IEC 07] together with a water-cooled substrate holder with vacuum chucks for good thermal contact between the cooling plate and the substrates. The spectrum of the solar simulator is shown in Fig. 2.11d.

In 2013, an issue with reflectors inside the solar simulator led to a drop in the light intensity. For solar cells light soaked at that time, we mention that the intensity was 500 $\frac{\mathrm{W}}{\mathrm{m}^2}$, which is a lower limit. If nothing is mentioned, the solar simulator was operated at a light intensity of 1000 $\frac{\mathrm{W}}{\mathrm{m}^2}$.

---

[10] These conditions are established as a light-soaking standard in research, followed by many laboratories. This research standard is derived from the international light-soaking standards as defined in [IEC 08], however, the IEC-norm does not fix the light-soaking time absolutely but demands: “Subject each module to irradiation until its maximum power value stabilizes. Stabilization occurs when measurements from two consecutive periods of at least 43 kWh/m^2 each integrated over periods when the temperature is between 40 °C and 60 °C, meet the following criteria: $(P_{\mathrm{max}} - P_{\mathrm{min}})/P_{\mathrm{average}} < 2\%$.” Only a class CCC solar simulator is required, providing light intensities of 600 to 1000 $\frac{\mathrm{W}}{\mathrm{m}^2}$. On one hand, this is very demanding—no laboratory performs light soaking of all solar cells at their maximum power point which would require contacting every solar cell—on the other hand by far not strong enough to provide reproducible light-soaking results. For example, a module could be light soaked at 40 °C in 43-day blocks at 1000 $\frac{\mathrm{W}}{\mathrm{m}^2}$ in a solar simulator whose spectrum is bluish (class C allows for 25% deviation from AM1.5g in the integrated spectrum of each 100-nm wavelength block). This module will show much faster degradation kinetics ending at a lower “stabilized efficiency” than a module that is light soaked at 60 °C in 72-day blocks at 600 W/m^2 of a red-shifted spectrum, both conditions being within the IEC norm.

2.6 Software

In addition to standard software like Microsoft Office, we used extensively SolidWorks [SolidWorks 14] for the design of mechanical pieces, LabView [LabVIEW 14] for interaction with and programming of experimental setups, ASA (Advanced Semiconductor Analysis) [ASA 14] for TF-Si solar cell simulation, and IGOR [WaveMetrics 14] for data analysis. Appendix D gives an overview of the most important software codes we wrote.

3 Class AAA LED-based solar simulator for steady-state measurements and light soaking

Recent improvements in light-emitting diode (LED) technology allow for the use of LEDs for solar simulators with excellent characteristics. In this chapter, we present a solar simulator prototype fully based on LEDs. Our prototype has been designed specifically for light soaking and current-voltage measurements of hydrogenated amorphous silicon (a-Si:H) solar cells. With 11 different LED types, the spectrum from 400 to 750 nm can be adapted to any reference spectrum—such as AM1.5g—with a spectral match corresponding to class A+ or better.

The densely packed LEDs provide power densities equivalent to four suns for AM1.5g or five suns with all LEDs at full power, without any concentrator optics. The concept of modular LED blocks and electronics guarantees good uniformity and easy up-scalability. Instead of cost-intensive LED drivers, low-cost power supplies were used with current control including a feedback loop on in-house developed electronics. This prototype satisfies the highest classifications (better than AAA from 400 to 750 nm) with an illuminated area of 18 cm × 18 cm.

For a broader spectrum, the spectral range could be extended by using other types of LEDs or by adding halogen lamps. The space required for this can be saved by using LEDs with higher power, or by reducing the maximum light intensity.

This chapter is organized as follows: After the introduction in section 3.1, we give in section 3.2 details about the solar simulator, discussing in particular the outer structure, the optics with the LED configuration, and electronic circuits for LED control. In section 3.3, we show the results of the solar-simulator characterization with respect to its spectral match to sunlight, temporal stability, and spatial homogeneity. These measurements were performed with calibrated equipment and we can classify the solar simulator to be much better than class AAA from 400 to 750 nm. Finally, we conclude this chapter with section 3.4.

The main results of this chapter were published in the Journal of Photovoltaics [Stuckelberger 14c].

We acknowledge B. Perruche for contributions in designing the electronic circuits and M. Pravettoni from the University of Applied Sciences and Arts of Southern Switzerland (SUPSI) for assistance in characterization with a calibrated spectrometer.

3.1 Introduction

Light-induced degradation or improvement is observed for many photovoltaic technologies, including crystalline silicon (c-Si) solar cells. The Staebler-Wronski effect [Staebler 77], for example, is a key problem for thin-film silicon solar cells. This reversible degradation typically stabilizes after 1000 hours under one-sun illumination, a common standard derived from the international light-soaking norms of such solar cells [IEC 08]. Accelerated degradation, as observed under increased light intensity, can save time in research and industry and is used in many laboratories [Kondo 04, Matsui 14a], including ours. In addition, altering the spectrum of the light source enables one to test the different degradation mechanisms of distinct layers [Schouten 13, Ding 14]. Further insight into the origins of electrical losses of solar cells can be obtained by measuring the degradation kinetics [Fischer 13] or by performing light soaking at different temperatures.

To our knowledge, no single solar simulator has had such comprehensive functionality (e.g. [Bliss 09a, Bliss 09b, Lo 10, Newport 14]). Nevertheless, we wanted to perform such light-soaking experiments and built the solar simulator from scratch. Here, we present the result—a solar simulator that is fully based on computer-controlled LEDs, with a light intensity equivalent up to five suns, the possibility to alter the spectrum, and a temperature-controlled sample stage. The simulator is easily up-scalable and is connected to a current-voltage ($I(V)$) measurement setup for in-situ measurements of the kinetics of the electronic characteristics of samples.

3.2 Description of the solar simulator

3.2.1 Design and construction

Mechanically, the solar simulator consists of a tower containing a height-adjustable, water-cooled aluminum block, on which the LEDs are mounted. Figure 3.1 gives an overview of the solar simulator. It was designed and built in-house. We used SolidWorks software for the mechanical design. The mechanical pieces (two cooling blocks, for the LEDs and substrates) were manufactured by our own workshop; item profiles were used for the outer structures.

We designed the printed circuit boards (PCBs) with Altium software. Printing and assembly were performed partially in-house and partially by an external company.

We wrote the software to control the simulator in LabVIEW. We also used LabVIEW to write the $I(V)$ measurement software; the $I(V)$ setup—consisting of a Keithley-238 source-meter, an Agilent 34972A data acquisition unit with three cards 34901A providing $3 \times 10 \times 4$-point switches—can sequentially measure up to 30 solar cells with four-point contacting, and track their degradation kinetics over time. The substrate holder itself consists of a water-cooled, height-adjustable aluminum block on which the solar cells can be mounted; it is the same size as the LED block, 18 cm × 18 cm, with threads for mounting solar cells.

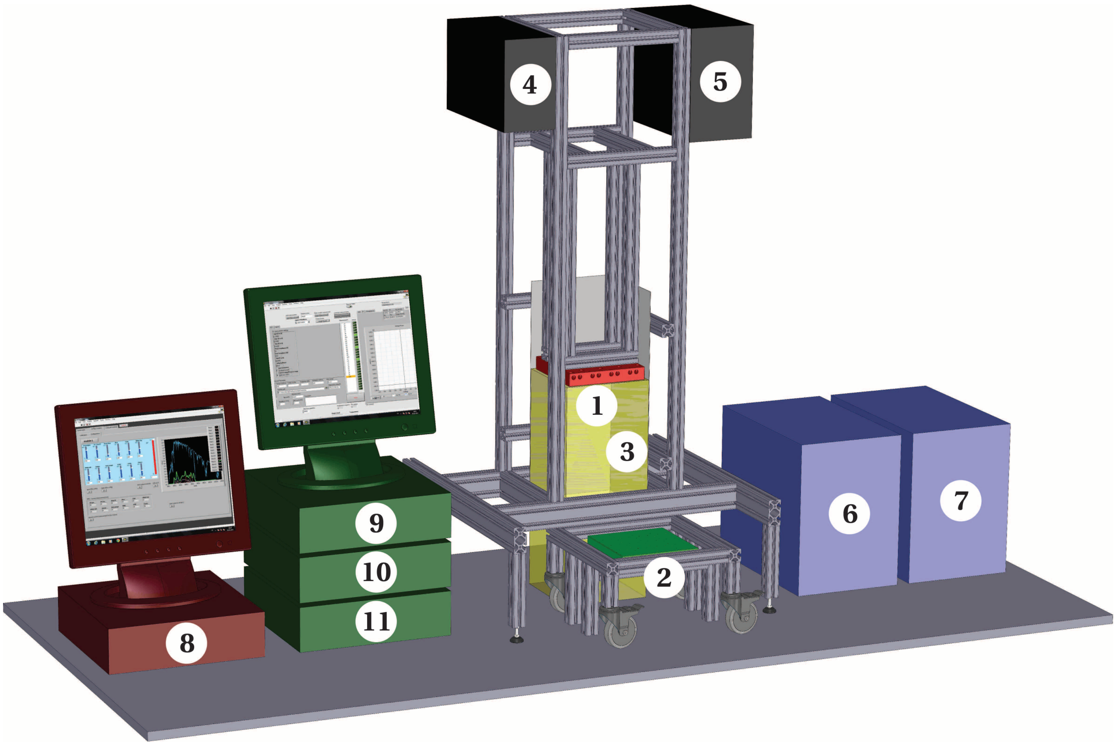

Figure 3.1: Schematic of the solar simulator with the following elements:
1) LEDs mounted on a cooling block
2) Temperature-controlled substrate holder
3) Mirrors around the LED cooling block and light path
4) Power supplies for the LEDs
5) Electronics for LED control
6) Chiller for the LED cooling circuit
7) Chiller for temperature control of the substrate holder
8) Computer to control the solar simulator
9) Computer for $I(V)$ measurements
10) Source meter for $I(V)$ measurements
11) Switch (30 × 4 channels) for $I(V)$ measurements

The LEDs and substrates are cooled by two separate closed water-cooling circuits, a more powerful with cooling capability only for the LEDs, and a smaller one (Huber Ministat 125ccNR) with precise temperature control from −30 to 100 °C for the substrates. The electronic circuits are cooled by fans.

3.2.2 Optics

Sixteen identical PCBs made of aluminum, on which the LEDs are soldered face down, are mounted in good thermal contact with the cooling block. Four of the PCBs are shown in Fig. 3.2a. To save space and allow for up-scalability, the power supply of the LEDs is connected

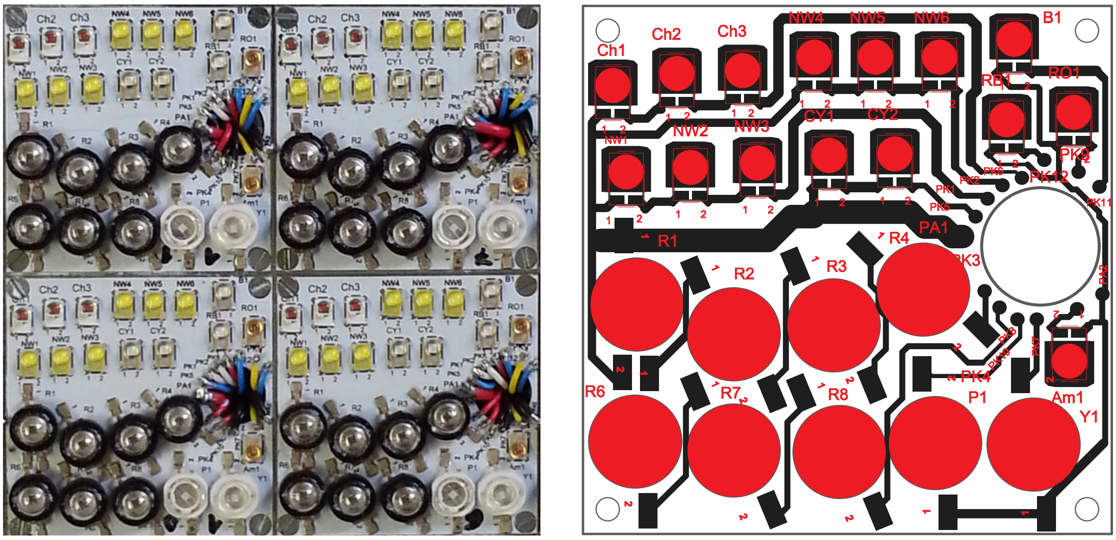

a **b**

Figure 3.2: (a): Photograph of four PCBs with mounted LEDs. (b): Technical drawing of one PCB with LEDs.

individually to each PCB from the back through the cooling block. Each PCB contains 11 types of LED that are organized into 12 channels. An overview of their main characteristics is given in Table 3.1. Note that we did not use any concentrator optics. The illuminated surface is parallel to and of the same size as the block to which the LEDs are mounted. At the borders, reflecting foils serve as mirrors to reduce intensity losses and to improve homogeneity.

Figure 2.10a shows the external quantum efficiency (*EQE*) for a typical *a*-Si:H solar cell, measured on the solar cell with highest efficiency after light soaking of all solar cells presented in chapter 6 and [Stuckelberger 13]. This motivates the restriction of the solar simulator

Table 3.1: Main characteristics of the LEDs mounted on each of the 16 identical PCBs.

Channel	Peak intensity	$\frac{\#\text{LED}}{\text{PCB}}$	$\frac{\text{max. current}}{\text{LED}}$	Circuit	LED names	Channel names
1	399 nm	1	350 mA	5 V	P1	UV 2
2	417 nm	1	350 mA	5 V	Y1	UV 1
3	457 nm	1	700 mA	5 V	B1	Blue
4	470 nm	1	700 mA	5 V	RB1	Royal blue
5	500 nm	2	700 mA	12 V	CY1-2	Cyan
6	441 & 585 nm	3	700 mA	12 V	NW1-3	White left
7	441 & 585 nm	3	700 mA	12 V	NW4-6	White top
8	596 nm	1	700 mA	5 V	RO1	Red-orange
9	624 nm	1	700 mA	5 V	Am1	Amber
10	658 nm	3	500 mA	12 V	R6-8	R660
11	685 nm	4	500 mA	12 V	R1–4	R690
12	728 nm	3	700 mA	12 V	Ch1–3	Cherry

spectrum to 400 to 750 nm. The types of LED and their number per PCB were chosen to simulate the AM1.5g solar spectrum [IEC 06] in that range, at a light intensity equivalent to three suns (see section 3.3). To maintain this intensity over time, LED wear had to be considered. For this reason, the system was designed to deliver a light intensity equivalent to five suns at the beginning of operation. Thus, there are six identical white-light LEDs instead of four due to these considerations. The electrical schema of the PCB with LEDs is shown in appendix B, Fig. B.3.

3.2.3 Electronic circuits for LED control

For maximum flexibility in tuning the spectrum and homogeneity, all 192 channels (12 channels for 16 PCBs) are controlled individually. Instead of buying an expensive LED driver for each channel, we use two power supplies commonly found in personal computers, each with 5 V and 12 V outputs, in combination with simple control electronics built in-house. The channels with only one LED are powered by a 5 V circuit (see Fig. 3.3a), and the channels with several LEDs serially interconnected are powered by a 12 V circuit.

The LEDs are serially interconnected with a MOSFET (metal-oxide-semiconductor field-effect transistor) and a small ohmic resistance R. The potential difference over R is proportional to the current flowing through the LED. This voltage is converted by a 16-bit analog-to-digital converter (ADC) to numerical values that are transmitted via an inter-integrated circuit (I^2C) bus and an I^2C-USB converter to the control computer. There, the measured current is compared with the reference current for adaptation. The same signal chain is then used in the opposite direction to set a current through a 12-bit digital-to-analog converter (DAC) that controls the MOSFET.

Practically, a dedicated PCB equipped with the electronic control circuit is connected to the corresponding LED PCB. Each unit consisting of a LED PCB and a control PCB works independently. In this solar simulator, they are powered in two groups of eight units, and two

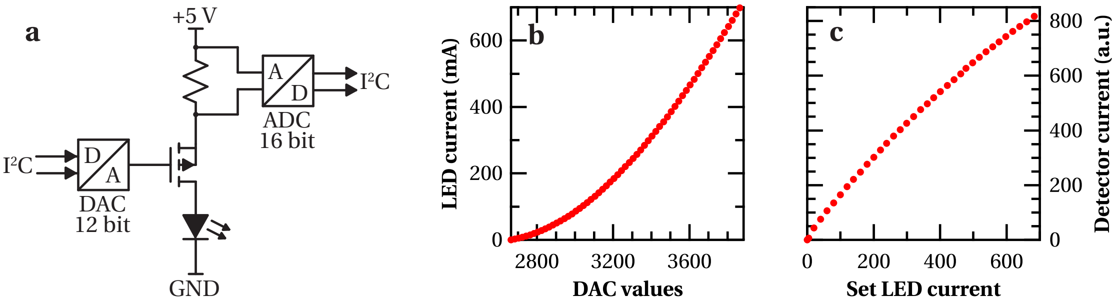

Figure 3.3: (a): Schematic of the current control circuit of the LEDs. (b): Calibration curve to correlate the set DAC register values with the measured LED currents. (c): Calibration curve to correlate the set LED currents—using calibration (b)—with light intensity, parameterized here by the photodiode current.

I^2C switches dispatch the signal from the computer to the 2 × 8 control PCBs. The design of the control PCBs is shown in appendix B in Fig. B.4, its schema in Fig. B.5.

Two calibrations are made for each LED channel to convert the desired spectrum into LED current. First, the LED current is measured by the ADC as a function of the DAC register values (see Fig. 3.3b). This is used to estimate the DAC register values necessary for a certain LED current, which is then finely adjusted via the ADC readout. A second calibration correlates the set LED current with the light intensity, parameterized here by the detector current of a photodiode (see Fig. 3.3c).

3.3 Characteristics of the solar simulator

3.3.1 Characterization methods

For characterization of the spectrum and light intensity of the solar simulator, several reference cells (calibrated *c*-Si solar cells with color filters) and photodiodes were used with different grey filters. In addition, *a*-Si:H solar cells fabricated in-house were used for intensity comparison to a four-lamp (one xenon, three halogen) class AAA [IEC 06, IEC 07] solar simulator from Wacom.

Spectral measurements were performed with two spectrometers. During development, relative irradiance measurements were performed using a SpectroInspect spectrometer from Pasan SA, which was also used to measure the single-LED spectra in Fig. 3.4b. For final characterization of the spectrum and light intensity (Figs. 3.4b, 3.5c, 3.6a, and 3.6b), an AVS-DESKTOP-USB2 spectrometer from Avantes was used with multichannel AvaSpec channel synchronization. Only the UV-VIS channel AvaSpec-2048-USB2-RM was used for this study with a 10 µm slit size (0.4 nm resolution), a diffuser, and trifurcated fiber optics (200 µm core each). This spectrometer was calibrated with a calibrated halogen lamp. Further details on light-intensity measurements in this solar simulator and in general are given in appendix B.

3.3.2 Spectrum

Figure 3.4b shows the measured spectra of all 11 types of LED (normalized to 1) included in the simulator, and a combination of them resulting in a class A+ AM1.5g spectrum between 400 and 750 nm. (Following the convention of TÜV Rheinland [Herrmann 12], "+" stands for dividing the accepted variance by 2.) The relative deviation from the true AM1.5g spectrum is shown in Fig. 3.4a. By further optimizing the different LED contributions, a better match can be obtained.

We would like to stress that we have used sequences of 50 instead of 100 nm for the comparison of AM1.5g and the solar simulator spectrum in Fig. 3.4a, hence stronger criteria than defined in the IEC norms [IEC 07].

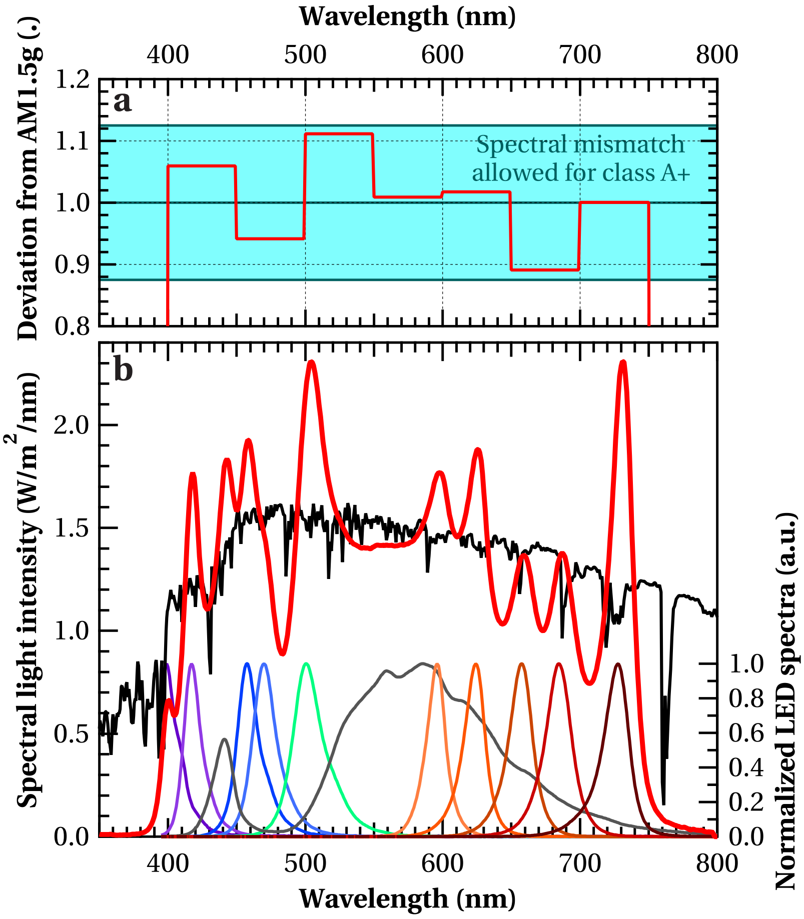

Figure 3.4: (a): Deviation of the simulator spectrum from AM1.5g. (b): Normalized spectra of all 11 types of LED included in the solar simulator with a combined spectrum simulating AM1.5g between 400 and 750 nm.

To our knowledge, there exists no specific norm for solar simulators for *a*-Si:H solar cells. Strictly speaking, spectral classification of solar simulators according to [IEC 07] requires a spectral match from 400 to 1100 nm. However, these norms were defined for *c*-Si solar cells that have a bandgap corresponding to about 1100 nm. Such solar simulators are not ideal for solar cells with a narrower absorber bandgap such as germanium, nor for solar cells with a wider bandgap such as *a*-Si:H. In that case, the bandgap corresponds to about 750 nm, which is the reason for the choice of the spectral range between 400 and 750 nm. Comparing Figs. 2.10a and 3.4, one can see that the solar simulator spectrum covers well the spectral range that is converted into electrical current by *a*-Si:H solar cells.

Using the same solar simulator design, one could extend the spectral range from 400 to 1100 nm. However, the range between 750 and 1100 nm leads to unwanted additional energy consumption and requires additional cooling capacities both of the LEDs and of the substrate holder. Further, to find space on the PCBs for LEDs of longer wavelength would necessitate a reduction of the density of each LED type, which would limit the maximum intensity.

3.3.3 Temporal stability

One of the main advantages of LEDs, in addition to their efficiency, is their long lifetime and light emission stability over time. However, their light intensity depends strongly on temperature. Therefore, cooling of the LEDs with a medium with a stable temperature is essential: Figure 3.5a shows the light intensity of the solar simulator operated at three sun-equivalents for 24 h. In this case, the LEDs were cooled with an open water circuit (connected to the fresh-water supply in Breguet 2), and whenever somebody in the building used water, the water temperature changed, immediately followed by the light intensity.[1] After moving to Microcity, we built a closed water circuit with a chiller, which improved the light stability dramatically as can be seen in Fig. 3.5b, although moving from a temperature-controlled to a non-temperature-controlled laboratory.

Figure 3.5b covers 24 h of illumination. This is the typical time for accelerated light soaking, hence this solar simulator satisfies the criterion for long-term stability as defined in [IEC 07]. The excellent classification as A++++ refers to the long-term stability and means “16 times better than class A”.

The short-term stability of the solar simulator is within measurement error and clearly better than the long-term stability, for which the temperature changes of the environment cause the largest fluctuations. Further, the working principle of LEDs gives no reason (as is the case for AC-driven lamps) for significant short-term stability issues.

---

[1] We could even correlate the flush of toilets with the LED light intensity.

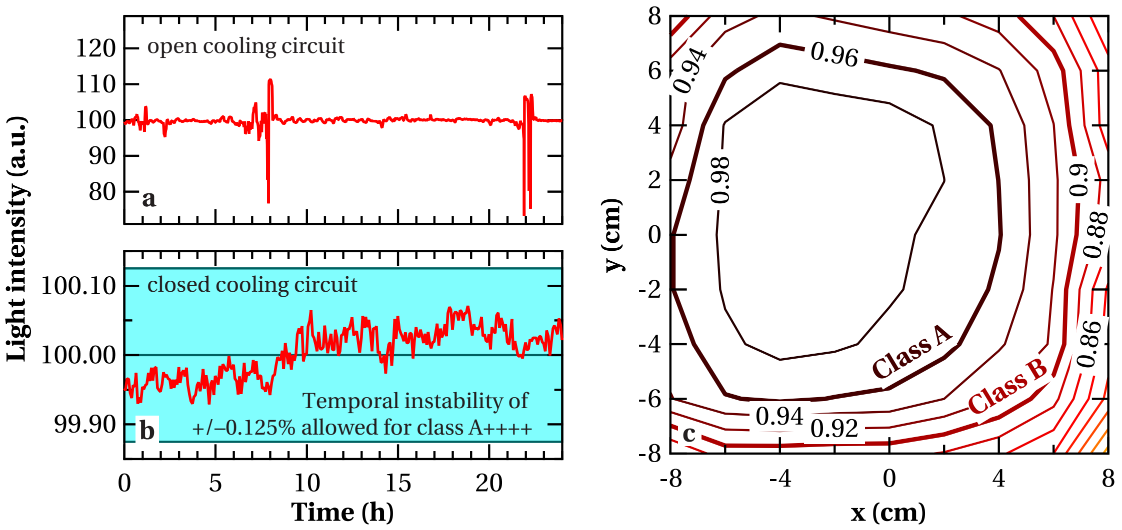

Figure 3.5: (a–b): Variation of the light intensity over 24 h with LEDs cooled by an open (a) and a closed (b) water circuit. Note that the scale in (a) is more than 100 times larger than that of (b). (c): Spatial distribution of the light intensity (normalized to 1), when all LED PCBs are operated at the same power without optimization.

3.3.4 Spatial homogeneity

Figure 3.5c shows the spatial homogeneity of the simulator when all LED PCBs are operated at the same power, i.e. the intrinsic homogeneity of the system without any correction. Nevertheless, the inhomogeneity is class A for the largest part of the surface, and it is only towards the edges that the intensity drops due to imperfect mirrors on the sides. During operation of the simulator, the uniformity is increased to the needed level by simply increasing the LED current in the corners and along the borders.

For this solar simulator, the intensity of each LED channel on each module is controlled by a 12-bit DAC allowing for very precise correction of the intensity distribution. Therefore, the homogeneity is limited by the different reflectance of solar cells that are being measured, and not by the light source or the geometry of the solar simulator as is the case for most solar simulator concepts. If one wants to adapt the light intensity distribution to the reflectance of the measured sample, one can even do so. This conceptual difference allows for easy scalability of the solar simulator, by changing the number of LED modules and adapting the intensity distribution by the software, instead of changing the optics.

3.3.5 Light intensity

Figure 3.6a shows the intensity increase with increasing LED current. Here, we defined a sun equivalent as the light intensity of AM1.5g between 400 and 750 nm, with AM1.5g scaled to $1000\,\frac{\mathrm{W}}{\mathrm{m}^2}$. In other words, an a-Si:H solar cell illuminated with one sun equivalent = 487 W/m^2 within 400 to 750 nm shows the same current as if it were illuminated with the whole AM1.5g

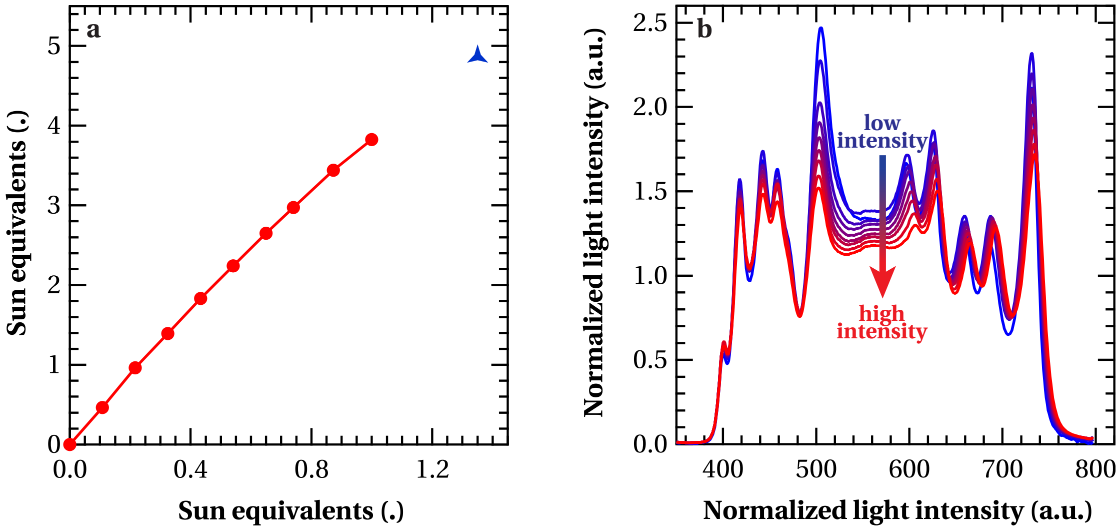

Figure 3.6: (a): Change of the relative light intensity expressed in sun equivalents as a function of the master power that is proportional to the set current. (b): Change of the solar simulator spectrum when the LED current is increased by ramping up the master power by the steps shown in (a).

spectrum at 1000 $\frac{\mathrm{W}}{\mathrm{m}^2}$. The master power is the parameter in the control software that operates all LED channels simultaneously, allowing for easy light intensity change of a predefined spectral and spatial distribution. This graph shows that the solar simulator reaches four sun equivalents with the AM1.5g-like spectrum shown in Fig. 3.4b, and five sun equivalents when all LEDs are set to maximum power regardless of the spectrum. With increasing intensity, the LED efficiency drops slightly. Therefore, the curve in Fig. 3.6a is sub-linear.

Figure 3.6b shows the spectra of the data points shown in Fig. 3.6a, normalized by the master power. The general drop in light intensity for higher intensities indicates decreasing LED efficiency. The shape of the spectrum does not change significantly. However, a small shift of the peak heights can be observed in the red part of the spectrum, and the intensity dependence on the current is not the same for all LED types. However, these non-linearities are small compared to other light sources—the light intensity was changed by a factor of 10 for these graphs—and a correction can be implemented in the software if necessary.

3.4 Conclusions

We have demonstrated a solar simulator that is fully based on LEDs. Eleven types of LED provide full flexibility in the spectrum from 400 to 750 nm. Although no concentrator optics are used and the illuminated area equals the light source area, the light intensity reaches up to five sun equivalents in continuous operation. The simulator is connected to an $I(V)$ measurement setup and a temperature-controlled sample stage that allows in-situ measurements for standard solar cell characterization or tracking of solar cell performance during light soaking.

The modular design and low-cost components of this solar simulator allow for easy up- and down-scalability. With faster electronics, our LED solar simulator designed for continuous operation with high light intensity is also well suited for flash measurements of $I(V)$ curves. If the spectrum needs to be expanded into the UV or IR (e.g. for c-Si, organic, or perovskite solar cell measurements), the choice of LEDs can be adapted.

4 Modeling and solar cell analysis

The drift length (L_{drift}) within the i-layer of hydrogenated amorphous silicon (a-Si:H) solar cells is a crucial parameter for charge collection which limits the conversion efficiency in most cases. It is given by $L_{\text{drift}} = \mu\tau \cdot E$ and strongly reduced not only by light-induced reduction of the mobility-lifetime product ($\mu\tau$), but also by deformation of the electric field (E) due to charges close to the p-i and i-n interfaces that shield the built-in potential difference between the doped layers.

We present a simple model based on a combination of equivalent electronic circuits with the amphoteric-defect model and estimate the contributions of free carriers, charges trapped in band tails, and charged dangling bonds to the electric-field deformation (ΔE). We show that this model is able to correctly reproduce observed trends and we point out its limits by comparing it with ASA simulations and experimental solar cell series. In particular, we demonstrate by modeling and measurements of the collection voltage of our i-layer thickness series that ΔE is governed by negative charges close to the i-n interface in the initial state, but that positively charged defect states close to the p-i interface detrimentally govern the degraded state.

This chapter is organized as follows: Section 4.1 discusses the role of different model types. In the following sections, we focus on two models that were intensively used for this thesis and developed further: equivalent electronic circuits (section 4.2) and the model of amphoteric defect states (section 4.3). This model was used to estimate different contributions to ΔE within the solar cell absorber in section 4.4. After the introduction of the collection voltage in section 4.5, we use this parameter to compare the model results with more rigorous simulations and experimental results with respect to charge collection in section 4.5.4. Section 4.6 concludes this chapter.

The main results of this chapter were presented at the IEEE PVSC 2010 (Hawaii, USA) and at the ICANS 2011 (Nara, Japan) and published in [Shah 10, Stuckelberger 10, Stuckelberger 12].

4.1 Introduction

4.1.1 Motivation

The interpretation of single-layer characterization is often straightforward if the parameter of interest is measurable (for instance, the activation energy by dark-conductivty measurements). In contrast, measurements of functional devices consisting of different layers like p-i-n solar cells with typically 2 p-type, 2 intrinsic (i), and 2 n-type a-Si:H based layers together with front and back electrodes (cf. Fig. 8.1) are often more difficult to interpret, as similar experimental signatures can have different causes in devices.

As compared to layer measurements, two additional difficulties arise from the measurement interpretation of complex devices: First, there are material-property-related effects that are relevant in solar cells (e.g. ΔE), only showing up in functional devices but not being measurable as properties of single layers. Second, layer properties of individual layers can differ significantly from nominally the same layer in the solar cell stack, as substrate and subsequent manufacturing steps can modify them. For example, identical deposition conditions may lead to no deposition on glass but to the deposition of microcrystalline silicon (μc-Si:H) on ZnO (glass and ZnO have different sticking coefficients); another example are hydrogenated silane plasmas that can reduce the front electrode (in the case of SnO_2 substrates), etch the previous layer, or hydrogenate it, changing its bandgap.

In order to gain information about interfaces or material properties implemented in devices, it is therefore necessary to work with models. There exist basically two approaches that we classify by macro- and micro-models discussed in the following sections, but also combinations of them evolve promising approaches [Lanz 13]. A third approach starts with simulations of atomic environments; however, we will not enter into that field.

4.1.2 Micro-model: Layer-by-layer simulations

Software codes that simulate thin-film silicon (TF-Si) solar cells in layer-by-layer approaches including one, two, or three dimensions are very powerful tools.

In most cases, one starts with the calculation of an electron–hole pair generation profile based on measurements of the refractive indices (n, k) and the morphology of the individual layers. Optical models are not the main focus of this work will not be discussed hereafter.

The electron–hole pair generation profile, layer morphology, and electrical properties of the layers and interfaces serve as the input for electric simulation of the solar cells, for which the set of the coupled Poisson and Maxwell equations is solved.

Several programs exist and provide band diagrams, charge distributions and current-density–voltage ($J(V)$) curves as output. An overview including the most often used programs (ASA, AMPS, PC1D, AFORS-HET) is given in [Burgelman 04].

A general difficulty of such complex simulation programs is their large quantity of parameters that allows in most cases a good fit of the model results to device measurements, but these parameters are not easy to correlate to experimentally determined layer properties.

For this chapter, we used the software SunShine [Krc 03] for optical simulations, and ASA for optical and electrical simulations [Zeman 97]. A further study using ASA is presented in section 8.4.

4.1.3 Macro-model: Equivalent electronic circuits

In equivalent electronic circuits, properties of individual layers or even atomic environments are not considered directly. Instead, one correlates macroscopic measurements of the solar cells—in particular of the $J(V)$ curve, but not restricted to that—with electronic circuits including known elements such as resistances and diodes. In contrast to layer-by-layer approaches, equivalent electronic circuits often lead to analytically solvable equations, which allows e.g. the fitting of $J(V)$ curves to an equivalent electronic circuit, and a more straightforward interpretation of detrimental elements for the device performance than in layer-by-layer approaches. Limitations of equivalent electronic circuit models arise often from too crude assumptions and difficult integration of inhomogeneous structures.

Different elements of an equivalent electronic circuit for TF-Si solar cells are presented in section 4.2.

4.2 Equivalent electronic circuits for hydrogenated amorphous silicon solar cells

The most simple equivalent electronic circuit that can represent many single-junction TF-Si devices with reasonable accuracy is shown in Fig. 4.1a. It consists of five elements, a resistance in series with four parallel elements. While V is the voltage over the whole device for a current

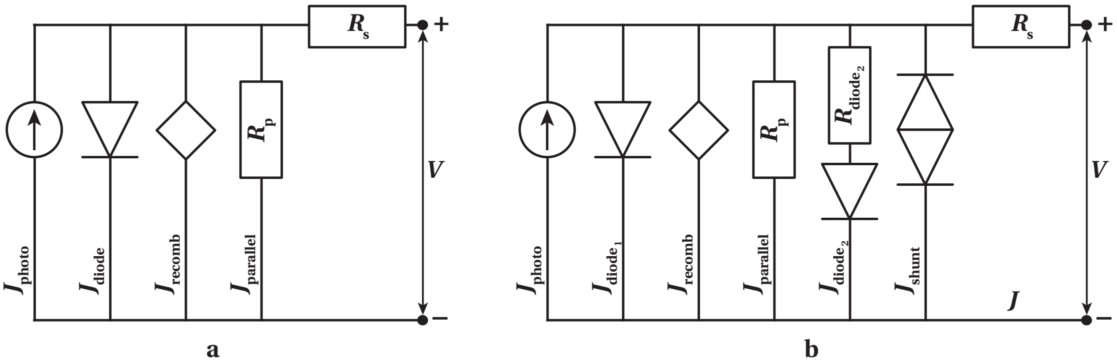

Figure 4.1: Equivalent electronic circuits for a thin-film silicon single-junction solar cell in a simple (a) and a more complex version (b).

density J, V^* denotes the voltage over the parallel elements. Each element has its analytical expression for $J(V^*)$ and correspondence in solar cells:

- *Photogenerator*: This element simply considers the photogenerated current density J_{photo} that depends—to first approximation—only on the incident light intensity. Numerically, it is the only negative term (contributing current): all other terms are positive (reducing current). Therefore, we call $J_{\text{ph}} \doteq |J_{\text{photo}}| = -J_{\text{photo}}$.

- *Diode*: The diode represents the $p(\text{-}i\text{-})n$ structure that allows current in one direction—inverse to the photocurrent—and blocks it in the other direction. The diode current density J_{diode} is described as

  $$J_{\text{diode}} = J_0 \cdot \left[e^{\frac{qV^*}{nk_\text{B}T}} - 1 \right], \quad \text{with} \quad J_0 = J_{00} \cdot \left[e^{\frac{-E_\text{g}}{k_\text{B}T}} \right]. \tag{4.1}$$

  Here, q denotes the elementary charge, V^* the voltage over the diode, n the diode ideality factor, k_B the Boltzmann constant, T the temperature, and E_g the bandgap of the semiconductor the diode consists of. This equation is also known as the Shockley equation, derived in [Shockley 49] and discussed in [Sze 07] and [Shah 10], including the expression for the diode saturation current density J_0 that is derived in [Green 82b] based on estimations and experiment with $J_{00} \approx 1.5 \times 10^8\,\text{mA/cm}^2$. Especially for temperature coefficients, it is important to consider $J_0(J_{00}, T)$ and not $J_0 = \text{const.}$, as the T dependence of J_{diode} is governed by the T dependence of J_0 which is inverse to the T dependence of $e^{\frac{qV^*}{nk_\text{B}T}}$.

  An ideal solar cell has only two elements: the photogenerator and the diode.

- *Recombination*: This term considers electron–hole pair recombination in the absorber material that reduces charge collection; it is of special importance for the simulation of a-Si:H solar cells in the degraded state. Several models with different mathematical representations are described in section 4.5. One of them is developed in [Hof 00], with the recombination current density

  $$J_{\text{rec}_\text{H}} = J_{\text{ph}} \cdot \left[1 - \frac{1}{1 + \frac{\varphi \cdot d_i^2}{(\mu\tau)_{\text{eff}} \cdot (V_{\text{bi}} - V^*)}} \right], \tag{4.2}$$

  which is a generalization of the recombination term developed in [Hubin 92] and [Hubin 95] (there, $\varphi \equiv 1$). Here φ accounts for the dependence of the electric field on the position in the solar cell, and is in the range $1 \leq \varphi \leq 3$ as found in [Hof 99].[1] The intrinsic absorber layer has a thickness of d_i, $(\mu\tau)_{\text{eff}}$ is the effective mobility-lifetime product in the absorber layer, and V_{bi} is the built-in potential spanned by the p and the n layers.

---

[1] The introduction of φ provides more flexibility if the effective mobility-lifetime product $(\mu\tau)_{\text{eff}}$ is known; for fitting with $(\mu\tau)_{\text{eff}}$ as a free parameter, however, φ can be set to 1 as it is perfectly correlated with $(\mu\tau)_{\text{eff}}$.

- A parallel resistance accounts for ohmic shunt paths between the doped layers: $J_{\text{parallel}} = \frac{V^*}{R_\text{p}}$,with J_{parallel} being the current density flowing through the parallel resistor with the resistance R_p.

- A resistor in series to all other elements takes into account resistances outside of the p-i-n junction such as the (transverse) resistance in electronically dead layers, (lateral) resistances of front and back contacts, or laser scribe connections and cabling in modules. The current through the series resistance is the current measured on the device, hence $J = \frac{V_\text{s}}{R_\text{s}}$, with the voltage being reduced by $V_\text{s} = V - V^*$ over the resistance R_s.

We call this equivalent electronic circuit model with five elements including the recombination term as defined above the Hof model. It is the same as the Merten model presented in [Merten 98] and others, but with a different recombination term (see section 4.5).

Often, these five elements are not sufficient to describe actual devices, and we add two terms:

- Poor material quality in the p-i-n junction [Bugnon 13] that leads to dark degradation [Boccard 11] can be represented by a second, weaker, diode with J_{diode_2}, n_2. This negative effect occurring predominantly at high deposition rates on rough substrates can be limited by the use of doped silicon oxide layers [Despeisse 10b]. In [Despeisse 10a], it was suggested that these oxide layers limit the effect of weak diodes by adding an ohmic resistance R_{diode_2}—justified by the high resistivity of the oxide layers in the lateral direction, and low resistivity in the transverse direction, due to phase segragation into silicon and oxygen-rich filaments [Buehlmann 07, Cuony 12]. Although these references focus on μc-Si:H absorber layers, similar issues of poor material quality on rough substrates are known for a-Si:H as well, as discussed in chapters 6 and 8 and in [Stuckelberger 13].

- Shunts leading to superlinear current increase under reverse bias voltage cannot be adequately represented by the terms described above. A possible representation of such non-linear shunt current densities as $J_{\text{shunt}} \propto \text{sign}(V^*) \cdot |V^*|^\gamma$ with $\gamma \approx 2$ was suggested phenomenologically for different kinds of thin-film solar cells in [Dongaonkar 10]. However, testing different terms for shunt current densities, we found phenomenologically better agreement with shunted a-Si:H solar cells using the term

$$J_{\text{shunt}} = \text{sign}(V^*) \cdot J_{0_{\text{shunt}}} \cdot \left[e^{\frac{q|V^*|}{n_{\text{shunt}} k_\text{B} T}} - 1 \right], \tag{4.3}$$

referring to the Shockley equation (4.1).

These two elements combined with those of the Hof model lead to the equivalent electronic circuit shown in Fig. 4.1b. It is described by

$$
\begin{aligned}
J \quad = \quad & J_{\mathrm{photo}} && = \; - \; J_{\mathrm{ph}} && (4.4)\\
+ \quad & J_{\mathrm{recomb}} && + \; J_{\mathrm{ph}} \cdot \left[1 - \frac{1}{1 + \frac{\varphi \cdot d_i^2}{(\mu\tau)_{\mathrm{eff}} \cdot [V_{\mathrm{bi}} - (V - R_{\mathrm{s}} \cdot J)]}} \right] && (4.5)\\
+ \quad & J_{\mathrm{diode}_1} && + \; J_{00} \cdot \left[e^{\frac{-E_{\mathrm{g}}}{k_{\mathrm{B}} T}} \right] \cdot \left[e^{\frac{q(V - R_{\mathrm{S}} \cdot J)}{n_1 k_{\mathrm{B}} T}} - 1 \right] && (4.6)\\
+ \quad & J_{\mathrm{diode}_2} && + \; J_{00} \cdot \left[e^{\frac{-E_{\mathrm{g}}}{k_{\mathrm{B}} T}} \right] \cdot \left[e^{\frac{q\left(V - R_{\mathrm{S}} \cdot J - R_{\mathrm{diode}_2} \cdot J_{\mathrm{diode}_2}\right)}{n_2 k_{\mathrm{B}} T}} - 1 \right] && (4.7)\\
+ \quad & J_{\mathrm{shunt}} && + \; \mathrm{sign}\,(V - R_{\mathrm{s}} \cdot J) \cdot J_{0_{\mathrm{shunt}}} \cdot \left[e^{\frac{q|(V - R_{\mathrm{S}} \cdot J)|}{n_{\mathrm{shunt}} k_{\mathrm{B}} T}} - 1 \right] && (4.8)\\
+ \quad & J_{\mathrm{parallel}} && + \; \frac{V - R_{\mathrm{s}} \cdot J}{R_{\mathrm{p}}} && (4.9)
\end{aligned}
$$

This equation is not solvable analytically for J due to its occurrence in $V^* = V - R_{\mathrm{s}} \cdot J$ and J_{diode_2} in the term (4.7). Numerically, we chose a value for $V^{**} \doteq V - R_{\mathrm{s}} \cdot J - R_{\mathrm{diode}_2} \cdot J_{\mathrm{diode}_2}$, calculated J_{diode_2} and with that V^*. Considering all terms (4.4) to (4.9), one gets J and finally $V = V^* + R_{\mathrm{s}} \cdot J$.

Such equivalent electronic circuits for single-junction devices can be easily expanded for stacked cells by connecting several of them in series, as was done in [Repmann 03] with a recombination term based on [Crandall 83].

The calculations for the Merten model [Merten 98], the model described in equation (4.4) to (4.9), a model for micromorph tandem cells using two of these circuits in series, and others are included in the simulation code mentioned in appendix D; a screenprint of the graphical user interface of the simulation of micromorph tandem cells is shown in Fig. D.1.

4.3 Defect models in hydrogenated amorphous silicon

In this section, we focus on recombination processes in *a*-Si:H—in particular on a model that describes the defects that are responsible for most recombination events.

4.3.1 Recombination processes in hydrogenated amorphous silicon

Figure 4.2 shows the basic recombination processes in semiconductors. Radiative direct recombination (Fig. 4.2a) between the conduction and valence band (photoluminescence) is the process utilized in light-emitting diodes (LEDs). In crystalline silicon, photoluminescence can be measured, e.g. for defect analysis. In *a*-Si:H, this is possible only at very low temperatures; at higher temperatures, other recombination paths are dominating.

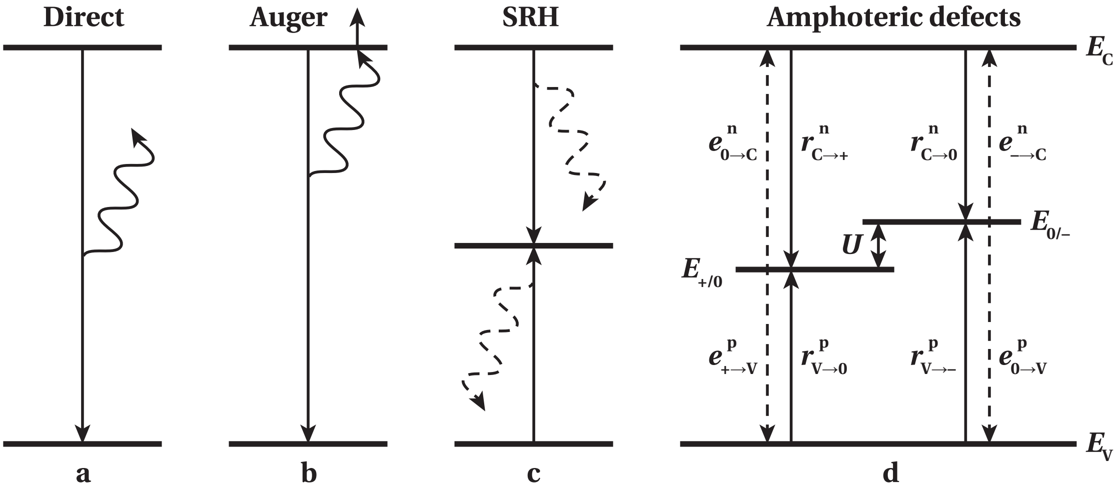

Figure 4.2: Basic recombination processes in semiconductors: Radiative direct recombination (a), Auger recombination (b), and recombination through defect states in the Shockley-Read-Hall model (c) and the amphoteric-defect model (d).

Auger recombination (Fig. 4.2b) is also a direct recombination, but the energy is not released through a photon like in photoluminescence, but through an electron in the conduction band that occupies either a higher energy level (releasing the energy afterwards by thermalization) or—if it is close to vacuum energy—leaves the material. As this recombination path is a three-particle reaction, it is very rare and does not play any role in *a*-Si:H.

Shockley-Read-Hall (SRH) recombination [Shockley 52, Hall 52] describes the recombination process through defect states (Fig. 4.2c); it is in most cases dominant in crystalline silicon. The mathematical description of amphoteric defect states (Fig. 4.2d), described in the following sections, is formulated very similarly. However, the nature of defect states is fundamentally different in these two models, leading to other recombination dependencies: While a SRH defect is described by a single energy level that serves as a recombination center, amphoteric defects are considered to provide two electronic states.

4.3.2 Amphoteric defect states and the defect-pool model

It is questionable whether the well-defined terminology from semiconductors shall be adapted for amorphous materials, where definitions must be weaker. However, this is common use and justified by often comparable properties. Nevertheless, the definitions of terms like bandgap need more discussion (see also section 2.3.2).

Density of states in *a*-Si:H

With defect states, we mean electronic states close to mid gap. They are deeper in the bandgap than band tail states and act differently. Bandgap states serve predominantly as traps, and

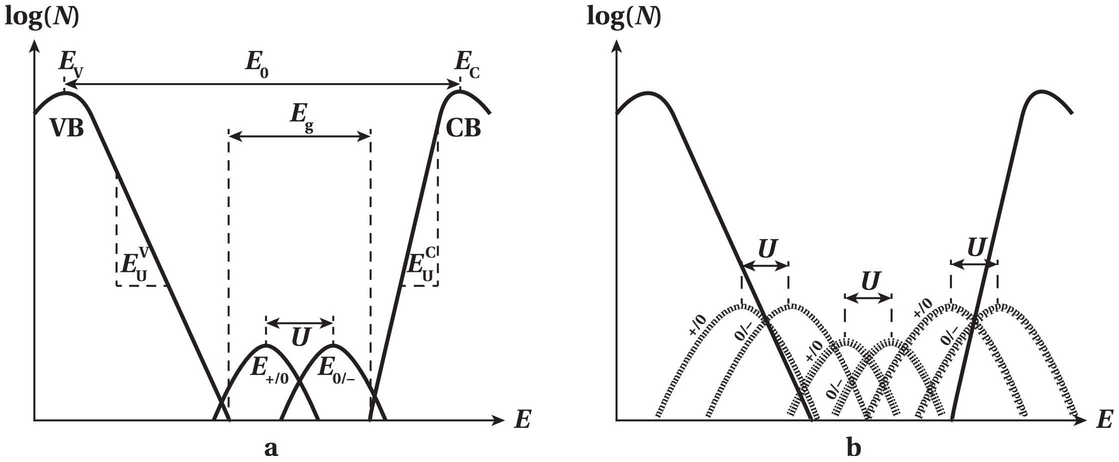

Figure 4.3: Schematic band diagram of hydrogenated amorphous silicon in the amphoteric-defect model (a) and in the defect-pool model (b). Note that the scales are not proportional.

electrons or holes captured in the conduction or valence band tail are released back to the same band by thermal excitation [Comber 72, Tiedje 81]. In contrast, it is more likely for electrons or holes captured in mid-gap states to recombine with an opposite charge carrier from the other band. The limit is on the order of the thermal activation energy: the release rate from these states is given by

$$\frac{1}{\tau} = \nu \cdot e^{-\frac{\Delta\epsilon}{kT}}, \tag{4.10}$$

where $\Delta\epsilon$ is the energy between the state level and the mobility-band edge, ν the attempt frequency, and kT for room temperature about 26 meV.

The schematic band diagram for *a*-Si:H with band tails and defect states is shown in Fig. 4.3a. The density of states (DOS) is denoted N. It is orders of magnitude higher in the valence band (VB) and the conduction band (CB) than in the bandgap between. The energy between the two DOS maxima in the bands is denoted E_0. Hence, the absorption coefficient is highest for photons with the energy E_0, with typically $E_0 \approx 3.7\,\text{eV}$.[2]

The DOS decreases exponentially from the bands towards the bandgap, forming the band tail. The band tail slopes are characteristic for a given amorphous material and are an indicator of material quality. They are described by $N \propto e^{\frac{E_U^{(V,C)}}{kT}}$ for the valence and conduction band tail, respectively, and are typically $E_U^V \approx -50\,\text{meV}$ and $E_U^C \approx 20\,\text{meV}$. In optical absorption measurements, one can not differentiate between the transitions between the valence band tail/conduction band and the conduction band tail/valence band (see also section 2.3.2); the experimental slope is called Urbach energy (E_U) and is governed by the stronger tail (typically the valence band tail). Between the exponential slope and DOS maxima in the bands, the DOS is typically described by a parabolic curve [Jackson 85].

---

[2] In the literature, the notation E_0 is used for different parameters, including the Urbach energy called here E_U.

Defect states are located in the bandgap. In the DOS diagram, they are often denoted by Gaussian distributions. The defect states arise from dangling bonds that are the dominant defects in *a*-Si:H, and they can be modeled by amphoteric states.

Structure of hydrogenated amorphous silicon

In a perfect silicon crystal, each silicon atom has four tetrahedrally coordinated bonds, i.e. the four valence electrons are in (sp^3) hybridization (see Fig. 1.6a). Each bond contains two electrons on different energy levels, split by the correlation energy $U \approx 130\,\text{meV}$ [Street 91]. This is basically the same if one silicon atom contributing to the bond is missing: in that case, four unilateral bonds are left. The remaining atoms with the dangling bonds are neutral with one electron, whose electronic state is represented by D^0. If this electron is missing, the net charge of the silicon atom is positive, represented by D^+; in case of a second electron in the dangling bond, the atom is negatively charged, represented by D^-. More than these three charge states are forbidden by the Pauli exclusion principle, which allows a maximum of two electrons per energy level.

These defect states serve as recombination centers like defects do in the SRH model (see Fig. 4.2d), and their predominantly amphoteric nature as dangling bonds is confirmed experimentally as detailed in [Street 91] and the references therein, summarizing measurements of paramagnetic defect states by the electron-spin resonance (ESR) method and DOS measurements by different methods.

The defect-pool model as explained in [Winer 89, Winer 91, Powell 92, Deane 93] utilizes the same concept as the amphoteric-defect model with states D^+, D^0, and D^-, with the transition energies $E_{+/0}$ and $E_{0/-}$ separated by the energy U as indicated in Fig. 4.3b. However, the absolute position and the DOS of these energy levels depend here on the Fermi-level position E_F: for *p*-doped layers, E_F is close to the VB, and most defects are located close to the CB; for *n*-doped layers vice versa, and for intrinsic layers, E_F and the DOS maxima of defects are around mid gap.

We did not investigate whether the defect-pool model with the dependence of the DOS on the Fermi level corresponds better to the nature of *a*-Si:H than the simple amphoteric-defect model. From an experimental point of view, however, the amphoteric-defect model is of more use for our needs. In particular, the defect-pool model's dependence of the defect concentration and energy level on the Fermi-level position prohibits intuitive understanding and modeling of solar cells, and the input parameters for the model are hardly accessible experimentally. This problem arose e.g. for the simulations of the effect of the *p*-type hydrogenated amorphous silicon carbide (*p*-(*a*-SiC:H))-layer thickness on the open-circuit voltage (V_oc) in chapter 8: although we could reproduce the experimental results using the defect-pool model, they were difficult to interpret because of a closed feedback loop: *p*-(*a*-SiC:H) thickness changes E_F directly which in turn modifies the defect-state density, influencing again the E_F. Using the amphoteric-defect model, we could fix the defect-state concentration (or study the effect of its change during light soaking), and hence study the effect of the p-(a-SiC:H) layer thickness on the E_F through the whole solar cell.

4.3.3 Occupation functions of amphoteric defect states

In this section, we calculate the occupation functions f_+, f_0, and f_-, which are the probabilities that an amphoteric defect D is in its state D^+, D^0, or D^-.

Transition rates and lifetimes

By definition of the state D as an amphoteric state that is positively charged, neutral, or negatively charged with a probability f_+ f_0, and f_-, we have

$$f_+ + f_0 + f_- = 1. \tag{4.11}$$

Further, we have the four basic equations for the transition rates between the states D^+, D^0, D^- and the bands, as indicated in Fig. 4.2d:

$$r^n_{\mathrm{C}\to+} \overset{(*)}{=} v^n_{\mathrm{th}}\cdot\sigma^n_+\cdot n_\mathrm{f}\cdot N_{\mathrm{D}_+} \overset{(**)}{=} v^n_{\mathrm{th}}\cdot\sigma^n_+\cdot n_\mathrm{f}\cdot f_+\cdot N_\mathrm{D} \overset{(***)}{=} \frac{n_\mathrm{f}}{\tau^n_+}\cdot f_+, \tag{4.12}$$

$$r^n_{\mathrm{C}\to0} \overset{(*)}{=} v^n_{\mathrm{th}}\cdot\sigma^n_0\cdot n_\mathrm{f}\cdot N_{\mathrm{D}_0} \overset{(**)}{=} v^n_{\mathrm{th}}\cdot\sigma^n_0\cdot n_\mathrm{f}\cdot f_0\cdot N_\mathrm{D} \overset{(***)}{=} \frac{n_\mathrm{f}}{\tau^n_0}\cdot f_0, \tag{4.13}$$

$$r^p_{\mathrm{V}\to0} \overset{(*)}{=} v^p_{\mathrm{th}}\cdot\sigma^p_0\cdot p_\mathrm{f}\cdot N_{\mathrm{D}_0} \overset{(**)}{=} v^p_{\mathrm{th}}\cdot\sigma^n_0\cdot p_\mathrm{f}\cdot f_0\cdot N_\mathrm{D} \overset{(***)}{=} \frac{p_\mathrm{f}}{\tau^p_0}\cdot f_0, \tag{4.14}$$

$$r^p_{\mathrm{V}\to-} \overset{(*)}{=} v^p_{\mathrm{th}}\cdot\sigma^p_-\cdot p_\mathrm{f}\cdot N_{\mathrm{D}_-} \overset{(**)}{=} v^p_{\mathrm{th}}\cdot\sigma^p_-\cdot p_\mathrm{f}\cdot f_-\cdot N_\mathrm{D} \overset{(***)}{=} \frac{p_\mathrm{f}}{\tau^p_-}\cdot f_-. \tag{4.15}$$

Here, the variables are defined as follows:

n, p	electrons and holes $[.]$,
$r^n_{\mathrm{C}\to+}, r^n_{\mathrm{C}\to0}, r^p_{\mathrm{V}\to0}, r^p_{\mathrm{V}\to-}$	transition rates as described in Fig. 4.2d $\left[\frac{1}{\mathrm{cm}^3\mathrm{s}}\right]$,
$v^n_{\mathrm{th}}, v^p_{\mathrm{th}}$	thermal velocities of n, p $\left[\frac{\mathrm{cm}}{\mathrm{s}}\right]$,
$\sigma^p_-, \sigma^p_0, \sigma^n_0, \sigma^n_+$	cross sections of n, p into D^+, D^0 and D^- $[\mathrm{cm}^2]$,
$p_\mathrm{f}, n_\mathrm{f}$	free hole and electron concentrations $\left[\frac{1}{\mathrm{cm}^3}\right]$,
N_D	concentration of amphoteric defect states D $\left[\frac{1}{\mathrm{cm}^3}\right]$,
$N_{\mathrm{D}_+}, N_{\mathrm{D}_0}, N_{\mathrm{D}_-}$	concentrations of N_D with charge $+/0/-$ $\left[\frac{1}{\mathrm{cm}^3}\right]$,
$\tau^n_+, \tau^n_0, \tau^p_0, \tau^p_-$	lifetimes for n and p before capture by D $[\mathrm{s}]$.

In general, the total transition rates as written in equations (4.12) to (4.15) depend on the energies of the defect states D, $E_{+/0}$ and $E_{0/-}$. Therefore, these equations are valid only under the assumption that the thermal velocities and especially the cross sections and occupation functions do not depend on the energy levels $E_{+/0}$ and $E_{0/-}$, and we can write

$$r_{X\to x}^{(p,n)} = v_{\mathrm{th}}^{(p,n)} \cdot \sigma_x^{(p,n)} \cdot (n_{\mathrm{f}}, p_{\mathrm{f}}) \cdot f_x \cdot \int_{E_{\mathrm{V}}}^{E_{\mathrm{C}}} \frac{\mathrm{d}N_{\mathrm{D}_x}(\epsilon)}{\mathrm{d}\epsilon}\,\mathrm{d}\epsilon = v_{\mathrm{th}}^{(p,n)} \cdot \sigma_x^{(p,n)} \cdot (n_{\mathrm{f}}, p_{\mathrm{f}}) \cdot f_x \cdot N_{\mathrm{D}_x}, \quad (4.16)$$

which was used for $(*)$. Thus, the radical assumption that $\sigma_x^{(p,n)}$ and $v_{\mathrm{th}}^{(p,n)}$ do not depend on the defect distribution in energy and space has the consequence that the reaction rates do not depend on the energy level of the amphoteric defect state. From the definition of the occupation functions follows $(**)$, and $(***)$ includes the definition of the (inverse) lifetimes as

$$\frac{1}{\tau_+^n} \doteq v_{\mathrm{th}}^n \cdot \sigma_+^n \cdot N_{\mathrm{D}}, \qquad \frac{1}{\tau_-^p} \doteq v_{\mathrm{th}}^p \cdot \sigma_-^p \cdot N_{\mathrm{D}}, \quad (4.17)$$

$$\frac{1}{\tau_0^n} \doteq v_{\mathrm{th}}^n \cdot \sigma_0^n \cdot N_{\mathrm{D}}, \qquad \frac{1}{\tau_0^p} \doteq v_{\mathrm{th}}^p \cdot \sigma_0^p \cdot N_{\mathrm{D}}. \quad (4.18)$$

These definitions are noteworthy, as τ_+^n should intuitively be the lifetime of an electron before it is captured by a positively charged defect state, hence $\frac{1}{\tau_+^n} \doteq v_{\mathrm{th}}^n \cdot \sigma_+^n \cdot N_{\mathrm{D}_+} = v_{\mathrm{th}}^n \cdot \sigma_+^n \cdot f_+ \cdot N_{\mathrm{D}}$. Instead, it is defined as the time before an electron is captured by any defect state, which are all supposed to be positively charged, i.e. $f_+ \equiv 1$.

Mainly two reasons are responsible for the choice of the lifetime definition (4.17) and (4.18). First, this definition was used by J. Hubin and A. Shah for the description of amphoteric defect states in [Hubin 92, Hubin 94], for which the concepts were taken from the Shockley-Read-Hall (SRH) description of defects and recombination [Shockley 52, Hall 52] that are still common [Sze 07]. In [Sah 57], the inverse SRH lifetime $\frac{1}{\tau} \doteq v_{\mathrm{th}} \cdot \sigma_n \cdot N_{\mathrm{D}}$ is described as the «lifetime for electrons injected into highly p-type specimen» implying $f_+ \equiv 1$. This definition was used by all later authors both for SRH and for amphoteric-defect models.

Second, one is interested to have an expression of the occupation functions as $f_x = f_x\left(\tau_{(+,0,-)}^{(p,n)}\right)$ and not only as $f_x = f_x\left(\sigma_{(+,0,-)}^{(p,n)}\right)$ because $\tau_{(+,0,-)}^{(p,n)}$ is more directly measureable than $\sigma_{(+,0,-)}^{(p,n)}$. However, if f_x were included in the definition of $\tau_{(+,0,-)}^{(p,n)}$, the transition rates could no longer be expressed as a function of f_x, hence f_x would no longer be a function of τ.

Occupation functions as functions of lifetimes

In thermal equilibrium, the thermal emission rates e equal the transition rates r. Here, we consider the case of sufficiently high illumination such that thermal emission is negligible.

Further, we consider the charge distribution of dangling bonds constant in time, which is the steady state condition for each energy level independently:

$$r_{\mathrm{C}\to +}^n = r_{\mathrm{V}\to 0}^p, \quad (4.19)$$

$$r_{\mathrm{C}\to 0}^n = r_{\mathrm{V}\to -}^p. \quad (4.20)$$

Inserting equations (4.12) to (4.15) into equations (4.19) and (4.20) gives

$$\frac{n_\mathrm{f}}{\tau^n_+}\cdot f_+ = \frac{p_\mathrm{f}}{\tau^p_0}\cdot f_0 \overset{(4.11)}{=} \frac{p_\mathrm{f}}{\tau^p_0}\cdot(1-f_- - f_+) \quad\Rightarrow\quad \overbrace{\frac{n_\mathrm{f}}{p_\mathrm{f}}\cdot\frac{\tau^p_0}{\tau^n_+}}^{\alpha}\cdot f_+ = (1-f_- - f_+), \tag{4.21}$$

$$\frac{p_\mathrm{f}}{\tau^p_-}\cdot f_- = \frac{n_\mathrm{f}}{\tau^n_0}\cdot f_0 \overset{(4.11)}{=} \frac{n_\mathrm{f}}{\tau^n_0}\cdot(1-f_- - f_+) \quad\Rightarrow\quad \underbrace{\frac{p_\mathrm{f}}{n_\mathrm{f}}\cdot\frac{\tau^n_0}{\tau^p_-}}_{\beta}\cdot f_- = (1-f_- - f_+). \tag{4.22}$$

Building the sum and difference of these equations leads to

$$f_- = \frac{\alpha}{\beta}\cdot f_+ \quad\text{and}\quad f_+ = \frac{1}{1+\alpha+\frac{\alpha}{\beta}} \tag{4.23}$$

and finally to

$$\boxed{f_+ = \frac{\frac{p_\mathrm{f}^2}{\tau^p_0\cdot\tau^p_-}}{\frac{p_\mathrm{f}^2}{\tau^p_0\cdot\tau^p_-}+\frac{n_\mathrm{f}\cdot p_\mathrm{f}}{\tau^p_-\cdot\tau^n_+}+\frac{n_\mathrm{f}^2}{\tau^n_0\cdot\tau^n_+}},\quad f_0 = \frac{\frac{n_\mathrm{f}\cdot p_\mathrm{f}}{\tau^p_-\cdot\tau^n_+}}{\frac{p_\mathrm{f}^2}{\tau^p_0\cdot\tau^p_-}+\frac{n_\mathrm{f}\cdot p_\mathrm{f}}{\tau^p_-\cdot\tau^n_+}+\frac{n_\mathrm{f}^2}{\tau^n_0\cdot\tau^n_+}},\quad f_- = \frac{\frac{n_\mathrm{f}^2}{\tau^n_0\cdot\tau^n_+}}{\frac{p_\mathrm{f}^2}{\tau^p_0\cdot\tau^p_-}+\frac{n_\mathrm{f}\cdot p_\mathrm{f}}{\tau^p_-\cdot\tau^n_+}+\frac{n_\mathrm{f}^2}{\tau^n_0\cdot\tau^n_+}}.} \tag{4.24}$$

These equations are equivalent to equations in [Hubin 94] and [Shah 10]. However, note that they used implicitly $v^n_\mathrm{th} = v^p_\mathrm{th}$, which is not a necessary condition in the derivation.

Occupation functions as functions of cross sections

For the expression of f_x as a function of $\sigma^{(p,n)}_{(+,0,-)}$, we insert (4.17) and (4.18) into (4.24) and get

$$f_+ = \frac{\sigma^p_0\cdot\sigma^p_-\cdot p_\mathrm{f}^2}{\sigma^p_0\cdot\sigma^p_-\cdot p_\mathrm{f}^2+\gamma\cdot\sigma^n_+\cdot\sigma^p_-\cdot n_\mathrm{f}\cdot p_\mathrm{f}+\gamma^2\cdot\sigma^n_+\cdot\sigma^n_0\cdot n_\mathrm{f}^2}, \tag{4.25}$$

$$f_0 = \frac{\gamma\cdot\sigma^n_+\cdot\sigma^p_-\cdot n_\mathrm{f}\cdot p_\mathrm{f}}{\sigma^p_0\cdot\sigma^p_-\cdot p_\mathrm{f}^2+\gamma\cdot\sigma^n_+\cdot\sigma^p_-\cdot n_\mathrm{f}\cdot p_\mathrm{f}+\gamma^2\cdot\sigma^n_+\cdot\sigma^n_0\cdot n_\mathrm{f}^2}, \tag{4.26}$$

$$f_- = \frac{\gamma^2\cdot\sigma^n_+\cdot\sigma^n_0\cdot n_\mathrm{f}^2}{\sigma^p_0\cdot\sigma^p_-\cdot p_\mathrm{f}^2+\gamma\cdot\sigma^n_+\cdot\sigma^p_-\cdot n_\mathrm{f}\cdot p_\mathrm{f}+\gamma^2\cdot\sigma^n_+\cdot\sigma^n_0\cdot n_\mathrm{f}^2}. \tag{4.27}$$

Here, we have defined

$$\gamma \doteq \frac{v^n_\mathrm{th}}{v^p_\mathrm{th}}, \tag{4.28}$$

which makes a physical difference to expressions of $f_x = f_x\left(\sigma^{(p,n)}_{(+,0,-)}\right)$ in [Hubin 92] and [Shah 10], where $\gamma \equiv 1$.

For further studies, we simplify these equations by making assumptions about the capture cross sections: the two processes with σ^n_+ and σ^p_- implied are charge assisted (Coulomb attraction) and assumed to be the same, while σ_0^n and σ_0^p involve neutral states, also assumed to be the same:

$$\sigma_+^n = \sigma_\pm = \sigma_-^p \quad \text{and} \quad \sigma_0^n = \sigma_0 = \sigma_0^p. \tag{4.29}$$

Further, we define

$$\zeta \doteq \frac{\sigma_\pm}{\sigma_0}, \tag{4.30}$$

which is typically larger than one. This leads to the expressions of $f_x = f_x(\sigma_\pm, \sigma_0)$ as published in [Stuckelberger 10]:

$$\boxed{f_+ = \frac{1}{1+\gamma\cdot\zeta\cdot\frac{n_\mathrm{f}}{p_\mathrm{f}}+\gamma^2\cdot\left(\frac{n_\mathrm{f}}{p_\mathrm{f}}\right)^2},\ f_0 = \frac{\gamma\cdot\zeta\cdot\frac{n_\mathrm{f}}{p_\mathrm{f}}}{1+\gamma\cdot\zeta\cdot\frac{n_\mathrm{f}}{p_\mathrm{f}}+\gamma^2\cdot\left(\frac{n_\mathrm{f}}{p_\mathrm{f}}\right)^2},\ f_- = \frac{\gamma^2\cdot\left(\frac{n_\mathrm{f}}{p_\mathrm{f}}\right)^2}{1+\gamma\cdot\zeta\cdot\frac{n_\mathrm{f}}{p_\mathrm{f}}+\gamma^2\cdot\left(\frac{n_\mathrm{f}}{p_\mathrm{f}}\right)^2}.} \tag{4.31}$$

Numerical values of occupation functions

Figure 4.4 shows the occupation functions (4.31) as a function of $\frac{n_\mathrm{f}}{p_\mathrm{f}}$ for different γ and ζ. For $\zeta = 1, \gamma = 1$, f_0 is significant only in a small range of $\frac{n_\mathrm{f}}{p_\mathrm{f}}$ around unity, where all three occupations have the same probability.

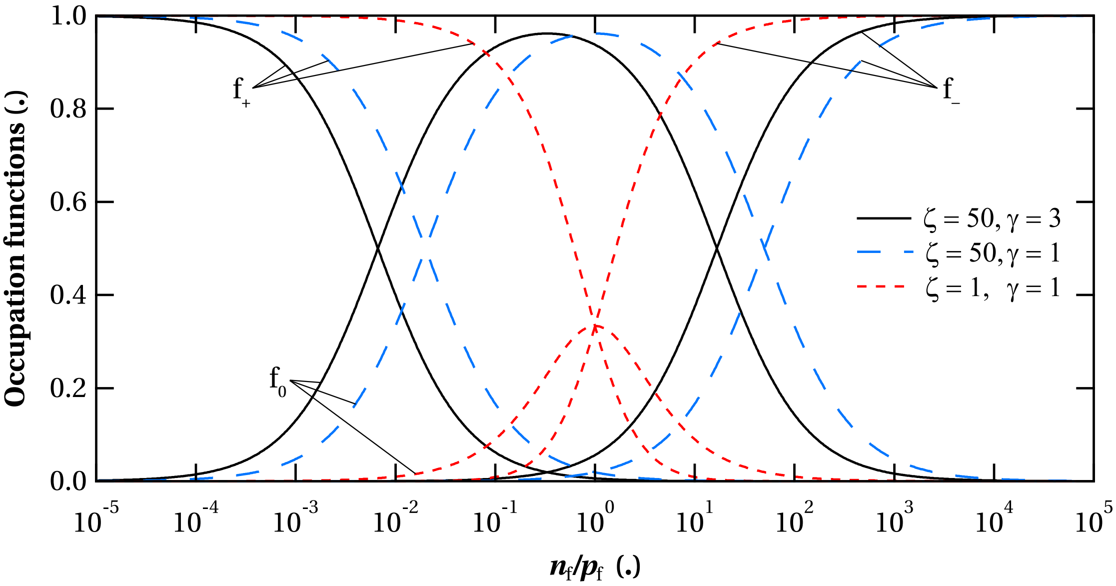

Figure 4.4: Probability that an amphoteric defect state is positively charged (f_+), neutral (f_0), or negatively charged (f_-), as a function of the ratio of free electrons to free holes. These calculations are made for the different ratios of capture cross sections (ζ) for charged and neutral states, and for different thermal velocities (γ) of electrons and holes.

For further calculations, we use $\zeta = 50$ as reported in [Beck 96] and later in [Shah 10], based on experiments with a tolerance of about 2. An increase of the ratio ζ leads to shorter lifetimes of charged defect states, hence the probability is increased that defect states are in state f_0.

For these calculations, we use further $\gamma = 3$, indicating that electrons are about three times more mobile than holes. This choice represents a difference in the effective mass m^* by a factor of nine according to $v_{\mathrm{th}} = \sqrt{\frac{3k_{\mathrm{B}}T}{m^*}}$ and is made by analogy of $\mu^n \approx 3 \cdot \mu^p$ [Stuckelberger 10, Shah 10]. As a consequence, the transition rates of electrons are higher than those of holes. Hence, the recombination process, being limited by the slower processes, is in the case of equal hole and electron concentrations limited by holes, while electrons are “waiting” at the energy levels $E_{+/0}$ and $E_{0/-}$. In Fig. 4.4, this is seen as a shift of the occupation functions towards positive charges.

4.3.4 Recombination rates through amphoteric defect states

The total recombination rate through amphoteric defect states as described above is given by the sum of the rates for the two parallel recombination paths,

$$r_{\mathrm{D}} = r^n_{\mathrm{C}\to+} + r^n_{\mathrm{C}\to0} = r^p_{\mathrm{V}\to0} + r^p_{\mathrm{V}\to-} \tag{4.32}$$

$$= \frac{\frac{n_{\mathrm{f}} \cdot p_{\mathrm{f}}}{\tau^n_+ \cdot \tau^p_-} \cdot \left(\frac{p_{\mathrm{f}}}{\tau^p_0} + \frac{n_{\mathrm{f}}}{\tau^n_0} \right)}{\frac{p^2_{\mathrm{f}}}{\tau^p_0 \cdot \tau^p_-} + \frac{n_{\mathrm{f}} \cdot p_{\mathrm{f}}}{\tau^p_- \cdot \tau^n_+} + \frac{n^2_{\mathrm{f}}}{\tau^n_0 \cdot \tau^n_+}} \tag{4.33}$$

$$= \frac{v^n_{\mathrm{th}} \cdot N_{\mathrm{D}} \cdot \sigma^n_+ \cdot \sigma^p_- \cdot n_{\mathrm{f}} \cdot p_{\mathrm{f}} \cdot \left(\sigma^p_0 \cdot p_{\mathrm{f}} + \gamma \cdot \sigma^n_0 \cdot n_{\mathrm{f}}\right)}{\sigma^p_0 \cdot \sigma^p_- \cdot p^2_{\mathrm{f}} + \gamma \cdot \sigma^n_+ \cdot \sigma^p_- \cdot n_{\mathrm{f}} \cdot p_{\mathrm{f}} + \gamma^2 \cdot \sigma^n_+ \cdot \sigma^n_0 \cdot n^2_{\mathrm{f}}}, \tag{4.34}$$

where (4.33) follows from (4.24) and is the same as reported in [Hubin 92]. Equation (4.34) follows from (4.25) to (4.27) but differs from reported equations of $r_{\mathrm{D}}\left(\sigma_x^{(n,p)}\right)$ due to the generalization of $v^n_{\mathrm{th}} \neq v^p_{\mathrm{th}}$.

In the case of intrinsic a-Si:H material that is far away from depletion zones, the two conditions

$$\frac{\sigma^n_+}{\sigma^p_0} \gg \frac{p_{\mathrm{f}}}{n_{\mathrm{f}}} \quad \text{and} \quad \frac{\sigma^p_-}{\sigma^n_0} \gg \frac{n_{\mathrm{f}}}{p_{\mathrm{f}}} \tag{4.35}$$

are fulfilled simultaneously. In that limit, r_{D} reduces independently of γ to

$$r_{\mathrm{D}} \longrightarrow \frac{p_{\mathrm{f}}}{\tau^p_0} + \frac{n_{\mathrm{f}}}{\tau^n_0}, \tag{4.36}$$

which is the same as reported in [Hubin 95] but differs significantly from the SRH expression, where $r^{\mathrm{SRH}}_{\mathrm{D}} \longrightarrow \left(\frac{\tau_{\mathrm{p}}}{p_{\mathrm{f}}} + \frac{\tau_{\mathrm{n}}}{n_{\mathrm{f}}}\right)^{-1}$: while the majority carrier governs recombination in the case of amphoteric defect states, the minority carrier governs recombination in the case of SRH recombination.

4.4 Electric field deformation

It is commonly accepted that a strong internal electric field E in the intrinsic (i) layer is essential for the proper functioning of TF-Si solar cells. In fact, E determines the collection length (which is here the drift length $L_{\text{drift}} = \mu\tau \cdot E$) and thus governs in many cases the fill factor (FF) of these cells. Whereas μc-Si:H solar cells are generally not seriously affected by collection problems up to i-layer thicknesses of about 5 µm [Boccard 11], a-Si:H solar cells have to be kept very thin (< 300 nm) to avoid a breakdown of E in the degraded state.

In this section, we propose first a simple model for the estimation of the contributions of free and trapped charges (section 4.4.1) and of charged dangling bonds (section 4.4.2) to ΔE in the i-layer of a-Si:H solar cells. In section 4.4.3, we present numerical simulation results for p-i-n-type solar cells with i-layer thicknesses of 100, 200, 300 and 400 nm. This provides the basis for a comparison of the model with other simulations and experimental results in section 4.5.

4.4.1 Electric field deformation due to free and trapped charge carriers

To illustrate our model, we consider an a-Si:H single-junction solar cell with a 300-nm-thick absorber layer and assume:

(A) No recombination occurs in the i-layer.
(B) The carrier transport in the i-layer is purely drift driven (not by diffusion).

These drastic assumptions are far from being reached, but are taken as a starting point here to determine the electric field within the i-layer and to assess the impacts of free charges and charged band tail states and dangling bonds. Note that the aim here is not to provide precise simulations of solar cells, but to keep the model as simple as possible to provide intuitive insights into the physical processes of charge collection, and to explain measured trends. While resulting absolute values might differ substantially from real values according to the chosen parameters, relative comparisons are in good agreement with experiment and more precise ASA simulations as will be shown in section 4.5.4. The following calculations of ΔE are performed without iterations of the transport equations, which limits this model to cases in which $\Delta E \ll E$.

Electron–hole pair generation profiles

We start from electron–hole pair generation profiles $G(x)$ as shown in Fig. 4.5a. Here, x denotes the position in the i-layer, with $x = 0$ being at the p-i and $x = d$ at the i-n interface (here, the i-layer thickness $d = 300$ nm). In one case, denoted “AM1.5g”, $G(x)$ was calculated with the SunShine software [Krc 03] using the following device structure:

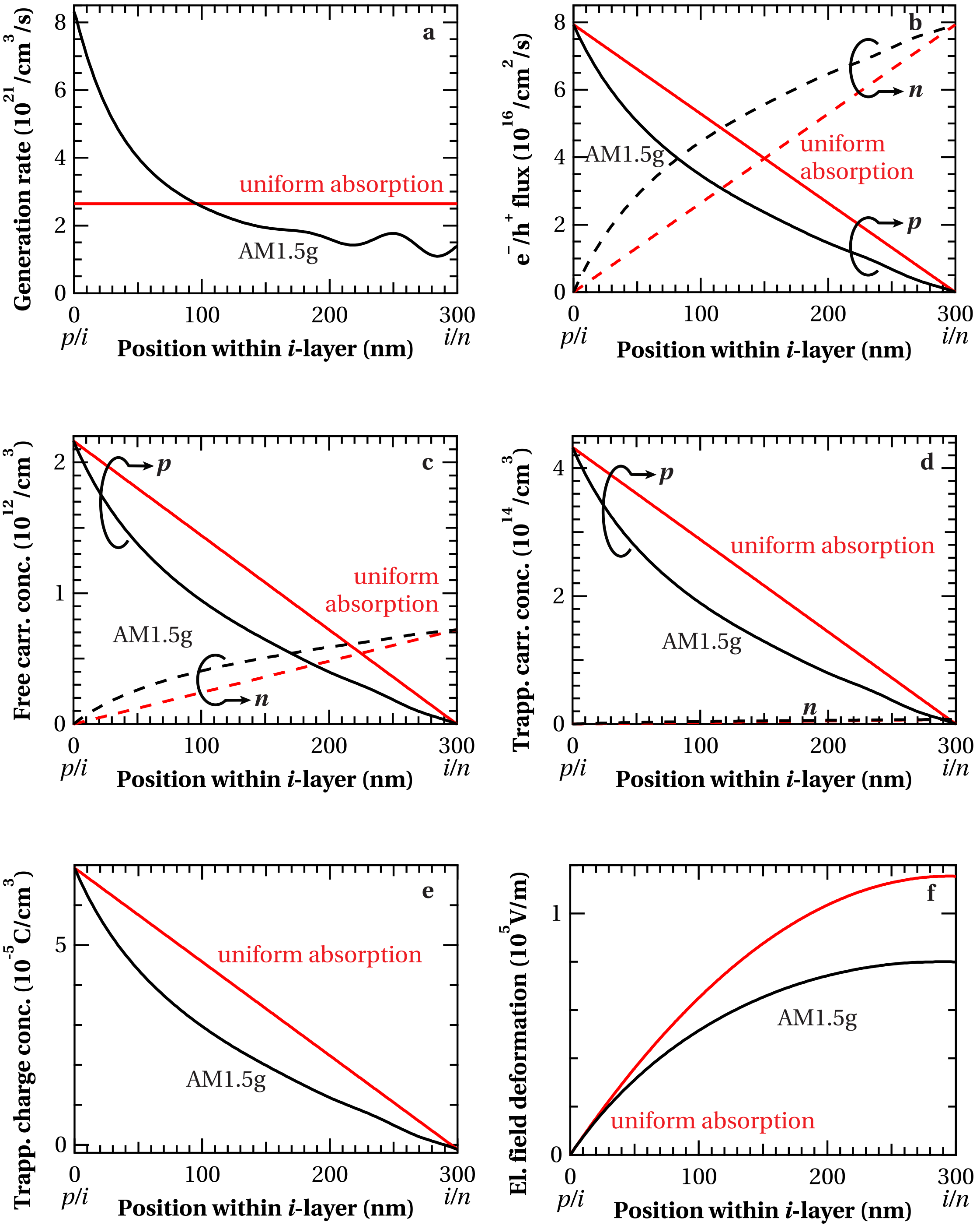

Figure 4.5: From the electron–hole pair generation rate (a) over the electron and hole fluxes (b), the free electron and hole concentration (c), the trapped electron and hole concentration (d), and the trapped charge concentration (e), an estimation of the electric field deformation (f) is derived. The hole fluxes in (b) are multiplied by (−1) in this graph to be positive (the negative sign comes from the flow direction).

0.5 mm Schott AF 45 glass
2 µm flat low-pressure chemical vapor deposition (LPCVD) ZnO
8 nm p-type microcrystalline silicon (p-(μc-Si:H)) layer
8 nm p-(a-SiC:H)-layer
300 nm a-Si:H i-layer
2 nm n-type hydrogenated amorphous silicon (n-(a-Si:H))-layer
20 nm n-type microcrystalline silicon (n-(μc-Si:H))-layer
2 µm LPCVD ZnO (Z2)
Scattering back reflector

The light (AM1.5g spectrum with 1000 $\frac{\mathrm{W}}{\mathrm{m}^2}$) was considered to enter through the glass substrate from the p-side. In the other case, denoted "uniform absorption", a constant electron–hole pair generation profile of 2.64×10^{21} pairs/cm^3/s throughout the i-layer was assumed, corresponding to long-wavelength light with low absorption. This value was chosen to provide the same generation rate as the AM1.5g case integrated over the i-layer thickness.

Fluxes of free electrons and holes

The fluxes of free electrons (n) and holes (p) are calculated as

$$\Phi_p(x) = \int_x^d G(\xi)\,\mathrm{d}\xi \quad \text{and} \quad \Phi_n(x) = \int_0^x G(\xi)\,\mathrm{d}\xi \tag{4.37}$$

and are shown in Fig. 4.5b, using assumption A.

Concentrations of free electrons and holes

Based on assumption B, the free hole and electron concentrations $p_\mathrm{f}(x)$ and $n_\mathrm{f}(x)$ (see Fig. 4.5c) are obtained via

$$p_\mathrm{f}(x) = \frac{\Phi_p(x)}{v^p} = \frac{\Phi_p(x)}{\mu^p \cdot E_\mathrm{nom}} \quad \text{and} \quad n_\mathrm{f}(x) = \frac{\Phi_n(x)}{v^n} = \frac{\Phi_n(x)}{\mu^n \cdot E_\mathrm{nom}}. \tag{4.38}$$

Here, v^p and v^n are the free-carrier velocities, determined in steady-state conditions by the nominal electrical field E_nom and the band mobilities, here considered as $\mu^p = 1\,\mathrm{cm}^2/(\mathrm{Vs})$ and $\mu^n = 3\,\mathrm{cm}^2/(\mathrm{Vs})$ (with $\gamma = 3$, see section 4.3.3). Note that a wide range of values for band mobilities can be found in the literature. The nominal electric field is

$$E_\mathrm{nom} = \frac{V_\mathrm{bi}}{d}, \tag{4.39}$$

with the built-in voltage $V_\mathrm{bi} \approx 1.1\,\mathrm{V}$ for a-Si:H solar cells. Because of the different mobilities of electrons and holes, the free-carrier concentration is not symmetric.

Here, we assumed implicitly E_nom (and hence, V_bi) to be constant. Thus, the calculations are strictly speaking valid only for a given applied voltage (here around V_oc) but could be repeated for other points of the $J(V)$ curve. However, note that no charge losses due to recombination are considered in equation (4.38) calculating p_f and n_f (assumption A), which is in contradiction to forward bias voltages above V_oc.[3]

Concentrations of trapped electrons and holes

The concentrations of charge carriers $p_\mathrm{t}(x)$ and $n_\mathrm{t}(x)$ that are trapped in band tail states, shown in Fig. 4.5d, are assumed to be proportional to the free-carrier concentrations:

$$p_\mathrm{t}(x) = \frac{p_\mathrm{f}}{\Theta_p} \quad \text{and} \quad n_\mathrm{t}(x) = \frac{n_\mathrm{f}}{\Theta_n}, \tag{4.40}$$

where the "Rose trapping factors" are around $\Theta_p = 0.005$ and $\Theta_n = 0.1$ [Shah 10]; see also the discussion in section 4.5.4. Note that choosing (within a reasonable range) different values for the Rose trapping factors as well as for the band mobilities will affect the results only quantitatively but not qualitatively. Due to the large ratio of Θ_n/Θ_p it is obvious that $p_\mathrm{t} \ll n_\mathrm{t}$ except very close to the i-n interface.

Trapped charge concentration

The trapped charge concentration

$$\rho_\mathrm{t}(x) = q \cdot \left(p_\mathrm{t} - n_\mathrm{t}\right), \tag{4.41}$$

shown in Fig. 4.5e, is dominated by p_t.

Electric field deformation

Finally, ΔE caused by trapped carriers relative to the p-i interface is calculated using Poissons equation

$$\Delta E_\mathrm{t} = \frac{1}{\epsilon_0 \epsilon_\mathrm{r}} \int_0^x \rho_\mathrm{t}(\xi)\,\mathrm{d}\xi, \tag{4.42}$$

where $\epsilon_0 = 8.854 \times 10^{-14}\,\mathrm{F/cm}$ and $\epsilon_\mathrm{r} \approx 10$. Note that ΔE, shown in Fig. 4.5f, is positive, as the electric field in the i-layer is negative for the chosen coordinate system.

For the estimation of ΔE for electrons and holes separately, we considered either of them for ρ_t; for the estimation of ΔE for free carriers, we used in analogy to ρ_t the free charge concentration ρ_f considering holes, electrons, or both.

Figure 4.6a illustrates schematically the simulated charge collection process: free charge carriers cause space charge concentrations, typically positive charges at the p-i, and negative

---

[3] However, even under forward voltage with large recombination currents, recombination takes place to a large extent in the doped layers as shown in Fig. 8.9a.

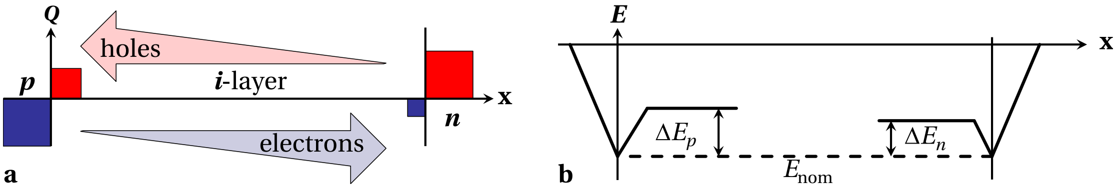

Figure 4.6: Schema of charge collection: the free charges cause positive space charge at the p-i and negative space charge at the i-n interface (a), causing electric field deformations ΔE^p and ΔE^n (b).

charges at the i-n interface. These charges shield the charges of the depletion zone, hence reducing the electric field as shown in Fig. 4.6b by $\Delta E(x)$ from $E_{\text{nom}} = \text{const.}$ (compare to the model derived in [Schiff 03]).

4.4.2 Electric field deformation due to charged dangling bonds

Not only free charge carriers and charged band tail states as described above, but also charged defects lead to ΔE within the i-layer.[4] To estimate these contributions originating from positively and negatively charged defects, ΔE^p_{db} and ΔE^n_{db}, we simplify the occupation functions to step functions and consider the defects to be in the states

$$D^+, \quad \text{if} \quad f_+ \geq f_0 \quad \overset{(4.31)}{\Longleftrightarrow} \quad \gamma \cdot \frac{n_{\text{f}}}{p_{\text{f}}} \leq \frac{1}{\zeta} \quad \overset{(4.28)}{\Longleftrightarrow} \quad \frac{\Phi_n}{\Phi_p} \leq \frac{1}{\zeta}, \tag{4.43}$$

$$D^0, \quad \text{if} \quad (f_0 > f_+) \wedge (f_0 > f_-) \quad \overset{(4.28)}{\Longleftrightarrow} \quad \left(\frac{\Phi_n}{\Phi_p} > \frac{1}{\zeta}\right) \wedge \left(\frac{\Phi_n}{\Phi_p} < \zeta\right), \tag{4.44}$$

$$D^-, \quad \text{if} \quad f_- \geq f_0 \quad \overset{(4.31)}{\Longleftrightarrow} \quad \gamma \cdot \frac{n_{\text{f}}}{p_{\text{f}}} \geq \zeta \quad \overset{(4.28)}{\Longleftrightarrow} \quad \frac{\Phi_n}{\Phi_p} \geq \zeta. \tag{4.45}$$

In addition to assumptions (A) and (B) of section 4.4.1, we assume further

(C) The defects can be described by amphoteric states as described in section 4.3 with the three charge states D^+, D^0, D^-, with their occupation functions f_+, f_0, f_- as given in equation (4.31), determined by the competition of the four capture processes as shown in Fig. 4.2.

(D) $\zeta = 50$ and $\gamma = 3$, as established in section 4.3.3.

(E) The defect concentration $N_{\text{db}} = 2 \times 10^{16}\,\text{cm}^{-3}$.

Note that using equations (4.43) to (4.45) does not explicitly include γ; however, it is implicitly included in the particle fluxes. Here, we are interested in the position-dependent flow values only, not in their direction; therefore, we replaced in these equations and in the following figures $\Phi_p \rightarrow |\Phi_p| = -\Phi_p$.

---

[4] Defect states always play two roles that are inherently linked to each other: when they are charged, they modify the electric field distribution, and independently of their charge they serve as recombination centers. In this chapter, we focus on the electric field effect only.

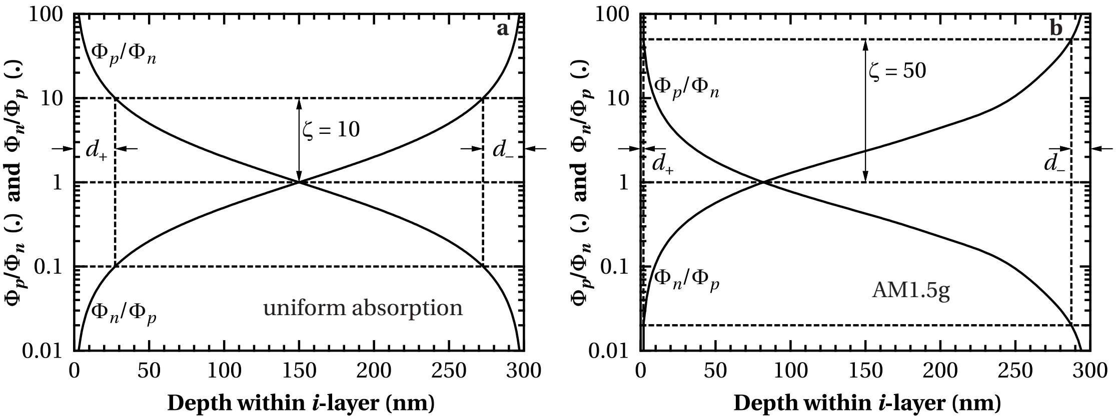

Figure 4.7: Ratios of non-directional hole and electron fluxes as a function of the position in the i-layer for uniform absorption (a) and AM1.5g illumination (b). For better visibility, $\zeta = 10$ is shown in graph (a), but $\zeta = 50$ was used for calculations.

Figure 4.7 shows the flux ratios for the two illumination cases detailed in section 4.4.1. From here, we define the thicknesses d_+ and d_- of the regions at the p-i and the i-n interfaces, respectively, where the dangling bonds are completely charged according to the equations (4.43) to (4.45).

Analogous to ΔE due to charged band tail states, ΔE due to charged defect states can therefore be calculated via adapted equations (4.41) and (4.42) for the two space charge regions. In this simple model, where ρ_{db} is a step function, ΔE^p_{db} and ΔE^n_{db} are constant within the i-layer except close to the p-i and i-n interfaces, where they are linear.

4.4.3 Numeric evaluation of the electric field deformation

In tables 4.1, 4.2, and 4.3, we show the calculated maximum ΔE as derived in the previous sections, for free and trapped charge carriers and charged dangling bonds, respectively, at AM1.5g illumination. We observe the following:

- ΔE generally increases with increasing i-layer thickness. On one hand, this is due to enhanced absorption, hence higher hole and electron fluxes and concentrations, which are correlated with ΔE. On the other hand, only the long-wavelength absorption is enhanced. Since holes are slower than electrons, the average charge-carrier concentration (and, hence, ΔE) is enhanced more by thickening the i-layer than would be the case by increasing the absorption equally for all wavelengths. This second effect amplifies the thickness dependence.
- Thicker i-layers enhance ΔE not only absolutely, but also relatively; the relative change is in fact more significant because of a weaker nominal electric field.
- The effect of free charge carriers is negligible compared to that of trapped charge carriers as a direct consequence of the choice of the Rose factor such that the trapped charge concentration is a multiple of the free charge concentration.

Table 4.1: Maximum electric field deformation caused by free charge carriers.

d	E_{nom}	$\max\left(\Delta E_{\text{f}}^{p}\right)$	$\frac{\max(\Delta E_{\text{f}}^{p})}{E_{\text{nom}}}$	$\max\left(\Delta E_{\text{f}}^{n}\right)$	$\frac{\max(\Delta E_{\text{f}}^{n})}{E_{\text{nom}}}$
100 nm	1.1×10^{7} V/m	4.1×10^{1} V/m	3.7×10^{-4}%	1.9×10^{1} V/m	1.7×10^{-4}%
200 nm	5.5×10^{6} V/m	1.8×10^{2} V/m	3.3×10^{-3}%	9.8×10^{1} V/m	1.8×10^{-3}%
300 nm	3.7×10^{6} V/m	4.1×10^{2} V/m	1.1×10^{-2}%	2.5×10^{2} V/m	6.9×10^{-3}%
400 nm	2.8×10^{6} V/m	7.3×10^{2} V/m	2.6×10^{-2}%	4.9×10^{2} V/m	1.8×10^{-2}%

Table 4.2: Maximum electric field deformation caused by trapped charge carriers.

d	E_{nom}	$\max\left(\Delta E_{\text{t}}^{p}\right)$	$\frac{\max(\Delta E_{\text{t}}^{p})}{E_{\text{nom}}}$	$\max\left(\Delta E_{\text{t}}^{n}\right)$	$\frac{\max(\Delta E_{\text{t}}^{n})}{E_{\text{nom}}}$
100 nm	1.1×10^{7} V/m	8.2×10^{3} V/m	7.5×10^{-2}%	1.9×10^{2} V/m	1.7×10^{-3}%
200 nm	5.5×10^{6} V/m	3.6×10^{4} V/m	6.6×10^{-1}%	9.8×10^{2} V/m	1.8×10^{-2}%
300 nm	3.7×10^{6} V/m	8.2×10^{4} V/m	2.2%	2.5×10^{3} V/m	6.9×10^{-2}%
400 nm	2.8×10^{6} V/m	1.5×10^{5} V/m	5.3%	4.9×10^{3} V/m	1.8×10^{-1}%

Table 4.3: Maximum electric field deformation caused by charged dangling bonds.

d	d_{+}	$\max\left(\Delta E_{\text{db}}^{p}\right)$	$\frac{\max(\Delta E_{\text{db}}^{p})}{E_{\text{nom}}}$	d_{-}	$\max\left(\Delta E_{\text{db}}^{n}\right)$	$\frac{\max(\Delta E_{\text{db}}^{n})}{E_{\text{nom}}}$
100 nm	1.2 nm	4.3×10^{4} V/m	0.4%	3.3 nm	1.2×10^{5} V/m	1.1%
200 nm	1.7 nm	6.0×10^{4} V/m	1.1%	7.3 nm	2.6×10^{5} V/m	4.8%
300 nm	1.9 nm	6.9×10^{4} V/m	1.9%	13 nm	4.6×10^{5} V/m	13%
400 nm	2.0 nm	7.4×10^{4} V/m	2.7%	19 nm	6.9×10^{5} V/m	25%

- The effects of free and trapped electrons are negligible compared to that of holes because of the different Rose factors and the higher mobility. The fact that the illumination enters the cell from the p-side mitigates this effect, but cannot compensate for it completely.
- With a constant defect concentration as assumed here, the negatively charged region at the i-n interface is larger than the positively charged region at the p-i interface due to the illumination from the p-side. However, with a non-constant defect concentration distribution in the i-layer (in real devices, the defect concentration is typically highest at p-i interface due to the deposition sequence and light-induced degradation), the effect of positively charged defects at the p-i interface can become more significant as will be shown in section 4.5.3.

We have seen that it is in practice sufficient to consider only trapped holes and charged defects of either charge; the concentrations of free charges and trapped electrons are too low to play a significant role.

4.5 Simulation and measurement of the collection voltage

4.5.1 From the collection efficiency to the collection voltage

We introduce here the concepts of the collection efficiency and collection voltage that were followed in different research laboratories [Merten 98, Hof 00, Sculati-Meillaud 06] and in industry [Shah 11]. Their strength is the easy experimental access to model parameters that allow the deduction of electrical bulk properties from device measurements. In particular, the collection efficiency parameterized by V_{coll} is accessible through variable illumination measurements (VIM) or external quantum efficiency (EQE) measurements by varying the bias voltage [Hof 00] as shown in section 4.5.2. Further, these concepts allow a direct comparison of recombination models with the ability to correlate them with experimentally accessible parameters.

The collection function (or collection efficiency) χ is defined as

$$\chi = \frac{Q_{\mathrm{coll}}}{Q_{\mathrm{photo}}} = \frac{J_{\mathrm{coll}}}{J_{\mathrm{photo}}} = 1 - \frac{\int R(x)\,\mathrm{d}x}{\int G(x)\,\mathrm{d}x}, \tag{4.46}$$

with Q_{coll}, Q_{photo}, J_{coll}, and J_{photo} the collected and photogenerated charge and current densities; R and G are the electron–hole pair recombination and generation rates that are integrated over the whole solar cell thickness. Different terms for χ were derived in the literature for various recombination models [Hecht 32, Crandall 83, Hubin 92, Hubin 95, Rech 97b, Merten 98, Hof 99]. In these cases, the collection losses do not depend on G and are therefore proportional to J_{photo}. Note that, despite the fact that these models are based on different assumptions, the formalism and measurements presented hereafter are independent of the choice of the mathematical representation of χ. Instead, the reported models provide only a different recombination term in equivalent electronic circuits as described in equation (4.5).

Describing a solar cell by the simple equivalent electronic circuit [Merten 98] as in Fig. 4.1a, its $J(V)$ characteristics can be written as

$$J(V) = -J_{\mathrm{ph}} + \chi \cdot J_{\mathrm{ph}} + J_0 \cdot \left(e^{\frac{q(V - R_{\mathrm{S}} \cdot J)}{n_1 k_{\mathrm{B}} T}} - 1 \right) + \frac{V - R_{\mathrm{S}} \cdot J}{R_{\mathrm{P}}}. \tag{4.47}$$

Between the high-illumination regime with dominant series-resistance losses and the low-illumination regime with dominant parallel-resistance losses, there exists a medium-illumination regime, where the recombination term is dominant. In this regime, we define independently of the form of χ the collection voltage

$$V_{\mathrm{coll}} \doteq \chi\big|_{V=0} \cdot \left(\frac{\partial \chi}{\partial V}\bigg|_{V=0} \right)^{-1}. \tag{4.48}$$

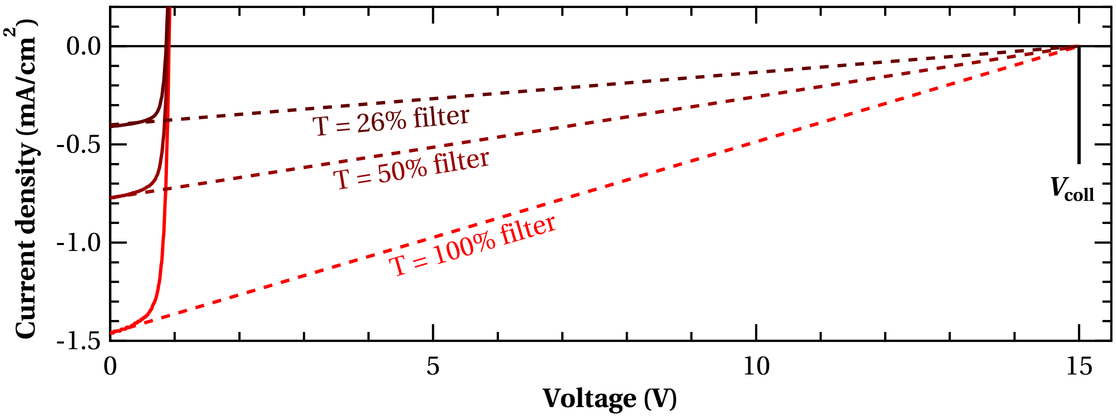

Figure 4.8: Illustration of a collection voltage (V_{coll}) measurement, in this case by a variable illumination measurement using different grey filters with 26, 50, and 100% transmittance. If the charge collection is limiting the current density in a medium-illumination regime, the tangents to the current-density–voltage curves at 0 V cross each other and the abscissa at V_{coll}.

Thanks to its independence from the collection model and other parameters such as parallel and series resistances, V_{coll} is an experimentally valuable parameter for charge collection that can provide additional information to e.g. *EQE* or *FF* [Shah 11].

4.5.2 Measuring the collection voltage

Intuitively, V_{coll} is the voltage that must be applied to the equivalent ohmic resistance R_{sc} for a current J_{sc} to flow as illustrated by Fig. 4.8, or the voltage, where the extrapolated tangent to a $J(V)$ curve at the short-circuit point meets the abscissa. There are different possibilities to measure V_{coll}, most common are VIM or *EQE* measurements varying the bias voltage.

Figure 4.9a shows one way to measure V_{coll} from VIM using

$$V_{\mathrm{coll}} = J(V=0) \cdot \left(\left. \frac{\partial J}{\partial V} \right|_{V=0} \right)^{-1} = R_{\mathrm{sc}} \cdot J_{\mathrm{sc}}. \tag{4.49}$$

The problematic part of V_{coll} measurements is usually to determine whether the given cell is in the medium-illumination regime where recombination is limiting the current. Plotting R_{sc} vs. J_{sc}^{-1} (or, in logarithmic scale also R_{sc} vs. J_{sc}) yields a linear slope, where this is the case and V_{coll} can be determined from the $R_{\mathrm{sc}} \cdot J_{\mathrm{sc}}$ product. Another way is to plot $J_{\mathrm{sc}} \times R_{\mathrm{sc}}$ vs. J_{sc} as demonstrated in Fig. 4.9b, where $J_{\mathrm{sc}} \times R_{\mathrm{sc}}$ is maximum forming a plateau, when recombination is limiting, being lower for limiting series or parallel resistances. Practically, a linear fit was performed in both cases as demonstrated in Fig. 4.9a and b. The evaluation of several hundred VIMs showed that the method as presented in Fig. 4.9b leads to better results due to more adequate weighting of measurement points and easier definition of the criteria of which points to include in the automated fitting. It is important to note that small laboratory-scale solar cells (e.g. the standard 0.25-cm^2 cells from PVLAB with Z2 or Z2.3 front and back contacts)

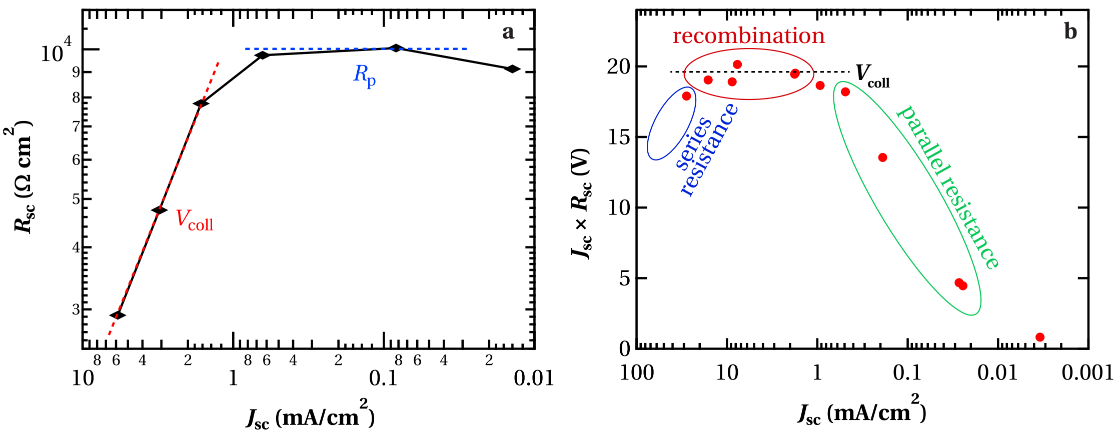

Figure 4.9: Experimental methods to determine the collection voltage (V_{coll}) from variable illumination measurements. (a): The region of charge collection limiting the current is characterized by a linear slope of the short-circuit resistance (R_{sc}) as a function of the inverse short-circuit current density $\left(J_{\text{sc}}^{-1}\right)$. The plateau indicates the parallel resistance (R_{p}). (b): Plotting $J_{\text{sc}} \times R_{\text{sc}}$ vs. J_{sc}, V_{coll} is given by the plateau. For higher illumiation, the $J_{\text{sc}} \times R_{\text{sc}}$ product is limited by the series resistance, for lower illumination by the parallel resistance.

typically reach the medium-illumination regime at illuminations above 1000 $\frac{\text{W}}{\text{m}^2}$. Hence, a concentrating Fresnel lens was often used for measurements under a one-sun solar simulator.

Alternatively, V_{coll} is determined from bias-voltage-dependent EQE measurements using

$$V_{\text{coll}} = EQE(0V) \cdot \left(\left. \frac{\partial EQE}{\partial V} \right|_{V=0} \right)^{-1} . \tag{4.50}$$

Figure 4.10a shows a standard EQE measurement over the full spectral range, and the same cell measured at different bias voltages for specific wavelengths. From there, the collection voltage can be extracted as shown in Fig. 4.10b. If V_{coll} is determined from EQE measurements, special attention must be given to the bias light so that the solar cell is in the medium-illumination regime, which is not directly seen in the measurement as in VIMs.

The explanatory power of V_{coll} measurements increases when the measurement conditions are specifically adapted. For example, we varied the spectrum for VIMs using blue or red filters. However, the measurement error (seen as large scattering among the 16 measured cells per substrate and hardly visible trends in series with varied deposition parameters) was often too large to extract significant information. At least for the setups at PVLAB, the determination of V_{coll} through EQE measurements is more time-consuming than through VIM. Nevertheless, the EQE method was preferred. On one hand, EQE measurements are very precise; on the other, it is easier to modify the conditions at which V_{coll} is measured. In particular, it is possible to choose the wavelength of the probe beam independently from the bias-light spectrum, and the probe side from the illumination side. An application of such measurements is shown in Fig. 4.12.

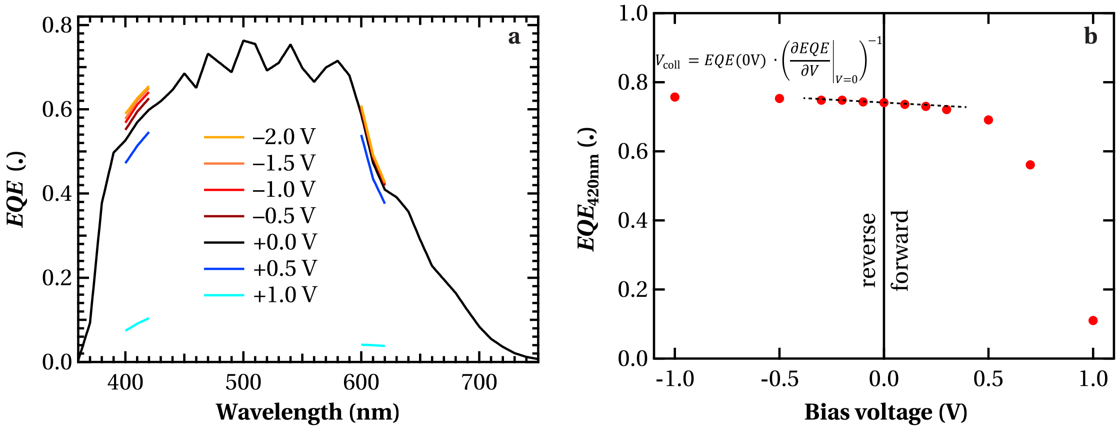

Figure 4.10: (a): External quantum efficiency (EQE) measurement over the full spectrum without applied bias voltage, and measured under different bias voltage between 400 and 420 nm. (b): From the slope of $EQE(V)$ at no bias voltage, we determined the collection voltage. (The cells in figures (a) and (b) are not the same).

4.5.3 Collection voltage for *i*-layer thickness series

We deposited in different systems three i-layer thickness series with thicknesses from 100 to 1000 nm. The solar cell design corresponds to the simulations described in section 4.4.1 that were motivated by these series. Typical solar cell efficiencies are above 10% in the initial state and above 8% after light soaking (1000 h under 1000 $\frac{W}{m^2}$ at 50 °C).

FF and V_{coll} vs. *i*-layer thickness

Figure 4.11 shows the FF and V_{coll} of two of these series with i-layer thicknesses up to 400 nm. Both were measured under a solar simulator with 1000 $\frac{W}{m^2}$ irradiance of AM1.5g spectrum; VIMs as described in section 4.5.2 were used to determine V_{coll}. We note that:

- The FF decreases generally with increasing i-layer thickness due to lower $E_{nom} = \frac{V_{bi}}{d}$ and stronger ΔE as indicated by the simulations presented in section 4.4. An exception is the initial FF in Fig. 4.11b, where shunts rather than recombination limit the FF. (This series was grown on a rough Z2 1' ZnO substrate, whereas the series of Fig. 4.11b was grown on polished ZnO substrates.)
- The light-induced degradation due to the Staebler-Wronski effect induces a small FF decrease for thin i-layers, and a large rone for thick i-layers. This is explained by the light-induced increase of the defect (or dangling-bond) concentration, hence more recombination centers and an increased ΔE. This effect is stronger for thicker cells, and it has more impact due to low E_{nom}, leading to more recombination of charge carriers.
- The V_{coll} generally follows the trend of the FF, which is expected as the FF of these solar cells is collection-limited. However, the increasing V_{coll} with the i-layer thickness in Fig. 4.11b is surprising. In this case, we expect a decreasing V_{coll} for the same reasons

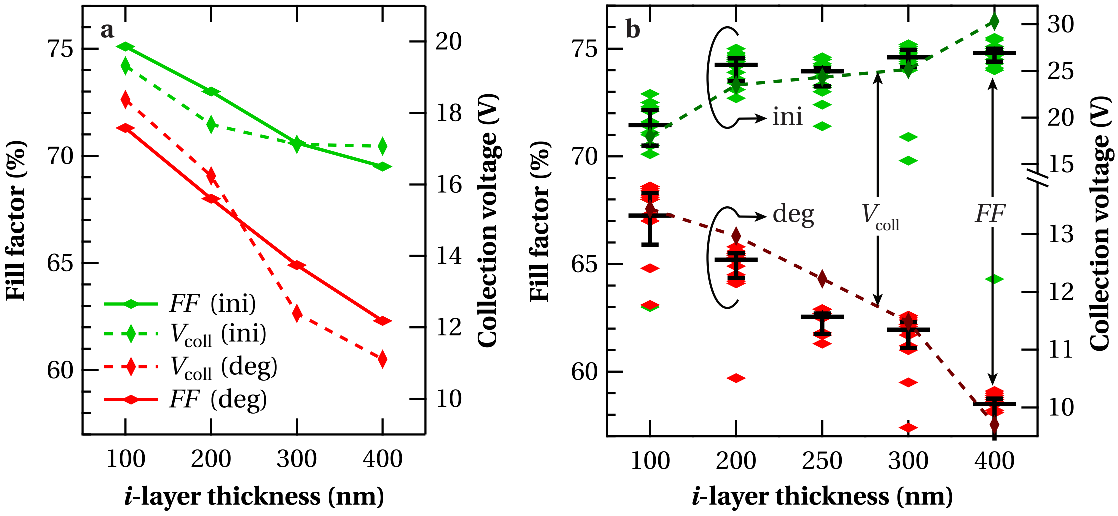

Figure 4.11: The fill factor (FF) and collection voltage (V_{coll}) for two series with i-layer thicknesses from 100 to 400 nm before (ini) and after (deg) light soaking. For (a), the cell with the highest fill factor–open-circuit voltage product ($FF \times V_{\mathrm{oc}}$) (after degradation) per substrate was considered, for (b) all 16 cells are shown with the median and the 25th/75th percentiles shown in black (left axis). For V_{coll}, only the median values are shown for clarity, connected by dashed lines (right axis).

as in the other cases, although the FF is increasing. Here, the $R_{\mathrm{sc}} \times J_{\mathrm{sc}}$ product for the V_{coll} determination was still limited by shunts, not by charge collection. Therefore, the values of V_{coll} obtained for thin i-layers is too low.

- Ideally, we wished to have a measurement parameter like V_{coll} that is universally correlated to charge collection, and hence to the FF, if it is limited by charge collection. However, these figures show that V_{coll} cannot meet these expectations: Already in Fig. 4.11a, a single axis of V_{coll} can hardly meet the single FF axis (it would need to be stretched for thin, and quenched for thick i-layers). This mismatch is even stronger in Fig. 4.11b.This means that there is no absolute correlation between V_{coll} and the FF, but other effects (doped layers etc.) play a significant role too. Still, trends can be observed and we found typically $V_{\mathrm{coll}} > 20$ V for good a-Si:H solar cells in the initial state, and $V_{\mathrm{coll}} > 12$ V for the degraded state.
- The maximum FF values for both series are about 75%, while the corresponding V_{coll} values are about 20% for one, and about 30% in the other. In the former, we found the boron-tailing characteristics to limit the charge collection, in the latter we did not. This shows that V_{coll} is indeed a better indicator of charge collection than the FF is.

Bifacial *EQE* measurements

Inspired by [Fischer 93], we determined V_{coll} from EQE measurements as detailed in section 4.5.2, varying the bias voltage, illumination intensity, spectrum, and illumination side. An example is shown in Fig. 4.12; the details of the measurement conditions are given in the

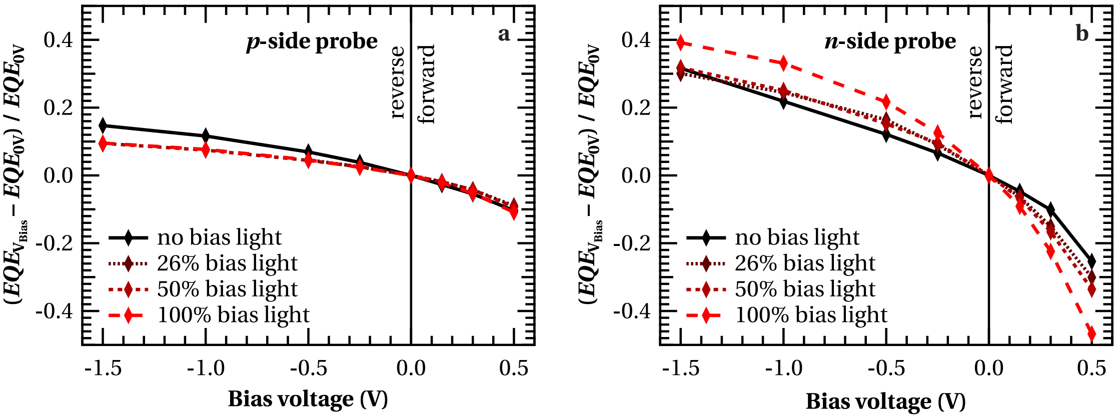

Figure 4.12: Bias-voltage dependent external quantum efficiency (*EQE*) measurements of the 300-nm-thick degraded solar cell of Fig. 4.11a, normalized to the *EQE* without bias voltage. White bias light with different intensities (0, 26, 50, and 100% of 1000 $\frac{W}{m^2}$) was applied. For (a), both bias light and probe light at 420 nm were applied from the *p*-side. Therefore, this measurement is sensitive mainly to collection phenomena close to the *p*-*i* interface. For (b), the bias light was applied from the *p*-side, and the probe light at 420 nm entered the cell from the *n*-side. Therefore, this measurement is sensitive mainly to phenomena close to the *i*-*n* interface.

caption. For the AM1.5g bias light, we used light-emitting diodes and a halogen lamp used for the solar simulator described in [Lo 10], and these were driven by laboratory current sources. Hence, these measurement conditions correspond to standard measurement conditions, with the solar cell being probed from the *p*- (Fig. 4.12a) and *n*-side (Fig. 4.12b) at 420 nm, hence being sensitive to processes close to the *p*-*i* and *i*-*n* interfaces, respectively.

The bias-voltage dependence of the *EQE* is weaker for the *p*-side measurement than for the *n*-side measurement, which is systematically observed throughout the series. Intuitively, one might expect the contrary for degraded solar cells with boron-tailing characteristics as is the case here. However, this can be explained by ΔE and underlines why TF-Si solar cells are illuminated through the *p*-layer: this way, the distance between the place of the charge collection and the *p*-layer is smaller, hence, the recombination probability is smaller. Further, ΔE due to defects at the *p*-*i* interface leads to a stronger electric field there. In this case, the low bias light intensity of 26% is sufficient to saturate most defects there and the *EQE* is close to that with 100% bias light.

This is not the case if the cell is probed from the *n*-side: the *EQE* continues to increase up to 100% illumination intensity because the electron–hole pair generation rate from the bias light is lower due to significant absorption of the bias light until the probed depth. Further, the electric field close to the *n*-side is weaker; hence the application of a bias voltage has a larger effect.

4.5.4 Collection voltage: measurement vs. simulation

In this section, we compare three different approaches related to charge collection on the example of an i-layer thickness series in the initial state and after light soaking under standard conditions:

1. *Measurements:* An i-layer thickness series of a-Si:H solar cells was deposited to determine V_{coll} using the EQE method (cf. section 4.5.2). Here, $EQE(V)$ was determined with a probe beam at 420 nm and blue bias light that entered with the probe beam either from the p- or from the n-side into the cell. This measurement is therefore sensitive mainly to the collection of charges generated close to the p-i and i-n interfaces. (The absorption lengths of the probe beam at 420 nm and of the blue bias light are on the order of 25 and 65 nm, respectively.) To determine V_{coll} from $EQE(V)$ via equation (4.50), we applied a linear fit from -0.3 to 0.3 V.
2. *ASA simulation:* The Advanced Semiconductor Analysis (ASA) package (version 5 [Pieters 06]) with the optical model GenPro3 was used for simulations of the solar cells. For the simulation parameters we took values obtained from layer measurements, where available, and reasonably chosen values otherwise. For the defect concentration, we chose $N_{\mathrm{db}}(x) = 3 \times 10^{15}\,\mathrm{cm}^{-3}$ for the initial state, and considered the light-induced degradation by assuming a linear increase of the defect concentration with the electron–hole pair generation rate according to $N_{\mathrm{db}}(x) = 3 \times 10^{15}\,\mathrm{cm}^{-3} + c \cdot G(x)$. We chose $c = 2.5 \times 10^{-5}\,\mathrm{s}$.
3. *Simple model:* The simple model derived in sections 4.3 and 4.4 was used to estimate the contributions of different charge carriers to ΔE for these solar cells and to test the model against the other approaches. The values of the model parameters were chosen to be the same as described in these sections, except the generation profile that was taken from the ASA simulations with adapted solar cell structure and, correspondingly, the defect concentration. Here, however, N_{db} was chosen to be 10 times smaller than in the ASA simulation to qualitatively reproduce trends observed without getting unphysically high ΔE, which would no longer justify assumption $\Delta E \ll E$.[5]

Simple model vs. ASA simulations

Figures 4.13a and b show the trapped-charge concentrations of electrons and holes in band tails and the positively and negatively charged dangling-bond concentrations, integrated over the i-layer thickness, in the initial and the degraded state, calculated from ASA simulations. (Free charge carriers are negligible as demonstrated in section 4.4.3.) Due to the coupling of different charge carriers, it is not possible to calculate with ASA the fraction of ΔE caused by each type of carrier. However, we can convert these integrated charges N into a maximum ΔE according to $\Delta E_{\mathrm{max}} = \frac{1}{\epsilon_0 \epsilon_{\mathrm{r}}} \cdot \int_0^x \rho(\xi)\,\mathrm{d}\xi = \frac{q}{\epsilon_0 \epsilon_{\mathrm{r}}} \cdot N$. This is shown on the right axes.

---

[5] This can indicate the limits of the simple model, but the choices of the initial N_{db} are questionable as well, being very optimistic for the initial and pessimistic for the degraded state.

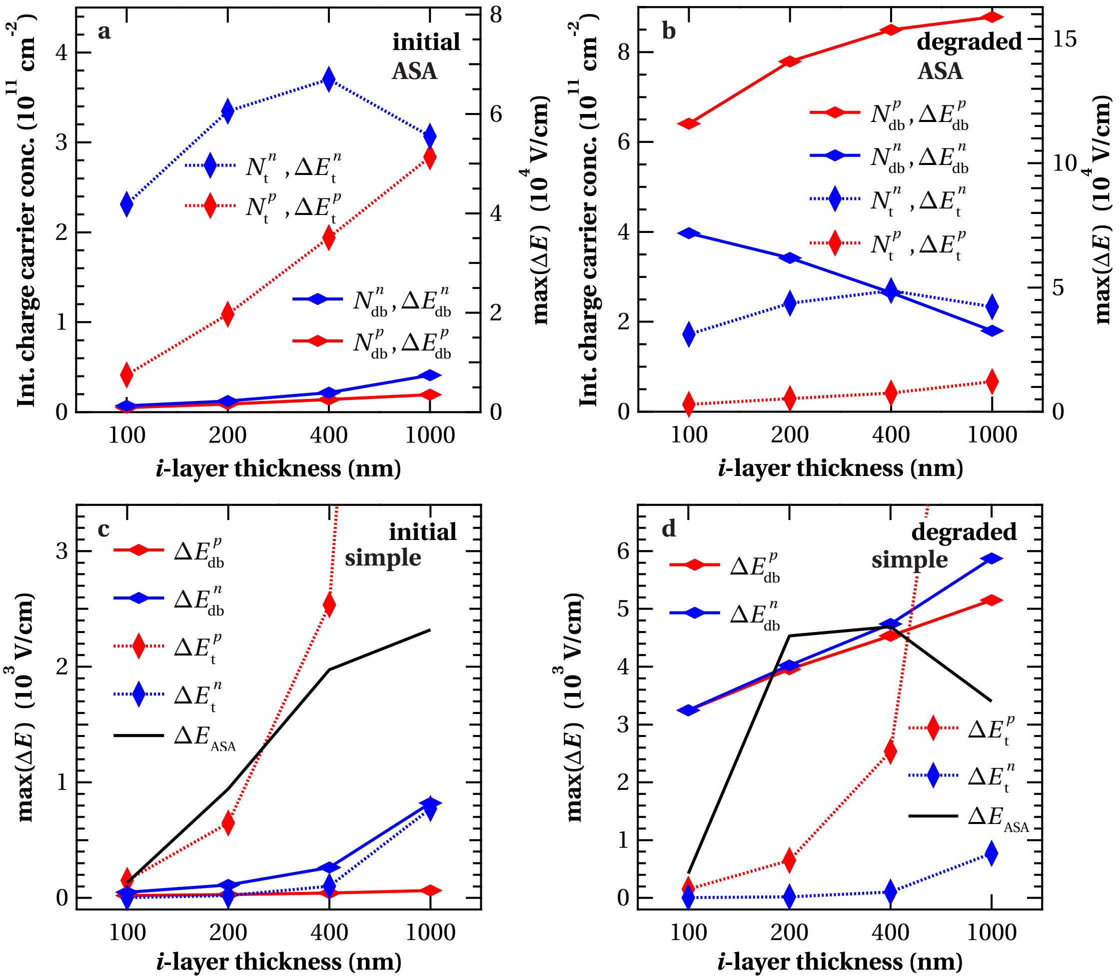

Figure 4.13: (a–b): ASA simulation of the concentrations of electrons (n) and holes (p) trapped in the band tails (integrated over the whole i-layer thickness), and negatively (n) and positively (p) charged dangling bonds (db) in the initial (a) and the degraded states (b) for cells with 100- to 1000-nm-thick i-layers. The right axes describe the maximum electric field deformation (ΔE) induced by these charges.
(c–d): Estimation of ΔE from the same type of charge carriers as in (a–b), but determined using the simple model. ΔE_{ASA} is the maximum deviation of the electric field from E_{nom}, determined from the electric field profile from ASA simulation as explained in the text.
Note that the ordinate scales of (b) and (d) are twice the scales of (a) and (c).

Figures 4.13c and d show the maximum ΔE for the same cases, but calculated with the simple model. For comparison, we added ΔE_{ASA}: from the electric field profile generated by ASA, we determined the minimum electric field in the i-layer $E_{\mathrm{min}}^{\mathrm{ASA}}$ and calculated $\Delta E_{\mathrm{ASA}} = E_{\mathrm{nom}} - E_{\mathrm{min}}^{\mathrm{ASA}}$ using V_{bi} = 1.3V and V_{bi} = 1.15V for $E_{\mathrm{nom}} = \frac{V_{\mathrm{bi}}}{d}$ in the initial and the degraded states, respectively. (Choosing smaller V_{bi} would lead to $E_{\mathrm{nom}} < E_{\mathrm{min}}^{\mathrm{ASA}}$).

In the initial state, ΔE is dominated by the negatively charged dangling bonds close to the i-n interface (for constant N_{db}), as indicated in Fig. 4.13a. However, the light-induced increase of defect states mainly close to the p-i interface strongly increases the contribution of the p-i interface to ΔE, indicated by a dominance of the positively charged dangling bonds in the degraded state (see Fig. 4.13b).

This effect is reproduced by the simple model, as seen in Fig. 4.13c and d: in the initial state, most electron–hole pairs are created close to the p-i interface and the electrons need to travel further, thus the mean electron flux $\overline{\Phi_n}$ is larger than the mean hole flux $\overline{\Phi_p}$, overcompensating the lower mobility of holes and leading to a higher electron concentration, and hence, $\Delta E^n_{\text{db}} > \Delta E^p_{\text{db}}$. After light soaking, most (light-induced) defect states close to the p-i (i-n) interfaces are in the D^+ (D^-) state and deform the field. There are now more defects to be positively charged near the p-i interface, leading to a larger ΔE than negatively charged dangling bonds close to the i-n interface. (In actual solar cells, this effect is even more pronounced, as the p-i interface is already in the initial state more defective than the i-n interface.)

Comparing the simple model (Fig. 4.13c and d) with the ASA simulation (Fig. 4.13a and b), the effect of trapped holes in the valence band tail seems to be strongly overestimated as compared to the electrons trapped in the conduction band tail. This suggests that the Rose trapping factor $\Theta_p = 0.005$ given in [Shah 10] and used for the simple model calculations might be underestimated. The very strong maximum ΔE for cells with thick absorber layers shows the limitation of non-iteration in the simple model: the more ΔE approaches E_{nom}, the larger the error gets.

Measurements vs. ASA simulations

Figure 4.14a shows V_{coll} measured from the p- and n-side on the i-layer thickness series. Figure 4.14b shows the same data but prior to the normalization of V_{coll} by $EQE(0V)$:

$$V^*_{\text{coll}} \doteq \left(\left.\frac{\partial \chi}{\partial V}\right|_{V=0} \right)^{-1} = \left(\left.\frac{\partial EQE}{\partial V}\right|_{V=0} \right)^{-1} = \frac{V_{\text{coll}}}{EQE(0V)}. \tag{4.51}$$

Figures 4.14c and d show the same parameters, but extracted from ASA-simulated bias-voltage dependent EQE curves.

While we observe a large numerical difference between simulated and measured V_{coll} and V^*_{coll} caused by too optimistic input parameters in the simulations, the observed trends are generally in good agreement.

As expected from the V_{coll} measurements presented in section 4.5.3, the collection voltage decreases with increasing i-layer thickness and with degradation for n- as well as for p-side measurements, in the measurement as well as in the simulation. This confirms the increased ΔE in the degraded state seen in Fig. 4.13 for ASA simulations as well as in the simple model.

Not surprisingly, V_{coll} is smaller for the n-side illumination, confirming the measurements shown in Fig. 4.12. The parameter V^*_{coll} is closer to the measurements than V_{coll}. Interestingly, it shows a different behavior than V_{coll} for n-side illumination: namely, it decreases first with

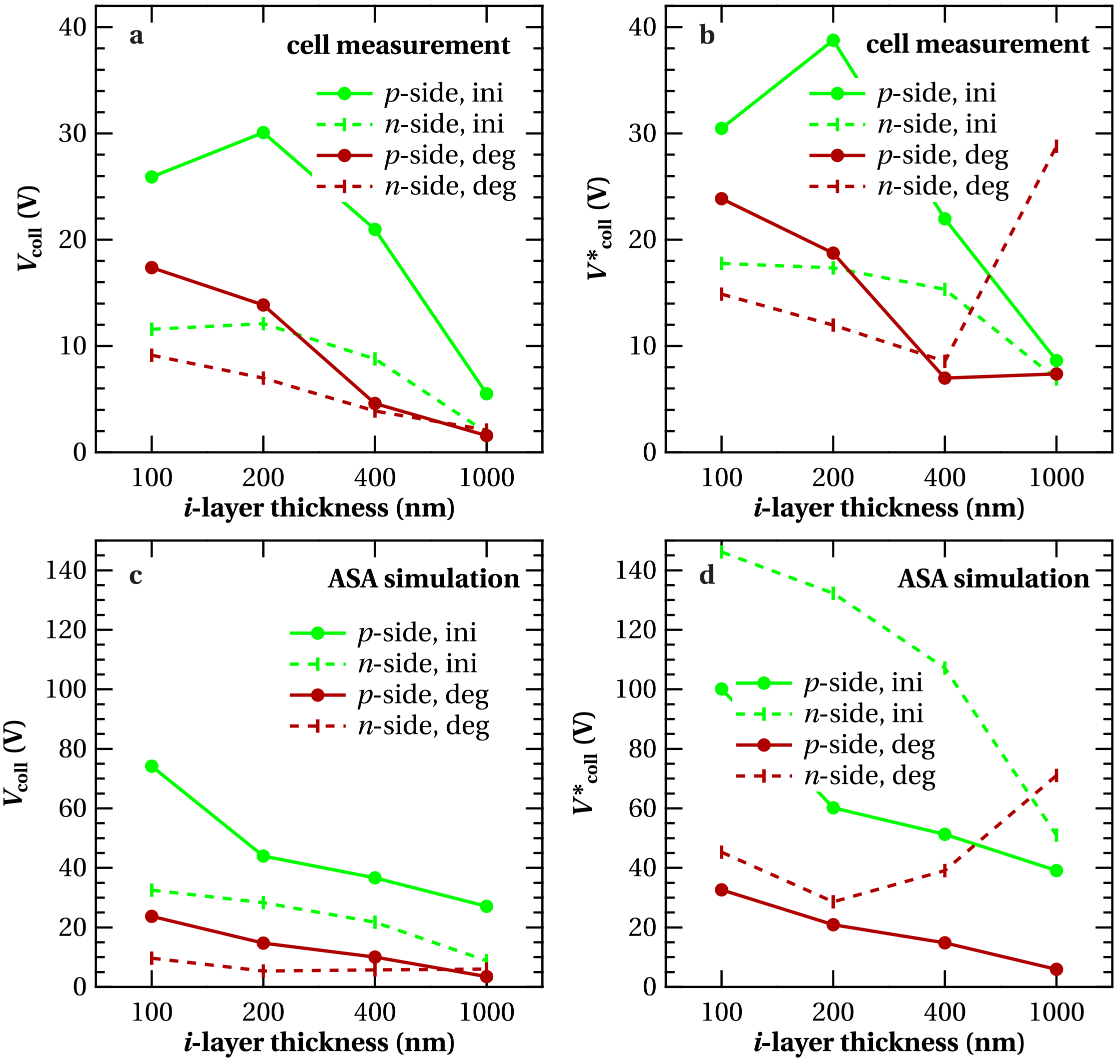

Figure 4.14: Collection voltage (V_{coll}) and $V^*_{\mathrm{coll}} = \frac{V_{\mathrm{coll}}}{EQE(0V)}$ determined from external quantum efficiency (EQE) measurements (a and b) and from ASA-simulated EQE curves (c and d) with the probe beam at 420 nm incident with the blue bias light from either the p- or the n-side for cells in the initial state (ini) and after light soaking (deg). Note the larger scale for the simulated data than for the measured data.

increasing i-layer thickness, but increases for thicker i-layers. The ASA simulation in Fig. 4.14d led to the same results, indicating that this is not a measurement artifact.

A comparison of the electric field and charge distributions from the ASA simulations (not shown here) shows that the different behavior under p- and n-side illumination is a field deformation effect that is directly caused by the spatial separation of defects and electron–hole pair generation in the case of n-side illumination, and their coincidence for p-side illumination. Hence, V^*_{coll} could be a parameter that allows insights into the distribution of defects in the i layer of working solar cells—this will have to be studied further.

4.6 Conclusions

The drift length $L_{\mathrm{drift}} = \mu\tau \cdot E$ within the i-layer of a-Si:H solar cells is a crucial parameter for charge collection, which limits the conversion efficiency in most cases. We presented different approaches to describe charge collection with the goal of contributing to its better understanding and improvement.

The first approach included equivalent electronic circuits representing macroscopic solar cell devices with known electronic elements. We presented state-of-the-art circuits including them in a simulation code and added a shunt term for adequate description of real devices that do not always follow ideal curves.

The second approach focused on the representation of defects—the catalyst for electron–hole recombination—by amphoteric defect states. Detailing the mathematical description of this model based on the application of the Shockley-Read-Hall formalism to amphoteric states, we distinguished—in contrast to in the literature—between the thermal velocities of electrons and holes. This led to the same formulation of the defect state occupation functions f_+, f_0, f_- reported in [Hubin 94] if they are written as a function of the lifetimes of electrons and holes, but to a different formulation if they are written as a function of their capture cross sections.

The third approach focused on solar cell simulation in a layer-by-layer approach, using the SunShine and ASA simulation software.

With the goal of creating a tool that intuitively describes charge collection effects in TF-Si solar cells, while providing experimental access to crucial parameters, we combined the first two approaches to a simple model of ΔE. With this model, we estimated the contributions of (a) free charge carriers, (b) charges trapped in the valence and conduction band tails, and (c) charged dangling bonds, represented by amphoteric defect states, on the ΔE and hence on the charge collection.

For experimental access to the charge collection, we chose the collection voltage V_{coll}. This parameter obtains its physical meaning through its definition via the collection function that is described for each recombination model by a different term, hence allowing a direct comparison of these models. We explored different measurement techniques of V_{coll} and presented measurements for three i-layer thickness series in the initial and degraded state. This allowed us to estimate measurement errors and to test the significance of this parameter by comparing it with the FF of charge-collection-limited devices. We found that the comparison of V_{coll} within solar cells of the same series is reliable, but that absolute values can only give an idea of the performance of the solar cell. In contrast, V_{coll} is sensitive to charge collection issues that are not yet detrimental for the FF, as we showed in the example of solar cells exhibiting boron-tailing characteristics.

The parameter V_{coll} was then used to compare the simple model, ASA simulations, and experimental devices. We found generally good agreement in the trends but numerical differences that are linked to the choice of simulation parameters and limitations of the simple model.

Both simulations showed that free electrons and holes do not contribute significantly to ΔE. They indicate—in agreement with the experimental results—that negative charges close to the i-n interface contribute most to ΔE if a constant defect concentration distribution is assumed. After light soaking that generates defects predominantly close to the p-i interface, the positively charged defects are detrimental. In devices deposited in the p-i-n configuration, there are more defects at the p-i interface that are positively charged and can compensate for the negative charges at the i-n interface. Therefore, such devices are already often limited by the p-i interface in the initial state.

5 Plasma physics of hydrogenated amorphous silicon deposition

This chapter focuses on the conditions under which thin-film silicon (TF-Si), and in particular hydrogenated amorphous silicon (*a*-Si:H), can be grown by plasma-enhanced chemical vapor deposition (PECVD). The scope of this chapter is to provide an experimental basis to fill in the gap between cold-plasma theory and experimental optimization of PECVD layers. The questions to be answered in this chapter are: What are the characteristics of industrial plasmas with different process gases involved? Which deposition parameters limit the multi-dimensional deposition parameter space for a given reactor?

Of special interest for TF-Si deposition are plasmas of H_2/SiH_4 mixtures. Therefore, we explain, for this case, why the H_2 concentration is critical for sustaining a plasma at low pressure, whereas the SiH_4 concentration limits the deposition parameter space at high pressures.

Plasma conditions have a direct consequence on the deposition rate, which is crucial for the industrial application of processes. Hence, we discuss how deposition parameters influence the deposition rate and we derive a simple model.

This chapter is organized as follows: section 5.1 starts with an introductory discussion of plasmas and compares different reactor types for PECVD. In section 5.2, we show optical emission spectra of the most common process gases used for TF-Si solar cell depositions, and in section 5.3 we show the corresponding Paschen curves, the plasma signature of each gas. Based on the position of deposition conditions on the Paschen curves and the consideration of layer growth mechanisms, we discuss the effects of different deposition parameters on the deposition rate in section 5.4. Finally, we conclude the chapter in section 5.5.

Some of the results of this chapter are published in the Journal of Applied Physics [Stuckelberger 13], and others are in preparation for a second publication.

5.1 Introduction

5.1.1 What is a plasma?

A fourth matter of state

Plasmas are often called the fourth aggregate state with the following argument: At low temperatures, every material is in its *solid* state, dense and well-ordered. With increasing temperature, the elements—atoms or molecules—become more mobile until most materials melt and become *liquid*. The material is still dense in this state, but far less structured. As the temperature is further increased, the density decreases first smoothly and then abruptly when the material evaporates and becomes a *gas*. Most processes on earth are limited to these three states of matter due to comparably low temperatures (not more than a few hundred degrees Celsius) corresponding to energies that are below typical binding and ionization energies.[1] Energies in that range are sufficient to govern many processes that constitute the fields of chemistry and biology, but not to change the state of matter of a gas. If a gas is further heated, chemical bonds break and the material splits up into single elements. As the temperature is increased even further, the elements split up—typically at a few thousand degrees Celsius—into negative electrons and positive ions, which is called a *plasma*.

Hot and cold plasmas

Most matter in the universe is in the plasma state, in particular in stars like our sun. In these cases, the matter is in thermal equilibrium. Thus, the energies or temperatures of electrons and positive ions are the same: $T_{\text{electron}} = T_{\text{ion}}$. Note that not all particles in a plasma are ionized: for most plasmas, $x_{\text{ion}} \ll 1$ holds, where $x_{\text{ion}} = \frac{n_{\text{ion}}}{n_{\text{ion}}+n_{\text{gas}}}$ is the fractional ionization with n_{ion} and n_{gas} the densities of ionized and gaseous particles.

Such high-temperature plasmas in thermal equilibrium as in stars or fusion reactors are denoted “hot plasmas.” In contrast, the industrially used plasmas that we discuss in this chapter are denoted “cold plasmas”: in this case, electrons have a much higher temperature (equivalent to energy) than the ions, $T_{\text{electron}} \gg T_{\text{ion}}$. The advantage for us is that the electrons enable the high-temperature chemistry we are interested in, while the ions and gas particles in the plasma remain at approximately the temperature of the environment, and these together enable the use of simple reactor designs. Such plasmas are not in thermal equilibrium, hence they need to be powered, in most cases by applying electric fields that accelerate the charged particles.

---

[1] $25\,°\mathrm{C} = 298.15\,\mathrm{K}$, which corresponds to $k_B \cdot 298.15\,\mathrm{K} \approx 26\,\mathrm{meV}$.

Energy distribution in plasmas

The energy distribution of the electrons in plasmas can often be approximated by a Maxwell distribution function. Many reactions in the plasma—collisions as well as chemical reactions—are activated and controlled by the electron energies. However, the mean electron energy is typically less important than the highly energetic tail of the distribution. For a detailed discussion of plasma physics related to TF-Si depositions we refer to textbooks, e.g. [Raizer 91, Konuma 91, Francombe 02, Lieberman 05, Fridman 08]; we will focus in this chapter on only a few aspects that are relevant for TF-Si depositions.

Plasma diagnostics

The most common methods to characterize cold plasmas include particle-based methods (mass spectroscopy and energy analysis of ions), measurements of electric potentials, and optical methods (absorption and emission spectroscopy). Methods of specific interest for TF-Si depositions (like laser detection of powder formation) are described in [Kharchenko 03, Bartlome 09, Bugnon 13].

For this thesis, we used only optical emission spectroscopy (OES). This technique uses the fact that atoms and ions get excited in plasmas due to collisions mainly with electrons, i.e. electrons change to higher energy electronic states. When the electrons fall back to the ground state, light is emitted at a well-defined wavelength that is characteristic for certain electronic transitions and chemical compounds. Hence, by analyzing the optical emission spectrum, one can draw conclusions on the type of excited species in the plasma, their quantity, and their distribution [Fantz 98, Howling 09]. In our case, we used an Ocean Optics 2000 OES, connected to a window lens at the side of the chambers of the Octopus system (cf. section 2.2.1).

5.1.2 Plasma-enhanced chemical vapor deposition (PECVD)

Most TF-Si materials are produced today with PECVD in dedicated reactors using cold plasmas between two capacitively coupled electrodes. The principle of PECVD is described in detail in textbooks such as [Raizer 91, Konuma 91, Francombe 02, Lieberman 05, Fridman 08]; we introduce here only briefly the terms we use later on.

Mass flow controllers control the flow of the precursor gases into the reactor with controlled deposition conditions. An electric field is applied between two parallel plates serving as electrodes, oscillating with a frequency of typically 13.56 MHz (radio frequency, RF); higher frequencies as used in this thesis are denoted very high frequency (VHF) which means 40.68 MHz if not stated otherwise.

The electric field, in combination with collisions of charged and uncharged particles, dissociates the precursor gases into radicals (neutral but unstable molecules), positively charged ions, and electrons. While the electrons oscillate with the electric field with an amplitude up to the inter-electrode distance, ions are too inert to oscillate considerably.

The two electrodes that confine the plasma are hit by free electrons, being accelerated by the electric field towards them. A part of these electrons is absorbed there, and only a fraction is reflected. Thus, the electron concentration is reduced close to the electrodes, which leads to a potential drop towards the electrodes. The space of the potential drop is called the sheath; positively charged particles are accelerated there towards the electrodes. This so-called ion bombardment can have positive effects, providing the activation energy to arrange atomic environments into a more stable configuration, or negative effects, if the energy serves as the activation energy for defect creation.

However, in most cases ions hitting the substrates do not contribute significantly to layer growth for TF-Si. For H_2/SiH_4 plasmas, SiH_3 radicals are believed to be the main film precursors. If silane radicals of the form Si_mH_n with $m \geq 2$ are dominant in the plasma phase, one talks of powder or cluster formation, and the corresponding operation conditions are denoted powdery or γ-regime. In most cases, such powder—if it is deposited on the substrate—yields poor-quality material; however, close to powdery plasma conditions, nanocrystalline cluster particles can be produced in the plasma phase and, embedded in a matrix of *a*-Si:H, can yield device-quality "polymorphous" materials.

Details on the layer growth of TF-Si from radicals to adatoms and consolidation with hydrogen effusion, including the competing processes of deposition and etching are presented e.g. in [Tsuda 89, Matsuda 90, Guizot 91, Hollenstein 94, Roca i Cabarrocas 00, Roca i Cabarrocas 02, Collins 02, Matsuda 03, Matsuda 04, Smets 07a].

5.1.3 Different reactor types for plasma-enhanced chemical vapor deposition

Three different types of PECVD reactors were used for this thesis, which are schematically presented in Fig. 5.1. Independent of the reactor type, we have drawn these schemata with the substrates hanging face-down, and with the substrate electrode grounded while the other electrode is powered. These choices are technologically driven but not linked to the reactor type. For instance, industrial-size reactors often have the substrates on the lower electrode, and the substrate-electrode can be isolated from the ground such that either a DC-bias voltage can be applied between both electrodes, or it can be on a floating potential. In these reactors, the gases are supplied through a showerhead cathode, while pumping is from the sides. This leads to better uniformity (particularly for depositions in high-depletion regimes) than if the gas inlet is from the side, but side-inlet reactors are also in use. Ideally, both electrodes are heated, but often only one is.

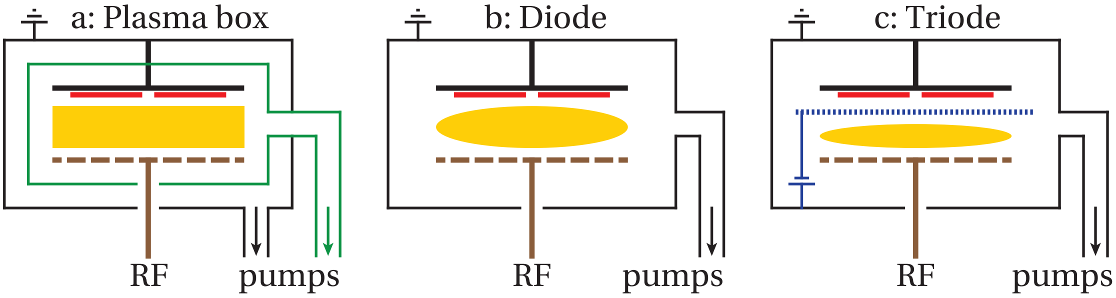

Figure 5.1: Three different reactor types used for plasma-enhanced chemical vapor deposition of thin-film silicon: Diode reactor with plasma box (a), standard diode reactor (b), and triode reactor (c). Black indicates the grounded electrode and chamber; brown: the RF-powered showerhead; red: the substrates; green: the plasma box; blue: the triode mesh; yellow: the plasma.

The *diode* configuration (Fig. 5.1b) is the simplest reactor; many laboratory-scale reactors (including system B, cf. section 2.2.2) and industrial reactors follow this design. The open reactor design is prone to contamination and inhomogeneous deposition but is easier and cheaper in the construction than other designs.

Particularly at AIST, diode reactors with an additional mesh between the two electrodes—hence, *triode* reactors—are investigated (see Fig. 5.1c). With the mesh being biased against the ground with a constant DC-bias voltage, the plasma is confined between the powered electrode and the mesh. Hence, layer precursors need to pass a plasma-free zone between the mesh and the substrates, which is believed [Shimizu 05] to induce a selective deposition of precursors. The sheath is formed at the mesh, reducing ion bombardment on the substrate, and higher-silane clusters, diffusing only slowly towards the substrates, tend to be pumped away, leaving predominantly SiH_3 radicals, which are believed to provide high-quality a-Si:H layers [Matsui 12], to be deposited. The deposition rate, being typically one order of magnitude below that of a diode reactor, is the main drawback of this reactor type. The grid reactor design as presented in [Chesaux 13] is related to the triode reactor design.

The third reactor concept (see Fig. 5.1a) uses a *plasma box* as in Kai reactors, or IRFE electrodes as in Octopus systems (cf. section 2.2.1), and is related to the reactor concept presented in [Roca i Cabarrocas 91]. They have in common that the plasma is confined in an inner chamber with hot walls, while the cold-walled outer chamber is at lower pressure, thus limiting contamination of the inner chamber. This reactor concept allows not only greater uniformity than diode reactors but the fact that all gas sees the plasma leads to faster plasma equilibration times as shown in [Howling 07].

5.2 Optical emission spectra of process gases used for thin-film silicon solar cells

We present in Fig. 5.2 the optical emission spectra of all process gases that we use regularly for TF-Si depositions.

All measurements at 13.56 MHz were taken in Octopus chamber A, those at 40.86 MHz in chamber C (Ar, CO_2, CH_4, $B(CH_3)_3$, H_2, SiH_4), in chamber D (PH_3), and in Kai-M (SiF_4).[2] The OES measurement conditions were kept the same (1 s integration time, averaging over four measurements). Differences in the peak height therefore represent intensity differences (except an experimental error that is induced by transferring the optical measurement setup from one chamber to another). The measurements were taken several minutes after plasma ignition and stabilization. Before measurement, the reactors had been cleaned to measure only the properties of the precursor-gas species excluding etched species from previously deposited layers. The power was 10 W for all plasmas, and the pressure was chosen around the Paschen-curve minimum (see section 5.3); the pressure settings are reported in Tab. 5.1.

Table 5.1: Pressures around the minimum in Paschen curves used for OES measurements presented in Fig. 5.2.

Pressures (mbar)	Ar	CO_2	CH_4	PH_3	$B(CH_3)_3$	H_2	SiH_4	SiF_4
13.56 MHz	0.20	0.86	0.28	-	-	1.71	0.40	-
40.86 MHz	0.20	0.05	0.05	0.30	0.30	0.30	0.05	0.80

The OES measurements were recorded for plasmas in chamber B at 81.36 MHz as well. However, the signal intensity was too low such that different integration times were necessary, allowing no direct comparison with the reported spectra.

The pictures included in each graph in Fig. 5.2 were taken for similar deposition conditions (the same pressure, power, and frequency for all gases) in system B due to a lack of a window into the Octopus IRFE that is large enough for a reflex camera. A white balance correction was performed before taking the pictures, and the colors correspond subjectively to the visual impressions of the plasmas in system B as well as in Octopus.

Note that the spectra of PH_3 and $B(CH_3)_3$ are very similar to that of H_2; the dilution of these gases in H_2 is the cause. In contrast, the spectra of hydrogenated (SiH_4) and fluorinated silane (SiF_4) are distinctly different, with main peaks at 415 and 440 nm, from SiH and SiF radicals, respectively.

---

[2] Measurements with SiF_4 were taken by S. Hänni. Depositions using gas mixtures of SiF_4, Ar, and H_2 are discussed in [Hänni 14].

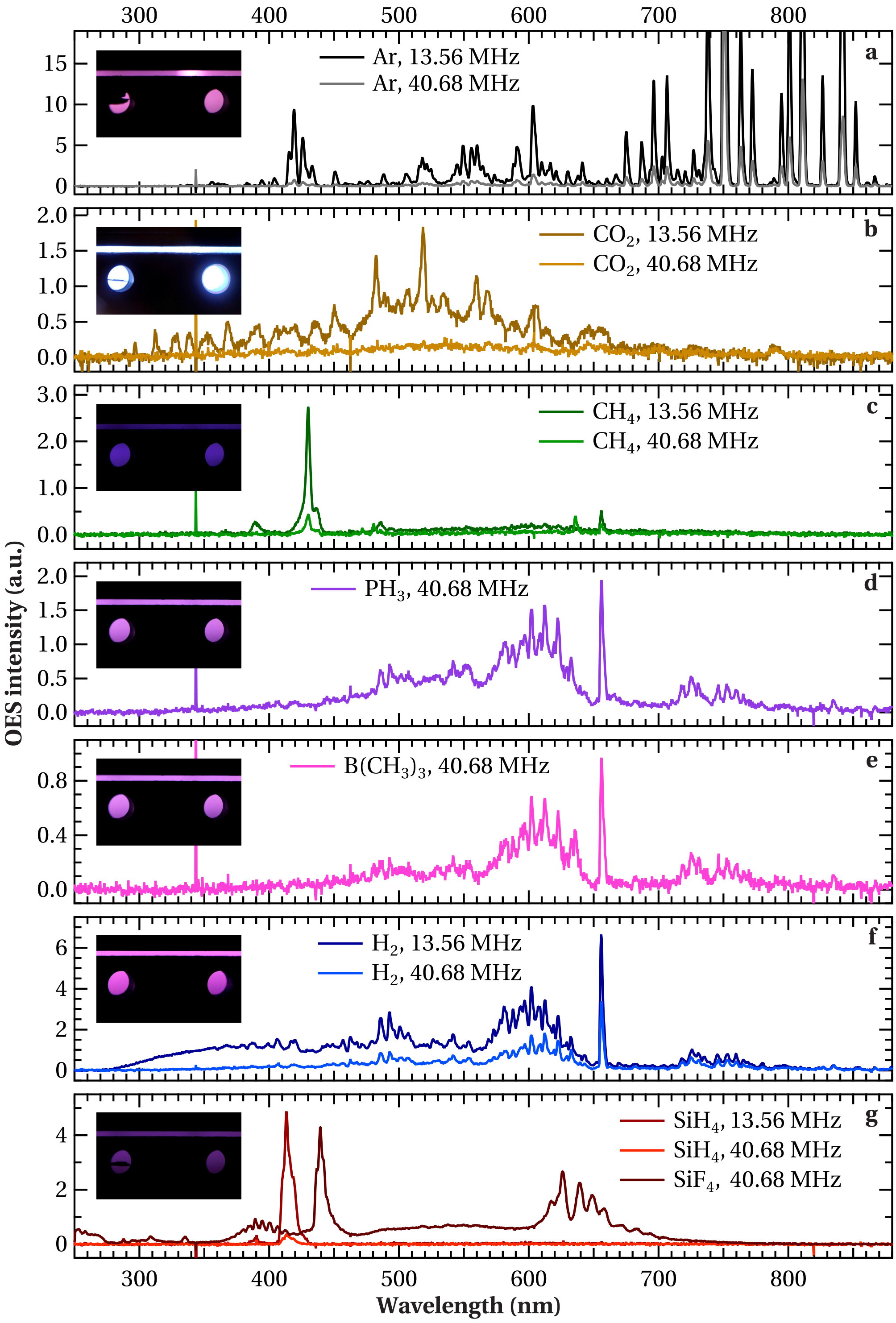

Figure 5.2: Optical emission spectra of plasmas with pure gases that are typically used in TF-Si depositions (exceptions: $B(CH_3)_3$ and PH_3 are diluted to 2% in H_2): argon (a), carbon dioxide (b), methane (c), phosphine (d), trimethylborane (e), hydrogen (f), and silane (g). The insets are photographs of the plasmas. The deposition and measurement parameters are detailed in the text.

5.3 Paschen curves of process gases used for thin-film silicon solar cells

5.3.1 Definition of Paschen curves

Friedrich Paschen found empirically that the breakdown voltage V_b, above which a plasma can be ignited between two electrodes, is a function of the product of the pressure p and the inter-electrode distance d [Paschen 89]; J. Townsend described this mathematically in the "Theory of ionization of gases by collision" [Townsend 10], defining the coefficient α, which is known today as the first Townsend ionization coefficient. In analogy to the absorption coefficient, α is an "enhancement coefficient," the inverse length within which the number of electrons N_{el} (and, hence, the number of electron–ion pairs) is enhanced by a factor e:

$$\frac{N_{\mathrm{el}}}{N_{\mathrm{el}}^0} = e^{\alpha \cdot x}, \tag{5.1}$$

where x denotes the distance covered by an electron. Considering the distance d between two electrodes, where an ion impact leads with the probability γ_{se} to the emission of a secondary electron, this gives the criterion for the sustainment of free charges or plasmas

$$\alpha \cdot d = \ln\left(1 + \frac{1}{\gamma_{\mathrm{se}}}\right). \tag{5.2}$$

This leads to the form of Paschen's law as we know it from textbooks (see e.g. [Lieberman 05]):

$$V_b = \frac{B \cdot pd}{\ln(A \cdot pd) - \ln\left[\ln\left(1 + \frac{1}{\gamma_{\mathrm{se}}}\right)\right]}. \tag{5.3}$$

Here, A and B are material constants that have to be determined experimentally for each gas and that are tabulated in textbooks of plasmas (e.g. [Lieberman 05, Fridman 08]). The parameter γ_{se} with $0 < \gamma_{\mathrm{se}} < 1$ for low-energy ions is determined experimentally for a given reactor, however, the dependence of Paschen's law on γ_{se} is weaker than on A and B.

Paschen's law in the formulation of equation (5.3) is of great universality, but is of limited use for industrial PECVD processes: in reactors that are not dedicated to plasma research, V_b is often not easily measurable because of the lack of electrical access to the electrodes to probe it. However, V_b is normally controlled through the generator power P_{rf}. Using P_{rf} as a parameterization of V_b, we can re-write equation (5.3) as

$$P_{\mathrm{rf}} = \frac{B^* \cdot pd}{\ln(A^* \cdot pd) - \ln\left[\ln\left(1 + \frac{1}{\gamma_{\mathrm{se}}}\right)\right]}. \tag{5.4}$$

We will see applications of this formulation of Paschen's law in section 5.3.2 with a discussion in section 5.3.3; in the discussion of the dependence of the deposition rate on different parameters in section 5.4 and the discussion of deposition regimes of *a*-Si:H in chapter 6, we will argue with Paschen's law at several instances.

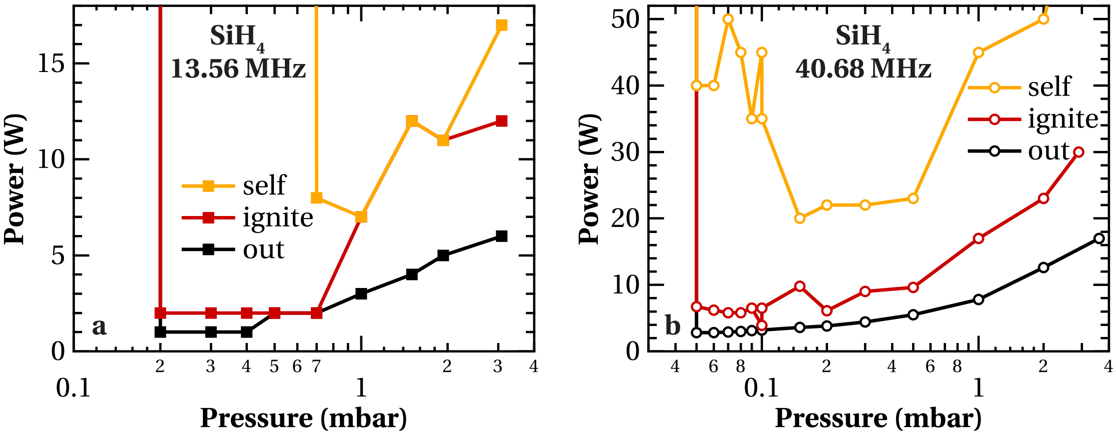

Figure 5.3: Paschen curves of silane taken in the Octopus PECVD system at 13.56 MHz in chamber A (a) and at 40.68 MHz in chamber D (b) measuring the power in three cases: the power of self-ignition of the plasma ("self"), the power at which it is possible to ignite the plasma with the built-in igniter ("ignite"), and the extinction power, at which the plasma extinguishes when decreasing the power ("out").

5.3.2 Paschen curve measurements

Prior to the investigation of deposition conditions for the best performance of the resulting layers it is crucial to know which are the physical and technical limits of the deposition parameter space. In the case of PECVD, this means one needs to know the Paschen curves of the gases for a given reactor, and the positioning of a deposition regime on the Paschen curve can tell us which plasma process governs there.

All measurements presented in this chapter were taken in the Octopus PECVD tool (see section 2.2.1) with a constant inter-electrode gap of $d = 15\,\mathrm{mm}$ and an electrode surface of $2 \times 15\,\mathrm{cm} \times 16\,\mathrm{cm}$. Therefore, we show P_{rf} as a function of the pressure p—for other reactors, these curves can easily be translated into power density as a function of pd. We used clean glass substrates in leak-free substrate holders. Note that we measured the power always at the generator output.

Different types of power measurements for Paschen curves

Figure 5.3 shows three different possible measurements of Paschen curves following equation (5.4) for RF and VHF excitation:

- *Self-ignition* ("self"): This is the power at which the plasma ignites without external means other than by increasing the power smoothly. This power corresponds most directly to the breakdown voltage but is of limited use for our means.

- *With igniter* (“ignite”): At this power, it is possible to ignite the plasma with an external igniter; in our case, this was a conventional charge source similar to those used for the ignition of gas stoves. This power is essential for PECVD in tools that are equipped with an igniter, as deposition conditions can be settled prior to ignition at this power.

- *Extinction* (“out”): This is the extinction power at which the plasma extinguishes when smoothly reducing the power; above this value, plasma conditions are stable and depositions can be performed (see also the comparison between the breakdown voltage and extinction voltage in [Lisovskiy 05]). For most of our applications, this value was considered most significant. Some high-quality materials for solar cells were reproducibly deposited at conditions at which plasmas could not be ignited but that were obtained by igniting at a different pressure, power, or gas composition. Hence, further graphs in this chapter concentrate on the extinction power.

The measurements shown in Fig. 5.3 suffer from larger measurement errors than Paschen curves presented later for two reasons: first, Paschen-curve measurements using pure SiH_4 gas in a clean reactor are problematic, as permanent deposition occurs such that the reactor is immediately covered with silicon. To limit this effect, measurements were not taken continuously in pressure but arbitrarily distributed, and pre-measurements were taken such that the critical power was found with very short times of ignited plasmas.

Second, the power measurements of self-ignition and ignition using an igniter depend strongly on the state of the reactor; small powder particles (in our case more critical than the mechanical unconformity of the electrodes) can locally increase the electric field dramatically or absorb electrons, changing the plasma conditions significantly as shown in Fig. 5.6. The measurement curves performed at 13.56 MHz are generally less smooth than those for higher frequencies due to a power measurement precision limit of 1 W in the former case.

Paschen curves of process gases

Figures 5.4a–e show the extinction power measurements as a function of the pressure for all process gases we used for TF-Si solar cell depositions. These measurements were performed at three frequencies in the Octopus system in chambers A and E (13.56 MHz), chambers C and D (40.68 MHz) and chamber B (81.36 MHz). Tests showed no significant difference for different clean chambers operated at the same frequency. The Paschen curves of doped gases were measured too (although with fewer measurement points) but are not shown here; as PH_3 and $B(CH_3)_3$ were diluted to at least 2% in H_2, the plasma properties of these gases are masked by the properties of H_2.

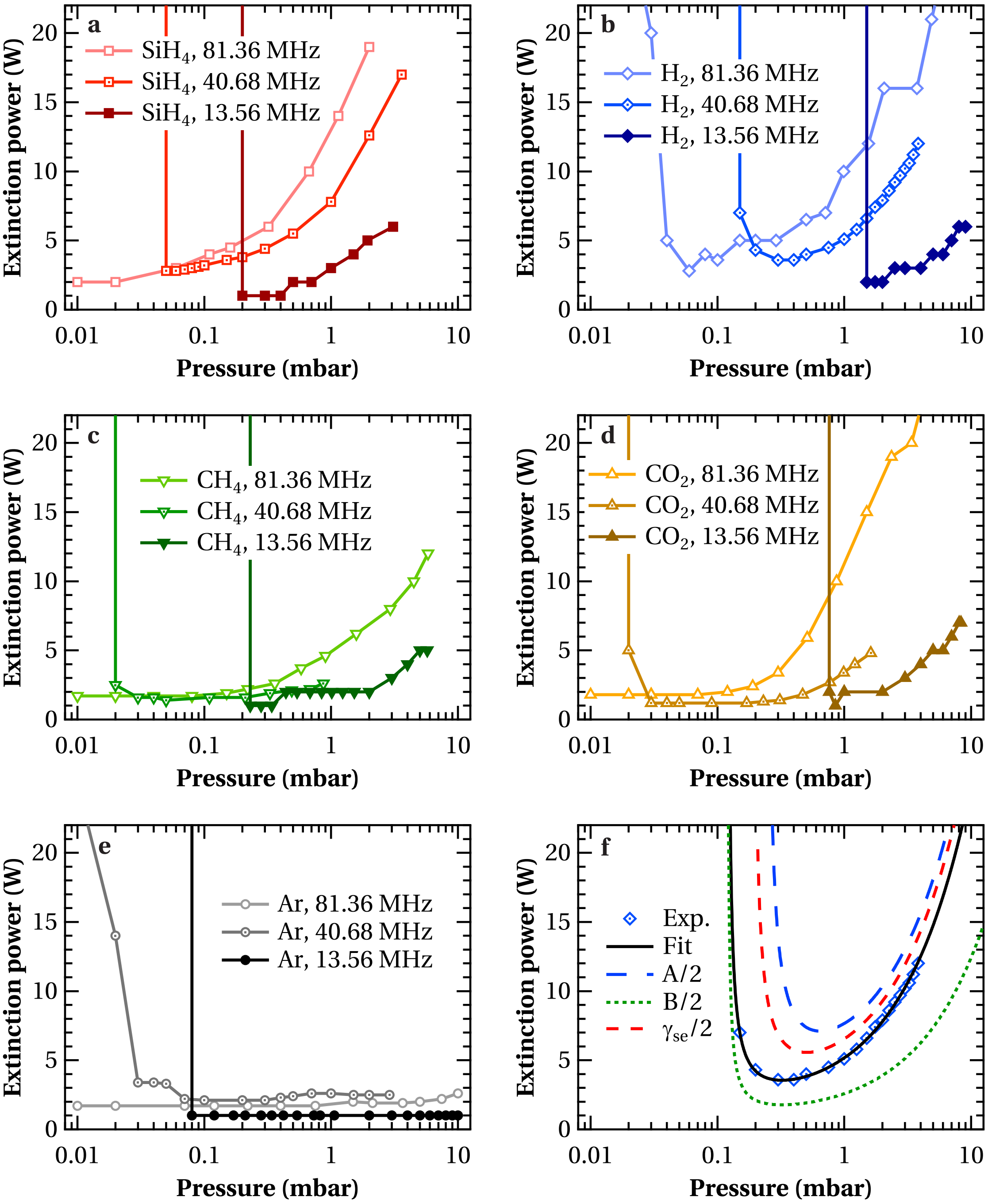

Figure 5.4: (a–e): Measurements of the extinction power for plasmas of silane (a), hydrogen (b), methane (c), carbon dioxide (d), and argon (e), performed in clean chambers for three excitation frequencies. (f): The Paschen curve of the hydrogen plasma at 40.68 MHz from (b) (symbols) fitted with the formulation of Paschen's law in equation (5.4) and variations of the fitted curve by division of single variables by a factor of two.

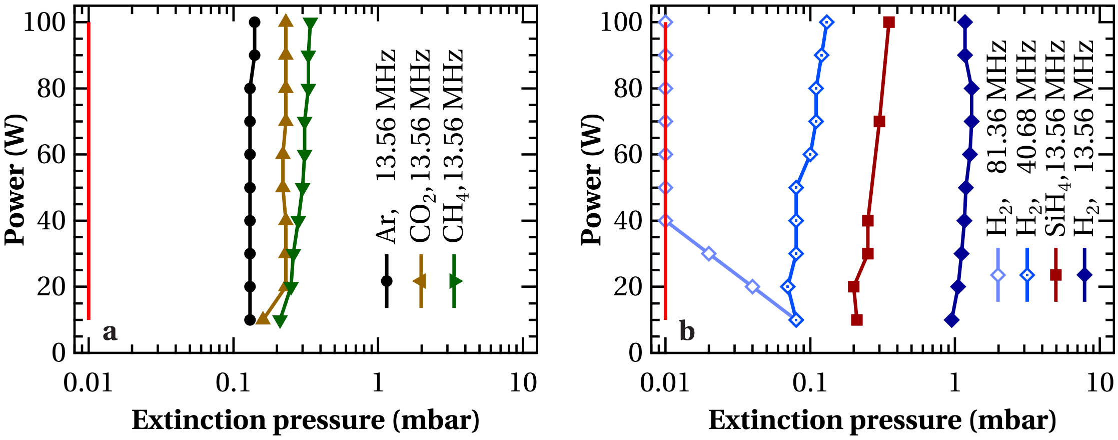

Figure 5.5: Measurements of the extinction pressure for plasmas of argon, carbon dioxide, and methane (a) and for hydrogen and silane (b) for excitation frequencies 13.56, 40.86, and 81.36 MHz. Plasmas without entry in the legends could be sustained down to 0.01 mbar, the measurement limit of the pressure gauge.

Figure 5.4f shows as an example the fit of Paschen's law (equation (5.4)) to the Paschen curve of H_2 plasmas at 40.68 MHz. With A, B and γ_{se} as fitting parameters, several parameter sets provide good fitting. Hence, we fixed γ_{se} to 0.9, in the absence of a measured value. The fit of Paschen's law is in good agreement with the measured curve and yields $A^* = 4.2\,\frac{1}{\mathrm{mbar\,cm}}$ and $B^* = 7.3\,\frac{\mathrm{W}}{\mathrm{mbar\,cm}}$.

In the literature [Lieberman 05], values of $A = 4.8\,\frac{1}{\mathrm{Torr\,cm}} = 3.6\,\frac{1}{\mathrm{mbar\,cm}}$ and $B = 136\,\frac{\mathrm{V}}{\mathrm{Torr\,cm}} = 102\,\frac{\mathrm{V}}{\mathrm{mbar\,cm}}$ are given for H_2 plasmas. Hence, for this example A and A^* are comparable; this may be a coincidence as the relation between the formulations of Paschen's law in power and in voltage is not direct as manifested by the strong frequency dependence of the extinction power.

Pressure-mode in Paschen curve measurements

The functions $P_{\mathrm{rf}}(pd)$ and $V_{\mathrm{b}}(pd)$ are not bijective as demonstrated and discussed e.g. in [Lisovskiy 98, Lisovskiy 05]; only one part of the multi-valued region at low pressures is represented by equations (5.3) and (5.4). Nevertheless, both parts of $P_{\mathrm{rf}}(pd)$ are measurable by decreasing either the power or the pressure until plasma extinction (or by increasing the power or pressure until ignition). The power-branch, where we decreased the power, is shown in Fig. 5.4. The corresponding pressure-branch, where we decreased the pressure until plasma extinction, is shown in Fig. 5.5 for all process gases. The power dependence of the extinction pressure is generally weak within the investigated power range. For Ar, CO_2, CH_4, and SiH_4, the plasma was sustained at the frequencies 40.68 MHz and 81.36 MHz down to pressures below 0.01 mbar, which was the measurement limit of the pressure gauge. However, we note that particularly for H_2 and, to a lesser extent for SiH_4, deposition conditions are limited at low pressures.

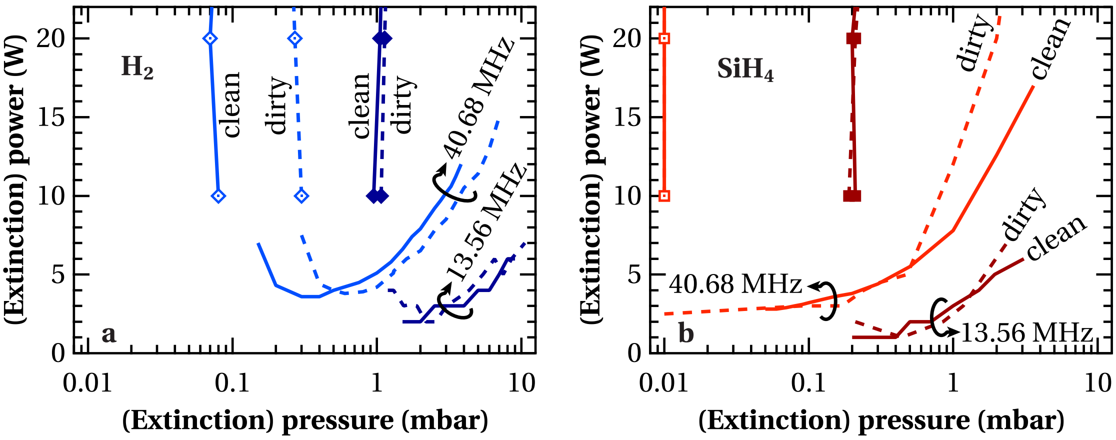

Figure 5.6: Comparison of the Paschen curves of hydrogen (a) and silane (b) for reactors after cleaning (“clean”) and with the electrodes covered with a few micrometers of hydrogenated amorphous silicon (“dirty”). Lines without symbols were measured in decreasing-power mode; lines with symbols were measured in decreasing-pressure mode.

Paschen curves of a dirty reactor

The state of a reactor, in particular the electrode surface, has a strong impact on the Paschen curves: Fig. 5.6 shows a comparison of the Paschen curves in Fig. 5.4a–b and Fig. 5.5b with the Paschen curves taken under the same measurement conditions but in a dirty reactor, where the electrodes were covered with a few micrometers of *a*-Si:H (however, a few hundred nanometers have the same effect). The largest effect of silicon-covered electrodes is seen in H_2 plasmas, where low-pressure regimes that are possible on a clean reactor are no longer accessible after the electrodes are covered with *a*-Si:H. This has a large impact on solar cell depositions: depositing under such conditions can lead to successful ignition of the plasma and deposition of part of the solar cell, with plasma extinction before the nominal end and no possibility to re-ignite and continue the deposition under the same conditions.

5.3.3 From Paschen curves to thin-film silicon deposition conditions

The conditions for TF-Si deposition are in most cases limited by the Paschen curves of H_2 and SiH_4, the main precursor gases for hydrogenated amorphous and microcrystalline silicon including the transition materials. Therefore, we explain trends visible in the Paschen curves presented in section 5.3.2 using the example of the Paschen curves of H_2 and SiH_4 at the excitation frequencies of 13.56 (RF) and 40.68 MHz (VHF) shown in Fig. 5.7. In further discussion, we refer to the “turning point” [Lisovskiy 98] as the lowest pressure at which the plasma could be sustained. Four observations that will be discussed in the following are particularly relevant for TF-Si deposition from H_2/SiH_4 plasmas by PECVD (they are indicated by arrows in Fig. 5.7):

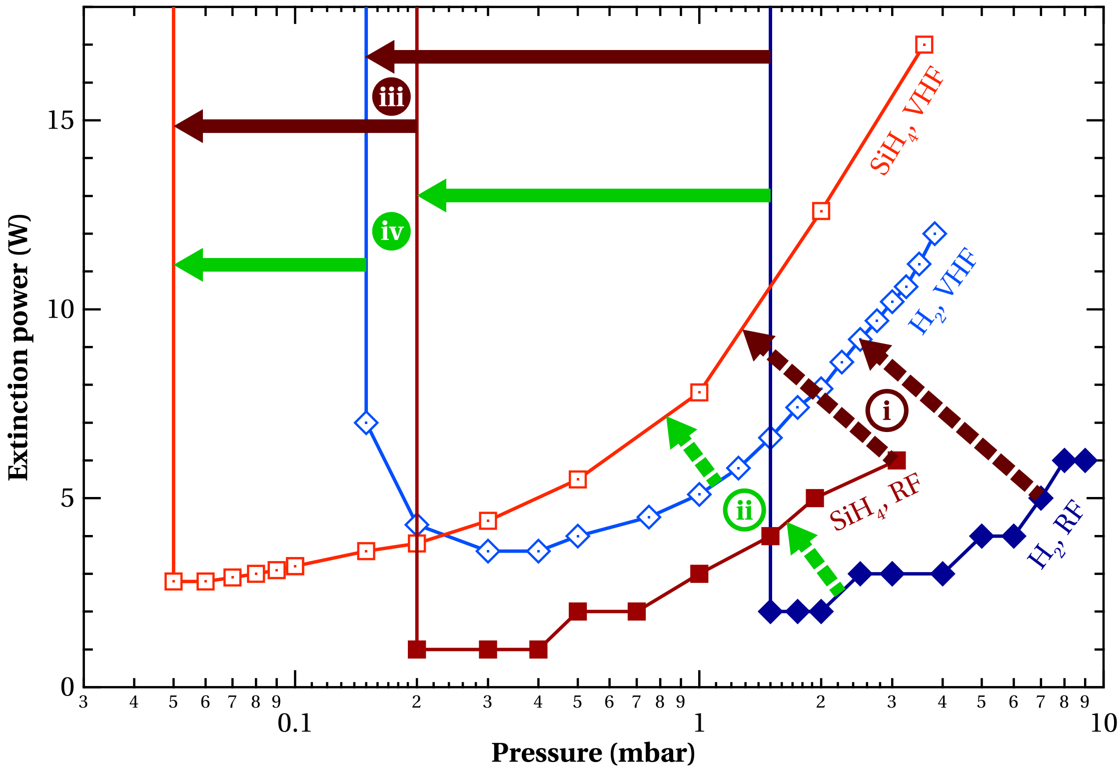

Figure 5.7: Plasma extinction power as a function of the gas pressure for pure H_2 and SiH_4 plasmas powered at 13.56 (RF) and 40.68 MHz (VHF). Arrows indicate trends detailed in the text.

(i) At high pressures, higher power is needed as the frequency is increased.

(ii) At high pressures, higher power is needed for SiH_4 than for H_2.

(iii) High-frequency excitation sustains plasmas at lower pressures than low frequency.

(iv) SiH_4 plasmas can be sustained at lower pressures than H_2 plasmas.

Assuming vanishing electron concentrations in the sheath close to the electrodes, the extinction power at high pressures is limited by the ionization rate ν_i of gas molecules via electron impact [Lisovskiy 08]:

$$\nu_\mathrm{i} = a + \frac{b}{(d - 2A_\mathrm{drift})^2} \quad \text{with} \quad A_\mathrm{drift} = \frac{v_\mathrm{drift}}{2\pi f}. \tag{5.5}$$

Here, a and b are constants that include the reactor size and electron diffusion coefficients, d denotes the inter-electrode gap, and A_drift is the electron displacement amplitude expressed in terms of the electron drift velocity v_drift and the RF field frequency f.

From equation (5.5) we see that an increase of the frequency leads to a lower electron displacement amplitude and a lower ionization rate. Hence, a stronger electric field may be needed for the electrons to acquire sufficient energy to perform electron-impact ionization of molecules, which may explain why a higher power is needed to sustain VHF plasmas, as observed in (i).

In contrast, equation (5.5) is not valid close to the turning point, where the mean free path of the electrons is of the same order of magnitude as the inter-electrode distance, $d \approx 2A_{\mathrm{drift}}$, and electron loss at the electrodes (due to an electron reflection coefficient that is smaller than one) limits the plasma-sustaining conditions. With increasing frequency (lower A_{drift}), fewer electrons are lost at the electrodes and the plasma can be sustained at lower pressures; this explains (iii).

Similar reasoning explains (iv): SiH_4 plasmas can be operated at lower pressures compared to H_2 plasmas due to a higher dissociation cross section of SiH_4 and hence a lower mean free path of the electrons, leading to fewer electron losses at the electrodes.

Observation (ii) has already been reported elsewhere [Lisovskiy 06, Lisovskiy 07]. For a given pressure, more electrons are lost in collisions in a SiH_4 plasma than in a H_2 plasma; hence, a higher power is needed.

The differences between H_2 and SiH_4 plasmas and the crossing of their Paschen curves are of great importance for depositions at low power as is desired for highly stable solar cells:

(a) For low pressures, H_2 dilution can make it impossible to sustain a plasma, while at high pressures it allows a plasma to be sustained at a lower power.

(b) For low pressures, where electron loss at the electrodes dominates, ignition with an external electron source can reduce the ignition power dramatically. However, this has hardly any effect at higher pressures, where electron loss by collisions in the gas phase limits the plasma ignition. Hence, plasmas for deposition conditions presented in section 5.4 were typically ignited with the help of an external electron source at pressures below about 2 (RF) and 0.5 mbar (VHF), respectively, while only slightly higher power but no external charges were required for the ignition of the plasmas at higher pressures.

5.4 Deposition rates

We present in this section experimental results of the deposition-rate measurements for deposition conditions of intrinsic *a*-Si:H layers including transition materials to microcrystalline silicon, exploring a wide parameter range varying deposition temperature, frequency, electric power, pressure, and H_2/SiH_4 ratio (dilution). The values of these five crucial deposition parameters are provided in the legends for all deposition conditions presented here.

The layers with thicknesses on the order of 200 nm were deposited in the Octopus system (cf. section 2.2.1) on glass substrates. The layer thicknesses were determined from the combined fitting of three-angle ellipsometry and transmittance measurements with a Tauc-Lorentz oscillator model as described in section 2.3.1.

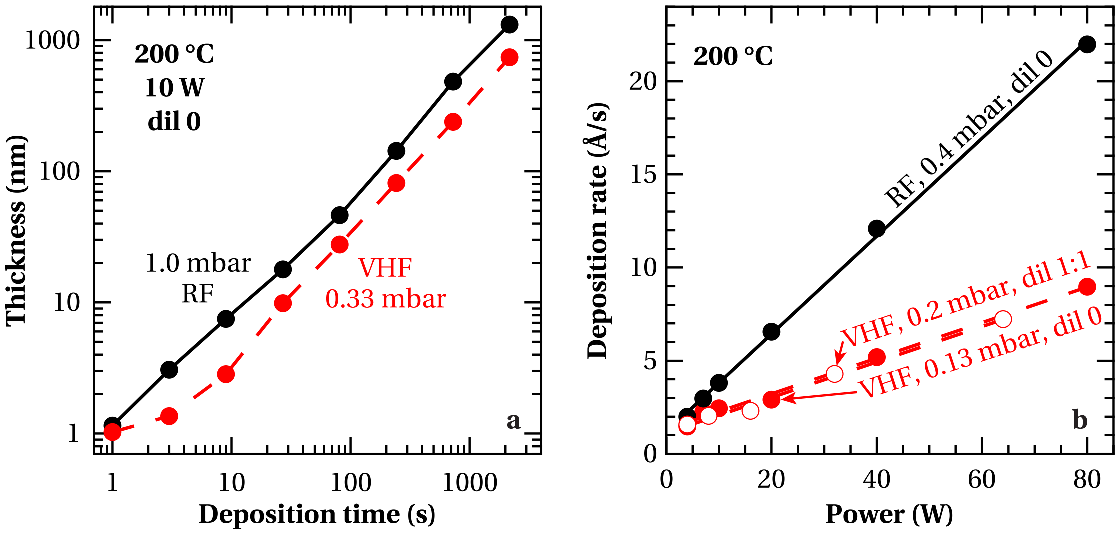

Figure 5.8: (a): Thickness of hydrogenated amorphous silicon layers as a function of the deposition time to verify the temporal stability of deposition rates. (b): Power dependence of the deposition rate for three different plasma regimes. In (a), lines are guides to the eye; in (b), they are linear fits.

5.4.1 Nucleation and deposition rate increase with power

Before starting with investigations of the deposition-rate dependencies, we consider the methodology of measuring layer thickness. Figure 5.8a shows layer thickness measurements for two series deposited at RF and VHF with the same nominal power, temperature and SiH_4 flows but different pressures to account for the different minimums in their Paschen curves. In both cases, the deposition rate does not change significantly with time as is expected for *a*-Si:H deposition regimes far from the transition to microcrystalline silicon. However, for VHF we observe a reduced deposition rate for very thin layers up to a few seconds of deposition time. This may be due to a more extended nucleation phase under these deposition conditions compared to the RF as it is closer to high depletion and, hence, to transition regimes. Note also the lower deposition rate of the VHF regime (3.04 Å/s) as compared to the RF regime (6.03 Å/s, values determined from the thickest layer). Part of this difference is due to higher power losses in the electric power circuit due to poorer matching but we doubt that this can justify the full difference. As we could not observe such a large difference at higher pressures, precursor radicals might be pumped away prior to their deposition due to the large ratio of SiH_4 flow to pressure (the SiH_4 flow was 10 sccm). An alternative explanation considers the electron-energy distribution: at lower frequency (enhanced electron acceleration time per cycle), the energy distribution of electrons is shifted towards higher energy, hence more electrons may possess enough energy to dissociate SiH_4.

Figure 5.8b shows the dependence of the deposition rate on the electric power of two series with the same frequency and temperature as the series presented in Fig. 5.8a. However, the SiH_4 flow was 60 sccm here to avoid limitation of the deposition rate by SiH_4 supply. For comparison with the VHF series, we show a power series deposited at 0.2 mbar with a dilution

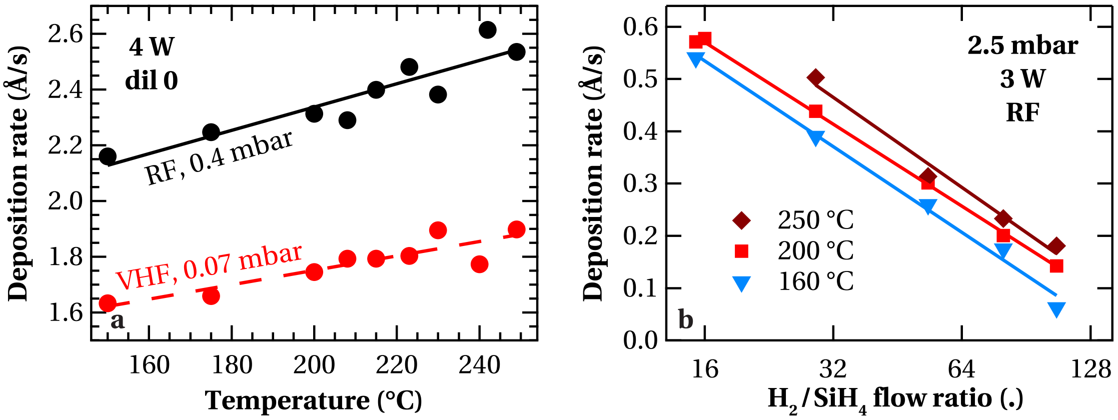

Figure 5.9: Temperature dependence of the deposition rate for two series deposited with undiluted SiH_4 powered by RF and VHF (a), and for different H_2 dilutions (b). Lines represent linear fits in linear scale in (a) and in semilogarithmic scale in (b).

of 1:1 using gas flows of 30 sccm H_2 and 30 sccm SiH_4. We find the same power dependence of the deposition rate for both VHF series. We assume that two competing processes led to this coincidence: increasing the pressure reduces the loss of precursor radicals by pumping (which should increase the deposition rate, as collision losses are limiting only at higher pressures), but the increased dilution reduces the SiH_4 power fraction, and hence, the deposition rate (see section 5.4.4). Note that the deposition rate depends linearly on the power in all three plasma regimes. This is a strong indicator that the power (via SiH_4 dissociation) is limiting the deposition rate in these cases. The proportionality constants, determined from linear fits, are 0.262 $\frac{\text{Å}}{\text{sW}}$ (RF), 0.0957 $\frac{\text{Å}}{\text{sW}}$ (VHF, 0.13 mbar, dil 0), and 0.0953 $\frac{\text{Å}}{\text{sW}}$ (VHF, 0.2 mbar, dil 1:1). Similarly as in Fig. 5.8a, the deposition rate at RF is significantly higher than at VHF, likely for the same reasons.

5.4.2 Temperature dependence of the deposition rate

The temperature dependence of the deposition rate is rather weak as can be seen in Fig. 5.9. However, we observed systematically for different pressures, frequencies and dilutions (cf. Fig. 5.9) that the deposition rate increases with increasing temperature, in agreement with measurements by Andújar et al. [Andújar 91] and Böhm et al. [Böhm 93]. (For the triode reactor configuration, where we expect the temperature dependence of the deposition rate to be similar to that in the diode configuration, such a temperature dependence was not seen within the temperature range of interest [Matsuda 83, Matsuda 04]). From the linear fits of the data shown in Fig. 5.9a, we determined the proportionality constants 4.2×10^{-3} $\frac{\text{Å}}{\text{sK}}$ or 1.8 $\frac{‰}{\text{K}}$ for the series deposited at RF, and 2.6×10^{-3} $\frac{\text{Å}}{\text{sK}}$ or 1.5 $\frac{‰}{\text{K}}$ for the series deposited at VHF.

We suggest the following explanation: With increasing temperature, the desorption rate of hydrogen from the surface is higher, and hence less hydrogen is available at the surface. At the same time, more dangling bonds provide "sticking places" for film precursors, thus leading to a higher deposition rate. One may imagine that powder formation could also be responsible:

There tends to be less powder at higher temperatures [Dorier 92]; therefore, the deposition rate could be higher because fewer film precursors are lost to powder that is pumped away. Further, following the ideal gas law, a higher temperature means a lower gas number density, and hence fewer gas-phase collisions and less powder. However, no powder formation was observed for the layers presented in Fig. 5.9 or for other series in which this temperature dependence was observed. Therefore, we conclude that powder formation does not play a major role in the deposition rate increase with temperature.

With only three temperature data points per dilution, we did not perform fits on the temperature-dependence data shown in Fig. 5.9b. However, it seems that the temperature gradient does not significantly vary with the dilution, whether the absolute deposition rate is 0.5 (low dilutions) or 0.1 $\frac{\text{Å}}{\text{s}}$ (high dilutions). This consideration indicates that the temperature increase enhances the deposition rate by a constant rather than by a factor, which supports the explanation of the temperature dependence by hydrogen desorption.

5.4.3 Pressure and hydrogen dilution dependence of the deposition rate

In this subsection we investigate the deposition rates of the *a*-Si:H materials that will be investigated in chapter 6. The deposition parameter space is spanned by the deposition pressure, H_2 dilution, and excitation frequency. These layers are grouped into dilution series for different pressure regimes at RF and VHF that are summarized in Tab. 5.2; the power was chosen slightly above the minimum in the Paschen curve at a given pressure for varying dilutions (resulting from the combined curves of H_2 and SiH_4). It was kept the same for all dilutions. The total flow was kept constant for each dilution series (with few exceptions under extreme conditions, where the limits of the mass flow controllers were reached), hence varying the H_2 and SiH_4 flows with dilutions. The low-dilution limitation of each series was given either by dilution 0 or by the Paschen curve, meaning that a plasma could not be sustained at lower H_2/SiH_4 flow ratios (these were often very powdery regimes requiring reactor cleaning afterwards); at high dilutions, the limitation was a vanishing deposition rate or resulting microcrystalline materials that are not the main subject of this thesis.

Figure 5.10 show the deposition rates of the investigated plasma conditions for the five dilution series deposited at RF. For each H_2 dilution series, one can distinguish two different branches: the deposition rate increases with increasing H_2 dilution at low dilution, and seems to decrease logarithmically at high dilution.

Table 5.2: Pressure and power values for the H_2 dilution series performed at 13.56 (RF) and 40.68 MHz (VHF) at 200 °C from the lowest possible dilution up to the transition to microcrystalline silicon.

	13.56 MHz					40.68 MHz				
Pressure (mbar)	0.4	1.0	2.5	5.0	9.0	0.07	0.2	0.5	1.0	2.5
Power (W)	4	4	3	10	20	3	3	7	12	15

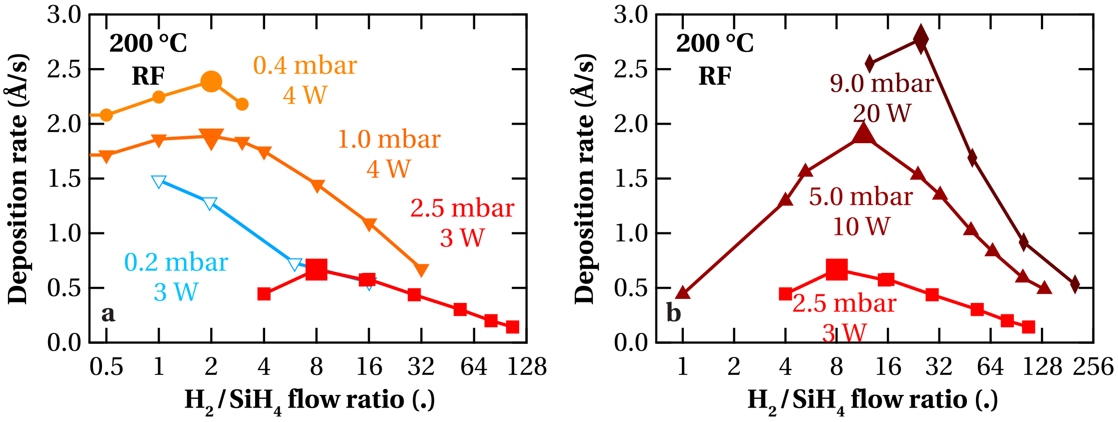

Figure 5.10: Deposition rate as a function of the H_2 dilution for series deposited in different pressure regimes keeping frequency (13.56 MHz, RF) and temperature (200 °C) constant. (a): The deposition rate generally decreases with increasing pressure up to 2.5 mbar due to film-precursor collisions in the plasma phase. (b): The series deposited at higher pressures, where the deposition rate increases with pressure due to increased power. For comparison, a dilution series deposited at 40.68 MHz (VHF, see Fig. 5.11a) is added in blue. Large symbols mark the maximum deposition rate for each dilution series.

At low H_2 dilutions, powder formation with non-uniform deposition of the layer is observed. Hence, the deposition rate is lowered by polymerization of SiH_4 towards higher silanes, which are pumped away and do not contribute to the growing film.

For the same reason, the H_2 dilution with the highest deposition rate (indicated with larger symbols) increases with pressure; this is also the case if the power is kept the same for all pressures (results not shown here). The number of film-precursor collisions in the plasma phase increases with increasing pressure; hence, more powder is produced and fewer film precursors reach the surface to contribute to layer growth. However, collisions in the gas phase do not always lead to powder production. Particularly at low pressures other reactions are dominant (cf. Fig. 5.10a): scattering of film precursors with gas particles reduces the diffusion length of the film precursors and hence the deposition rate as the pressure increases, but does not lead to visible powder.

At higher pressures (cf. Fig. 5.10b), another mechanism is dominant: for a sustainable plasma, the power needed to be increased significantly which leads to an increased deposition rate—at least for high dilutions, where powder production is not limiting. Still, the trend continues that the dilution of the highest deposition rate increases with increasing pressure.

For direct comparison between RF and VHF, a dilution series of VHF is included in Fig. 5.10, deposited at the same power as the 2.5-mbar series deposited at RF. Interestingly, they coincide for high dilutions, but differ for low dilutions, where powder production limits the deposition rate in case of RF, but not in case of VHF.

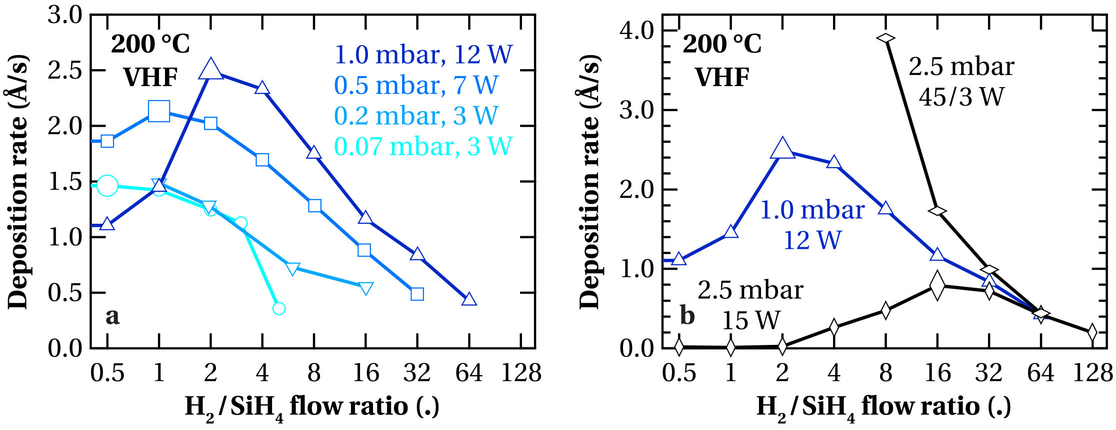

Figure 5.11: Deposition rate as a function of the H_2 dilution for series deposited in different pressure regimes keeping frequency (40.68 MHz, VHF) and temperature (200 °C) constant. (a): The deposition rate generally decreases with increasing pressure up to 1.0 mbar due to increased power. (b): The series deposited at higher pressures, where the deposition rate decreases with pressure due to powder production. A dilution series deposited at 45 W is added in (b). In this case, the measured deposition rate was divided by three for comparison with the series deposited at three times lower power. Large symbols mark the maximum deposition rate for each dilution series.

Figure 5.11 shows the analogous dilution series of deposition rates for different pressure regimes deposited at VHF, as shown in Fig. 5.10 for series deposited at RF. The same trends are visible in both cases, however, weighted differently: In contrast to RF, for VHF the power needed to be increased with increasing pressure for low pressures (cf. Fig. 5.11a), which was less necessary for high pressures (cf. Fig. 5.11b). Correspondingly, we observe a deposition-rate increase with pressure for low pressures (due to increased power), and a decrease for higher pressures due to powder production.

In Fig. 5.11b, we added a dilution series deposited at 45 W but otherwise under the same conditions as the 2.5-mbar VHF dilution series. The measured deposition rates of the former were divided by three due to the three times higher power, justified by the linear relation between power and deposition rate shown in Fig. 5.8b. For high dilutions, where SiH_4 dissociation is limiting (see section 5.4.4), these curves coincide as expected. However, the deposition rate vanishes in the case of the 15-W series for high dilutions but increases in the case of the 45-W series. The vanishing deposition rate is obviously due to severe powder production.[3] In contrast, it seems that the deposition conditions at 45 W are in the high-depletion region [Strahm 07], where a large fraction of the SiH_4 molecules are dissociated, and hence the deposition rate is increased. This demonstrates that in cases where the SiH_4 dissociation is not limiting, the deposition does not need to depend linearly on the power.

---

[3] In some cases, the “layer” could be blown or wiped away or built up to millimeter-thick powder in the corners, leaving no deposition in the center of the substrates.

5.4.4 The concept of partial silane power

For all pressure regimes shown in Figs. 5.10 and 5.11, we observed a decrease of the deposition rate with increasing H_2 dilution for high dilutions. One might think that increasing the dilution (by decreasing the SiH_4 flow while keeping the total flow constant) would reduce the deposition rate because of the low SiH_4 flow (which would lead to highly depleted plasma conditions). However, this mechanism can be excluded for our situation. A simple estimate of the maximum deposition rate [Strahm 07]

$$r_{\mathrm{max}} = 0.0962 \frac{\Phi_{\mathrm{SiH_4}}}{S} \left(\mathrm{m^2\,Å/sccm/s}\right), \tag{5.6}$$

with $\Phi_{\mathrm{SiH_4}}$ the SiH_4 flow and S the inner PECVD chamber surface, predicts that at least twice the measured deposition rate would be possible, even for the most diluted deposition conditions.

We suggest another mechanism for the deposition-rate decrease with H_2 dilution based on a diminishing fraction of the power being used to dissociate SiH_4 compared to that used for H_2 dissociation, where the latter does not directly contribute to layer growth. First, we define the partial power available for SiH_4 dissociation:

$$P_{\mathrm{SiH_4}} \doteq P \cdot \frac{\Phi_{\mathrm{SiH_4}}}{\Phi_{\mathrm{SiH_4}} + \Phi_{\mathrm{H_2}}}. \tag{5.7}$$

Here, P is the total power, and the H_2 and SiH_4 flow rates are given by $\Phi_{\mathrm{H_2}}$ and $\Phi_{\mathrm{SiH_4}}$, respectively. For the investigated deposition conditions, the deposition rate r should be proportional to the concentration $c_{\mathrm{SiH_3}}$ of the main film precursor in the plasma, SiH_3, which in turn depends on N_{e3}, the number of electrons [Niikura 07] with a sufficiently high energy to initiate the $SiH_4 \rightarrow SiH_3 + H$ reaction. The electron impact energy needed for this reaction path (8.75 eV) [Tsuda 89] is close to the dissociation energy of molecular H_2 (8.85 eV) [Perrin 93]. Thus, the number of electrons used for SiH_4 dissociation is proportional to $N_{e3} \cdot \frac{\Phi_{\mathrm{SiH_4}}}{\Phi_{\mathrm{SiH_4}} + \Phi_{\mathrm{H_2}}}$ and we conclude that

$$r \propto c_{\mathrm{SiH_3}} \overset{*}{\propto} N_{e3} \cdot \frac{\Phi_{\mathrm{SiH_4}}}{\Phi_{\mathrm{SiH_4}} + \Phi_{\mathrm{H_2}}} \propto P \cdot \frac{\Phi_{\mathrm{SiH_4}}}{\Phi_{\mathrm{SiH_4}} + \Phi_{\mathrm{H_2}}} \doteq P_{\mathrm{SiH_4}}. \tag{5.8}$$

Note that $*$ is valid only because the dissociation energies of molecular hydrogen and silane into silyl, the two dominant species in the investigated plasma regimes, are similar.

The deposition rate as a function of the partial power is plotted in Fig. 5.12 for all H_2 dilution series presented in section 5.4.3. Indeed, we see that the deposition rate increases linearly with the partial power for low $P_{\mathrm{SiH_4}}$. Note that the curves for different pressures and powers overlap well within experimental error. The proportionality constants estimated from these

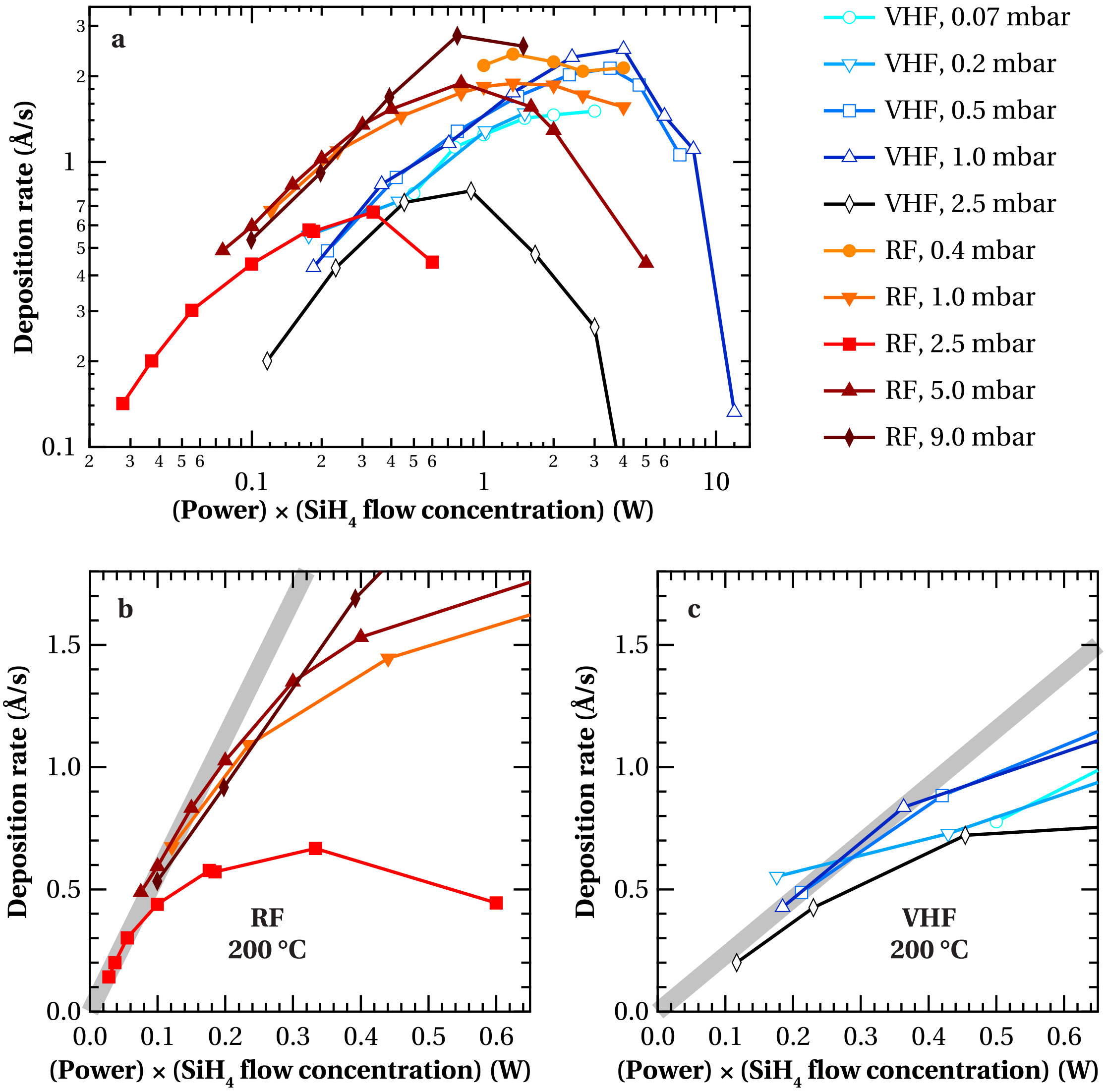

Figure 5.12: Deposition rate as a function of the partial power $P_{\mathrm{SiH_4}} \doteq P \cdot \frac{\Phi_{\mathrm{SiH_4}}}{\Phi_{\mathrm{SiH_4}}+\Phi_{\mathrm{H_2}}}$. (a): The data for all dilution series presented in section 5.4.3; the lower panels show the same data but separated into depositions at 13.56 MHz (b) and 40.68 MHz (c) and with the regions of low partial power (corresponding to high dilutions) magnified, where the deposition rate is limited by the SiH_4 dissociation. The gray zones in (b) and (c) are the maximum deposition rates for a given partial power, estimated from these data. Note the logarithmic scale in (a) but linear scale in (b) and (c).

data are on the order of $5.6\,\frac{\text{Å}}{\text{W s}}$ (RF) and $2.3\,\frac{\text{Å}}{\text{W s}}$ (VHF). Considering only one electrode surface (hence multiplying with the surface area), this is $1300\,\frac{\text{Å cm}^2}{\text{W s}}$ (RF) and $550\,\frac{\text{Å cm}^2}{\text{W s}}$ (VHF). This value allows us to estimate the maximum deposition rate as a function of the RF power for a given H_2 dilution. For higher partial powers, the deposition rate stays below the linear behavior due to increasing utilization of SiH_4 for species that are not deposited, e.g. powder.

5.5 Conclusions

We have elaborated the basic conditions of PECVD for TF-Si solar cells but not limited to this application. After discussing different reactor designs, we focused on the Octopus system with an onion-chamber design allowing for differential pressures. We explored extensively the deposition parameter space including temperature, frequency, power, gas composition and pressure, focusing on:

- *OES:* We provided optical emission spectra (and photographs for the visual experimentalist) of the plasmas for all process gases typically used for TF-Si solar cells, measured at RF and VHF. Here, we kept the measurement and plasma conditions constant (only the pressures were adapted to the Paschen-curve minimum of each gas) for comparability of frequencies and gases, including Ar, CO_2, CH_4, PH_3 (diluted in H_2), $B(CH_3)_3$ (diluted in H_2), H_2, and SiH_4.

- *Paschen curves:* We presented measurements of the extinction power and extinction pressure as a function of the pressure and power, respectively. These measurements were performed for all process gases mentioned above at excitation frequencies of 13.56, 40.68, and 81.36 MHz. These measurements describe the fundamental limits of a given reactor analogous to the more general Paschen's law but with the advantage of easy experimental access in reactors that are not equipped for plasma research but for industrial production. We showed that the measured curves can be fitted to an adapted form of Paschen's law. With the examples of the H_2 and SiH_4 Paschen curve measurements, we explained that:

  (i) At high pressures, higher power is needed as the frequency is increased, as a stronger electric field is needed such that electrons acquire enough energy for the ionization of SiH_4 within half the cycle time given by the excitation frequency.
  (ii) At high pressures, higher power is needed for SiH_4 than for H_2 because the higher collision cross section of SiH_4 leads to more electron losses in the plasma phase.
  (iii) High frequencies sustain plasmas at lower pressures than low frequencies because of smaller electron losses at the electrodes due to the lower electron displacement amplitude.
  (iv) SiH_4 plasmas can be sustained at lower pressures than H_2 plasmas because of larger collision cross sections of SiH_4 molecules with electrons.

  For the deposition of low-defect *a*-Si:H materials at low power, this is of great importance because it means that:

  (a) At low pressures, H_2 dilution can make it impossible to sustain a SiH_4 plasma.
  (b) At high pressures, H_2 dilution allows a plasma to be sustained at a lower power.
  (c) At low pressures, ignition with an external electron source can reduce the ignition power dramatically, but not at high pressures.

- *Deposition rates:* For a wide deposition parameter space covering deposition conditions of hydrogenated amorphous, protocrystalline, polymorphous and other thin-film silicon materials, we determined the deposition rates as a function of pressure, H_2/SiH_4 flow ratio, power, temperature, and frequency. In particular, we showed experimentally and provided explanations for the:

    (a) Time-stability of the deposition rate for *a*-Si:H materials with an eventual short nucleation phase.
    (b) Linearity of the deposition rate with power.
    (c) Deposition rate increase with increasing temperature by a constant rather than by a factor.
    (d) Deposition rate increase with increasing dilution for low dilutions.
    (e) Deposition rate decrease with increasing dilution for high dilutions.
    (f) Shift of the maximum deposition rate for a given pressure regime towards higher dilutions as the pressure increases.

    Based on this large data set of deposition rates, we introduced the concept of partial power. This allowed us to ascribe the deposition-rate decrease with increasing dilution to the increasing fraction of power that is used for the dissociation of H_2 molecules instead of SiH_4, which leads to fewer layer precursors.

6 Comparison of intrinsic hydrogenated amorphous silicon absorber layers

Several deposition conditions have been reported to produce hydrogenated amorphous silicon (a-Si:H) films that degrade less under light soaking when incorporated as intrinsic (i) absorber materials into a-Si:H solar cells. However, a systematic comparison of these a-Si:H materials has never been presented. Here, we present the properties of different types of a-Si:H, covering standard low-pressure a-Si:H, protocrystalline, polymorphous, and high-pressure a-Si:H materials.

In chapter 5, we presented the boundary conditions for the growth of intrinsic a-Si:H materials by plasma-enhanced chemical vapor deposition (PECVD). Within the given limits, we have explored this deposition parameter space, varying deposition pressure, temperature, power, frequency, and the H_2 dilution of SiH_4. We compare the resulting materials with respect to their optical properties (particularly, their bandgap) and their behavior when incorporated into single-junction solar cells. Finally, a consistent picture of a-Si:H materials that are currently used for a-Si:H solar cells emerges.

The applications of these materials in single- and multi-junction solar cells are discussed, as well as their deposition compatibility with rough substrates, taking into account aspects of voltage, current, and charge collection. In sum, this contributes to answering the question, “Which material is best for which type of solar cell?” The answer is not only significant for thin-film silicon solar cells, but a-Si:H solar cells are used here also as very sensitive measurement method to test a-Si:H material properties for other applications such as in heterojunction solar cells or others.

This chapter is organized as follows: in section 6.1, we present a summary of the different a-Si:H materials for solar cells reported in the literature, which motivates our studies. This section is followed by a short description of our experimental methods in section 6.2. Section 6.3 describes the properties of a select set of a-Si:H layers; solar cells results with these layers included—focusing on solar cell efficiencies after light soaking and relative degradation—are presented in section 6.4, and we relate the solar cell degradation with absorber layer properties. Further, we discuss the substrate dependence of solar cell performance that motivates microstructure investigations by scanning transmission electron microscopy (STEM). We conclude this chapter with a general discussion of *a*-Si:H applications in section 6.5.

The main results of this chapter were published in the Journal of Applied Physics [Stuckelberger 13], and other parts are in preparation for further publications.

6.1 Motivation and prior art

Since the discovery of the Staebler-Wronski effect in 1977 [Staebler 77], light-induced degradation (LID) of *a*-Si:H has been widely discussed in the literature. Nevertheless, the processes that lead to (partially reversible) deteriorated conductivity and enhanced recombination in solar cells are not yet fully understood at the atomic and energy-band levels. Thus, LID remains an active field of research for *a*-Si:H solar cells. Several models exist that explain aspects of LID, see e.g. the review article [Shimizu 04]. Recently, the role of vacancies and voids in LID have received increased attention [Zhang 01, Smets 03, Smets 10]. Here, we shall not give evidence for one or the other model, but rather quantify the LID of different *a*-Si:H materials in a direct comparison of these materials incorporated as absorber layers in *a*-Si:H single-junction solar cells.

Leading institutes in the development of *a*-Si:H solar cells have claimed different PECVD conditions for *a*-Si:H absorber materials to be best suited for high-efficiency solar cells (with low LID), with an obvious lack of systematic comparisons. We group these materials into these classes: *low-pressure a-Si:H*, *protocrystalline silicon (pc-Si:H)*, *polymorphous silicon (pm-Si:H)*, *high-pressure a-Si:H*, and *triode a-Si:H*. These terms are established in the literature, although it is questionable whether they are suitable as terms for material classes: we reproduced many recipes reported in the literature but could not identify a specific deposition condition but rather general trends that lead to poorer or better materials. These trends are in agreement with measured layer properties and can be traced back to the plasma conditions during deposition. In the following sections we give a short overview of these material classes with the properties as they are reported, not necessarily corresponding to our own measurements. Later, we will use the term *hydrogenated amorphous silicon* or *a*-Si:H for all these classes and differentiate the materials among deposition conditions and properties rather than using this terminology except when directly referring to work by other authors.

The classifications of materials under investigation here were performed with the application of absorber layers for solar cells in mind; they are valid for other applications as well—e.g. for particle detectors, waveguides for opto-electronic devices, adhesion layers, passivation layers, etc.—but these are not the main focus of this thesis. However, it might contribute to a better understanding of amorphous silicon materials that need to be optimized for such applications, in particular for the passivation of crystalline silicon (*c*-Si) surfaces in heterojunction solar cells [De Wolf 12], which hold the world record for single-junction solar cells based on *c*-Si [Panasonic 14].

6.1.1 Low-pressure hydrogenated amorphous silicon

"Standard hydrogenated amorphous silicon"

Deposited at low pressure and typically very high frequency (VHF) (typically 0.2 to 0.8 mbar, 40 to 140 MHz) with rather low H_2 dilution, these materials have narrow bandgaps and provide high currents. Therefore, their main application is the use in single-junction or micromorph tandem solar cells, and they have led to several world-record efficiency devices [Benagli 09, TEL solar 14a, Boccard 14]. Other applications are the prevention of nucleation such as epitaxial growth on c-Si [Demaurex 14] or microcrystalline growth in thick pc-Si:H layers [van Elzakker 10]. The key properties of low-pressure a-Si:H are:

- Comparatively narrow optical bandgap (around 1.7 eV).
- Low medium- or long-range order observed in X-ray diffraction.
- Low charge-carrier mobility.
- Significant degradation during light soaking.

6.1.2 Protocrystalline silicon (*pc*-Si:H)

"Extended nucleation phase of μc-Si:H that has not yet grown crystallites but does so for thicker layers"

Deposited at moderate pressure with a H_2 dilution close to the transition from a-Si:H to microcrystalline silicon (μc-Si:H), these materials have a wide bandgap. If grown thick enough, this material can turn into μc-Si:H with increasing crystallinity [Collins 00, Collins 02, Collins 03, Yan 03a, Schropp 09]. The main characteristics of pc-Si:H are:

- Wider bandgap than low-pressure a-Si:H and pm-Si:H.
- Enhanced medium-range order compared to low-pressure a-Si:H [van Elzakker 09].
- Less dense material, containing many/large voids [Collins 03].
- Limited thickness: layers grow microcrystalline after a critical thickness.
- Strong substrate dependence (nucleation of microcrystals) [van Elzakker 07].
- Fast but limited LID [Collins 03, van Elzakker 09].

The wide bandgap and limited LID are the reasons for the choice of this material as the top-cell absorber layer for junctions of three or more thin-film silicon subcells such as commercialized by United Solar Systems Corp. [Yang 03].

6.1.3 Polymorphous silicon (*pm*-Si:H)

"Silicon on the transition between a-Si:H and μc-Si:H: nanocrystals, grown in the plasma phase, can be homogeneously distributed over the whole layer depth"

The deposition conditions of *pm*-Si:H are similar to those of *pc*-Si:H, but closer to the "dusty", "powdery" or "γ" regime [de Jong 10], which is entered by going to higher pressure. In contrast to *pc*-Si:H, this material can be grown thick without a transition to *μc*-Si:H. Small crystallites, likely produced in the plasma phase, can be distributed homogeneously throughout the thickness. Polymorphous silicon has mainly been investigated at Ecole Polytechnique in Palaiseau [Fontcuberta i Morral 01a, Fontcuberta i Morral 01b, Roca i Cabarrocas 02, Fontcuberta i Morral 04] and is characterized by:

- Embedded crystallites in the amorphous matrix.
- Wide bandgap [Soro 08].
- Enhanced short-range order as compared to low-pressure *a*-Si:H.
- High density [Middya 01].
- Small void-volume fraction [Fontcuberta i Morral 02].
- Low and very fast degradation [Middya 01, Poissant 03].
- Delamination issues that can arise during light soaking [Kim 12b, Kim 12a].

6.1.4 High-pressure hydrogenated amorphous silicon

These materials are deposited at high pressures, often with a smaller inter-electrode gap [Rech 01, Fischer 13]. These deposition regimes have received increased attention in the last decade, parallel to microcrystalline silicon deposition at high pressures; they can be deposited in high-depletion regions [Strahm 07] for transition-material properties.

6.1.5 Triode hydrogenated amorphous silicon

Particularly at the National Institute of Advanced Industrial Science and Technology (AIST) in Tsukuba (Japan), the deposition of *a*-Si:H in a triode reactor—a diode PECVD reactor with an additional mesh between the electrodes serving as a third electrode, see section 5.1.3—has been investigated [Matsuda 83, Matsuda 04, Shimizu 05, Matsui 12, Matsui 13a]. Deposition conditions are otherwise often similar to those of low-pressure *a*-Si:H. The material differs from other *a*-Si:H materials by:

- Very low deposition rate (typically a factor of 10 lower).
- Low defect concentration.
- Low H_2 content.
- Low microstructure factor R^* (see definition in section 2.3.3).
- Lowest LID among *a*-Si:H materials.

The current world record of a-Si:H single-junction solar cells is held by cells including triode-deposited a-Si:H absorber layers [Matsui 13b].

6.1.6 Other materials

We believe that the following terms for amorphous silicon materials are redundant but mention them here for completeness:

Nanocrystalline silicon

The etymology of this word suggests that the material that we call microcrystalline silicon (μc-Si:H) in our institute is called nanocrystalline silicon (nc-Si:H) as the crystallite size is rather in the range of nano- than of micrometers. Often, this terminology is used indeed (e.g. in [Yan 04]). However, this term is sometimes used for materials that we presume are polymorphous (e.g. [Hazra 99]), in other cases it is used for mixed-phase materials a-Si:H/μc-Si:H (e.g. in [Collins 00]), in contrast to μc-Si:H material with higher Raman crystallinity. (In our institute we call such mixed-phase material simply microcrystalline and provide the Raman crystallinity ratio to differentiate further.)

Paracrystalline silicon

Mainly in the context of simulations, e.g. in [Gibson 98, Pan 04], the term paracrystalline silicon is used as a generic term for different kinds of a-Si:H with embedded crystallites, in analogy to other fields of material science where it is more often used.

Quasi-amorphous silicon

In early publications from Palaiseau (e.g. [Middya 01]), a new material called quasi-amorphous silicon (qm-Si:H) was introduced. Comparing the deposition conditions and properties of that material, we assume it is the material later called polymorphous silicon.

Columnar growth of a-Si:H

At low deposition temperatures (typically below 100 °C), columnar growth of a-Si:H is observed, sometimes in mixed-phase with microcrystalline silicon [Bronsveld 06, Bronsveld 10]. The electronic properties of low-temperature-grown material are rather poor, but nevertheless interesting for the growth of solar cells on substrates that do not withstand high temperatures [Rath 09, Fathi 09, Söderström 11].

6.1.7 Alternative processing

Alternative gas precursors

Most research laboratories and industry use only H_2 and SiH_4 as gas precursors for intrinsic *a*-Si:H. However, many deposition regimes have been explored using the inert gases Ar or He [Sriraman 02, Gogoi 07, Funde 09] that can play different roles depending on the process conditions: they can densify layers or create defects through ion bombardment, help the nucleation (enhancing the surface mobility of adatoms), etch already deposited material or dilute the plasma similar to H_2, provide access to deposition conditions that would not be accessible according to the Paschen curve of the residual gas mixture (see chapter 5), or simply enhance the safety if the provided SiH_4 is already diluted.

Another approach is the (partial) substitution of SiH_4 with SiF_4 [Dornstetter 13, Hänni 14], Si_2H_6 [Chatham 89, Hou 11], or with SiH_2Cl_2 as investigated in [Azuma 94, Bullock 94]. In analogy, the use of BF_3 led to high-quality *p*-type doped layers [Guha 86, Pearce 07, Jiang 09]. More for the supply of carbon than of silicon, different silylmethanes [Beyer 89, Fölsch 92] or methyltrichlorosilane [Ivashchenko 09] have been tested. We will not enter into the field of amorphous silicon alloys further.

Alternative deposition steps

Different gradients of the H_2/SiH_4 flow ratio during deposition have been investigated—either to introduce a bandgap profile [Muthmann 11], or to avoid growing larger crystallites during deposition [Yan 10].

Different research groups reported high-quality materials resulting from layer-by-layer (LBL) deposition. One type of LBL deposition includes the subsequent deposition of alternating layer stacks of *pc*-Si:H with low-pressure *a*-Si:H [Layadi 95, van Elzakker 07] where the role of *a*-Si:H is to interrupt nucleation as an alternative to H_2 dilution profiling for the deposition of thick transition material layers. In a second type of LBL deposition [Bieberícher 02, Descoeudres 11], deposition intervals alternate with surface treatments, typically an inert gas or H_2, e.g. to densify the layer or passivate defects.

Alternative deposition techniques to PECVD

Defect passivation in *a*-Si:H is an important challenge for PECVD-produced materials and even more for other techniques. Poor electronic material properties or difficult commercialization prevented the industrial deposition of *a*-Si:H materials for solar cell applications by other techniques such as plasma spray [Kopecki 10], reactive chemical vapor deposition [Minowa 09], ion-beam-assisted evaporation [Rinnert 98], electron cyclotron resonance [Kasouit 10], sputtering [Moustakas 82], hot-wire deposition [Alpuim 99, Schroeder 01, Filonovich 08, Xin 11], or expanded thermal plasma deposition [Korevaar 02, Smets 02]. These techniques will not be discussed here further.

6.2 Experimental

6.2.1 Deposition conditions for intrinsic hydrogenated amorphous silicon

For the systematic study of different deposition conditions, we tried to cover most *a*-Si:H materials presented in section 6.1 that showed promising results for solar cell applications. We restricted our study to PECVD with two electrodes (a few results obtained with a triode reactor are presented in section 9.3), and only SiH_4 and H_2 were used as gaseous precursors. We varied the H_2 dilution, pressure, power, temperature, and excitation frequency of *a*-Si:H films incorporated as the absorber layer in single-junction solar cells.

All silicon layers were deposited by PECVD in the Octopus cluster tool described in section 2.2.1, which allowed a wide variety of deposition conditions and fast equilibration times thanks to its closed reactor design [Howling 07]. The symmetric electrodes in each chamber were 15 cm × 16 cm, the inter-electrode gap was 15 mm, and the excitation frequency was 13.56 MHz (RF) or 40.68 MHz (VHF). Dedicated chambers were used for *p*-layer, *n*-layer, and *i*-layer depositions, and different chambers were used for *i*-layers deposited at RF or VHF.

Table 6.1: Deposition conditions for intrinsic *a*-Si:H absorber layers that were incorporated into single-junction solar cells.

Pressure	Power	Total gas flow	Frequency
0.2 mbar	3 W	30 sccm	40.68 MHz
2.5 mbar	3 W	85 sccm	13.56 MHz
5.0 mbar	10 W	100 sccm	13.56 MHz
9.0 mbar	20 W	100 sccm	13.56 MHz

Table 6.1 summarizes the deposition parameters of the four main plasma regimes investigated in this study. They are a subset of the regimes for which the deposition rates were discussed in section 5.4.3 and summarized in Tab. 5.2.[1] For each of these regimes, the H_2 dilution was varied widely while keeping the total gas flow constant. Exceptions for very high or low dilutions were made due to limitations of the mass flow controllers.

The deposition temperature was kept at 200 °C. For the best bulk material quality in the different pressure regimes, we chose the lowest power density that allowed plasma ignition for all H_2 dilutions. Note that the power was measured at the generator output.

For completeness, further *a*-Si:H layers were deposited but without incorporating them in solar cells; deposition conditions are given when discussing these results.

---

[1] For all other regimes presented in Tab. 5.2, dilution series of *a*-Si:H absorber layers were incorporated into solar cells, too. However, due to the moving of the institute, light soaking of these solar cells was finished only shortly before finishing this manuscript. The results will be published later.

6.2.2 Solar cell design

For the incorporation of the absorber layers (deposited according to the parameters given in Tab. 6.1) into solar cells, we used the cell design shown in Fig. 6.1. We changed only the intrinsic bulk layer i_{bulk} to obtain a direct comparison of bulk layer properties resulting from the investigated deposition conditions.

The *a*-Si:H solar cells were deposited in the superstrate configuration (p-i-n) on 0.5-mm-thick Schott AF 32 glass substrates. All solar cells were co-deposited on four different substrates with varying roughness: Three substrates consisted of 2-µm-thick co-deposited, boron-doped zinc oxide (ZnO:B), deposited by low-pressure chemical vapor deposition (LPCVD) on glass. On one, as-deposited ZnO:B was used (denoted Z2); on two others, the ZnO:B was treated for 4 and 10 minutes (denoted Z2 4' and Z2 10', respectively) with an Ar plasma to smoothen the surface texture from V- into U-shaped. This leads to less shunting but also less light scattering [Python 08]. All results shown below except in section 6.4.5 refer only to the Z2 4' substrate. The presented trends, however, were consistent across all substrates. As a flat reference, a fourth substrate with smoothly grown LPCVD ZnO:B (0.8 µm thick) was used, also treated for 4 minutes with an Ar plasma (denoted smooth 4') [Nicolay 12, Fanni 14].

Solar cell deposition began with a p-type bilayer. Directly on the ZnO, we deposited a microcrystalline silicon oxide layer (p-(μc-SiO:H)) for good electrical contact, enhanced transparency, and shunt-quentching [Cuony 10, Despeisse 10b]. This was followed by an amorphous silicon carbide layer (p-(a-SiC:H)) with a wide bandgap to provide a strong electric field. The p-type layers were deposited at nominally 150 °C and 40.68 MHz.

In order to keep the sensitive p-i and i-n interfaces as similar as possible from one deposition to the next, we sandwiched the 220-nm-thick intrinsic bulk absorber layer under investigation between 10-nm-thick intrinsic *a*-Si:H buffer layers at both interfaces, deposited at 200 °C, RF, with H_2 and SiH_4 flows of 80 and 2.5 sccm at a power of 3 W and a pressure of 2.5 mbar. These buffer layers (as well as the doped layers and ZnO contacts) were the same on all solar cells, regardless of the intrinsic bulk layer. The deposition conditions were chosen right at the transition from *a*-Si:H to μc-Si:H—when grown thicker than about 300 nm, crystallite growth was observed in Raman measurements.

The three i-layer depositions were followed by an n-type bilayer consisting of a hydrogenated amorphous silicon layer (n-(a-Si:H)) and a microcrystalline silicon oxide layer (n-(μc-SiO:H)). They were deposited at 200 °C and 40.68 MHz. The back electrode consisted of 2-µm-thick LPCVD ZnO:B.

In addition to SiH_4 and H_2, CO_2 was used for oxide layers, $B(CH_3)_3$ for p-type layers, PH_3 for n-type layers, and CH_4 for the carbide layer. For better reproducibility and to ensure that cell performance was not limited by the doped layers, all doped layers were thicker than those in cells optimized for high efficiency. For each substrate, an array of 16 cells, each 0.25 cm^2 in size, was defined.

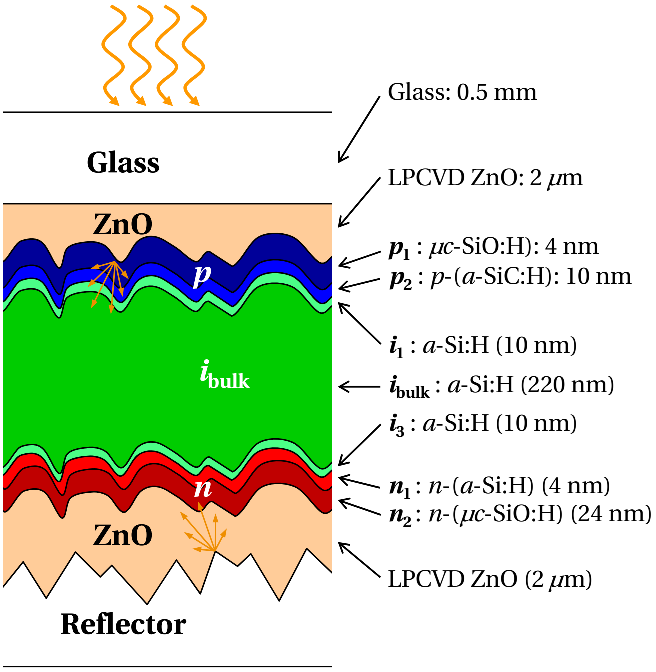

Figure 6.1: Solar cell structure used for all *p*-*i*-*n* solar cells presented in this chapter.

6.2.3 Layer and cell characterization

For measurements of intrinsic bulk layer properties, the layers were co-deposited on 0.5-mm-thick Schott AF 32 glass substrates and 250-μm-thick double-side-polished intrinsic (100) crystalline silicon (*c*-Si) wafers.

Ellipsometry measurements were performed using a UVISEL ellipsometer from Horiba Jobin Yvon (with monochromators for IR and UV/Vis) between 0.6 and 6 eV, and transmission measurements using a Lambda 900 spectrometer from Perkin Elmer between 300 and 2000 nm; optical layer properties were obtained from combined fitting of three-angle ellipsometry and transmission measurements of layers deposited on glass with a Tauc-Lorentz model [Jellison 96a, Jellison 96b], taking into account surface roughness as described in section 2.3.1.

For Fourier transform infrared (FTIR) spectroscopy measurements, a Spectrum 2000 spectrometer from Perkin Elmer and a Nicolet 8700 spectrometer from Thermo Scientific were used. Raman crystallinity was measured on an Invia Raman microscope from Renishaw and on a Senterra Raman microscope from Bruker with green lasers.

Current–voltage ($I(V)$) characteristics were measured with a four-lamp solar simulator from Wacom (class AAA) under standard conditions (AM1.5g, 1000 $\frac{\text{W}}{\text{m}^2}$, 25 °C), and the current was determined from an external quantum efficiency (EQE) system built in-house using polytetrafluoroethylene (PTFE) as a white back reflector. Efficiencies are calculated with the fill factor (FF) and open-circuit voltage (V_{oc}) values from $I(V)$ and short-circuit current densities (J_{sc}) from EQE measurements. Light soaking was performed in a sun simulator from Solaronix (class AAA) under standard conditions (AM1.5g, 1000 $\frac{\text{W}}{\text{m}^2}$, 50 °C).

6.3 Properties of intrinsic hydrogenated amorphous silicon layers

6.3.1 Bandgap

Bandgap vs. *a*-Si:H layer thickness

Figure 6.2a shows two different bandgap parameterizations, the Tauc-Lorentz bandgap (E_g^{TL}) and E_{04} (cf. section 2.3.2 for the definitions of different bandgap parameterizations), for two layer thickness series. These series were deposited under similar deposition conditions given in the figure; the corresponding thicknesses are shown in Fig. 5.8a.

For thicker layers, the bandgaps do not depend on the thickness: under the deposition conditions for *a*-Si:H that are far away from the transition region to *μc*-Si:H, no shift of layer properties with deposition time is expected. The bandgaps of $E_g^{TL} \approx 1.7\,\text{eV}$ (slightly above for RF and below for VHF) and around $E_{04} \approx 1.95\,\text{eV}$ are typical for high-quality *a*-Si:H materials deposited at low H_2 dilutions; the two bandgap parameterizations are not fundamentally correlated (E_g^{TL} is a fitting result of a whole absorption curve measurement while E_{04} is the energy at a specific absorption coefficient), but the difference of 0.25 eV can serve as a rule of thumb for many *a*-Si:H materials. Due to the independence of E_{04} from fitting models and the fact that this bandgap value can be determined for each absorption measurement, we continue to show this parameter further on, although all values were obtained from ellipsometry/transmittance fitting with a Tauc-Lorentz oscillator model.

For thin layers with a deposition time below 10 s corresponding to layer thicknesses in the order of 10 nm, we observe a dramatic increase of the bandgaps for both deposition conditions. Although the layers were stored in N_2 between deposition and measurement, we assume that the short air exposure led to the oxidation of the layer surfaces rather than changing layer properties due to plasma stabilization after ignition. Hence, the measured wide bandgap for thin layers is dominated by SiO_x, while the same oxide layer thickness, taken into account by a surface-roughness layer in an effective-medium approach in the fitting, is less detrimental for thicker layers. For this reason, all layers presented in the following sections were grown to a thickness on the order of 200 nm.

Bandgap vs. deposition power

Figure 6.2b shows the bandgap dependence on deposition power for three deposition regimes with the deposition parameters given in the figure; the deposition rates of the same series are discussed in Fig. 5.8b.

Compared to variations we will see later, the bandgap dependence on power is rather weak. We note two opposite trends: for the RF series, the bandgap increases with power, for VHF, it decreases for both series. We explain these trends by the following mechanisms: in the case of RF, increasing the power leads to increasing depletion which plays a similar role as increasing

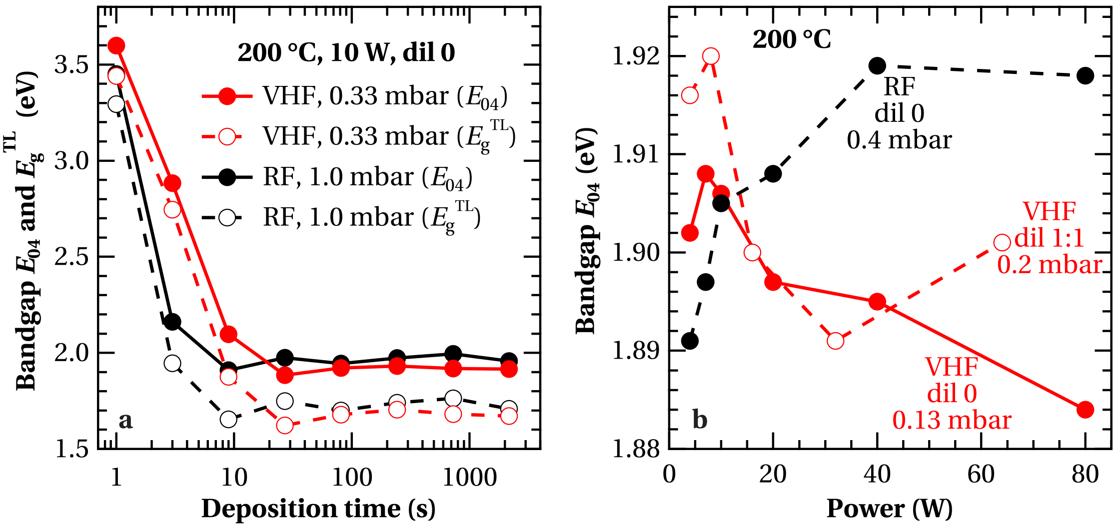

Figure 6.2: (a): Two bandgap definitions E_{04} and E_g^{TL}, measured for layers deposited under the same conditions but for different times resulting in different thicknesses (compare with the layer thicknesses given in Fig. 5.8a). (b): Bandgap measurement of three power series with adapted deposition time for resulting thicknesses around 200 nm.

the H_2 dilution (see later), approaching the transition to μc-Si:H deposition conditions which is accompanied by a bandgap increase.

For VHF regimes, another effect dominates: the number of layer precursor collisions in the plasma phase increases with increasing power, which leads to the formation of higher silanes in the plasma phase, approaching the powdery plasma regimes more easily than at RF (cf. the discussions on powdery deposition regimes in chapter 5). This leads to porous layers with generally poor material quality and a narrower bandgap. This explanation is in agreement with the lower deposition rate for VHF than for RF as shown in Fig. 5.8b.

Bandgap vs. deposition temperature

Figure 6.3a demonstrates the strong dependence of the bandgap on the deposition temperature for the case of two series deposited under similar conditions, with only the pressure being adapted to compensate for the frequency difference. Both regimes provide high-quality materials that lead to high-efficiency solar cells—the RF series includes the *a*-Si:H absorber material that led to record currents presented in section 9.1.

The slopes of the linear fits of $E_{04}(T)$ are $-6.1 \times 10^{-4}\,\frac{\text{eV}}{^\circ\text{C}}$ for RF, and $-4.0 \times 10^{-4}\,\frac{\text{eV}}{^\circ\text{C}}$ for VHF. In the literature, the bandgap decrease with increasing temperature is attributed mostly to the lower hydrogen content, as hydrogen effuses already during layer deposition (see e.g. [Zanzucchi 77, Smets 12]). However, it is not fully clear why this dependence is stronger for RF than for VHF. A possible explanation is that the enhanced ion bombardment at RF promotes the hydrogen effusion by providing activation energy at the surface. The deposition chambers

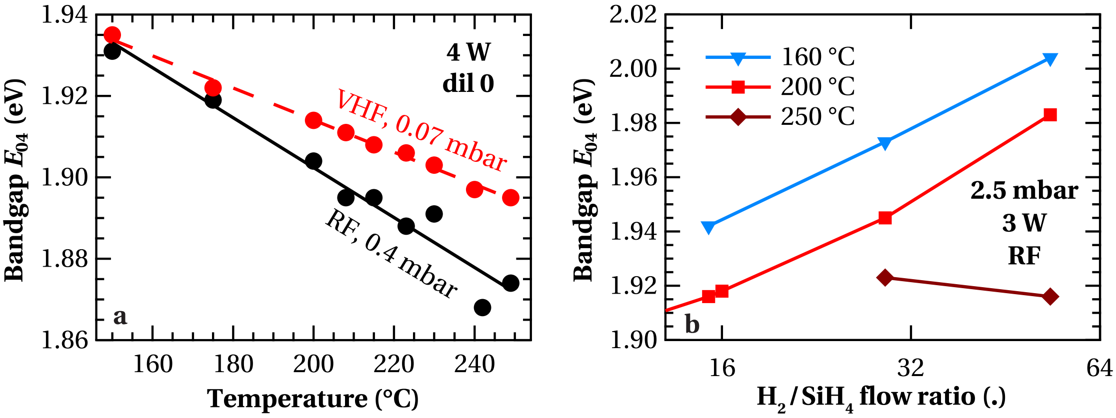

Figure 6.3: (a): Temperature dependence of the bandgap for two series deposited at 13.56 MHz (RF) and 40.68 MHz (VHF), both at 4 W, the lowest power allowing stable plasma conditions without H_2 dilution. The lines are linear fits. (b): Bandgap measurements for three H_2 dilution series deposited at different temperatures. The lines are guides to the eye.

for RF and VHF are technically identical (including the heating), and the deposition power is the same for both regimes (and very low, thus having a negligible impact on the substrate temperature). Therefore, we exclude different substrate temperatures as the cause of the temperature-dependence difference between RF and VHF. Also, the deposition times of both regimes were comparable (17 min for RF, 20 min for VHF) such that the time of the layer exposure to the deposition temperature can not justify the difference between RF and VHF.

Figure 6.3b shows the combined temperature and H_2dilution dependence of the bandgap for RF, though at considerably higher pressure than Fig. 6.3b. The temperature range from 160 to 250 °C and dilution from 16 to 64 span most of the parameter space that leads to high-quality materials for solar cell absorber layers. The dilution dependence will be discussed in more detail in the following subsection; here, we note that the possibility of bandgap tuning via temperature and H_2 dilution are comparable but that the effect of dilution is rather stronger than that of temperature. The two effects are additive; hence the combination of both leads to the strongest effects on the bandgap.

Bandgap vs. H_2 dilution and pressure

In this subsection, we discuss the influence of H_2 dilution and pressure on the bandgap based on the same ten series for which the deposition rate was presented in section 5.4.3. The depositions were performed at 200 °C at the lowest power allowing stable plasmas. The values for each series are given in Tab. 5.2.

Figure 6.4 shows the bandgaps in terms of E_{04} of the layers deposited at RF and VHF. As for the previous subsections, other bandgap parameterizations like the Tauc-Lorentz bandgap E_g^{TL} or the Tauc bandgap E_g^T show the same trends. We note:

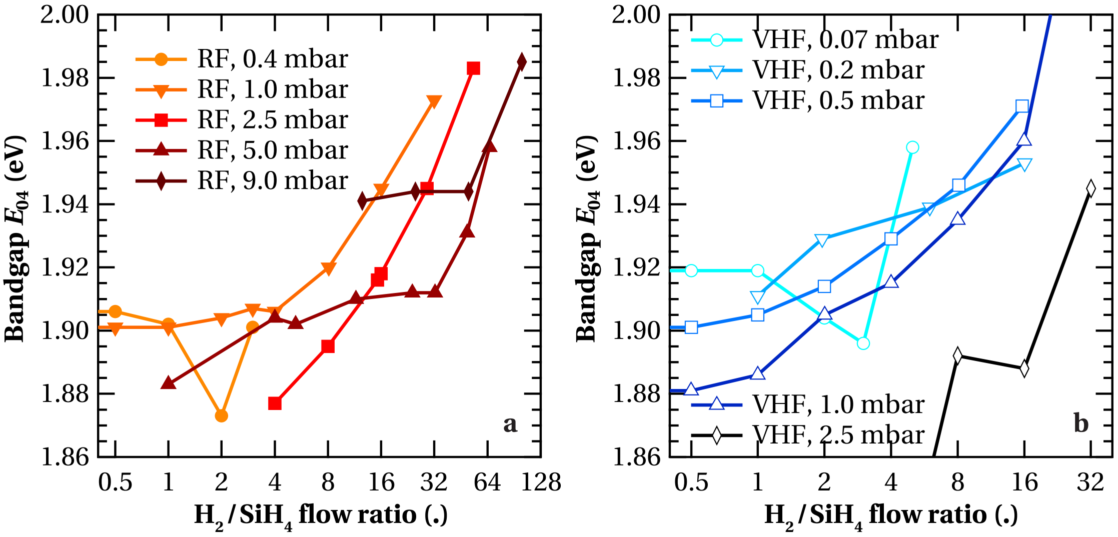

Figure 6.4: Bandgap as a function of the H_2 dilution for ten series deposited in different pressure regimes at 13.56 MHz (a) and 40.68 MHz (b).

1. *The bandgap increases with H_2 dilution.*

   As reported elsewhere [Kroll 98, Yan 03b, Smets 12], the bandgap increases with increasing H_2 dilution—moderately at low dilutions and stronger close to the transition to μc-Si:H deposition conditions. Whether this is due to a depletion of states close to the valence band [von Roedern 77], to decreased structural disorder [Cody 81], to compressive stress associated with hydrogen incorporation in divacancies and nanosized voids [Smets 12], or to a combination of these effects is not clear.

2. *The H_2 dilution at which the transition from a-Si:H to μc-Si:H takes place increases with increasing pressure.*

   For higher H_2 dilutions than those shown in Fig. 6.4, Raman measurements showed a crystalline peak at around 520 $\frac{1}{\text{cm}}$; in these cases, the fitting of the ellipsometry/transmittance data with a single Tauc-Lorentz oscillator was no longer adequate and the measurements are not shown here. Thus, the data at the highest H_2 dilution mark the transition from *a*-Si:H to μc-Si:H. The dilution at which the transition takes place increases with increasing pressure due to decreased ion bombardment on the surface and hence a lower surface mobility of the adatoms [Kalache 03].

3. *With increasing pressure, higher H_2 dilutions are needed for the same bandgap.*

   The reason for this effect is similar to the argument for item 2: with increasing pressure, the H_2 dilution needs to be increased adequately for comparable plasma and layer-growth properties.

4. *Narrower bandgaps are obtained with VHF than with RF.*

   As the frequency is increased, powder formation is enhanced with otherwise similar parameters, leading to porous materials with poor electrical properties but a narrower

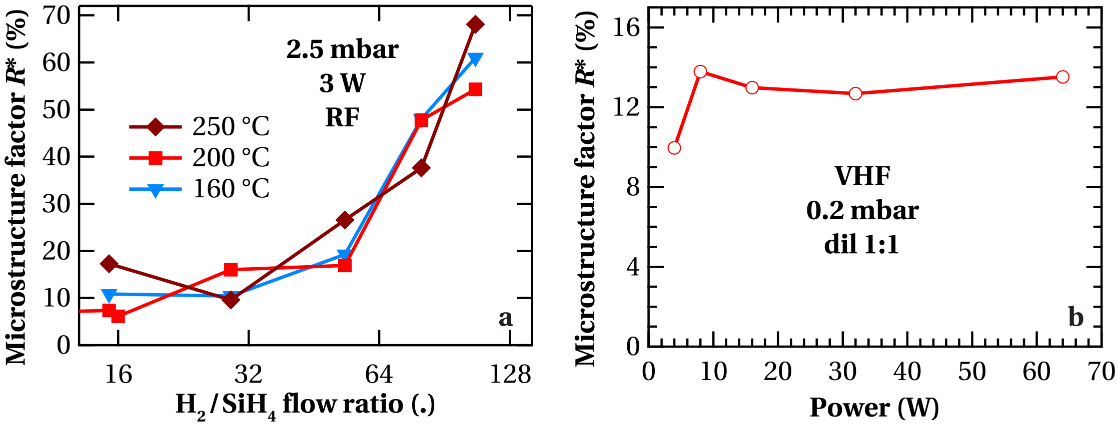

Figure 6.5: Microstructure factor R^* as a function of deposition temperature and H_2 dilution (a) and deposition power (b).

> bandgap. Powder production that led to a vanishing deposition rate in some cases marked mostly the low-dilution end of the series at VHF, while the impossibility of sustaining a stable plasma (Paschen-curve limitation) marked it for the RF series.

By simply changing the H_2 dilution of SiH_4, we were able to vary the bandgap by about 100 meV.

6.3.2 Microstructure factor *R**

We determined the microstructure factor R^* as introduced in section 2.3.3 and defined in equation 2.5 from infrared absorption measurements. This parameter, expressing the ratio of high-to-low stretching-mode intensities of Si–H bonds, is of particular interest because it includes information about the atomic bonding environment of silicon atoms in *a*-Si:H on one hand, and is correlated to the LID of solar cells on the other: absorber materials with increased R^* exhibit enhanced LID both as layers and when incorporated in solar cells [Bhattacharya 88, Fecioru-Morariu 10, Shah 10]. This motivates our studies of the dependence of R^* on specific deposition parameters in the following subsections.

*R** vs. temperature and power

Figure 6.5a shows R^* as a function of dilution for different temperatures. The dependence of R^* on the deposition temperature is weak and within the scattering of measurements. Note that the error of R^* measurement is on the order of a few percent absolute—in many cases, the measurement precision is not the limiting factor but the choice of the fitting parameters for the baseline and the Gaussian fits. The increase of R^* with dilution in this range will be discussed in the following paragraphs.

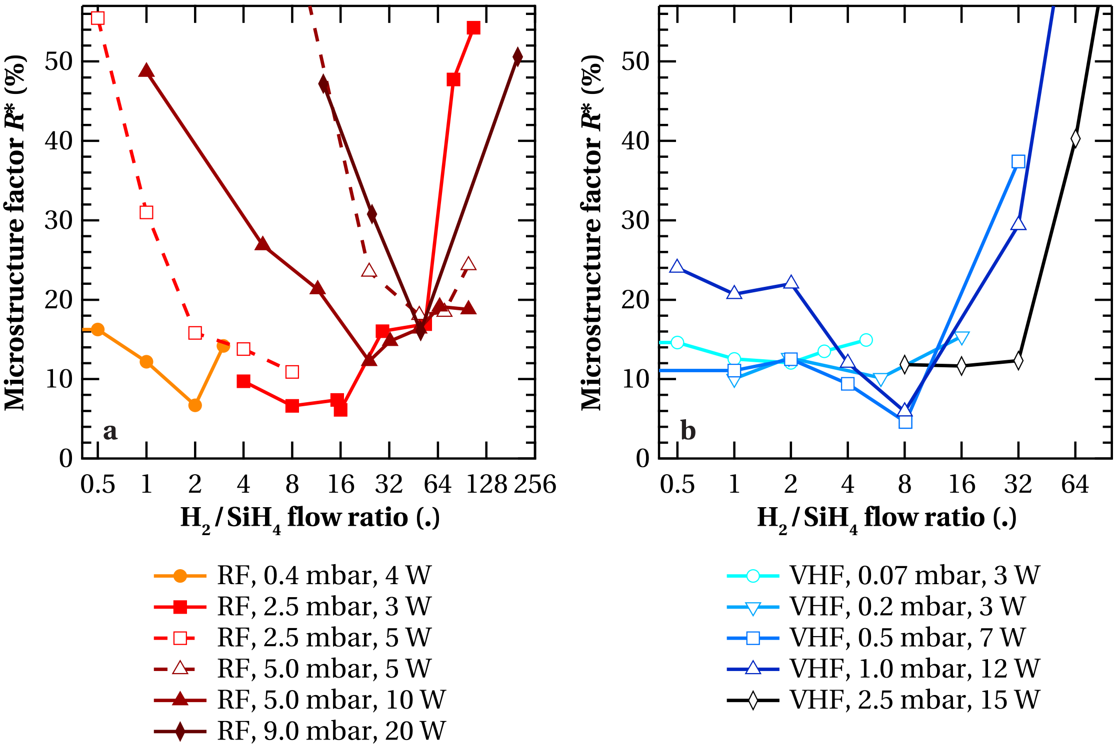

Figure 6.6: Microstructure factor R^* as a function of the H_2 dilution for different deposition regimes.

Figure 6.5b shows the dependence of R^* on the deposition power. As solar cells deposited at a power as high as 60 W show very strong degradation, we would expect a strongly increasing R^* with power; further series should check this dependence.

R^* vs. H_2 dilution and pressure

Figure 6.6 shows the dependence of R^* on the H_2 dilution for the ten pressure regimes discussed in sections 5.4.3 and 6.3.1 for RF and VHF. Further, we added two series deposited at alternative power; the deposition parameters are given in the caption.

Each dilution series exhibits a minimum R^*. Hence, we differentiate a low-dilution and a high-dilution branch of R^* with increasing R^* for both extremes. As the pressure is increased, the minimum R^* is attained at increased dilutions. For depositions at RF, for instance, it is at a flow ratio 2 at 0.4 mbar but increasing to 50 at 9 mbar. The range of small R^* appears to become narrower and more pronounced as the pressure is increased, but this might be exaggerated by the logarithmic scale. The broad minimum of low R^* for low pressures is consistent with the series at 100 mTorr of Alpuim et al. [Alpuim 99].

The increase of R^* for lower dilutions is attributed to the approaching of powdery deposition regimes as stated above. However, we also observe an increase of R^* for increasing dilution approaching the transition to μc-Si:H. This is in agreement with the enhanced hydrogen incorporation, but in contrast to [Kroll 98], where a continuous decrease of R^* until the transition was observed. The high-dilution branch is shown also in Fig. 6.5a: the transition from a-Si:H to μc-Si:H is located around dilution 80, but R^* increases already significantly from the minimum around dilution 16.

6.4 Solar cell properties with different hydrogenated amorphous silicon absorber layers

6.4.1 Initial state

The solar cell results reported in this section are taken from the cell on each substrate that showed the highest $V_{\mathrm{oc}} \times FF$ product in the initial state (as deposited). These cells are most often also the best on their respective substrate after light soaking (degraded state). Figure 6.7 shows the performance of solar cells (in terms of V_{oc}, FF, J_{sc}, and conversion efficiency) with different i-layers included, varying the H_2 dilution for four plasma regimes that are described in Tab. 6.1 and that have been discussed in the previous sections. Although these solar cells were not optimized for high efficiency, they show high initial efficiencies up to 10.4%. The trends are discussed on the basis of the properties of the degraded state and relative degradation in the following sections.

6.4.2 Degraded state

Differences among various absorber layers are often visible only after light soaking, when the conversion efficiency is typically limited by electron–hole recombination at light-induced defects. Therefore, and due to the higher significance for most applications, we concentrate on solar cell performance, shown in Fig. 6.8, after light soaking under standard conditions.

As expected from the layer properties of the bulk absorber material, V_{oc} increases generally with H_2 dilution due to a bandgap widening (see Fig. 6.8a), until it drops sharply as soon as crystallites start to grow near the i-n interface at the transition to μc-Si:H. The highest V_{oc} that can be obtained by varying the H_2 dilution for a given pressure increases with pressure (emphasized with larger symbols in Fig. 6.8a). This can be partially explained by the increased bandgap of the corresponding layers as shown in Fig. 6.4a. In addition, the decreased ion bombardment of the underlying p- and buffer layers at the beginning of the i-layer deposition could create fewer defects at the p-i interface.

In Fig. 6.8c we see that the increased bandgap with dilution leads to a decreased current due to less absorption of low-energy photons, consistent with Fig. 6.4a and 6.8a. At very high dilutions, where crystallites start to grow near the i-n interface, the current drops quickly due to poor collection of charge carriers that are excited in the crystalline phase (too high barrier for holes at the crystalline/amorphous interface). However, these charge carriers generated

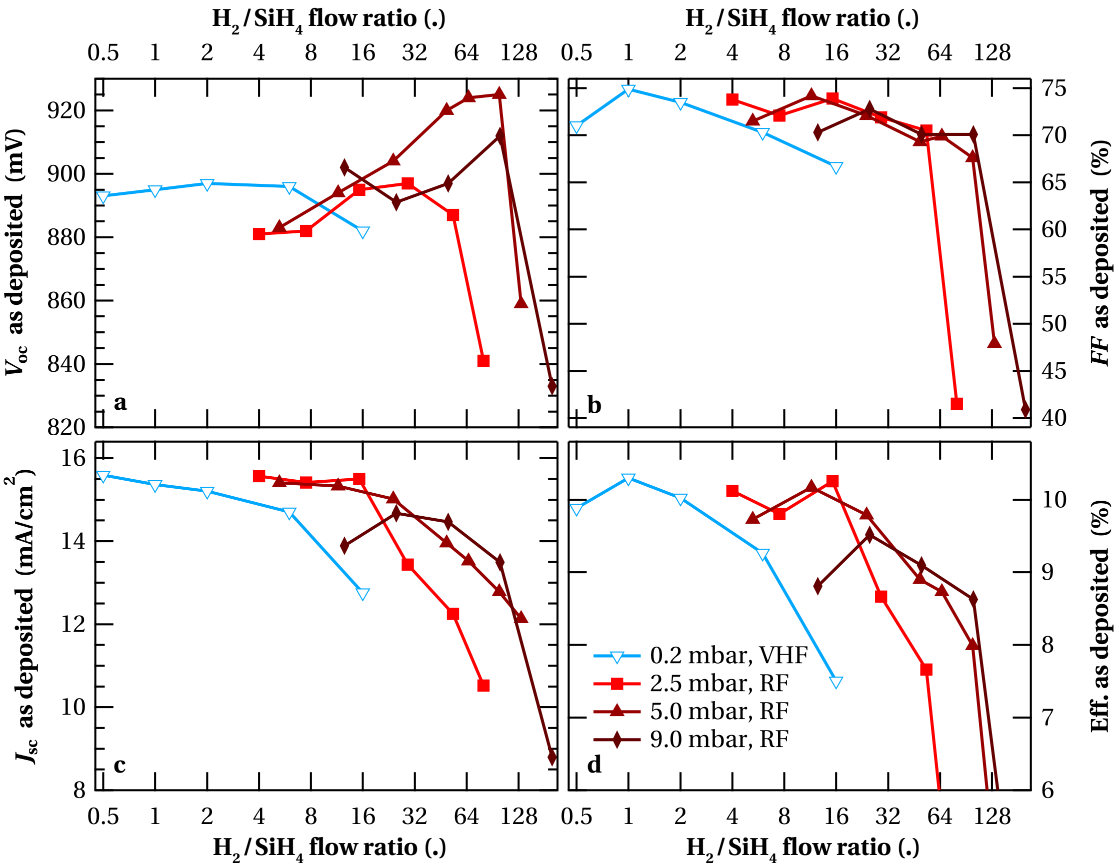

Figure 6.7: Performance of *a*-Si:H solar cells with a 220-nm-thick absorber layer, sandwiched between two wide-bandgap intrinsic *a*-Si:H layers at the *p*-*i* and the *i*-*n* interfaces to reduce their influence and compare the properties of different bulk absorbers. All absorber layers were deposited at 200 °C.

from photons at wavelengths above 800 nm are collected in *EQE* measurements under reverse bias voltage.

For the combination of very low H_2 dilutions and high pressures, the current is lower than expected from the bandgap of the absorber layers. The difference between *EQE* measurements performed under −1 V bias voltage (EQE(−1 V)) and without bias voltage (EQE(0 V)) shows that in these cases there is a large collection problem over the entire absorption spectrum but it is accentuated for blue light. Further, visual inspection of the corresponding layers and substrate holders showed powder deposition. These two observations support the hypothesis that *a*-Si:H deposited under these conditions contains many defects and is porous. The poor material quality resulting from high-pressure and low-H_2-dilution depositions affects the *FF* even more than the J_{sc} as we see to the left of the maximum (for low H_2 dilutions) in Fig. 6.8b. This is in full agreement with plasma considerations in chapter 5 and layer property measurements—particularly of R^*—in section 6.3.2.

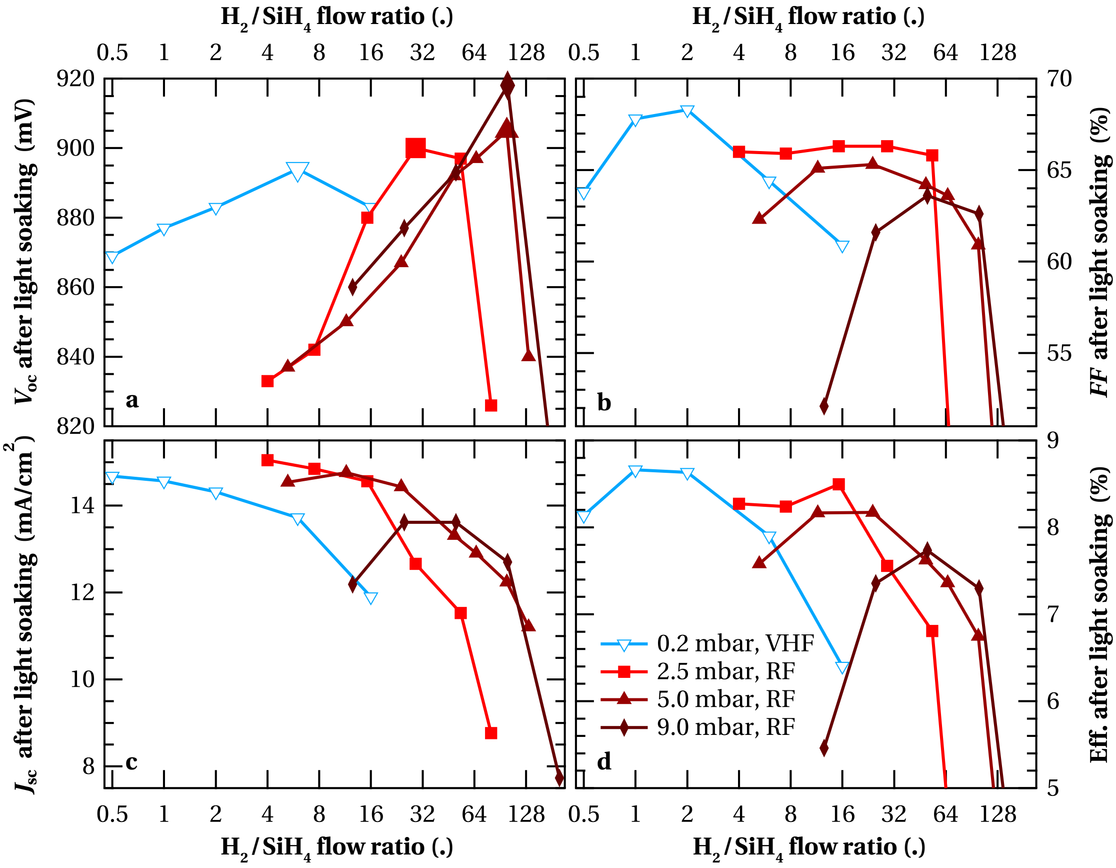

Figure 6.8: Performance of the *a*-Si:H solar cells whose initial state is shown in Fig. 6.7, after 1000 h of light soaking under AM1.5g light (1000 $\frac{W}{m^2}$) at 50 °C.

Note another aspect: The maximum *FF* obtained for a given series decreases with increasing pressure. This is in agreement with a generally lower current for high pressures that can not be justified by the bandgap; both effects can be seen already in the initial state (cf. Fig. 6.8b–c). Indeed, a comparison of the quantum efficiency with and without bias voltage reveals that there is a charge-collection problem that is wavelength independent, i.e. the relative difference between EQE(−1 V) and EQE(0 V) is constant for high-pressure depositions. However, the absorber material quality of the best cells deposited at 9.0 mbar does not seem to be worse than at lower pressures, as the relative LID is similar (see the discussion in section 6.4.3).

So, why does the maximum *FF* decrease with increasing pressure? The underlying reason is not clear, but we note that it is not necessarily linked to the intrinsic bulk properties since the doped and buffer layers were developed for bulk absorbers deposited at low pressure. Consequently, there may be a bandgap mismatch, a difference in the amount of hydrogen incorporated at the *p*-*i* interface, *p*-layer etching, or other interface problems that reduce the charge collection. We were able to confirm this by inserting the best-performing absorber layers of each pressure regime into cells with other doped layers; the initial *FF* was very close and relative degradation was similar.

Figure 6.8d shows the conversion efficiencies of the solar cells calculated from the V_{oc}, J_{sc}, and FF values shown in Fig. 6.8a–c. It shows the trade-off between high voltage (wide-bandgap absorber), high current (narrow-bandgap absorber), and high FF (good charge collection). As the FF varies most for the different deposition conditions, trends in efficiency mainly reflect trends in FF, which turns out to be the most crucial parameter when optimizing solar cell efficiency after light soaking.

In contrast to United Solar Systems Corp.'s and LG's successful industrial production of top cells for n-i-p and p-i-n triple-junction solar cells with wide-bandgap absorber layers and good charge collection [Yan 03a, Kim 13b], it is questionable whether wide-bandgap absorber materials are well suited for high-efficiency single-junction or tandem solar cells with *a*-Si:H top-cell absorber layers: in these cases, the current that is needed in the *a*-Si:H cell for a high-efficiency solar cell cannot be obtained with a wide-bandgap absorber layer, as an increase of $V_{oc} \times FF$ can never compensate for the lower current. For top cells in triple-junctions, it is not clear whether a wide-bandgap top cell (higher $V_{oc} \times FF$ but lower current and thicker; hence stronger LID) or a narrow-bandgap top cell (lower $V_{oc} \times FF$ but higher current; can be made thinner and hence lower LID) gives better performance. This depends on the quality of each layer and on the roughness of the used substrate (see the discussion in section 6.4.5 and chapter 8).

Overall it is important to note that with increasing pressure, the process window within which high-efficency solar cells can be obtained gets smaller. Even H_2 dilutions that are not far from the transition from *a*-Si:H to *μc*-Si:H tend to lead to powdery plasmas and poor material quality.

Note that we did not optimize the doped layers for record efficiency, nor adapt them to different i-layer deposition conditions. Nevertheless, efficiencies above 7.5% were obtained for each processing pressure and the best cells reached a high efficiency of 8.7% with a FF of 68% after light soaking, without using anti-reflective coatings.

6.4.3 Relative light-induced degradation

Figure 6.9 shows the relative LID of the solar cell performance in terms of

$$\Delta X = \frac{X_{\text{after light soaking}} - X_{\text{before light soaking}}}{X_{\text{before light soaking}}} \tag{6.1}$$

with X equaling V_{oc}, FF, J_{sc}, or efficiency (d). Most trends observed in Fig. 6.8 are reproduced here, which reflects the fact that the i-layer quality governs the initial state less than the light-soaked state. Moreover, the FF is the parameter that dominates the efficiency after light soaking. We see that cells deposited under higher pressure degrade more, especially for low H_2 dilutions. For lower pressures, there is a wider range of dilutions that provides low-degradation cells than for higher pressures. However, at all pressures there is an optimum H_2 dilution for which the cells degrade only about 15%, which is remarkably low. These solar cell results are in agreement with the conclusions from our plasma and layer analysis.

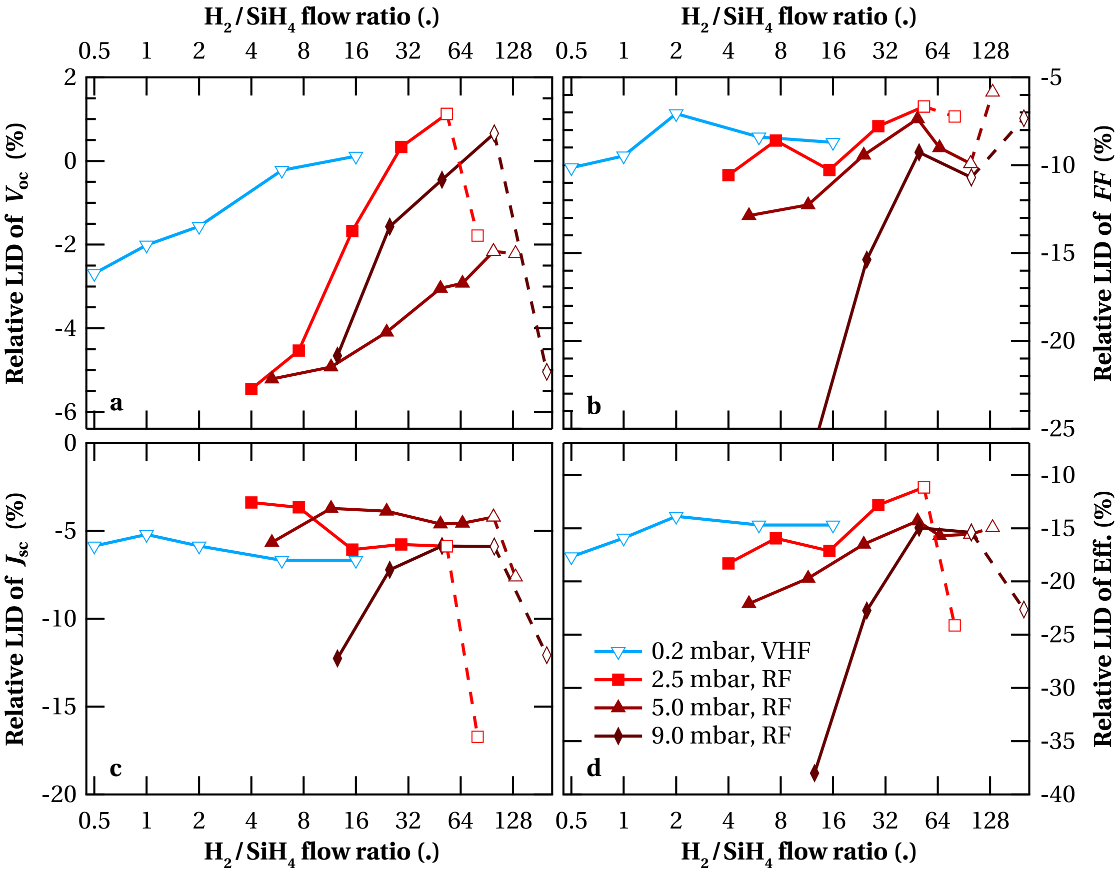

Figure 6.9: Relative light-induced degradation of the solar cell performance for the cells with initial and degraded performance shown in Fig. 6.7 and 6.8, respectively. Open symbols indicate cells with a non-zero *μc*-Si:H fraction of the absorber layer and hence different degradation mechanisms.

Note that the V_{oc} of the solar cell dilutions series deposited at 5 mbar degrades more than one would expect from the other series deposited at lower and higher pressures. We attribute this effect to an experimental artifact: the 5-mbar series was deposited a few months later than the three other series; in between, we observed a drift of the *p*-layer stack deposition conditions that we tried to compensate for, but it seems that this compensation was not complete.

6.4.4 Correlation between *R** and light-induced degradation

We have correlated the microstructure factor R^* with deposition conditions in section 6.3.2, and we have correlated the LID of solar cells with the deposition conditions of their absorber layers. In both cases, we were able to explain the correlations by different material properties based on the plasma conditions during growth. Figure 6.10 directly correlates R^* of the absorber layers with the LID of the solar cells with these absorber layers incorporated. The relative *FF* degradation depends more than other solar cell parameters on the charge-collection changes of the absorber layer, hence on its defect concentration and microstructure.

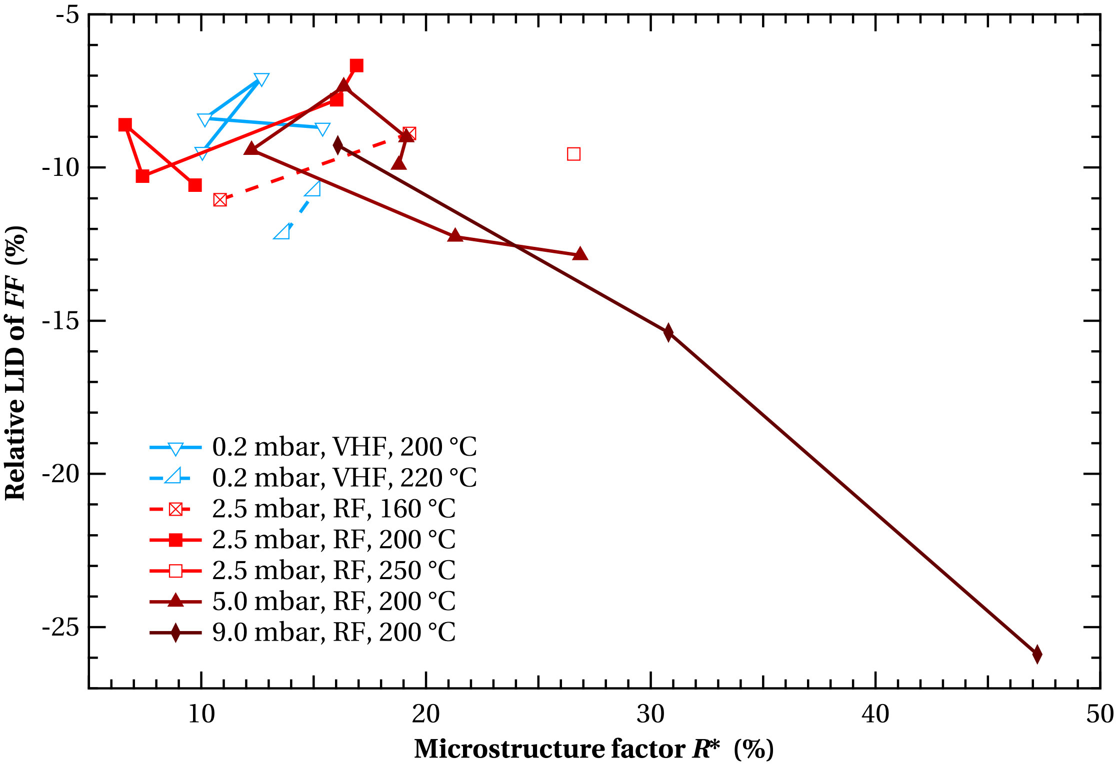

Figure 6.10: Microstructure factor R^* measured on layers deposited on glass, correlated with the relative LID of the FF of solar cells with these layers incorporated as absorbers between two buffer layers at the p-i and i-n interfaces for H_2 dilution series at different pressures, frequencies and temperatures. Lines connect H_2 dilution series with all other deposition parameters kept constant.

Therefore, we chose the relative LID of FF for the correlation with R^*. For this correlation we considered all pairs of layers and solar cells of the series with the deposition conditions given in Tab. 6.1 but excluded pairs where we measured non-zero Raman crystallinity in the solar cells as different degradation mechanisms can dominate there. Further, we included (layer, cell) pairs deposited at different temperatures but with the same solar cell design and deposition parameters as the other pairs; the deposition conditions of the H_2 dilution series are given in the legend of Fig. 6.10.

We note a general correlation between the relative LID of the FF and R^*: cells with an enhanced microstructure factor of the corresponding absorber layer tend to degrade more. For all well-performing layers in solar cells, R^* was below 20%, in agreement with [Kroll 98]. However, this correlation shows a large scattering that is well above experimental uncertainty: well-performing layers in cells showed R^* values over a wide range. Particularly at low pressures, R^* depends only weakly on the H_2 dilution up to the transition to μc-Si:H growth. In contrast, it strongly depends on the H_2 dilution for higher pressures which can be attributed to the powdery deposition conditions that result in larger voids and more SiH_n bonds with $n \geq 2$ [Smets 07b], leading to strong LID.

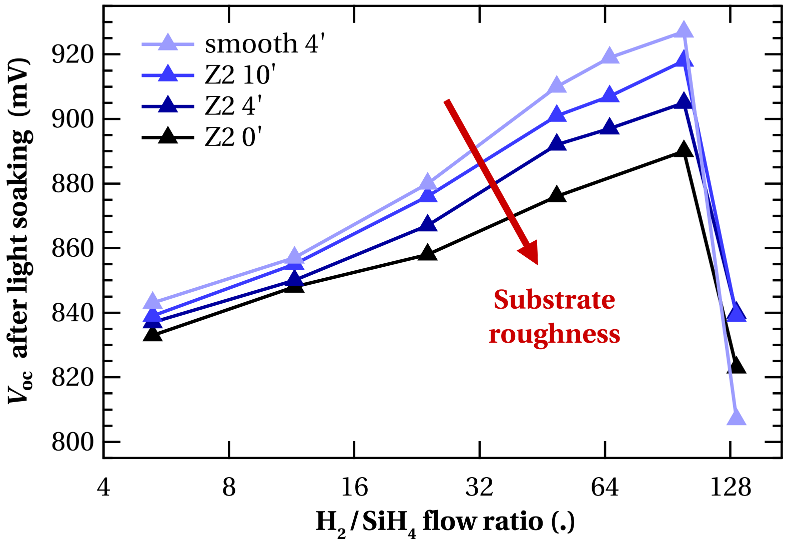

Figure 6.11: Open-circuit voltage after light soaking for a H_2 dilution series of solar cells co-deposited on four substrates with different roughnesses.

Concluding the significance of R^*, we can state that it correlates with LID of solar cells on a large scale but is not sensitive enough for solar cell development: to study LID in solar cells, solar cells are the better measurement instrument to assess the absorber layer quality.

6.4.5 Substrate dependence of hydrogenated amorphous silicon solar cells

Until now, the substrate dependence of solar cell performance was not addressed because the discussed trends were observed for all substrates. Nevertheless, solar cell performance, and in particular V_{oc}, can strongly depend on the substrate roughness. In Fig. 6.11, V_{oc} is shown for cells co-deposited on four different substrates for the H_2 dilution series deposited at 5.0 mbar, RF. For all other H_2 dilution series (alternating pressure, frequency, and temperature), the same trends were observed.

For low H_2 dilutions, V_{oc} decreases only slightly with increasing roughness. At least two mechanisms can lead to this substrate dependence: First, the surface area of a rough substrate is larger than that of a smooth substrate, leading to thinner doped layers. Second, non-conformal or even non-homogeneous deposition on a rough substrate leads to a higher probability that the front and back electrode may be nearly touching or may be poorly covered by the doped and intrinsic layers. This can introduce weak diodes (parallel to the standard diode in an equivalent electronic circuit) that lower V_{oc} on rough substrates similar to porous zones in amorphous [Sakai 90] and microcrystalline [Python 08] silicon solar cells.

Higher H_2 dilution increases the substrate dependence of V_{oc} dramatically from about 10 to 40 mV, and this cannot be explained in the same manner. To understand this substrate dependence, two solar cells were deposited right at the transition from *a*-Si:H (close to the *p*-*i*

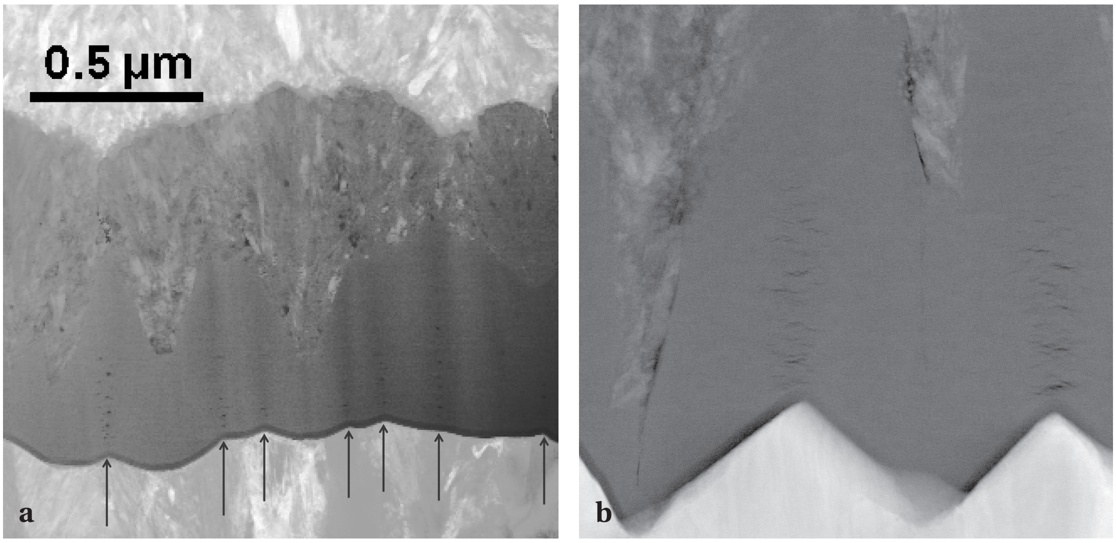

Figure 6.12: Scanning transmission electron microscope images (STEM) of a 1-µm-thick solar cell with an *i*-layer deposited at the transition from *a*-Si:H to *µc*-Si:H. (a): Overview of the cell cross section with arrows indicating peaks of the ZnO substrate, above which chains of voids are located that are magnified in (b). These images were taken by D. Alexander (a) and M. Duchamp (b).

interface) to *µc*-Si:H (close to *i*-*n* interface). The only difference between the cells was the *i*-layer thickness. Because of the thickness dependence of crystallinity close to the transition, the *i*-layer was purely amorphous for the thinner cell (providing 950 mV V_{oc} after light soaking) but grew microcrystalline after a few hundred nanometers in the 1-µm-thick solar cell. A transmission electron microscope (TEM) image of the thick cell is shown in Fig. 6.12a. It reveals substrate-dependent porous zones, seen as chains of voids located above peaks of the underlying ZnO texture and highlighted by arrows in the figure. These zones could create weak diodes similar to porous zones in *µc*-Si:H and thus decrease V_{oc}. (Note that in *µc*-Si:H porous zones are located above ZnO valleys.) Figure 6.12b shows a magnification of such porous zones. While the porous zones evolve in the growth direction (vertical), the expansion of single voids is parallel to that, making them to appear as platelets. Further investigations of these zones are ongoing.

While the increased dependence on substrate roughness for high H_2 dilutions is less an issue for triple junctions, where one can use wide-bandgap *a*-Si:H materials together with smoother substrates, better light trapping, and hence rougher substrates, are necessary for single-junction or micromorph tandem devices.

However, on rougher substrates, the bandgap increase (compared to lower H_2 dilutions) is not fully reflected in the V_{oc}. The slightly increased V_{oc} does not compensate for the lower current, and thus wide-bandgap materials deposited at high dilution are not optimal for *a*-Si:H single-junction or micromorph tandem devices.

6.5 Conclusions

Using VHF and RF PECVD, intrinsic *a*-Si:H layers were deposited in a single deposition system varying the H_2 dilution, pressure, temperature and power, covering low-pressure VHF *a*-Si:H, *pc*-Si:H, *pm*-Si:H, and high-pressure RF *a*-Si:H materials. This allowed for the first time a direct comparison of the optical properties of these materials and the performance of solar cells using them as absorber layers. A consistent picture of the deposition parameter space for *a*-Si:H solar cell deposition evolved from plasma to layer and solar cell performance. This allows us to judge which absorber material best suits the needs for a given application.[2]

While optimum H_2 dilutions leading to relative LID below 15% were identified for all process pressures, the process windows leading to such results narrow for increasing deposition pressure due to powdery plasmas at low dilutions. The best cells reach post-light-soaking efficiencies of 8.7% and FF of 68% without an anti-reflective coating.

Light-induced degradation was shown to correlate with the microstructure factor R^*, which has a sharp minimum for high pressures but which exhibits limited dependence on the H_2 dilution for lower pressures. Although R^* is not as sensitive as direct measurement of the LID of solar cells, it can distinguish layers that will show poor performance in solar cells ($R^* > 20\%$) from layers that have the potential to perform well as absorber layers.

While the same trends were observed for cells co-deposited on four substrates with different roughnesses, the sensitivity of the cells changed considerably with the substrate roughness. In particular, the substrate dependence of V_{oc} increases dramatically from about 10 to 40 mV from low to high H_2 dilutions (narrow- to wide-bandgap material). In STEM images of solar cells with very wide-bandgap absorber layers, deposited right at the transition between amorphous and microcrystalline silicon, chains of small voids or porous zones were identified above peaks of the underlying ZnO. On rough substrates, these zones may create weak diodes that lead to a decrease of V_{oc} and limit the use of wide-bandgap materials to rather smooth substrates.

Further insight into the microstructure of *a*-Si:H materials can be expected from systematic comparison of FTIR and ellipsometry data (e.g. using the approach suggested in [Kageyama 11, Kageyama 12]), and combining them with data from electron paramagnetic resonance (EPR) experiments such as in [Fehr 14] as well as from advanced TEM methods as suggested in [Voyles 03].

---

[2] For this study, we kept the absorber layer thickness constant (220 nm). The choice to fix the thickness had practical reasons and allowed for co-deposition on different substrates. However, it is discussable: to compare relative LID of devices, one can argue that the current density of each device should be the same, as a wide-bandgap absorber layer will always absorb less light, and hence degrade less. This is particularly important for the choice of an *a*-Si:H cell as a sub-cell in multi-junction solar cells, where a certain current is typically requested and it is not always easy to judge whether a thick wide-bandgap absorber or a thin narrow-bandgap absorber layer will perform better. However, such a constant-current approach would require a thickness series for each absorber layer and each substrate to determine the thickness corresponding to the fixed current, and thickness-dependent effects would bias this type of comparison.

7 Kinetics of light-induced degradation

We investigate the influence of the deposition parameters for intrinsic hydrogenated amorphous silicon (a-Si:H) absorber layers on light-induced degradation (LID) of thin-film silicon solar cells with respect to the degradation kinetics under accelerated light soaking.

The focus is on different absorber layers with varying bandgaps and defect densities, incorporated into high-efficiency single-junction solar cells, while keeping the rest of the solar cell structure as constant as possible. This experimental comparison not only helps us to relate the deposition conditions with LID, but also allows us, in combination with the results of previous chapters, to determine which absorber material is best suited for a given application.

We find that the kinetics depends, in semi-logarithmic scale, only weakly on time but much more on deposition conditions. Within the investigated time, we do not observe a stabilization of the solar cells.

This chapter is organized as follows: After a short introduction in section 7.1 and detailing the experimental methods in section 7.2, we focus on the impact of selected deposition parameters on LID kinetics: we alternate the deposition temperature for wide-bandgap absorber layers (section 7.3), the thickness of narrow-bandgap absorber layers (section 7.4), the H_2/SiH_4 flow ratio during absorber layer deposition (section 7.5), and the deposition rate of the absorber layer via plasma power (7.6). Finally, we compare solar cells with polymorphous (pm-Si:H) and a-Si:H buffer and absorber layers in section 7.7 and conclude this chapter in section 7.8. Measurements of the LID kinetics for solar cells with alternating thickness of the boron-doped hydrogenated amorphous silicon carbide (p-(a-SiC:H)) layer are presented in section 8.3.4.

The main results of this chapter were accepted for publication in Progress in Photovoltaics [Stuckelberger 14b].

7.1 Introduction

Nearly 40 years after the discovery of LID of *a*-Si:H and its partial reversibility by thermal annealing, this so-called Staebler-Wronski effect (SWE) [Staebler 77] is still not fully understood, although several models exist for its explanation [Shimizu 04, Zhang 01, Smets 03, Smets 10]; of particular importance are the "weak-bond model" [Stutzmann 85], the "H-collision model" [Branz 99], and Smets' model with divacancies playing an important role [Smets 10].

To understand the processes of light-induced defect generation and thermal annealing, studies of LID kinetics were typically conducted on layers, and M. Stutzmann et al. found experimentally (based on electron spin resonance (ESR) measurements of the neutral dangling bonds) in agreement with the "weak-bond model" [Stutzmann 84] the dependence of the dangling bond concentration N_{db}

$$N_{\text{db}}(t) \propto G^{\frac{2}{3}} \cdot t^{\frac{1}{3}} \tag{7.1}$$

on the time t and on the electron–hole pair generation rate G. (After correction for initial dangling bonds, Deng et al. found rather $N_{\text{db}}(t) \propto G \cdot t^{\frac{1}{2}}$ for protocrystalline silicon [Deng 06]).

A saturation of N_{db} was found at an equilibrium dangling bond concentration $N_{\text{db}}^{\text{eq}} \propto G^{\frac{1}{3}}$. This justifies the terminology of "stabilized defect concentration" if the equilibrium state is reached after light soaking. However, in solar cells we typically observe continuing degradation during the usual tests of 1000 h under one-sun-equivalent light soaking or 24 h under three-sun-equivalent light soaking; the degradation is approximately linear in semi-logarithmic scale as will be shown in the following sections. Due to the ongoing LID, we avoid the term "stabilized" to describe solar cell performance after light soaking.

The correlation between N_{db} and the fill factor (FF) or other parameters measured directly on solar cells is not direct. Therefore, we propose that a correlation of experimental solar cell degradation kinetics data with a defect-generation model is not appropriate.

7.2 Experimental

7.2.1 Solar cell design

All solar cells presented in this study were made in the *p*-*i*-*n* configuration (superstrate) on ZnO:B grown by low-pressure chemical vapor deposition (LPCVD) as the front electrode. We treated these substrates partially with an Ar plasma to smoothen the surface texture [Python 08].

As the back electrode, 2.3-µm-thick LPCVD ZnO:B was used for all cells except those presented in section 7.7, where metallic back electrodes were used.

The silicon layers of the solar cells described in section 7.3 were grown by plasma-enhanced chemical vapor deposition (PECVD) in a two-chamber system built in-house (system B). The solar cells described in sections 7.4 to 7.6 were grown by PECVD in a cluster tool (Octopus I) with dedicated chambers for p-type, n-type, and intrinsic layers.

The p-i-n junctions include p- and n-type microcrystalline silicon oxide layers, p-(μc-SiO:H) and n-(μc-SiO:H), in direct contact with the front and back ZnO for good electrical contact, transparency, and shunt quenching [Cuony 10, Despeisse 10a]. At the p-i interface, we used a p-(a-SiC:H) layer, and as intrinsic buffer layers either an intrinsic hydrogenated amorphous silicon oxide layer, a-SiO:H, [Bugnon 14] (i-layer thickness series in section 7.4 and power series in section 7.6), a hydrogenated amorphous silicon carbide layer, a-SiC:H (temperature series in section 7.3), or a layer without other precursor gases than H_2 and SiH_4 (H_2 dilution series in section 7.5). As we kept the buffer layer as well as the doped layers the same within a series, we do not expect a significant influence of them on the reported trends. Further, the comparison of oxygenated and carbonated buffer layers revealed no significant difference in light soaking between cells with small flows of CO_2 and CH_4 as compared to SiH_4 and H_2. After the absorber layer, we deposited a phosphorus-doped hydrogenated amorphous silicon layer, n-(a-Si:H), at the i-n interface.

Except for the i-layer thickness series in section 7.4, the i-layers were always 220 nm thick (i-layer thicknesses are given as nominal thicknesses on flat substrates). As precursor gases for the intrinsic a-Si:H absorber layers, only SiH_4 and H_2 were used.

Finally, solar cells were defined by a combination of wet and dry etching. The size is typically 0.25 cm^2 unless specified otherwise. Further details on the solar cell processing and tools are given in sections 2.1 and 2.2.

7.2.2 Measurements

Details on the standard characterization (current–voltage ($I(V)$) characteristics and external quantum efficiency (EQE) measurements) are given in section 2.4.

For in-situ measurement of the LID kinetics, the solar cells were contacted by ultrasonic soldering, with one contact at the front and one at the back of the solar cell. After 10 cm, the two wires were split into two, continuing with a four-wire measurement. A comparison with a proper four-point probe measurement (soldering two wires on the front and two on the back) revealed no significant difference. A photograph of solar cells used for kinetics measurements is shown in Fig. 2.1d. The solar cells were attached to the cooled sample holder with a 1-mm-thick soft thermal conductive pad (TG-2030 from T-Global [t-global 14]) that fulfilled four functions: (a) it provided thermal conductivity with the sample holder for cooling, (b) it served as the back reflector, (c) it compensated for height differences from the soldering, and (d) it electrically isolated the contacts of the solar cells.

These degradation kinetics measurements were performed at three-sun-equivalent illumination for about 24 h at 50 °C, for which a dedicated solar simulator fully based on light-emitting diodes (LEDs) and built by the author, was used. It is described in detail in chapter 3 and [Stuckelberger 14c].

Solar cell series were always light soaked simultaneously for a fair comparison. Therefore, experimental issues like temperature instability of the environment that induced instabilities in LED illumination (seen e.g. as instabilities of current-voltage ($I(V)$) curve measurements) were the same for all solar cells shown in the same graph. To check reproducibility, we always tracked the performance of three to four cells on the same substrate. In Figure 7.7, we show the results of several cells per substrate, but everywhere else only one, which is typical for the sake of clarity. Dots present single measurements; lines are smoothed.

7.3 Wide bandgap for high voltages

Recently, a-Si:H solar cells with a wide-bandgap absorber layer were used as top cells in quadruple-junction solar cells [Schüttauf 14b], and are regularly used as top cells in triple-junction solar cells [Yan 12, Schüttauf 14a], which currently hold the world record for thin-film silicon solar cell technology [Green 14, Kim 13b].

For such applications, we developed wide-bandgap a-Si:H materials by increasing the H_2 dilution close to the transition to microcrystalline silicon and slightly lowering the deposition temperature. Incorporating this material as an absorber layer in solar cells that were optimized for narrower-bandgap absorbers provides already an open-circuit voltage (V_{oc}) above 1 V with $FF = 71\%$ on smooth substrates (measured under standard conditions). Further details on these solar cells are given in section 9.1.

In addition to H_2 dilution, on which we focus in section 7.5, the deposition temperature has a major impact on the bandgap. Therefore, we investigated the degradation kinetics of solar cells for which the deposition temperature was varied from 140 to 200 °C. In this series, the temperature was kept the same for all layers of the stack, including the doped layers. Different from the variation of the absorber layer deposition conditions in the remainder of this thesis, this has the advantage that hydrogen effusion from the absorber layer (accompanied by the bandgap reduction) during the deposition of subsequent layers at higher temperatures should not be an issue, and the bandgap mismatch between the doped layers and the absorber layer is kept small, as the bandgap changes of doped and intrinsic layers with temperature show the same trends. However, it means that differences between solar cells cannot simply be ascribed to absorber layer effects.

Figure 7.1c shows the V_{oc} degradation kinetics of this series during light soaking at three-sun-equivalent illumination and 50 °C. The solar cell whose $I(V)$ characteristics are shown in Fig. 9.7 was co-deposited at 180 °C with the cells presented here, but on a flatter substrate. Due to issues with ultrasonic soldering on smooth substrates, we show in this analysis cells co-deposited on a rougher substrate type.

As expected, the V_{oc} increases with decreasing deposition temperature due to wider bandgaps. However, the V_{oc} of the cells deposited at very low temperatures decreases again, not because

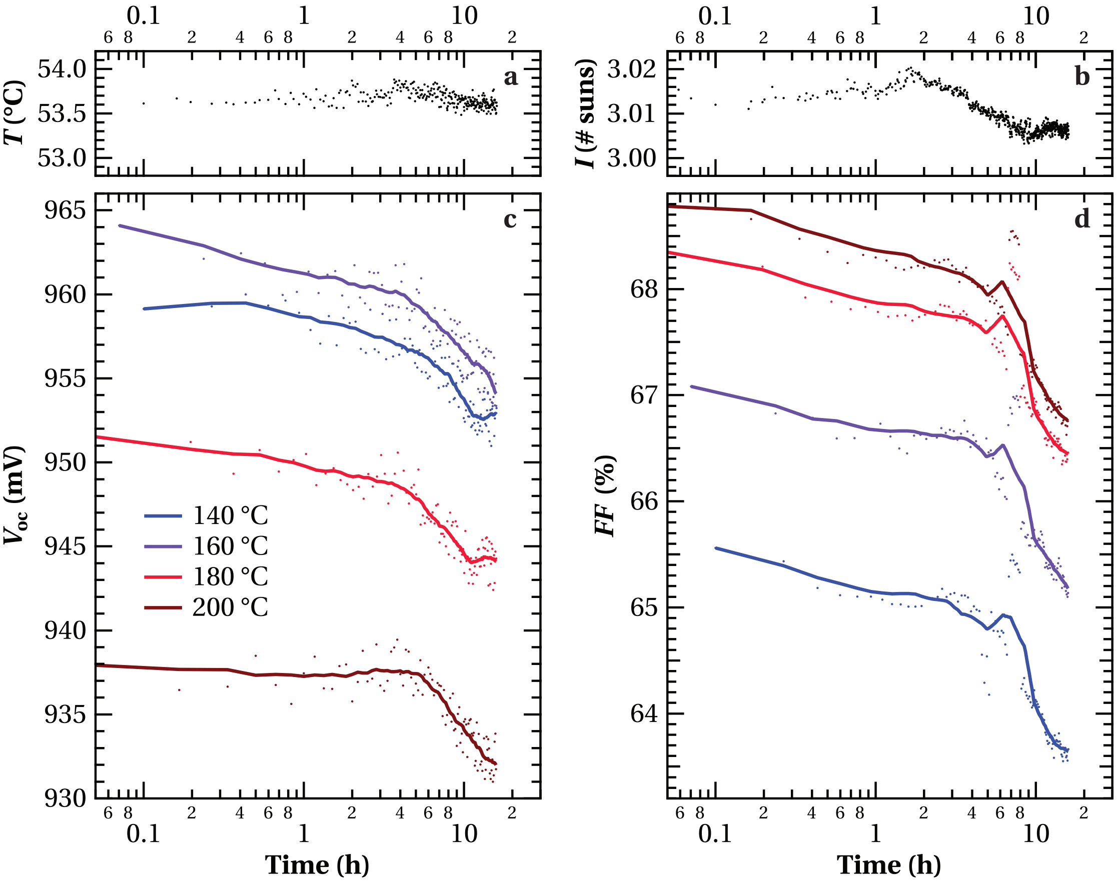

Figure 7.1: Degradation kinetics of open-circuit voltage (c) and fill factor (d) during light soaking under three-sun-equivalent illumination at 50 °C for solar cells deposited at different temperatures, with the light intensity (a) and substrate temperature (b) during light soaking.

of the bandgap but because of a higher defect concentration which is also reflected in significantly lower FF as shown in Fig. 7.1d.

Both V_{oc} and FF show two regions with different slopes in logarithmic scale with a change after a few hours, which could indicate two distinct degradation mechanisms as concluded elsewhere [Fischer 13], where "fast" degradation in the beginning was attributed to nanosized voids, and later "slow" degradation to metastable defects. In contrast, here we observe slow degradation in the beginning and fast degradation afterwards, both in V_{oc} and FF. Figures 7.1a and b show the light intensity and substrate temperature during light soaking. The light intensity curve seems to be correlated with the V_{oc} and FF curves and one could attribute the change of slopes to a measurement effect of instable light intensity. However, the change in the light intensity slope takes place at least two hours before the V_{oc} and FF slope changes. Further, it is questionable whether such small variations of half a percent in intensity can cause such changes in solar cell performance (note the logarithmic dependence of V_{oc} on light intensity). At this point, we do not know the reason for the change in slope but will investigate it further.

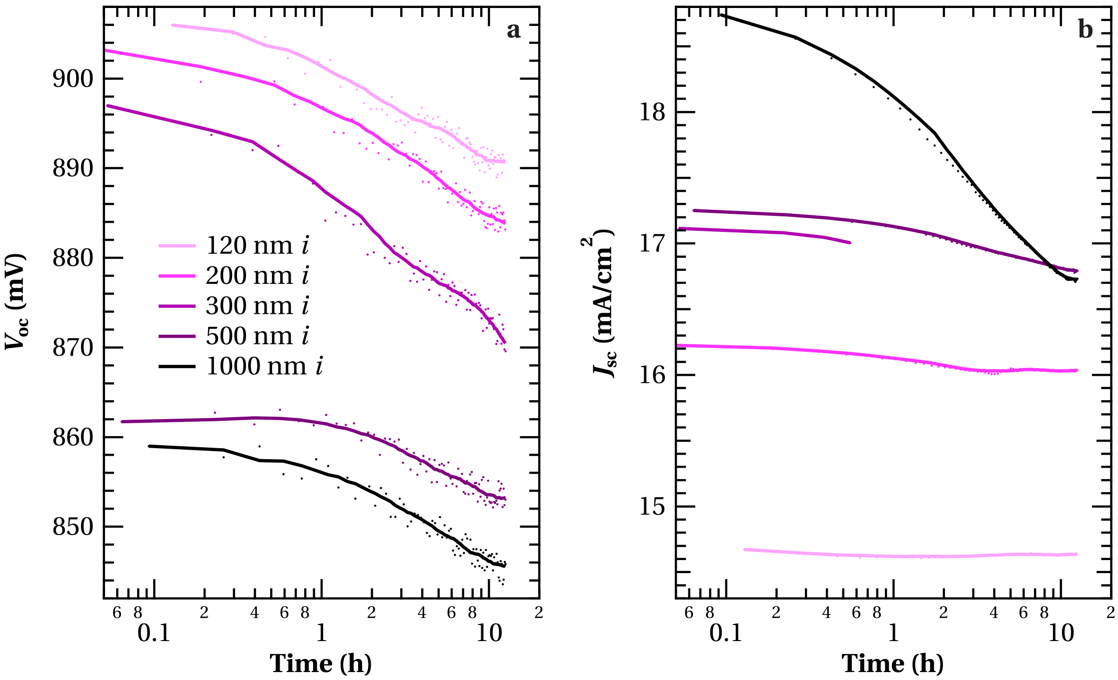

Figure 7.2: Open-circuit voltage (a) and short-circuit current density (b, normalized to the initial measurements under standard conditions) of a solar cells series with narrow-bandgap absorber layers of different thickness, during light soaking.

7.4 Narrow bandgap for high currents

We have developed narrow-bandgap *a*-Si:H materials for application as the absorber layer in the top cell in micromorph tandem solar cells. In this section, we present a thickness series of this material from 120 to 1000 nm, deposited at 230 °C at radio frequency (RF), included in single-junction *a*-Si:H solar cells. Further details on these solar cells are given in section 9.1.

Such narrow-bandgap materials are of great importance for high current densities and efficiencies in micromorph tandem solar cells [Meillaud 12]—the stronger LID as compared to materials with a wider bandgap is in this case compensated for by the higher current, which allows bottom-limited devices.

Figure 7.2 shows the degradation kinetics of solar cells with different thicknesses of the narrow-bandgap absorber layer, in terms of V_{oc} and short-circuit current density (J_{sc}). The current densities were measured during light soaking by $I(V)$ measurements and normalized to the initial currents as determined under standard conditions by EQE measurements; the current results for the cell with a 300-nm-thick absorber layer are not shown for the full light soaking time because this substrate detached progressively during light soaking from the cooling unit and heated up, and therefore the current increased stepwise (cf. Fig. 7.6).

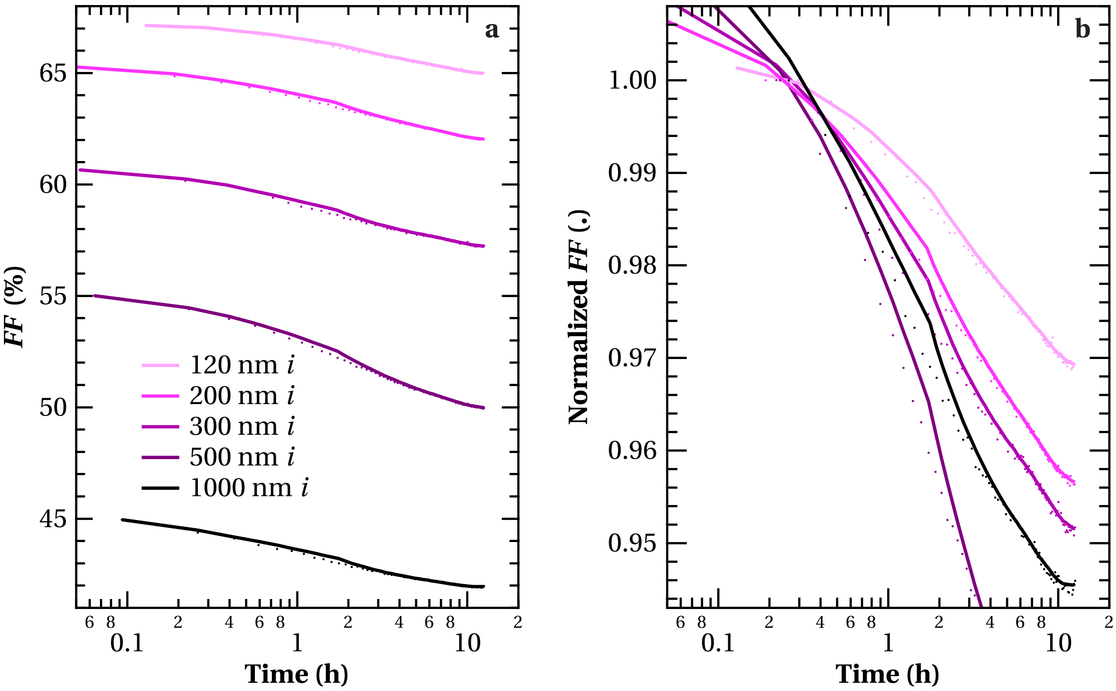

Figure 7.3: Fill factor in absolute terms (a) and normalized to the second measurement (b) of the solar cells presented in Fig. 7.2, during light soaking.

Comparing the absolute V_{oc} values, we note that they are lower for thicker substrates due to enhanced recombination. However, the thickness dependence only spans about 50 mV for cells whose absorber thicknesses vary by nearly a factor of 10. For the V_{oc}, the degradation slope is comparable for all i-layer thicknesses; this is not the case for the current, where the more strongly pronounced i-layer degradation for thick cells is seen as an enhanced recombination, and hence, lower collected current. This effect is strong enough to lower the current density of the cell with a 1000-nm-thick absorber layer by more than 2 $\frac{\text{mA}}{\text{cm}^2}$ such that the current density after light soaking is even lower than for cells with a thinner absorber layer.

We note the stronger degradation of thicker layers also in the FF shown in Fig. 7.3: generally, solar cells with a thick absorber layer suffer from poor charge collection, manifested by a lower FF (see Fig. 7.3a). The spread of the initial FF is larger under three-sun-equivalent illumination than for the standard measurement conditions. One reason is that the current is about three times larger than under one-sun illumination. Front and back electrodes were optimized for one-sun illumination and thin absorber layers. Hence, the FF is significantly limited by series resistance which is more pronounced for thicker cells and higher illumination.

Thick absorber layers degrade more as shown in Fig. 7.3b by the relative FF: thicker i-layers lead to a reduction of the charge collection due to a lower electric field that is given in first approximation by the built-in voltage (V_{bi}) divided by the i-layer thickness. Enhanced defect concentration and recombination due to degradation further reduce the electric field in the bulk, which is more detrimental for thicker i-layers. This is confirmed and discussed in more detail with the i-layer thickness series presented in section 4.5 and in [Stuckelberger 10, Stuckelberger 12]. The solar cells with a 500-nm-thick absorber layer show even stronger degradation than cells with a 1000-nm-thick absorber layer; in the former case, a plasma problem occurred during buffer layer deposition, which probably caused the unusually strong degradation.

7.5 The role of the hydrogen dilution

In this section, we look at the degradation kinetics of a H_2 dilution series that was deposited using the same cell design as the solar cells presented in chapter 6 (only drifts of deposition parameters were corrected), using an intermediate pressure of 1 mbar, an excitation frequency of 40.68 MHz, and 12 W power.

Figure 7.4 shows the LID kinetics of the V_{oc} and FF for these solar cells. As discussed in section 6.4, the initial V_{oc} increases with the H_2 dilution until it drops when passing the transition to microcrystalline deposition conditions; in this series, the transition takes place between dilutions 32 and 64. For the FF, different effects are visible:

First, the cells with an absorber layer deposited with dilution 64 suffered from "S-shaped" $I(V)$ curves due to the bi-phase material, leading to FF below 50 %, not shown in the graph.

Second, the slope of the FF degradation is steepest for the lowest dilution and flattest for dilution 32. This is due to the higher defect concentration in low-dilution absorber materials leading to enhanced recombination, hence stronger LID due to the SWE.

Third, the initial FF is the highest for low H_2 dilutions (74 % measured under standard conditions). A high FF in the initial state for low H_2 dilutions is not unusual, as defect states in the absorber layer are typically not yet limiting. Why the initial FF at higher dilutions are lower in that case is not completely clear. We suppose that the bandgaps of the doped layers are not adapted for these high dilutions, or that the bombardment of a strongly hydrogenated plasma has negative effects on the underlying buffer and p-layers. Using other doped layers, the FF with high-dilution i-layers can be easily as high as with low-dilution i-layers.

Note also the relative degradation trends that are the same as for other dilution series reported in section 6.4.3: with higher dilution (fewer defects), the V_{oc} is not only higher in the initial state but also degrades less. This supports the mechanisms of light-induced V_{oc} changes suggested in chapter 8 and is in agreement with the literature (see the discussion in section 8.5).

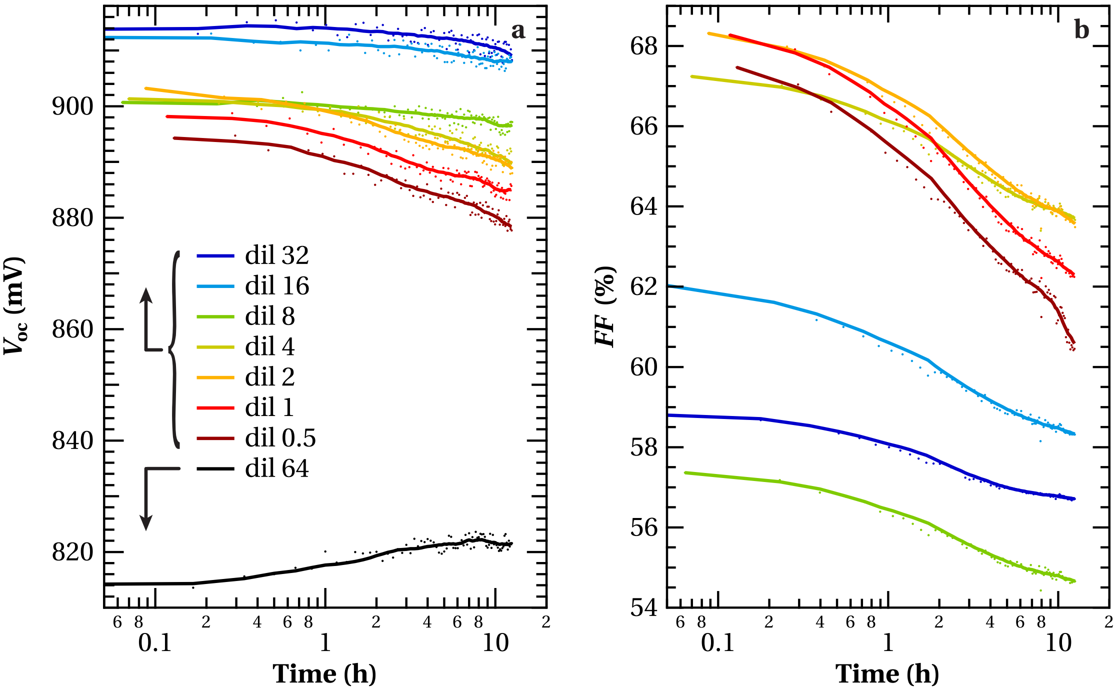

Figure 7.4: Light-induced change of the open-circuit voltage (a) and fill factor (b) of a solar cell series with absorber layers for which the H_2/SiH_4 ratio was increased from 0.5 to 64.

7.6 The role of the deposition rate

In this section, we investigate the role of the deposition rate on the LID. The deposition rate is most directly influenced by the plasma power—at least for the chosen deposition conditions, the impact of plasma power on other parameters such as bandgap is minor—and the relationship is linear within the investigated range [Stuckelberger 13, Matsuda 98].

In Fig. 7.5, we compare the V_{oc} of two power series, where we varied the plasma power of the absorber layer from 4 to 80 W at two frequencies, which corresponds to deposition times of about 25 to 1.5 min for the 220-nm-thick absorber layers. The deposition regimes of these absorber layers are discussed in more detail in sections 5.4.1 (Fig. 5.8b) and 6.3 (Fig. 6.2b). The deposition pressure was 0.4 mbar for the depositions at 13.56 MHz. For 40.68 MHz, we chose 0.13 mbar. No H_2 dilution was used for the absorber layers; nevertheless, these plasma conditions—using low power and pressure—lead to high-efficiency solar cells with efficiencies well above 10% in the initial state.

High deposition rates lead to a high defect concentration in the absorber layers [Knights 79, Stutzmann 84, Stutzmann 85]. Hence, the V_{oc} should decrease with increasing power, which we see for both frequencies.

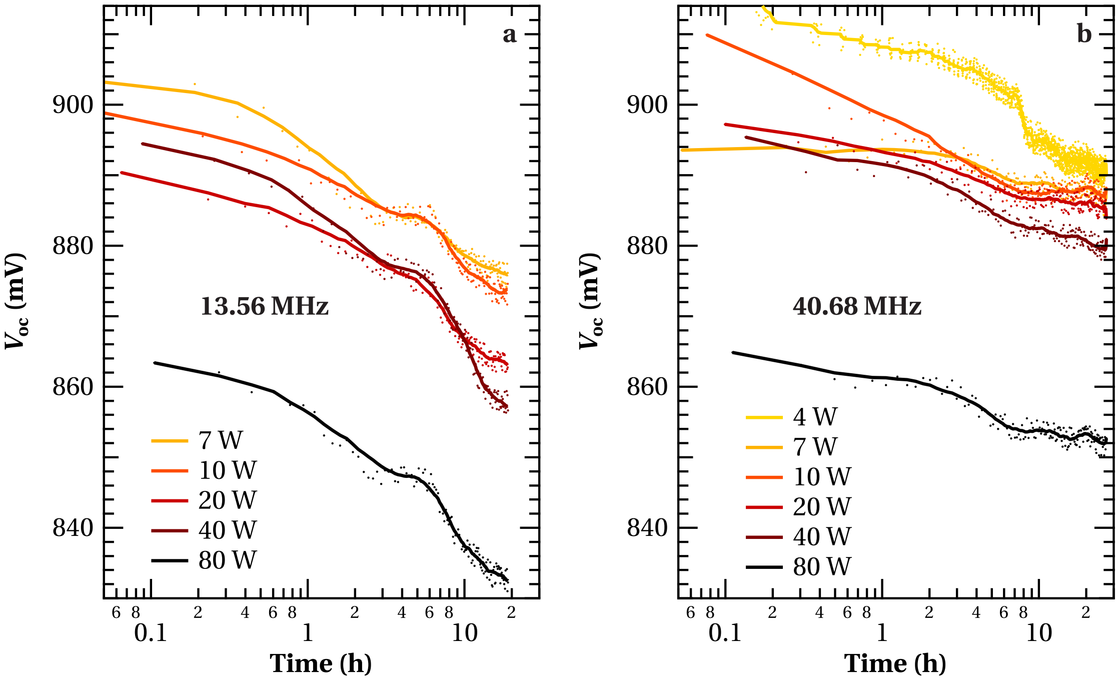

Figure 7.5: Light-induced change of the open-circuit voltage of cells with an absorber layer for which the deposition rate was varied via the power at 13.56 (a) and 40.68 MHz (b).

The degradation rate seems to be independent of the power, but we note a slightly lower degradation at higher frequency. This could be due to better material quality due to lower ion bombardment [Howling 92], but could also be a measurement effect (the cells of both frequencies were light soaked in batches one after the other).

Figure 7.6 shows the *FF* and J_{sc} normalized to the first measurement, for the cells shown in Fig. 7.5a. We see that the *FF* decreases more strongly with increasing power. However, the slope of the degradation separates into two groups: there is a threshold power between 20 and 40 W, below which LID is considerably weaker than above it.

Also the current degradation depends strongly on the deposition power, being stronger for high power. For the solar cells deposited at 7 and 10 W, one can see a stepwise increase of the current density (marked by arrows). We suspect that the substrates detached at this moment from the cooling unit and the solar cells heated up, which leads to higher currents.

In LID kinetics measurements reported in [Fischer 13], the authors observed for high-quality materials a single slope of the *FF* degradation as a function of time in semi-logarithmic scale, but an additional, stronger slope in the beginning of light soaking that they attributed to a different nanostructure, i.e. additional degradation due to void-related defects. As we varied the absorber-layer quality dramatically by increasing the power by a factor of 20, we expected to observe two distinct slopes in Fig. 7.6a. This is not the case. In particular, we cannot confirm a “fast degradation” first and a “slow degradation” later, with the former apparent

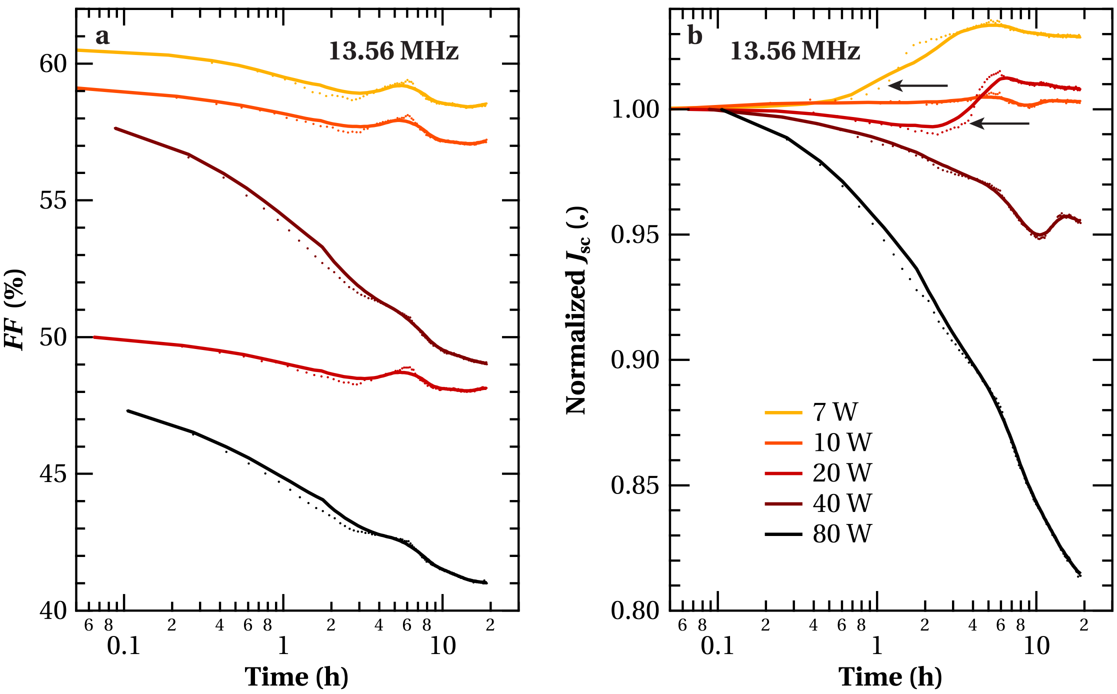

Figure 7.6: Light-induced change of the fill factor (a) and normalized short-circuit current density (b) of the cells shown in Fig. 7.5 with the absorber layer deposited at 13.56 MHz.

only for poor-quality absorber layers. For the moment we do not have an explanation for this difference except that the material quality was experimentally varied by increasing the pressure in [Fischer 13] but by power here, and that light-soaking conditions were different.

7.7 Degradation kinetics of polymorphous silicon

It was claimed in earlier studies of polymorphous silicon (pm-Si:H) [Roca i Cabarrocas 02, Kim 12a, Kim 13a] that this material degrades less during light soaking compared to standard a-Si:H. However, in the study presented in chapter 6, we could not find any specific deposition conditions where unusually low degradation could be observed except the generally lower degradation close to the amorphous-to-microcrystalline silicon transition. Note that we investigated deposition conditions that were close to reported conditions for the deposition of pm-Si:H.

For a direct comparison of pm-Si:H and a-Si:H, solar cells with these absorber layers were deposited on LPCVD ZnO substrates.[1] Three different types of cells were deposited, choosing the buffer layer at the p-i interface and the bulk absorber layer as pm-Si:H or a-Si:H.

---

[1] We obtained these results within a collaboration between PVLAB and the Laboratory of Physics of Interfaces and Thin Films (LPICM), Ecole Polytechnique, Palaiseau (France), where S. Abolmasov, E. Johnson, and P. Roca i Cabarrocas were responsible for the depositions of the solar cells presented in this section on substrates from PVLAB.

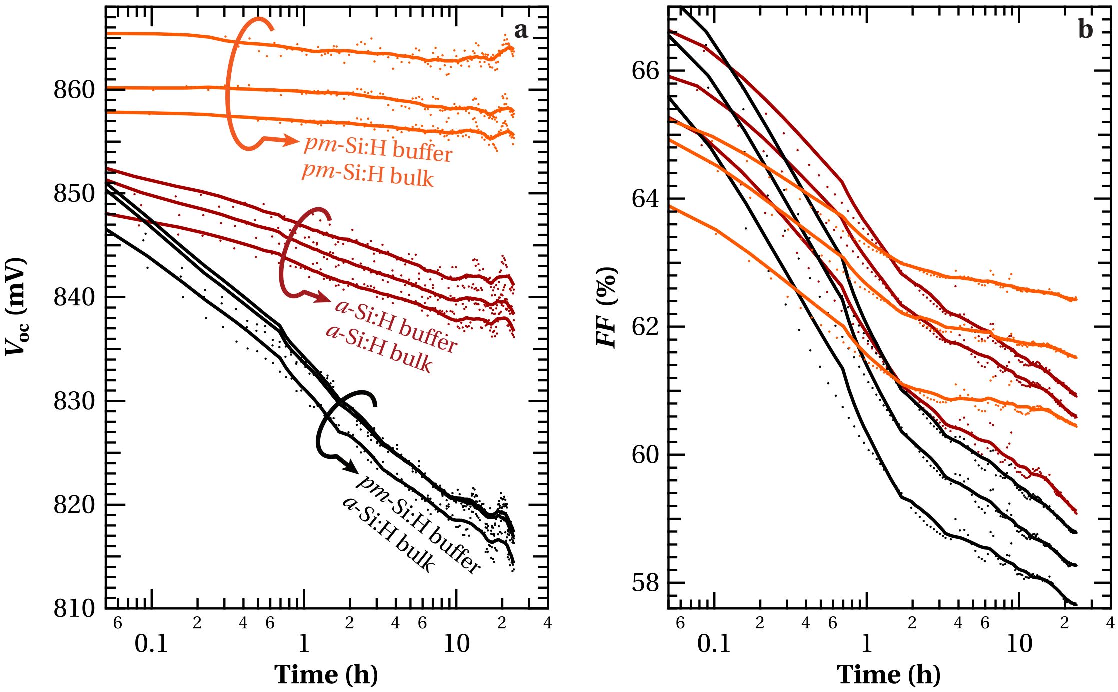

Figure 7.7: Open-circuit voltage (a) and fill factor (b) degradation kinetics of polymorphous and hydrogenated amorphous silicon solar cells produced at LPICM (Palaiseau, France), during light-soaking.

Figure 7.7a shows the LID of the V_{oc} of these cells. With pm-Si:H absorber and buffer layers, the V_{oc} is hardly affected during light soaking. In contrast, the V_{oc} of solar cells with a-Si:H absorber and buffer layers slightly decreases. Interestingly, the LID of the V_{oc} is even stronger when a pm-Si:H buffer layer is used in combination with an a-Si:H absorber layer. The same trend shows up in FF in Fig. 7.7b, where one can see that the fully polymorphous cells degrade least and the mixed cells degrade most.

A possible interpretation is that the polymorphous silicon suffers less from light-induced degradation than standard amorphous silicon. This is in agreement with specific literature on pm-Si:H [Roca i Cabarrocas 02, Kim 12a, Kim 13a] and generally observed for materials that are deposited close to the transition between a-Si:H and μc-Si:H (see section 6.4). For the mixed cell, interface effects can play a major role: using a low-quality buffer layer at the p-i interface is more detrimental than a poor i-layer absorber material. Further, charge accumulation in the buffer layer in light-induced defect states can lead to a strong reduction of the electric field in the absorber layer, and hence, to strong light-induced degradation (see section 4.4).

7.8 Conclusions

We incorporated different a-Si:H absorber layers into single-junction solar cells and compared their performance with respect to LID and its kinetics.

Although the accelerated LID at three-sun-equivalent illumination for 24 h led in most cases to similar or even stronger degradation of solar cell performance (particularly of the FF) as compared to the common light soaking at one-sun-equivalent illumination for 1000 h, we do generally not observe a stabilization.[2] Instead, the solar cells continue to degrade with time. In most cases, we observed a single linear slope in semi-logarithmic scale—strong degradation for poor-quality absorber layers, less degradation for high-quality absorber layers—but, based on our measurements, we cannot confirm the presence of faster degradation in the beginning due to void-related defects as reported in the literature.

With varying deposition parameters, we observed the following trends with respect to LID:

- *H_2 dilution:* The higher the better. The upper limit is given by the amorphous-to-microcrystalline transition or acceptable current density.
- *Power:* The lower the better, if the deposition temperature is not too high. The lower limit is given by plasma extinction and economical considerations of deposition rate and throughput.
- *Absorber-layer thickness:* The thinner the better. The lower limit is given by the acceptable current density or shunt issues.
- *Excitation frequency:* No significant difference if the deposition pressure and dilution are adapted to the frequency. Eventually, higher frequencies lead to slightly more stable materials.
- *Temperature:* Only a weak deposition-temperature dependence of LID was found. The lower limit is given by too many defects, the upper limit by H_2 effusion.

In a direct comparison of solar cells with pm-Si:H and a-Si:H buffer and absorber layers, the cells with pm-Si:H buffer and absorber layers degraded least, followed by cells with a-Si:H buffer and absorber layers; at this moment, we do not understand why the combination of a pm-Si:H buffer and an a-Si:H absorber layer led to the largest LID. This effect needs further investigation.

---

[2] Still, the standard of 1000 h of light soaking can be justified: 1000 h at one-sun-equivalent illumination leads to LID on the same order as outdoor exposure during one season, before oscillation of the solar cell efficiency with annealing/degradation cycles starts.

8 Light-induced changes of the open-circuit voltage

High-efficiency hydrogenated amorphous silicon (a-Si:H) solar cells were deposited with different thicknesses of the p-type hydrogenated amorphous silicon carbide (p-(a-SiC:H)) layer on substrates of varying roughness. We observed a light-induced open-circuit voltage (V_{oc}) increase upon light soaking for thin p-layers, but a decrease for thick p-layers. Further, the V_{oc} increase is enhanced with increasing substrate roughness. After correction of the p-layer thickness for the increased surface area of rough substrates, we can exclude varying effective p-layer thickness as the cause of the substrate-roughness dependence. Instead, we explain the observations by an increase of the defect concentration in both the p-layer—causing a V_{oc} increase—and in the intrinsic absorber layer, causing a V_{oc} decrease. The p-layer thickness decides which of the two mechanisms dominates. We present a mechanism for the light-induced increase and decrease, justified by the investigation of light-induced changes of the p-layer and supported by ASA simulation. We conclude that a shift of the electron quasi-Fermi level towards the conduction band is the reason for the observed V_{oc} increase, and poor a-Si:H quality on rough substrates enhances this effect.

This chapter is organized as follows: After the introduction in section 8.1 and detailing of the experimental methods in section 8.2, we show in section 8.3 under which circumstances V_{oc} increase can occur, and we discuss light-induced changes of single layers, mainly of the p-(a-SiC:H) layer, which is proven to be electronically dead. Then, we discuss V_{oc} increase with respect to kinetics and with respect to substrate-roughness dependence. In section 8.4 we provide an explanation of the observed effects on the basis of a layer-by-layer simulation, using light-induced defects as the only changing parameter. Finally, we put our findings in relation to light-induced V_{oc} changes reported in the literature (section 8.5) and conclude the chapter in section 8.6.

The main results of this chapter were published in the Journal of Applied Physics [Stuckelberger 14d], and other parts are in preparation for a second publication.

We acknowledge Y. Riesen for assistance with ASA simulations.

8.1 Introduction

Light-induced changes of *a*-Si:H have been widely discussed in the literature since the discovery of the Staebler-Wronski effect (SWE) [Staebler 77] in 1977. Most of these studies refer to light-induced degradation (LID) of the intrinsic (*i*) absorber layer [Roca i Cabarrocas 02, Poissant 03, Melskens 14, Fehr 14, Matsui 13a, Matsui 13b]. Not only *a*-Si:H layers suffer from LID, but also *a*-Si:H alloys such as hydrogenated amorphous silicon carbide (*a*-SiC:H), oxide (*a*-SiO:H), or germanium (*a*-SiGe:H) degrade [Shah 10, Yunaz 09, Inthisang 09, Xu 96]. Both carbon and oxygen are often used to widen the bandgap of intrinsic or doped *a*-Si:H—and there is no reason why alloys using them would not degrade when they are boron doped.

Light-induced changes of the complete device can have different origins. One of them is the SWE in intrinsic *a*-Si:H layers. Also, ZnO, which is often used as a transparent conductive oxide (TCO) as the front and back electrodes of solar cells, degrades during light soaking [Ding 14]. The electrical contact between the TCO and a metallic back contact is improved by annealing, which is typically performed immediately after solar cell deposition, but the improvement can be seen during light soaking, if the solar cell is not annealed before. (This effect can be used to account for very low or even positive light-induced changes starting from low solar cell efficiencies.) In contrast to such irreversible light-induced changes, the SWE refers strictly speaking only to the part of LID that is due to a light-induced change of photoconductivity, and that is reversible by annealing [Staebler 77]. Solar cells can run through many degradation/annealing cycles during normal operation [Lechner 10, Isomura 98, El Mhamdi 14].

The underlying reason for the SWE is still under discussion. Several models [Shimizu 04, Stutzmann 85, Stutzmann 89, Branz 99, Zhang 01, Smets 03, Smets 10] provide explanations on the atomic level with or without an active role of mobile hydrogen and hydrogen–silicon bonds. They have in common that structural defects are created by recombination of charge carriers during light soaking. These defects form electronic states near mid-gap that act as recombination centers and limit efficient charge collection (see chapter 4).

Nearly 40 years after the discovery of the LID of *a*-Si:H, the negative impact of the SWE on thin-film silicon (TF-Si) solar cells has still not been significantly reduced, and it is questionable whether solar cells based on *a*-Si:H as the absorber will ever overcome this limitation that seems to be inherently linked to its amorphous nature.

However, the LID of solar cells can have a positive effect on solar cells. In particular, the V_{oc} can be increased during light soaking. This effect has been reported by several research institutes [Isomura 98, St'ahel 97, Roca i Cabarrocas 98, Lord 01, Yang 02, Yan 03c, Yue 03, Johnson 08, Johnson 10, Matsui 14b, Rech 97a, Stuckelberger 14a], however, it has never been studied thoroughly or been explained satisfyingly. Such light-induced V_{oc} increase is the subject of the present study.

8.2 Experimental details

8.2.1 Solar cell design

The main results of this study were obtained from a thickness series of the *p*-(*a*-SiC:H) layer incorporated in a high-efficiency *a*-Si:H solar cell.

Figure 8.1 gives an overview over the structure and layer thicknesses of the solar cells deposited in the *p*-*i*-*n* (superstrate) configuration on 0.5-mm-thick Schott AF 32 glass substrates. Single layers were co-deposited on 250-µm-thick double-side-polished intrinsic (100) crystalline silicon (*c*-Si) wafers for Fourier transform infrared spectroscopy (FTIR) measurements, and on 0.5-mm-thick Schott AF 32 glass substrates for all other measurements.

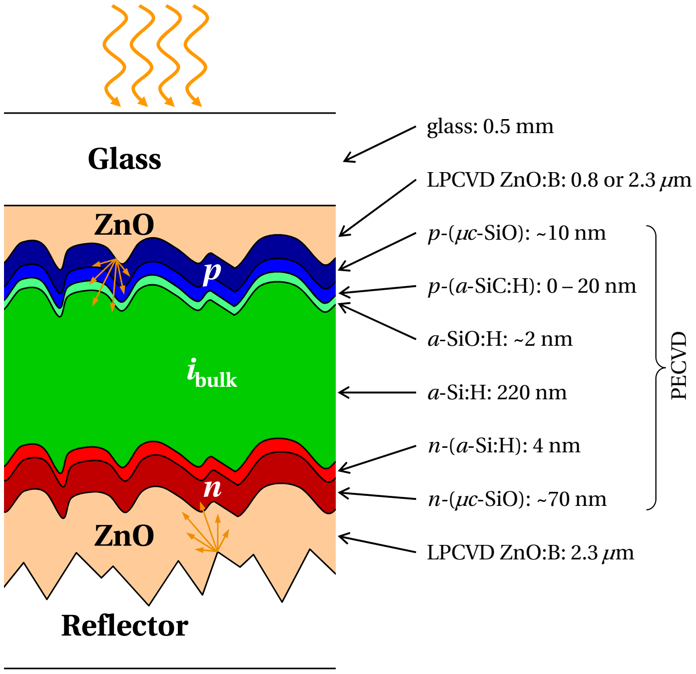

Figure 8.1: Solar cell structure used for the *p*-(*a*-SiC:H) thickness series on four different substrates.

For the front electrodes, boron-doped ZnO (ZnO:B) was deposited by low-pressure chemical vapor deposition (LPCVD). For each *p*-(*a*-SiC:H) thickness, the solar cells were co-deposited on four different substrates with varying roughness. Three substrates consisted of co-deposited 2.3-µm-thick ZnO:B on glass. On one of these, as-deposited ZnO:B was used (Z2.3 0'); on the two others, the ZnO:B was treated for 7 or 20 minutes with an Ar plasma to modify the surface texture from its initial V-shape into a smoother U-shape (Z2.3 7' and Z2.3 20', respectively) [Bailat 06]. This leads to less shunting but also less light scattering [Python 09]. The fourth substrate was a flat reference with smoothly grown 0.8-µm-thick LPCVD ZnO:B, treated for 4 minutes with an Ar plasma (Smooth 4') [Nicolay 12, Fanni 14].

Table 8.1: Deposition conditions of the p-(a-SiC:H) layer.

Pressure	Power	Frequency	Gas flows			
			H_2	SiH_4	CH_4	$B(CH_3)_3$ (2% in H_2)
0.5 mbar	8 W	40.68 MHz	16 sccm	14 sccm	16 sccm	8 sccm

We deposited a p-type microcrystalline silicon oxide layer, denoted by p-(μc-SiO:H), directly on the front ZnO for good electrical contact, transparency, and shunt quenching [Cuony 10, Despeisse 10a]. For a strong electric field, a p-(a-SiC:H) layer with a wide bandgap was deposited after the p-(μc-SiO:H) layer. The thickness of this layer was varied between 0 (no deposition) and about 20 nm. For consistency, the solar cells without a p-(a-SiC:H) layer were subjected to the same process flow (gas flows, heating times, etc.), but without igniting the plasma. The deposition conditions of this layer are given in Tab. 8.1; its characteristics are discussed in section 8.3.2. Between the p-type layers and the intrinsic absorber layer, we added a wide-bandgap a-SiO:H layer [Bugnon 14]. The a-Si:H absorber layer has a low Tauc-Lorentz bandgap [Jellison 96b, Jellison 96a] of 1.66 eV (cf. section 8.2.2). An n-type a-Si:H layer, n-(a-Si:H), and an n-type microcrystalline silicon oxide layer, n-(μc-SiO:H), were deposited after the absorber layer to complete the p-i-n junction. The back electrode consists of 2.3-µm-thick LPCVD-grown ZnO:B. For each substrate, an array of 12 cells, each 0.25 cm^2 in size, was defined by a combination of wet and dry etching.

All silicon layers were deposited by plasma-enhanced chemical vapor deposition (PECVD) in a cluster tool (Octopus I) from INDEOtec SA [INDEOtec 14] with dedicated chambers for p-type, n-type, and i-layers. All doped layers and the a-SiO:H buffer layer were deposited at 200 °C and 40.68 MHz. The absorber layer was deposited at 230 °C and 13.56 MHz. More details about individual layers, the reactor, and gas precursors can be found in [Stuckelberger 13] and chapter 2.

8.2.2 Characterization

Solar cell characterization

We measured current-voltage ($I(V)$) characteristics under a four-lamp (three halogen, one xenon) solar simulator from Wacom (class AAA) under standard conditions (AM1.5g, 1000 $\frac{W}{m^2}$, 25 °C) [IEC 07, IEC 06]. The current was determined from external quantum efficiency (EQE) measurements, taken with a system built in-house. Back reflectors made of polytetrafluoroethylene (PTFE) were used for current measurements.

Light soaking

Before light soaking of the solar cells, each substrate was cut into two. Eight of the 12 solar cells were light soaked in a solar simulator from Solaronix (class AAA) for 1000 h at 50 °C under

500 $\frac{\mathrm{W}}{\mathrm{m}^2}$ of AM1.5g light. The solar cell in the center of the substrate that performed best after light soaking was used for the analysis in sections 8.3.3 and 8.3.5. The other four solar cells were contacted by ultrasonic soldering and light soaked with in-situ measurement of the LID kinetics. These measurements were performed with three-sun-equivalent illumination for 24 h at 50 °C. A dedicated solar simulator presented in chapter 3 and [Stuckelberger 14c], fully based on LEDs and built in-house was used for these measurements, which are presented in section 8.3.2 and 8.3.4.

Layer characterization

The layer thicknesses and optical parameters were determined from combined fitting of three-angle ellipsometry and transmittance measurements of layers deposited on glass or wafers. A Tauc-Lorentz model [Jellison 96b, Jellison 96a], taking into account surface roughness, was used for the fitting. For bi-phase layers (microcrystalline silicon (μc-Si:H) and microcrystalline silicon oxide (μc-SiO:H)), a second oscillator was added to the model. However, the thicknesses for these layers are only approximate, as nucleation of these materials depends strongly on the substrate. We used a UVISEL ellipsometer from Horiba Jobin Yvon (with monochromators for IR and UV/Vis) for ellipsometry measurements. The measurements were performed between 0.6 and 6 eV. A Lambda 900 spectrometer with an integrating sphere from Perkin Elmer was used for transmission measurements between 300 and 2000 nm.

For precise measurement of the absorption coefficient also in the sub-bandgap range, photothermal deflection spectroscopy (PDS) [Boccara 80] measurements were performed on the p-(a-SiC:H) layer in a setup built in-house. For information about the hydrogen- and nano-void-related aspects of a-Si:H layers, FTIR measurements were performed using a Nicolet 8700 spectrometer from Thermo.

Activation energies (E_{act}) were determined by taking temperature-dependent dark conductivity (σ_{dark}) measurements in an in-house built setup. Therefore, two 8-mm-wide aluminum contacts spaced 0.5 mm apart were deposited by thermal evaporation. The measurements were taken under 7 V bias voltage. E_{act} was determined from a linear fit of

$$\ln(\sigma_{\mathrm{dark}}) = \ln(\sigma_0) - \frac{E_{\mathrm{act}}}{k_{\mathrm{B}} \cdot T}, \tag{8.1}$$

using the measurements from the cooling-down ramp. Here, σ_0 and E_{act} are the fitting parameters, T the absolute temperature, and k_{B} the Boltzmann constant.

8.2.3 Simulation

The simulations presented in section 8.4 were performed using the Advanced Semiconductor Analysis (ASA) software package (version 6) [Pieters 06, Zeman 13a]. The input parameters for the simulation are given in appendix C, and relevant choices are discussed in section 8.4.

8.3 Experimental results and discussion

8.3.1 Effect of the *p*-(*a*-SiC:H)-layer thickness on the external quantum efficiency

Figure 8.2a shows the dependence of the *EQE* on the *p*-(*a*-SiC:H) layer thickness. In the blue part of the spectrum, the *p*-(*a*-SiC:H) layer is strongly absorbing, which leads to a decrease of the *EQE* with increasing *p*-(*a*-SiC:H) layer thickness. These measurements were taken before light soaking, applying white bias light but no bias voltage.

Often (but not always) [Arch 91], *p*-(*a*-SiC:H) layers are considered to be “dead” layers, i.e. electron–hole pairs created there immediately recombine without being collected. Whether this is the case for high-efficiency devices with optimized *p*-(*a*-SiC:H) layers, is the subject of the following paragraphs.

For a *p*-(*a*-SiC:H)-layer thickness series, we expect a linearly decreasing *EQE* with increasing *p*-(*a*-SiC:H)-layer thickness. Let us now consider an active *p*-(*a*-SiC:H) layer, in which some of the electron–hole pairs generated there can be collected. In that case, the *EQE* is increased with applied bias voltage, as charge collection from the *p*-(*a*-SiC:H) layer is increased due to a stronger electric field. For a *p*-layer thickness series, we expect a different slope of *EQE* as a function of the *p*-layer thickness, measured with and without applied bias voltage: In thin *p*-layers, only few electron–hole pairs are created, hence the number of collected electron–hole pairs (or the *EQE*) is only slightly increased by applying a reverse bias voltage. In thicker *p*-layers, more electron–hole pairs are created, which results in a stronger increase of the *EQE* with applied bias voltage.

For a dead *p*-(*a*-SiC:H) layer, applying a reverse bias voltage can increase *EQE* as well due to enhanced charge collection from the *p*-*i* interface or from the *i*-layer. However, in a dead *p*-(*a*-SiC:H) layer, the charge collection cannot be improved, and we expect that the difference between *EQE* measurements with and without a reverse bias voltage is independent of the *p*-layer thickness.

In Fig. 8.2b, we show the *EQE* measurements at 0 and -1 V applied bias voltage, for the solar cells before (ini for initial state) and after light soaking (deg for degraded state). For this graph, we have selected the *EQE* at 420 nm. At this wavelength, the front ZnO does not absorb a significant amount, but the *p*-(*a*-SiC:H) layer does.

In both the initial and the degraded state, the slopes of the curves measured at 0 and -1 V are the same. The constant difference between them comes from non-perfect charge collection from the *i*-layer. We can therefore conclude that our *p*-(*a*-SiC:H) layer is dead and does not contribute to current.

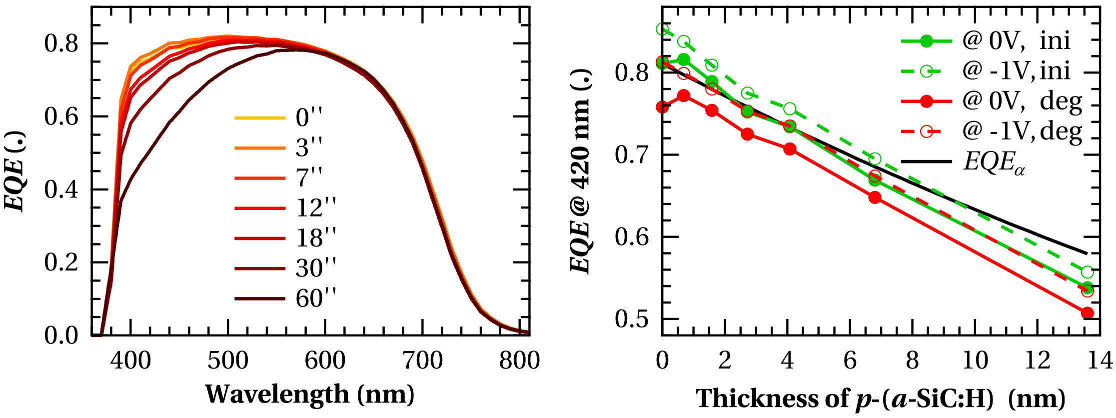

Figure 8.2: (a): External quantum efficiency (*EQE*) measurements for solar cells with different p-(a-SiC:H)-layer thicknesses from 0 to 13.6 nm, parameterized here by their deposition times. Z2.3 0' was used as the substrate. (b): *EQE* measurements at 0 and -1 V bias voltage at 420 nm, for solar cells with different p-(a-SiC:H)-layer thickness before (ini) and after (deg) light soaking. EQE_α is the *EQE* one can expect from absorption measurements of the p-(a-SiC:H) layer, if it is assumed to be dead.

Note that the *EQE* after light soaking is lower than in the initial state. This is true for all wavelengths and due partially to i-layer degradation and partially to ZnO degradation [Ding 14].

From ellipsometry and transmittance measurements, we have determined the absorption coefficient α of the p-(a-SiC:H) layer. To compare the absorption losses by the p-(a-SiC:H) layer with the decrease of *EQE*, we calculated

$$EQE_\alpha \doteq EQE\big(\text{ini}, 420\,\text{nm}, 0\,\text{V}, \text{no } p\big) \cdot e^{-\alpha(420\,\text{nm})\cdot x}, \tag{8.2}$$

which is the light intensity I attenuated by the p-(a-SiC:H) layer according to $I_{\text{after } p} = I_{\text{before } p} \cdot e^{-\alpha(420\,\text{nm})\cdot x}$ with the absorption coefficient α and the p-(a-SiC:H)-layer thickness x, referenced to the *EQE* of the cell without a p-(a-SiC:H) layer.

We see in Fig. 8.2b that the absorption losses calculated this way from layer measurements, considering all photons absorbed in the p-(a-SiC:H) layer to be lost (hence, a dead p-(a-SiC:H) layer), are in good agreement with the decrease of *EQE*, although this calculation neglects the effects of substrate roughness/light scattering and possible layer property differences between the layer deposited for optical characterization and the layer as deposited in the cell, where the strong hydrogenated plasma of the a-SiO:H layer can impact the underlying p-(a-SiC:H) layer.

Note that the p-(a-SiC:H) layer investigated here was optimized for a-Si:H single-junction solar cells. As even this p-(a-SiC:H) layer has been shown here to be electronically dead, we suspect that this is true also for other p-(a-SiC:H) layers that perform well in a-Si:H solar cells.

8.3.2 Light-induced changes of the *p*-(*a*-SiC:H)-layer

As we will see in sections 8.3.3 to 8.3.5, the *p*-(*a*-SiC:H) layer thickness has a large impact on light-induced changes of V_{oc}. To provide an experimental basis to evaluate different mechanisms, we investigate in this section how the properties of the *p*-(*a*-SiC:H) layer are affected by light soaking.

From the literature [Ding 14], we know that LPCVD ZnO degrades during light soaking (this is less the case for the *p*-(μc-SiO:H) layer). However, these effects (enhancement of conductivity and reduction of transparency) are independent of the *p*-(*a*-SiC:H) thickness that we investigate in this study and thus always affect the short-circuit current density (J_{sc}) and the fill factor (FF) the same way. Therefore, we concentrate here only on the *p*-(*a*-SiC:H)-layer degradation.

First, we look at the optical properties (n,k) that are shown in Fig. 8.3a. Between the initial and the degraded state, no significant difference could be observed. In both cases, the Tauc-Lorentz bandgap is about $E_{\mathrm{g}}^{\mathrm{TL}} = 1.85\,\mathrm{eV}$.

Second, we look at the absorption coefficient obtained from PDS measurements (see Fig. 8.3b). There is no difference visible between the initial and degraded state. Note the strong absorption at low energies due to many defects in the bandgap, such that these absorption curves have a different shape from those of typical semiconductors.

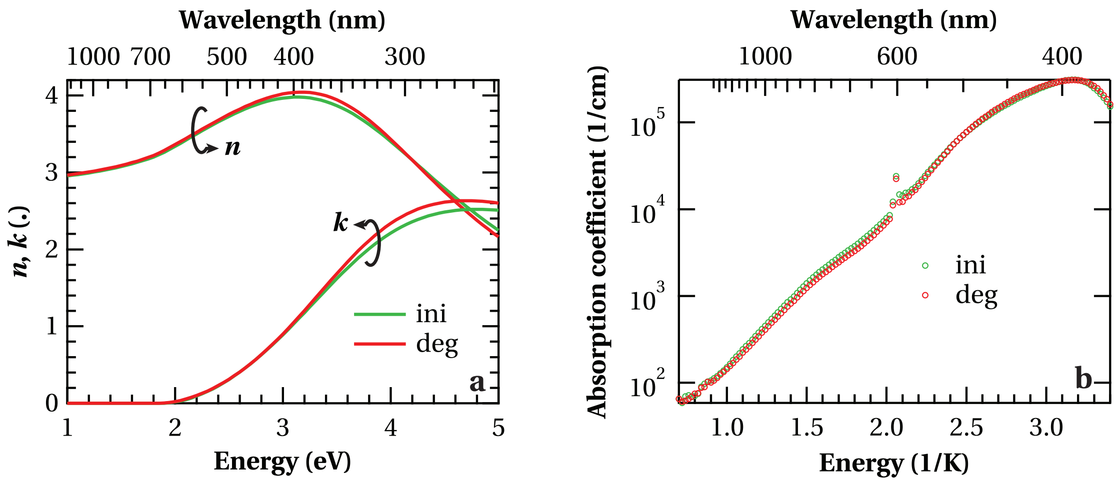

Figure 8.3: (a): (n,k) of the *p*-(*a*-SiC:H) layer, extracted from combined fitting of three-angle ellipsometry and transmittance measurements, before (ini) and after (deg) light soaking (three-sun-equivalent illumination for 24 h). (b): Absorption coefficient of the *p*-(*a*-SiC:H) layer from photothermal deflection spectroscopy measurements in the initial and the degraded state.

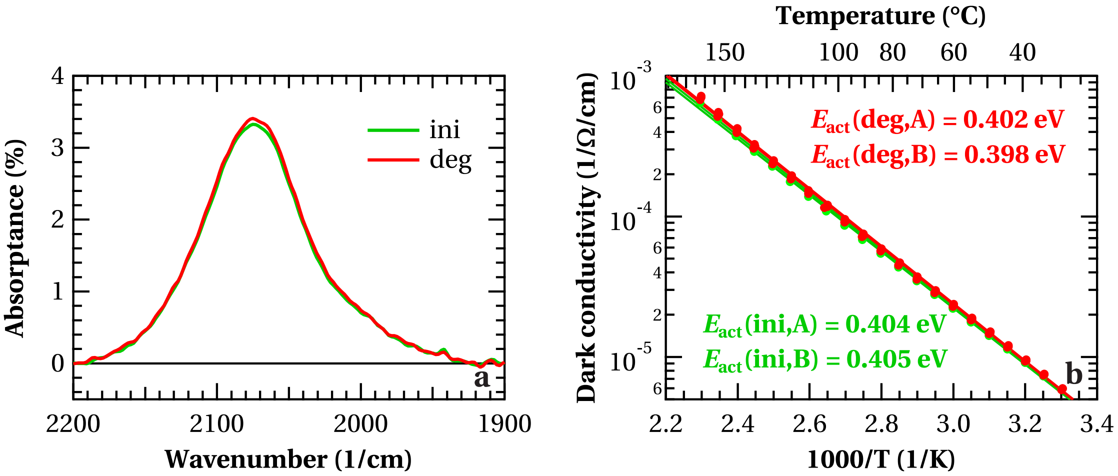

Figure 8.4: (a): Infrared absorptance of the p-(a-SiC:H) layer before (ini) and after (deg) light soaking (three-sun-equivalent illumination for 24 h), obtained from Fourier transform infrared spectroscopy measurements. (b): Temperature-dependent dark-conductivity measurements in the initial and the degraded state. The lines are fits from which the activation energies E_{act} were determined.

Third, we investigated the Si–H bonds from FTIR measurements. In Fig. 8.4a, we see the absorption by the Si–H stretching modes with absorption peaks between 2000 and 2100 cm^{-1} [Smets 07b]. (Boron- or carbon-related absorption peaks are located at different energies [Lin 87, Stavola 88].) We note that the surface below the peaks does not change with light soaking and conclude that H_2 effusion from the layer does not occur. Further, the peak position does not change. Hence, the hydrogen-related micro-structure does not change.

Fourth, we investigated the dark conductivity of the p-(a-SiC:H) layer, shown as a function of temperature in the initial and degraded state in Fig. 8.4b, and determined E_{act}. A change in E_{act} would be a good candidate to explain light-induced V_{oc} changes. However, such a change could not be confirmed by these measurements. Moreover, the repetition of the measurements on different samples did not show a significant difference between the initial and light-soaked state. Hence, another explanation must be found.

8.3.3 Light-induced changes of solar cells

In this section, we focus on light-induced changes of solar cells, especially of their V_{oc}. Figures 8.5a-d show the V_{oc} in the initial state, after light soaking, and after annealing for a p-(a-SiC:H)-layer thickness series on four substrates with increasing substrate roughness. We note:

(i) V_{oc} generally increases with increasing p-(a-SiC:H)-layer thickness; the effect is strong for thin layers and saturates with thicker layers.

(ii) For thick p-(a-SiC:H) layers ($> 10\,\mathrm{nm}$), V_{oc} decreases slightly with increasing layer thickness.

(iii) For thin p-(a-SiC:H) layers, V_{oc} increases during light soaking.

(iv) For thick p-(a-SiC:H) layers, V_{oc} decreases during light soaking.

(v) Annealing after light soaking returns the V_{oc} to the initial state, i.e. V_{oc} increases for thick and decreases for thin p-(a-SiC:H) layers. An exception is the flattest substrate. From preliminary studies we know that this kind of ZnO reacts strongly to light soaking and annealing. Therefore, we suppose that the different behavior of cells grown on this substrate is related to the ZnO and not to the p-(a-SiC:H) layer.

(vi) Rough substrates need a thicker effective p-(a-SiC:H) layer than smooth substrates for similar V_{oc}. However, the maximum V_{oc} of cells on rough substrates is lower than on smooth substrates.

(vii) The (reversible) increase of V_{oc} for thin, and decrease of V_{oc} for thick, p-(a-SiC:H) layers with light soaking is substrate-roughness dependent: The critical p-(a-SiC:H)-layer thickness at which V_{oc} does not change by light soaking is larger for rougher substrates.

We will provide explanations for each of these observations in the remaining parts of section 8.3. Note that these observations are not the result of a single experiment. Rather, we have reproduced these trends for p-(a-SiC:H)-layer thickness series in three different reactors ranging in size and type from laboratory to industrial (system B, Octopus I, Kai-S) using different recipes, with and without oxide in the microcrystalline silicon layers. Further, another laboratory has independently confirmed the results [Matsui 14a]. The observation that V_{oc} is hardly changing in Fig. 8.5a for no p-(a-SiC:H) layer is not systematic: in some cases, we have observed an increasing V_{oc} even for the smoothest substrate without a p-(a-SiC:H) layer.

Figures 8.5e-h show the solar cell parameters V_{oc}, J_{sc}, FF, and conversion efficiency as a function of the p-(a-SiC:H)-layer thickness for the smoothest (Smooth 4') and the roughest (Z2.3 0') substrates.

In Fig. 8.5f, we see that J_{sc} first increases with p-(a-SiC:H)-layer thickness. This is due to improved charge collection, which more than offsets the parasitic absorption in the p-(a-SiC:H) layer. For thicker layers, the electric field for current collection saturates, whereas absorption losses continue to grow. For very thick layers, the light intensity being absorbed in the i-layer is sufficiently reduced that quasi-Fermi-level splitting and hence V_{oc} get smaller. This explains observation (ii). Note that J_{sc} is about 30% higher for the rough substrate as compared to the smooth substrate due to better light scattering.

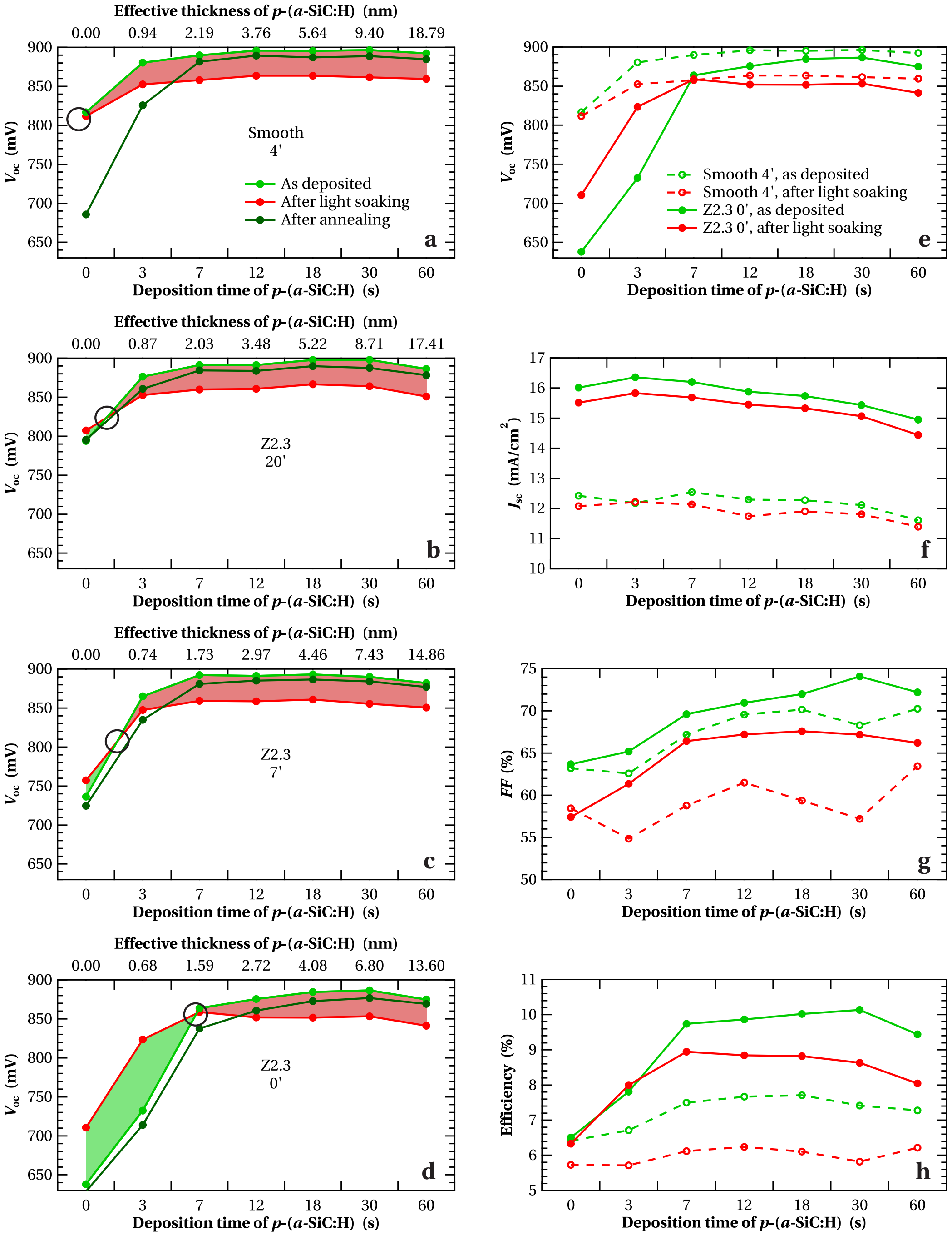

Figure 8.5: (a–d): Open-circuit voltage (V_{oc}) in the initial state (as deposited), after light soaking, and after annealing for a p-(a-SiC:H)-layer thickness series in a-Si:H solar cells on substrates with increasing roughness from (a) to (d). The shading represents gain (green) and loss (red) of V_{oc} during light soaking, and black circles mark the critical p-(a-SiC:H)-layer thickness for which the V_{oc} is not affected by light soaking.
(e–h): V_{oc}, short-circuit current density, fill factor, and conversion efficiency of the same series for the smoothest (a) and roughest (d) substrates in the initial state and after light soaking.

In Fig. 8.5g, we see that the FF generally increases with p-(a-SiC:H)-layer thickness. Obviously, the better charge collection overcompensates for the higher series resistance introduced by the p-(a-SiC:H) layer. On rough substrates, the FF is higher than on the smooth substrate. In fact, the smooth substrate is more resistive, which limits the FF, and the substrate itself degrades more during light soaking.

The combined changes of V_{oc}, J_{sc}, and FF are shown in the conversion efficiency in Fig. 8.5h. For the smooth substrate, the efficiency does not depend significantly on the p-(a-SiC:H)-layer thickness; the stronger degradation of V_{oc} for thicker layers offsets the initially higher V_{oc}. This is not the case for rougher substrates, where in some cases even a light-induced efficiency improvement caused by the V_{oc} increase was observed for thin p-(a-SiC:H) layers. For thicker p-(a-SiC:H) layers, LID is more important due to stronger degradation of V_{oc}. This leads to a shift in optimum p-(a-SiC:H)-layer thickness from about 7 nm in the initial state, to about 1.6 nm in the degraded state.

These findings have an impact on TF-Si solar cell development, especially on rough substrates which are required for good light trapping. The positive news, that V_{oc} increases with light soaking for thin p-(a-SiC:H) layers, leads to lower optimum thickness after light soaking, which is beneficial because of lower parasitic absorption, hence higher current densities—in particular for multi-junction solar cells. This study also reinforces the observation that solar cell optimization needs to be performed with respect to the light-soaked state.

8.3.4 Solar cell degradation kinetics

Figure 8.6b shows the kinetics of the light-induced V_{oc} changes for the solar cells on the rough Z2.3 0' substrates, during 24 h of light soaking under three-sun-equivalent light intensity. The substrate temperature and light intensity were stable within a few per mill (cf. Fig. 8.6a and 8.6c); the scattering in the V_{oc} measurements is caused mainly by noisy $I(V)$ measurements. The V_{oc} increase for thin and the decrease for thick p-(a-SiC:H) layers are confirmed by these light-soaking experiments. Also, the optimum layer thickness with the highest V_{oc} is the same (18 s of deposition time in the initial state, thinner layers after light soaking).

Note that all curves are linear in a semi-logarithmic scale, which means that these light-induced changes follow logarithmic laws. A single slope is observed for each curve. This observation is in contrast to recent degradation measurements [Fischer 13] that show a change in kinetics after about 10 h from fast to slower degradation. The authors attribute their observation to the nano-structure of the a-Si:H absorber layer. For denser absorber layers with fewer voids, the fast degradation was less pronounced, which could explain why we did not observe it for our optimized absorber layer.

Comparing V_{oc} values of Fig. 8.6 with Fig. 8.5e, we note that V_{oc} measured under these conditions (three sun equivalent, 50 °C and one sun equivalent, 25 °C) are close; two inverse

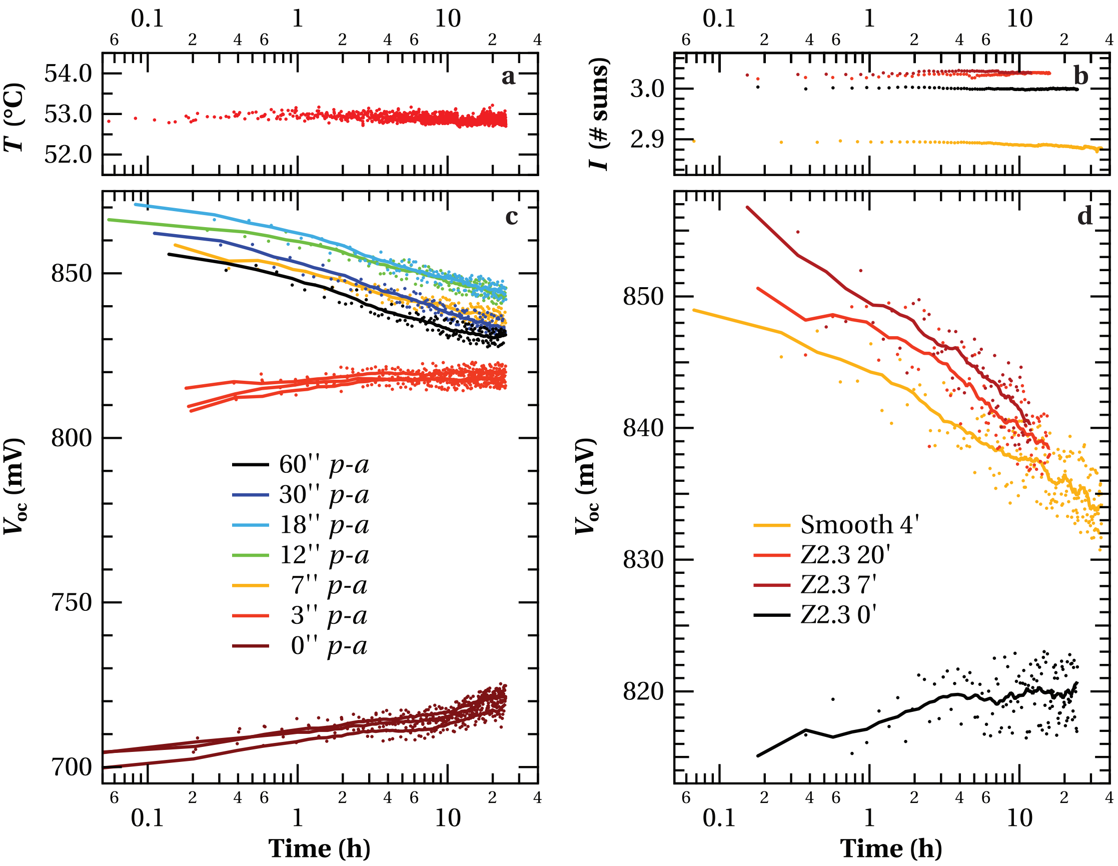

Figure 8.6: Kinetics of light-induced changes of the open-circuit voltage over 24 h under three-sun-equivalent light intensity for cells with different *p*-(*a*-SiC:H) layer thicknesses (c); (a) shows the corresponding substrate temperature. For thin *p*-(*a*-SiC:H) layers, measurements of three different cells are shown to demonstrate reproducibility. Lines are the smoothed measurements that are shown as spots.
(d): Kinetics of light-induced V_{oc} changes for solar cells co-deposited on substrates with different roughnesses; (c) shows the corresponding light intensities in number of sun equivalents. The *p*-(*a*-SiC:H)-layer deposition time for (b) and (d) was 3 s.

effects—positive light intensity coefficient and negative temperature coefficient of V_{oc}—partially cancel one another.

Figure 8.6d shows the substrate dependence of the degradation kinetics for all four substrates of the solar cells with 3 s of *p*-(*a*-SiC:H) deposition. For this layer thickness, the V_{oc} still increases for the roughest substrate, while it decreases for the other substrates, for which the *p*-(*a*-SiC:H) is thicker than the critical thickness as indicated in Fig. 8.5a-d by the crossing of the curves “as deposited” and “after light soaking”. Compared with the V_{oc} measurements there, the substrate order of Smooth 4’/Z2.3 20’/Z2.3 7’ is the opposite here. The reason is that, for kinetics measurements, the substrates could not be light soaked at once and the light intensity was slightly lower for smooth substrates than for rough substrates.

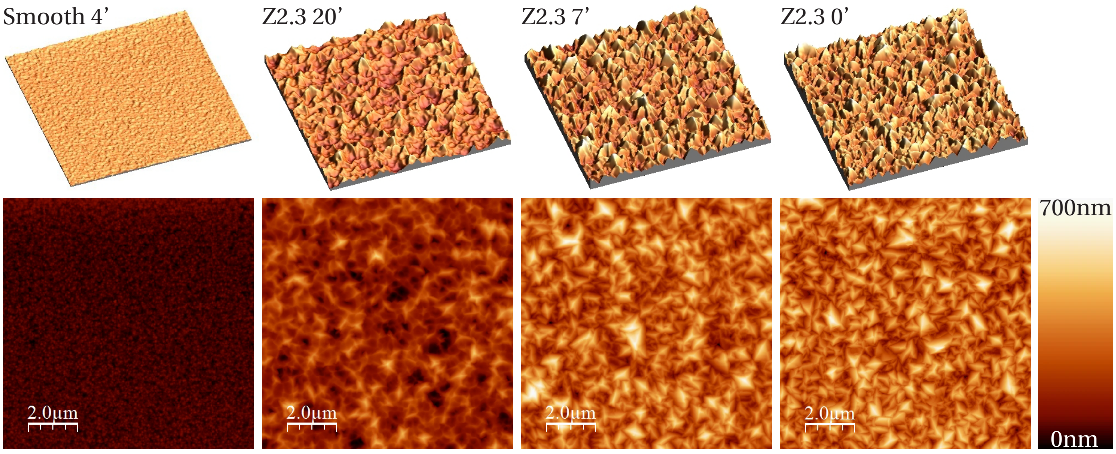

Figure 8.7: Atomic force microscopy images of the substrates used for the solar cells presented in Fig. 8.5. The measurement range was 10 µm × 10 µm. Top: 3-dimensional view, keeping the height scales constant (height is double proportional to the planar dimensions). Bottom: top-view, keeping the color scale constant for all images. These measurements were taken by M. Leboeuf from CSEM Neuchâtel, Switzerland and analyzed with WSxM software [Horcas 07].

8.3.5 Substrate-dependent effective thickness of the *p*-(*a*-SiC:H)-layer

In this section, we investigate whether the strong substrate dependence of light-induced V_{oc} changes seen in Fig. 8.5 could come from different effective p-(a-SiC:H) layer thicknesses altering the substrate roughnesses. Therefore, atomic force microscopy (AFM) images of the substrates, shown in Fig. 8.7, were recorded. The main results are summarized in Tab. 8.2.

Histograms of these measurements are shown in Fig. 8.8a with the flattened surfaces (s_{flat}) indicated. It is calculated from the effective substrate surface divided by the projected surface on the plane. We see from these calculations that the effective surface of the roughest substrate is less than 1.4 times larger than that of the smoothest substrate.

Let us assume that the total deposited volume of p-(a-SiC:H) material is the same on each substrate. This assumption can be justified by the facts that surface chemistry of all substrates is the same and the deposition rate is limited by the amount of dissociated layer precursors in the plasma. Therefore, we estimate the effective p-(a-SiC:H)-layer thickness in the solar cells as

$$d_{\mathrm{eff}} = r_{\mathrm{eff}} \cdot t_{\mathrm{depo}} \quad \text{with} \quad r_{\mathrm{eff}} = \frac{r_{\mathrm{nom}}}{s_{\mathrm{flat}}}. \tag{8.3}$$

Here, r_{eff} is the effective deposition rate, t_{depo} the deposition time, and $r_{\mathrm{nom}} = 3.41\,\text{Å/s}$ the nominal deposition rate of the p-(a-SiC:H) layer on flat glass, determined from ellipsometry and transmittance measurements. These effective thicknesses are given as the top axes in Fig. 8.5a-d.

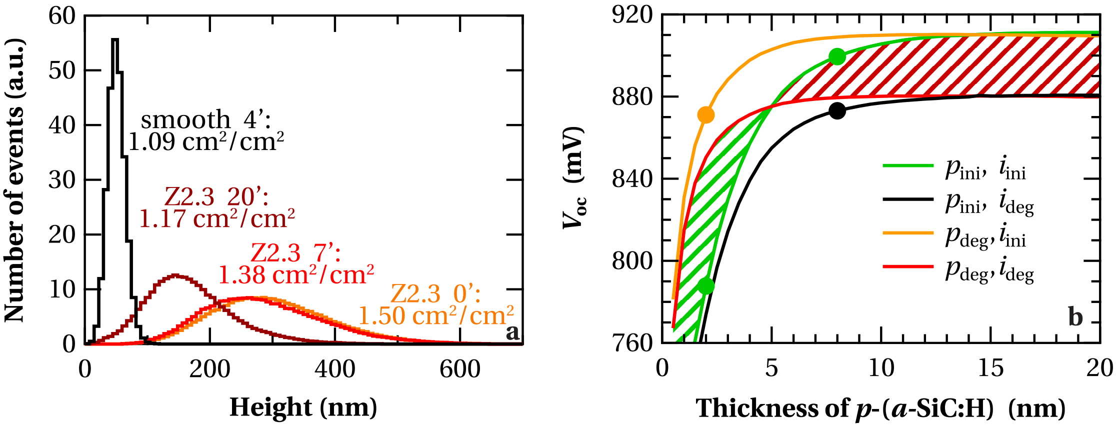

Figure 8.8: (a): Histograms of the AFM measurements of the substrates used, with the flattened surface extracted for each substrate. (b): Simulated V_{oc} of a p-(a-SiC:H) thickness series. Four cases are shown, differentiating between the initial and degraded states of the p-(a-SiC:H) and a-Si:H layers. The markers indicate solar cells that are discussed in greater detail later.

Comparing the effective p-(a-SiC:H)-layer thicknesses on different substrates, we see that they are less than 1.4 times thicker on the smoothest as compared to the roughest substrate. This cannot sufficiently explain the substrate-roughness dependence of V_{oc} in Fig. 8.5a-d, where the shift of the critical p-(a-SiC:H)-layer thickness is much larger than by a factor of 1.4. So, we have at least two effects for this shift—in section 8.4.5 we will present an additional explanation.

Table 8.2: ZnO substrate parameters extracted from AFM measurements. RMS stands for root-mean square, s_{flat} for the flattened surface.

Substrate	RMS roughness	Average height	s_{flat}
Smooth 4'	14.0 nm	51 nm	1.09 cm^2/cm^2
Z2.3 20'	68.9 nm	168 nm	1.17 cm^2/cm^2
Z2.3 7'	95.3 nm	289 nm	1.38 cm^2/cm^2
Z2.3 0'	92.7 nm	300 nm	1.50 cm^2/cm^2

8.4 Simulation

All input parameters for the simulation of the p-(a-SiC:H)-layer thickness series by the latest version of ASA are given in appendix C. Layer measurements, where they were available, were used for input parameters in the simulations.

The p-(a-SiC:H)-layer thickness was varied—as in the experiment—from 0 to 20 nm. In order to keep the model as simple as possible, the defect concentration was assumed to be constant in depth for all layers, however on a different level for each layer, similar to earlier simulation studies [Stuckelberger 12]. In our simulations, defects were represented by amphoteric defect states that represent dangling bonds and are discussed in detail in chapter 4. To simulate the LID, the defect concentration of the intrinsic *a*-Si:H and *a*-SiO:H layers was increased by a factor of 5,[1] and the defect concentration of the *p*-(*a*-SiC:H) layers was increased by a factor of 10, as reported in the following sections. We would like to stress that all other parameters were not modified for simulating LID, especially not E_{act}, bandgap (E_{g}), or other parameters linked to layer properties that were found to be stable in section 8.3.2.

8.4.1 ASA-simulated light-induced changes of the open-circuit voltage

The choices for the initial and degraded states are reported in Tab. 8.3. Here, the data sets *p*-(*a*-SiC:H) and *a*-Si:H (A) have been used. Figure 8.8b shows the results of these simulations.

Table 8.3: Defect concentrations of the *p*-(*a*-SiC:H) layer and intrinsic *a*-Si:H layer, for ASA input of the solar cell simulation in the initial and degraded states.

Layer	$N_{\mathrm{db}}^{\mathrm{ini}}$	$N_{\mathrm{db}}^{\mathrm{deg}}$
p-(*a*-SiC:H)	$1.0 \times 10^{19}\,\mathrm{cm}^{-3}$	$1.0 \times 10^{20}\,\mathrm{cm}^{-3}$
a-Si:H (A)	$5.0 \times 10^{16}\,\mathrm{cm}^{-3}$	$1.0 \times 10^{17}\,\mathrm{cm}^{-3}$
a-Si:H (B)	$1.5 \times 10^{17}\,\mathrm{cm}^{-3}$	$2.0 \times 10^{17}\,\mathrm{cm}^{-3}$
a-Si:H (C)	$1.5 \times 10^{17}\,\mathrm{cm}^{-3}$	$3.0 \times 10^{17}\,\mathrm{cm}^{-3}$

Starting from the initial state of the solar cells (p_{ini}, i_{ini}), the V_{oc} decreases with increasing defect concentration N_{db} in the *i*-layers (p_{ini}, i_{deg}), for all *p*-(*a*-SiC:H)-layer thicknesses.

However, if the N_{db} in the *p*-(*a*-SiC:H) layer is modified (from (p_{ini}, i_{ini}) to (p_{deg}, i_{ini})), an increase of V_{oc} is observed for all *p*-(*a*-SiC:H)-layer thicknesses. This is on first view surprising, as this layer is considered to be an electronically dead layer, and it seems counterintuitive that a solar cell can be improved by adding defects. In the following subsection, the underlying mechanism will be detailed.

Only when the N_{db} increases in both the *p*-(*a*-SiC:H) layer and the *i*-layers are combined does the simulation reproduce the characteristic light-induced changes of V_{oc}, i.e. an increase for thin, and a decrease for thick, *p*-(*a*-SiC:H) layers that we observed experimentally, with a critical layer thickness for which V_{oc} does not change during light soaking.

Note that these findings are not the result of a unique choice of simulation parameters. In fact, changing the input parameters such as E_{act}, E_{g}, or N_{db} within a reasonable range changes only the level of V_{oc} and the critical *p*-(*a*-SiC:H)-layer thickness, but the general trend of

---

[1] One would expect that a defect-concentration increase by a factor of 5 would be detected in the PDS measurements shown in Fig. 8.3b, which was not the case. We suppose that the additional absorption due to the light-induced defects is hidden in our measurements in the strong absorption of states that are not light-induced defects: the absorption of this *p*-(*a*-SiC:H) layer at 1.2 eV is about 100 times stronger than for intrinsic *a*-Si:H material. The absorption change by light-induced defects is smaller than the measurement error.

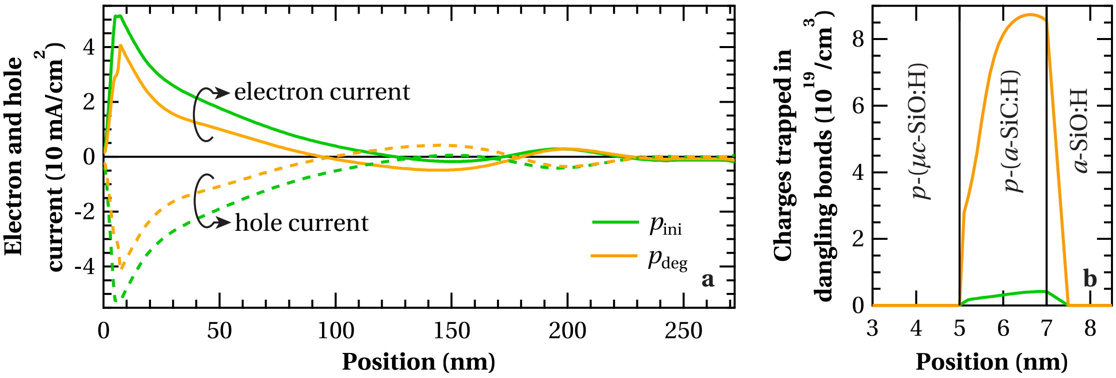

Figure 8.9: (a): Electron and hole current as a function of the position in the solar cell, where 0 marks the front ZnO/p interface and 272 nm the back n/ZnO interface. The two curves correspond to the solar cells with 2-nm-thick p-(a-SiC:H) layers marked in Fig. 8.8b. (b): Concentration of charges that are trapped in the defects in the p-(a-SiC:H) layer.

an increasing V_{oc} for thin and a decreasing V_{oc} for thick p-(a-SiC:H) layers is maintained. Depending on the choice of the input parameters, “thin” can mean 0 to more than 20 nm, and “thick” denotes thicknesses above the critical p-(a-SiC:H)-layer thickness.

8.4.2 The physics behind the light-induced increase of the open-circuit voltage

We focus here on solar cells with a 2-nm-thick p-(a-SiC:H) layer and compare the two cases (p_{ini}, i_{ini}) and (p_{deg}, i_{ini}), marked in Fig. 8.8b, to understand the V_{oc} increase.

Under open-circuit condition, the net current at the contacts is of course 0, all electron–hole pairs recombine somewhere in the solar cell, and the absolute values of the electron and the hole currents (both directional towards the p-layers at most positions in the solar cell) are the same, as shown in Fig. 8.9a.

We see there that the currents are lower for a degraded p-(a-SiC:H) layer as compared to its initial state. This is related to the increase of N_{db} which leads to an increase in the charges that are trapped in the p-(a-SiC:H) layer, and as this layer is p-type doped, the trapped charges are positive (see Fig. 8.9b). Vertical black lines represent here and in the following figures the simulated interfaces between layers as tabulated in Tab. 8.4.

Table 8.4: Positions of the layer interfaces in the ASA simulation that leads to a V_{oc} increase.

Layer 1	Layer 2	Position
p-(μc-SiO:H)	p-(a-SiC:H)	5 nm
p-(a-SiC:H)	a-SiO:H	7 nm
a-SiO:H	a-Si:H	17 nm

Figure 8.10a shows that the increased N_{db} in the p-(a-SiC:H) layer leads to an increased recombination there. Here, only the recombination increase due to the increased N_{db} is taken

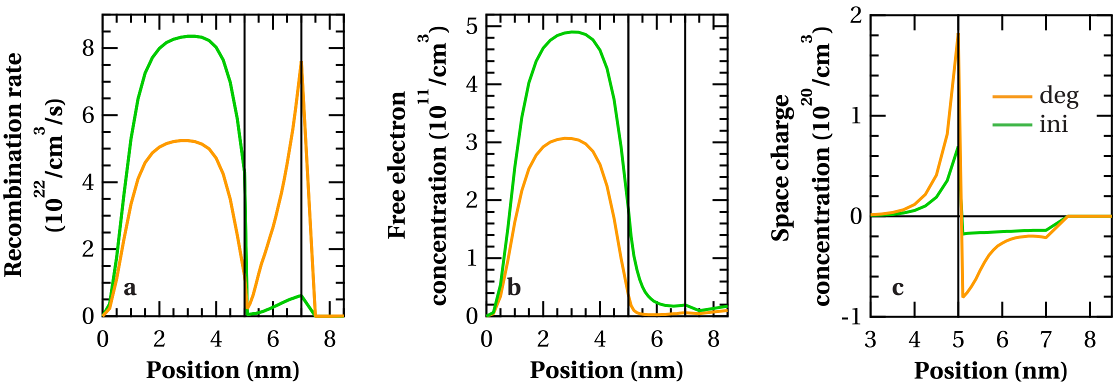

Figure 8.10: Electron–hole recombination rate (a), free-electron concentration (b), and space charge concentration in the p-(μc-SiO:H) and the p-(a-SiC:H) layers (c).

into account. This effect would even be enhanced if the increase of the capture cross section for electrons (the minority charge carriers here) were taken into account when the defects are charged [Beck 96, Shah 10, Stuckelberger 10, Stuckelberger 12].

As not many electron–hole pairs are generated in the p-type layers, the increased recombination in the p-(a-SiC:H) layer must lead to a decrease in recombination in the adjacent p-(μc-SiO:H) layer. However, since recombination decreases there more than it increases in the p-(a-SiC:H) layer, the total recombination in p-layers is reduced, but it is enhanced in the i-layers.

With increased N_{db} and recombination in the p-(a-SiC:H) layer, the mobility-lifetime product ($\mu\tau$) decreases, and hence the series resistance of that layer increases for charge carriers diffusing from the i-layers through the p-(a-SiC:H) layer and into the p-(μc-SiO:H) layer. These two effects reduce the recombination rate in the p-(μc-SiO:H) layer more than they increase it in the p-(a-SiC:H) layer, and lead therefore to a reduced concentration of free electrons as shown in Fig. 8.10b.

If there are fewer free electrons in the p-(μc-SiO:H) layer, the occupation probability of the states around the electron quasi-Fermi level (E_{F}^{n}) is reduced and E_{F}^{n} shifts towards mid-gap. Hence, the (positive) space charge concentration is increased (see Fig. 8.10c), and the electrons pushed out of the p-(μc-SiO:H) layer populate the p-(a-SiC:H) layer, where the (negative) space charge concentration increases. As an alternative picture, one can imagine a p^{+}/p interface (the activation energies of p-(μc-SiO:H) and p-(a-SiC:H) are 0.1 and 0.4 eV) where the free-electron concentration in the p^{+} layer is reduced, and hence the doping efficiency is increased.

Finally, the increased negative space charge concentration in the p-(a-SiC:H) layer shifts E_{F}^{n} there towards the conduction band edge, enhancing the quasi-Fermi-level splitting and thus the V_{oc}, as shown in the band diagram of the p-layers in Fig. 8.11. This mechanism explains observation (iii).

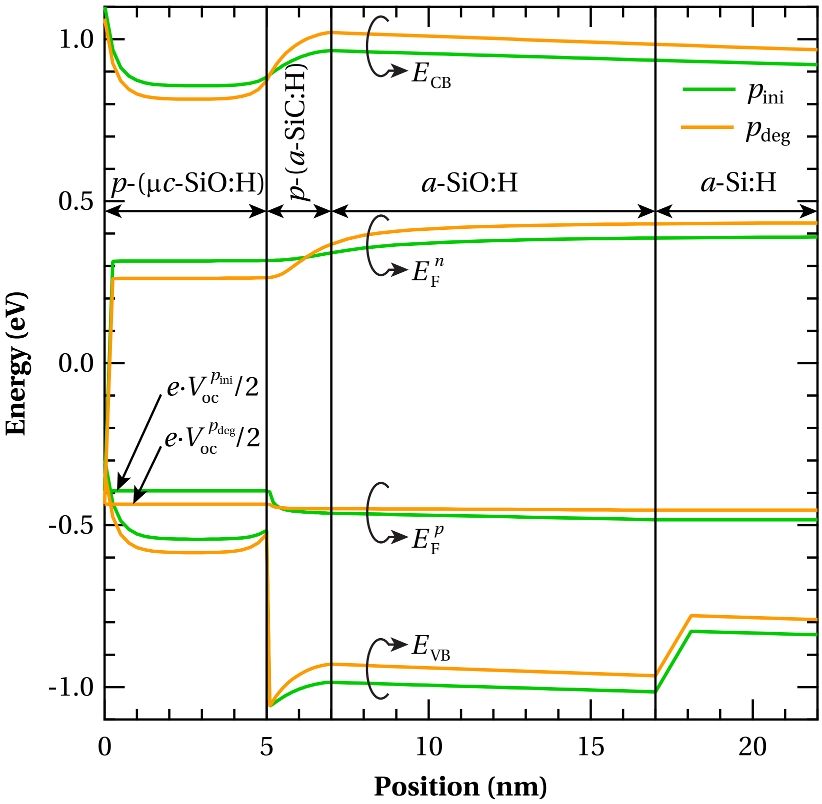

Figure 8.11: Band diagram of the p-i interface of a-Si:H solar cells with a 2-nm-thick p-(a-SiC:H) layer that explains the experimentally observed V_{oc} increase in that case.

8.4.3 The physics behind the light-induced decrease of the open-circuit voltage

Here, we focus on solar cells with an 8-nm-thick p-(a-SiC:H) layer, where a light-induced V_{oc} decrease is observed. All other simulation parameters are the same as before. Now, the V_{oc} decrease due to the i-layer degradation dominates the V_{oc} increase due to the p-(a-SiC:H)-layer degradation.

Figure 8.12 shows the band diagram for solar cells with a focus on the essential parts in the p-, i-, and n-layers. In order not to confuse the degradation effects of the p- with the i-layers, we consider here only the N_{db} increase from the initial (p_{ini}, i_{ini}) to the degraded (p_{ini}, i_{deg}) state as marked in Fig. 8.8b. We see that the quasi-Fermi-level splitting in the i-layer decreases with the creation of electronic states in the bandgap, which leads directly to a V_{oc} decrease and explains observation (iv).

Thus, we could explain the light-induced V_{oc} increase for thin, and the V_{oc} decrease for thick, p-(a-SiC:H) layers only by increasing the N_{db} in the p-(a-SiC:H) and i-layers. This corresponds exactly to the common understanding of the SWE and should therefore be reversible by annealing, which is observation (v).

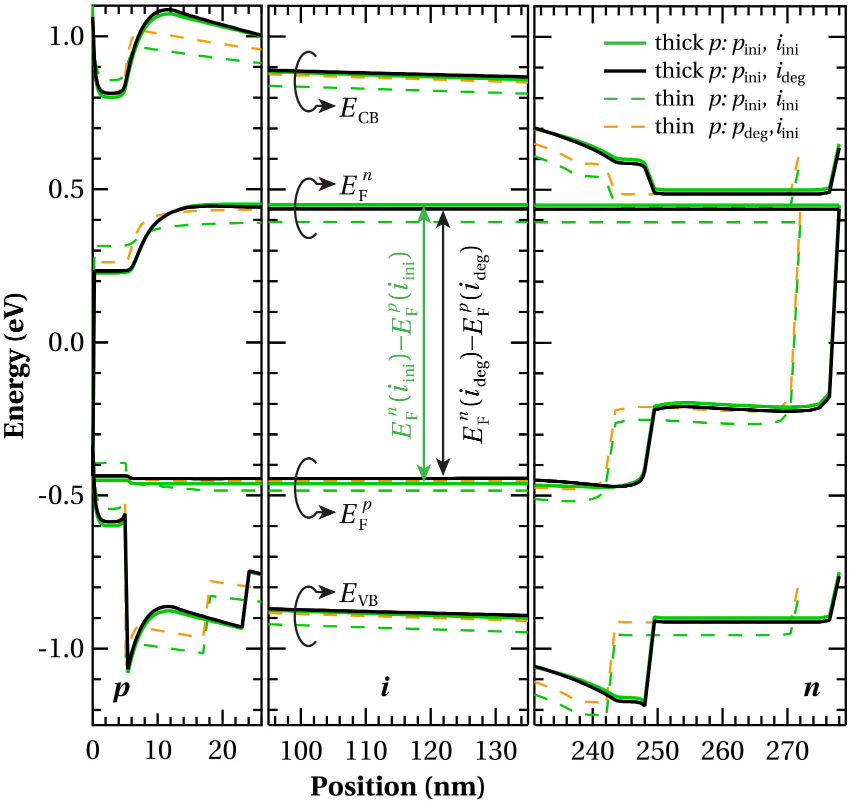

Figure 8.12: Band diagram of *a*-Si:H solar cells with an 8-nm-thick *p*-(*a*-SiC:H) layer that explains the experimentally observed V_{oc} decrease in that case.

In Fig. 8.12, the band diagrams of the cell with the 2-nm-thick *p*-(*a*-SiC:H) layers (shown in Fig. 8.11) are overlaid. The solar cell with the degraded *p*-(*a*-SiC:H) layer (p_{deg}, i_{ini}) has the same V_{oc} as the cell with the 8-nm-thick *p*-(*a*-SiC:H) layer in the (p_{ini}, i_{ini}) state, and the energy levels follow each other closely. This demonstrates, as suggested above, that the quasi-Fermi-level splitting in the *p*-(*a*-SiC:H) layer is larger for degraded *p*-(*a*-SiC:H) layers, and that this layer can fulfill its task as well as a thicker *p*-(*a*-SiC:H) layer in the initial state. In contrast, the thinner *p*-(*a*-SiC:H) layer in the initial state is too thin—with its lower space charge concentration—to push the E_{F}^{n} level sufficiently towards the conduction band. Thicker *p*-(*a*-SiC:H) layers are needed for a sufficiently large integrated charge concentration, which explains observation (i).

8.4.4 Generalisation of the light-induced changes of the open-circuit voltage

For the experimental proof and explanations of the light-induced V_{oc} increase and decrease above, we used the full layer stack as detailed in Fig. 8.1, which corresponds to a standard cell design at our institute. However, the results are not specific for this layer combination but generally valid as the following considerations show:

- *a-SiO:H buffer not necessary:* Using the same ASA simulation parameters as used above and detailed in the appendix, but without the a-SiO:H buffer layer, a V_{oc} increase for thin and a V_{oc} decrease for thick p-(a-SiC:H) layers is revealed.
- *p-(μc-SiO:H) layer not necessary:* ASA simulations using the parameters described in the appendix but without the μc-SiO:H layer is physically only reasonable if the interface with the front contact (previously ZnO/p-(μc-SiO:H), now ZnO/p-(a-SiC:H)) is adapted. Taking the different bandgaps of p-(μc-SiO:H) and p-(a-SiC:H) into account, we reduced the Schottky barrier at the interface with ZnO from 1.5 to 1.25 eV. This revealed also a V_{oc} increase for thin and a V_{oc} decrease for thick p-(a-SiC:H) layers, similarly to the case with p-(μc-SiO:H) layer.
- *Different band offsets possible:* One could think that the V_{oc} increase for thin and the V_{oc} decrease for thick p-(a-SiC:H) layers in the simulation is due to the chosen band-offset between the p-(μc-SiO:H) and the p-(a-SiC:H) layer (strong band-offset at the valence band, zero for the conduction band). We investigated this by modifying the electron affinities ("chi" in ASA input) from 4.0 to 4.1 eV for the p-(μc-SiO:H) and to 3.9 eV for the p-(a-SiC:H) layer, hence reducing the valence-band offset and enhancing the conduction-band offset. To observe a V_{oc} increase for thin p-(a-SiC:H) layers, it was thus necessary to decrease the bandgap of the p-(μc-Si:H) layer from 1.4 to 1.2 eV, which is still reasonable.

We see that our explanations are generally valid for different p-layer stacks with reasonably chosen simulation parameters. However, it seems that a strong valence band offset at the front-interface of the p-layer (in these simulations this is the interface ZnO/p-(a-SiC:H) or p-(μc-SiO:H)/p-(a-SiC:H)) is a general condition for a light-induced V_{oc} increase for thin and a V_{oc} decrease for thick p-layers.

8.4.5 Simulated substrate dependence

Porous zones in intrinsic a-Si:H above peaks of underlying ZnO were detected to cause a drop of V_{oc} in a-Si:H single-junction solar cells [Stuckelberger 13]. The part of the substrate dependence of V_{oc} that was not linked to a different effective p-(a-SiC:H)-layer thickness could be correlated there to the roughness dependence of porous zones. Such porous zones with voids contain more defects than dense a-Si:H material [Smets 03].

The ASA software package is not designed for a precise simulation of the electrical behavior of solar cells with inhomogeneous absorber layers. Three-dimensional simulation would be needed for that. However, we can simulate an increased average defect concentration with ASA: Here, we have performed the same simulation as for Fig. 8.8b, but with N_{db} higher by 1×10^{17} cm^{-3}, i.e. 1.5×10^{17} cm^{-3} for the initial state and 2×10^{17} cm^{-3} for the degraded state (data set B in Tab. 8.3). Note that we added a constant defect concentration, as we consider the defects from these voids to be independent from light soaking. This is in contrast to the LID, which we accounted for by multiplying N_{db} with a constant, as SWE-related N_{db} creation is proportional to the recombination rate through already existing defects.

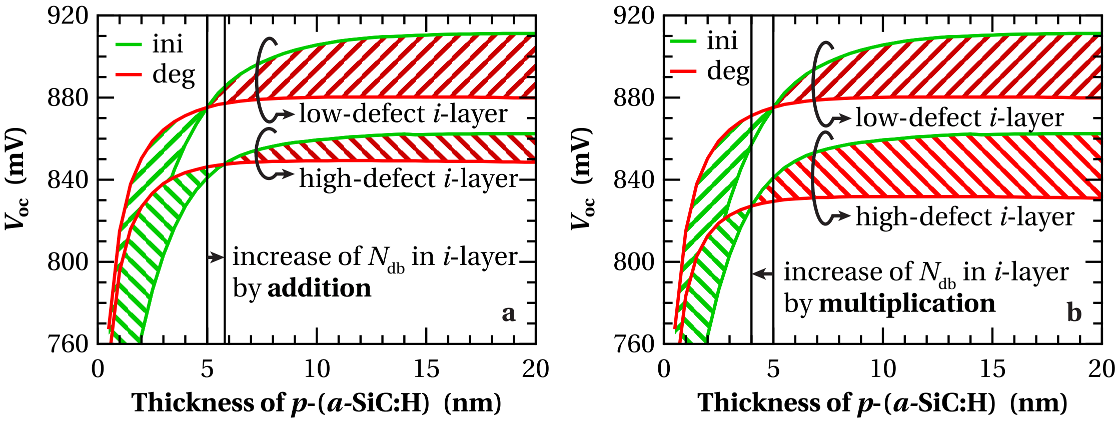

Figure 8.13: Simulation of the light-induced V_{oc} changes for solar cells with low and high defect concentrations in the absorber layer. The defect concentration is increased here by addition of a constant (a), simulating the presence of a porous phase in the absorber layer. In (b), the defect concentration is increased by multiplication with a constant, simulating poor absorber layer quality e.g. due to a high deposition rate.

Figure 8.13a shows the result of this simulation. We can clearly see that not only is the V_{oc} generally lower for more defective i-layers, but also that the critical p-(a-SiC:H)-layer thickness, for which V_{oc} before and after degradation is the same, is shifted towards thicker p-(a-SiC:H) layers (here, from 5 to 5.8 nm). Thus, the substrate-roughness-dependent shift of the critical p-(a-SiC:H)-layer thickness (observation (vii)) can be explained by a higher average defect concentration in the i-layer.

Similarly, observation (vi) can be explained: To compensate for the higher defect concentration in the i-layers and for charges trapped therein, thicker p-(a-SiC:H) layers are needed. However, V_{oc} saturates at lower values than for low-defect i-layers, because the quasi-Fermi-level splitting in the i-layer itself becomes the limiting factor.

8.5 Literature review

In this section, our explanations are discussed in context with reported observations of light-induced V_{oc} increase in the literature and put into relation with alternative explanations.

Among the reports on V_{oc} increase in the literature, this effect could often be observed for absorber layers with only a few defects, but not for high-defect absorber layers. To understand this, we need another simulation, whose result is presented in Fig. 8.13b.

The simulations with a low-defect i-layer are the same as those in Figs. 8.8a and 8.13a. There, we *added* a constant ($+1 \times 10^{17}\,\mathrm{cm}^{-3}$, data set B in Tab. 8.3) to N_{db} to simulate porous zones in the i-layer. Now, we would like to simulate homogeneous i-layers of bad quality and do so by *multiplying* N_{db} with a constant (×3), as changes in the light-induced defect concentration are assumed to be proportional to the initial state defect concentration (data set C). The degradation mechanisms of the p-(a-SiC:H) and the a-Si:H layers remain the same between the two cases. However, it is important to note that adding a constant shifts the critical p-(a-SiC:H)-layer thickness to higher values, while multiplication shifts it to lower values.

In this modeled solar cell, the case of a light-induced V_{oc} increase for low-defect i-layers but a V_{oc} decrease for high-defect i-layers corresponds to p-(a-SiC:H)-layer thicknesses between 4 and 5 nm—below the critical thickness for the low-defect i-layer, and above it for the high-defect i-layer. Solar cells optimized in the light-soaked state typically have p-(a-SiC:H)-layer thicknesses just below the critical thickness. Hence, a degrading V_{oc} during light soaking is often an indication that the stabilized solar cell efficiency could be higher with a thinner p-(a-SiC:H) layer.

These model results are in full agreement with experimental series of varying i-layer quality presented in other chapters: for the H_2 dilution series presented in sections 6.4.3 and 7.5 and the power series presented in section 7.6, we observed a stronger light-induced V_{oc} decrease for cells with poor absorber material (low dilution or high power) and a weak decrease (or even small increase) of V_{oc} for high-quality absorber materials. For these series, the critical p-layer thickness was known, but thicker p-layers were chosen on purpose for reproducibility. Therefore, we observed in most cases a light-induced V_{oc} decrease that was larger for poor-quality and smaller for high-quality absorber layers.

Our work relates to reported light-induced V_{oc} changes as follows:

- M. Isomura et al. [Isomura 98] point out that a relatively high H_2 dilution of the intrinsic a-Si:H absorber layer is needed (while not passing the transition to μc-Si:H), for an increase of V_{oc} during light soaking, and attribute this effect to the bulk rather than to the p-i interface without detailed explanation.

  Similarly, they see a strong enhancement of the light-induced V_{oc} increase with an enhanced ratio of high-dilution a-Si:Hto low-dilution a-Si:H thicknesses, while keeping the total thickness of these absorber layers constant.

  These observations are in agreement with our model, and might be a combination of two effects: The first one might be the one described by Fig. 8.13b: The absorber layer quality increases with increasing H_2 dilution up to the transition between a-Si:H and μc-Si:H. If the p-(a-SiC:H)-layer thickness is below the critical thickness for the low-defect i-layer, but above it for the high-defect i-layer, one observes a light-induced V_{oc} increase for the low-defect layer and a decrease for the high-defect layer.

  The second effect could be related to the bandgap increase of the absorber material with H_2 dilution: the reported V_{oc} in the initial state for low-dilution and high-dilution cells are very similar, which indicates that it is not the i-layer but the p-layer that is limits the V_{oc} for the high-dilution solar cell. With light soaking, the quasi-Fermi-level splitting in the p-(a-SiC:H) layer is increased, and V_{oc} is increased more strongly for the high-dilution cell because the p-(a-SiC:H) layer becomes less limiting, while the quasi-Fermi-level splitting in the i-layer becomes V_{oc}-limiting in the case of the low-dilution cell.

- P. St'ahel et al. [St'ahel 97, Roca i Cabarrocas 98] attribute the V_{oc} increase during light soaking to boron activation, based on experiments with absorber layers from H_2-diluted and pure SiH_4 plasmas, leading to low- and high-defect a-Si:H materials. Their conclusions were based on the constant photocurrent method (CPM) of layers and solar cells. However, they measured only dark conductivity without temperature dependence, hence a direct conclusion about E_{act} is not possible. Further, they observed in CPM measurements a light-induced increase of the defect absorption (ratio of absorption coefficient at 1.13 and 1.77 eV, $\frac{\alpha_{1.13}}{\alpha_{1.77}}$). As we and others [Matsui 14a] could not observe any change in E_{act} nor a change in defect absorption, they might have observed the effect that we explain by the simulations for Fig. 8.13b.
- K. Lord et al. [Lord 01] studied light-induced V_{oc} changes of solar cells with absorber layers right at the transition between a-Si:H and μc-Si:H. While hardly any change was observed for materials that are strongly dominated by a single phase (a-Si:H or μc-Si:H), a strong V_{oc} increase was observed for mixed-phase materials. These changes were explained by light-induced structural changes (light-induced amorphization), with details given on the reversibility of the structural changes at the phase interfaces.

  These observations may be related to the inhomogeneous biphasic structure that would require three-dimensional simulation and cannot be sufficiently explained by our simple model, although the effects described above (high-quality transition material, wide bandgap) may apply, and similar effects as at the p-(μc-SiO:H)/p-(a-SiC:H) interface could occur at the μc-Si:H/a-Si:H interface in the absorber layer.

  Later, the same authors reported [Yang 02, Yan 03c, Yue 03] that the V_{oc} increase of transition materials follows the characteristics of SWE (suppression of the V_{oc} increase by applying reverse bias voltage during light soaking, and observation of the V_{oc} increase by applying forward bias voltage in the dark). They concluded that V_{oc} increase should be caused by the same mechanisms as SWE, i.e. by recombination events. They explained the V_{oc} increase by a light-induced phase change (μc-Si:H to a-Si:H) that can be accounted for by a change in weighting between the diodes representing the μc-Si:H and a-Si:H phases.

  These studies are compatible with our models, but it remains unclear whether the process causing light-induced V_{oc} changes of these mixed-phase materials is similar to our explanations.
- E. Johnson et al. [Johnson 08, Johnson 10] observed the V_{oc} increase during light soaking for solar cells with absorbers grown at a low deposition rate (LR), but not at a high-deposition rate (HR), where V_{oc} decreased during light soaking.

  They attributed the V_{oc} increase to an increase of the built-in voltage (V_{bi}): "a redistribution (in energy) of states at the interface between the p and i-layers results in this increased effective mobility gap (most importantly, on the valence band side) and allows a greater band bending across the entire device" [Johnson 10]. This explanation is basically in agreement with ours of Fig. 8.13b. However, we think that it is sufficient to re-distribute the *occupation* of the energy states, but that a re-distribution of the energy of states themselves is not necessary, and that the quasi-Fermi-level change is mainly on the conduction band side. However, a re-distribution of the energy of states during degradation such as supported by the defect-pool model (discussed in section 4.3.2) would probably be in agreement with our model too; a verification of this would be possible with additional ASA simulations including the defect-pool model.

- Y. Poissant et al. [Poissant 03] from the same group reproduced different light-induced changes of solar cells with a-Si:H and polymorphous silicon absorber layers by modeling. However, they changed many simulation parameters between these materials, including capture cross sections, but did not consider defect generation in the p-(a-SiC:H) layer to play a significant role.

  Part of their experimental results can be explained by our Fig. 8.13b. For other parts, more simulations would be needed.

- T. Matsui et al. [Matsui 14b] presented V_{oc} increase during light soaking as a function of the p-(a-SiC:H)-layer thickness with similar results as presented here, but without a substrate dependence or detailing of the physical mechanisms behind the observed effects.

- B. Rech et al. [Rech 97a] correlated the light-induced V_{oc} changes with observed and simulated changes of dark $I(V)$ curves. They noted that, depending on the ratio of the interface recombination to volume recombination, a V_{oc} decrease or increase can be observed. Our observations generally agree with their explanations and with this contribution we provide the detailed simulations they asked for in their conclusions.

8.6 Conclusions

Series of a-Si:H single-junction solar cells were deposited using a high-efficiency baseline with initial efficiencies above 10%. Varying the p-(a-SiC:H)-layer thickness and the substrate roughness, we observed a light-induced V_{oc} increase for thin, and a light-induced V_{oc} decrease for thicker, p-(a-SiC:H) layers. The degradation kinetic measurements showed a logarithmic LID behavior with a single time constant.

By simulation of the experiments with ASA (a layer-by-layer approach), we reproduced all experimentally observed effects with a cell model that requires changing only the light-induced defect densities in the p-(a-SiC:H) and intrinsic layers. We attributed the light-induced V_{oc} increase to the creation of defects in the p-(a-SiC:H) layer that get charged and cause—via depletion of the p-(μc-SiO:H) layer—an increased negative space charge concentration in the adjacent p-(a-SiC:H) layer and thus an enhanced V_{oc}. In contrast, we attributed the V_{oc} decrease for thicker p-(a-SiC:H) layers to defect creation in the absorber layer, where the quasi-Fermi-level splitting is reduced. Simulations showed that these effects are not specific to our cell design but generally valid if the valence-band offset between the thickness-varied p-layer (here, the p-(a-SiC:H) layer) and the layer at the front of it (here, the p-(μc-SiO:H) layer) is large enough.

Earlier reported observations of V_{oc} increase by light soaking have been discussed and are generally in agreement with our experimental and simulated results. We were able to explain the often reported V_{oc} increase for high-quality absorber layers and a V_{oc} decrease for low-quality absorbers within the same model. No model reported before could explain so many aspects of reported light-induced V_{oc} changes with so few assumptions.

Measurements of p-(a-SiC:H)-layer properties by ellipsometry, photospectroscopy, PDS, FTIR, and dark conductivity revealed no obvious changes of this layer by light soaking. Although we took defect generation in the p-(a-SiC:H) layer into account in the simulations, we did not see such a change of defect states by PDS measurements (however, light-induced defect generation in doped a-Si:H layers is reported in literature, see e.g. [St'ahel 98]). We suppose that the additional absorption due to the light-induced defects is hidden in our measurements in the strong absorption of states that are not light-induced defects (the absorption of this p-(a-SiC:H) layer at 1.2 eV is about 100 times stronger than for intrinsic a-Si:H material)—measurements of higher precision could eventually clarify this.

For optimization of TF-Si solar cells, the fact that V_{oc} can be enhanced by light soaking with thin p-(a-SiC:H) layers is of great importance: despite the fact that V_{oc} stays in most cases below the V_{oc} for cells with thicker p-(a-SiC:H) layers, the efficiency can be higher (especially in multi-junction solar cells) due to less parasitic absorption. Further, thinner p-(a-SiC:H) layers lead to faster deposition; however, the effect of lower costs due to lower deposition times is negligible.

One can imagine that similar effects as presented in this chapter are also beneficial for other types of solar cells, especially for heterojunction solar cells with similar interfaces. Further, it should be investigated whether similar effects can be observed at the i-n interface. Typically, that interface is optimized much less than the p-i interface due to its lower impact on cell performance. However, more transparent, and hence thinner, n-layers get more important with increasing number of junctions in a solar cell stack.

9 Tuning hydrogenated amorphous silicon to its extremes

The studies of different absorber layers and development of doped layers led to remarkable results on the cell level. Particularly, we were able to tune the bandgap of hydrogenated amorphous silicon (a-Si:H) to its extremes, while keeping the material quality good enough for high solar cell performance.

On one hand, solar cells with a narrow-bandgap a-Si:H absorber layer provided short-circuit current densities (J_{sc}) of 18.2 $\frac{\mathrm{mA}}{\mathrm{cm}^2}$ with a 300-nm-thick absorber layer, and 20 $\frac{\mathrm{mA}}{\mathrm{cm}^2}$ at reverse bias for a cell with a 1000-nm-thick absorber layer. With the combination of a thick absorber layer and a rough substrate, we found a decrease in the external quantum efficiency (EQE) specific to short-wavelength light. We suggest that this charge-collection issue is a geometric electric-field effect.

On the other hand, the use of wide-bandgap a-Si:H absorber layers developed in two distinct deposition systems led to single-junction solar cells that provide open-circuit voltages (V_{oc}) above 1 V with fill factors (FF) of 71% (system B), and to $V_{\mathrm{oc}} \times FF$ products of 739 mV (Octopus system, with $V_{\mathrm{oc}} = 975\,\mathrm{mV}$ and $FF = 75.8\%$). The high-voltage cells from system B provided a V_{oc} of 760 mV under low illumination $\left(4\,\frac{\mathrm{W}}{\mathrm{m}^2}\right)$; this suggests that such cells are not only well suited for the application as top cells in triple- or quadruple-junction solar cells but also for low-illumination applications as single-junction solar cells.

In collaboration with T. Matsui, we developed a-Si:H solar cells on low-pressure chemical vapor deposition (LPCVD) ZnO in the triode reactor at AIST,[1] where SnO_2 substrates are standard. We obtained single-junction solar cells with efficiencies of 10% after light soaking and developed recipes for high-current applications varying the deposition recipe and the front and back electrode.

This chapter is organized as follows: section 9.1 focuses on achievements using narrow-bandgap absorber layers, section 9.2 on achievements using wide-bandgap absorber layers, and section 9.3 on achievements using absorber layers deposited in a triode reactor. Section 9.4 concludes this chapter.

Part of the results presented in this chapter were accepted for publication in Progress in Photovoltaics [Stuckelberger 14b].

---

[1] National Institute of Advanced Industrial Science and Technology (Japan), [AIST 14]

9.1 Narrow-bandgap absorber layers for high current densities

In this section, we show achievements of narrow-bandgap *a*-Si:H absorber layers for application in single-junction solar cells, as the top cell in micromorph tandem solar cells, as the bottom cell in *a*-Si:H/*a*-Si:H tandem solar cells, or as the second cell in quadruple-junction solar cells.

9.1.1 Motivation and deposition conditions

Based on the comparison of *a*-Si:H layers in chapter 6, we selected the absorber layer with the lowest bandgap still providing high-quality solar cells for this study.[2] This layer was deposited in the Octopus system at an excitation frequency of 13.56 MHz, a temperature of 230 °C, and a pressure of 0.4 mbar, using pure SiH_4 as the precursor gas (no H_2 dilution) and the lowest possible power, in this case 4 W. As detailed in chapter 5, it is not possible to ignite a plasma under these conditions. Hence, we ignited the plasma at higher pressure and using H_2, and swept to the nominal deposition conditions within a few seconds. The remainder of the solar cells presented in this section, particularly the doped layers, were made following the standard recipe presented in section 8.2.

To explore the maximum current density we can achieve in *a*-Si:H single-junction solar cells, we co-deposited a solar cell series varying the absorber layer thickness on substrates of five different roughnesses, all grown by LPCVD. These are, in the order of increasing thickness and substrate roughness: Z2 10', Z2 4', Z2 0', Z2.3 0', and Z5 0'. The solar cells on Z2.3 0' were structured into solar cells of 1.2 and of 0.25 cm^2 size; on the other substrates, the cell size was always 0.25 cm^2. The absorber layer thicknesses were 120, 200, 300, 500, and 1000 nm. Current densities were measured on the 1.2 cm^2 cells for more correct current measurement on rough substrates; the FF and V_{oc} were determined from the 0.25 cm^2 cells due to limitation of the large-cell performance by the series and parallel resistances.

9.1.2 Maximum current densities

Figures 9.1 and 9.2 show the EQE measurements and, for evaluation of the loss mechanisms, total absorption $(1-R)$ measurements of the solar cells with a 300- or 1000-nm-thick absorber layer, respectively; the deposition conditions are detailed in section 9.1.1. The abbreviation "no AR" indicates that no anti-reflective coating was applied; "with AR" means that pyramids providing geometrical light trapping [Escarré 12] were attached on the front glass. To access information about the charge collection, the EQE measurements were conducted at different reverse bias voltages.

---

[2] Preliminary tests indicate that higher deposition temperatures on the order of 250 °C are possible and lead to higher currents with good solar cell performance. However, the doped layers, particularly the *p*-type layers, need to be adapted correspondingly, or the cells suffer from boron-tailing characteristics.

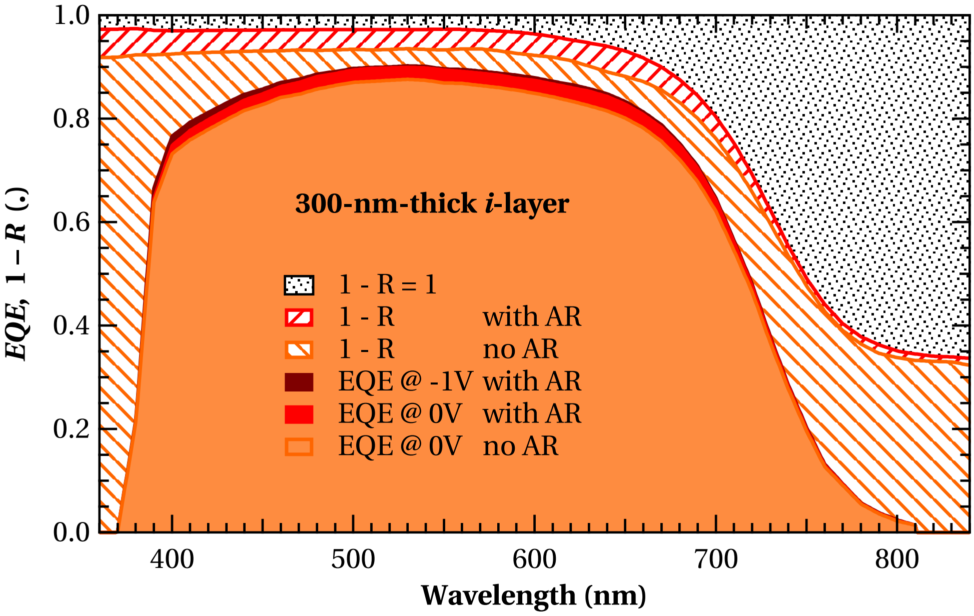

Figure 9.1: External quantum efficiency and 1 – reflectance measurements of a hydrogenated amorphous silicon single-junction solar cell deposited on Z2.3 0', providing a short-circuit current density of 18.2 $\frac{\text{mA}}{\text{cm}^2}$ with an anti-reflective coating (AR).

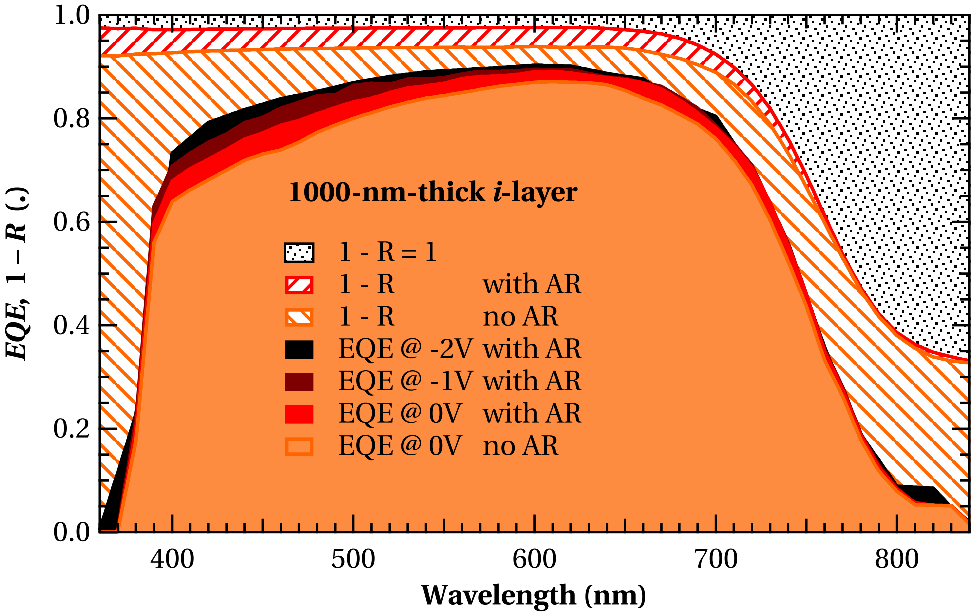

Figure 9.2: External quantum efficiency and 1 – reflectance measurements of a hydrogenated amorphous silicon single-junction solar cell providing a short-circuit current density of 19.5 $\frac{\text{mA}}{\text{cm}^2}$ and a current density of 20.0 $\frac{\text{mA}}{\text{cm}^2}$ under $-2\,\text{V}$ reverse bias voltage with an anti-reflective coating (AR).

We achieved a J_{sc} of 18.2 $\frac{\mathrm{mA}}{\mathrm{cm}^2}$ for solar cells with a 300-nm-thick absorber layer, V_{oc} of 880 mV, and FF of 72%.

The solar cell with a 1000-nm-thick absorber layer provides an even higher J_{sc} of 19.51 $\frac{\mathrm{mA}}{\mathrm{cm}^2}$ and shows the potential to achieve more than 20 $\frac{\mathrm{mA}}{\mathrm{cm}^2}$ by applying a reverse bias voltage. These current densities are among the highest reported for single-junction *a*-Si:H solar cells and higher than the current densities of the cells with highest certified efficiency (17.3 $\frac{\mathrm{mA}}{\mathrm{cm}^2}$ after light soaking) [Green 14, Benagli 09]. The EQE-based current density measurements were confirmed by current-density–voltage ($J(V)$) measurements using masks.

The J_{sc} values obtained for different measurement conditions are summarized in Tab. 9.1. We emphasize that the doped layers have standard thicknesses such that the solar cells are electrically still well performing, indicated by the good charge collection visible as a small difference between $EQE(-1\,\mathrm{V})$ and $EQE(0\,\mathrm{V})$ and high V_{oc} and FF.

Table 9.1: Measurement conditions and short-circuit current densities obtained from solar cells with a 300- or 1000-nm-thick absorber layer.

i-layer thickness (nm)	300	300	1000	1000	1000
AR	no	yes	no	yes	yes
Bias voltage (V)	0	0	0	0	-2
J_{sc} $\left(\frac{\mathrm{mA}}{\mathrm{cm}}\right)$	17.7	18.2	18.8	19.5	20.0

9.1.3 External quantum efficiency: Dependence of the absorber layer thickness and substrate roughness

Figure 9.3 shows the EQE curves for all absorber layer thicknesses of the solar cells grown on Z2.3 0'. With increasing thickness, we observe two trends: first, the EQE in the long-wavelength part of the spectrum increases due to enhanced absorption in the active layer. Second, the EQE decreases in the short-wavelength part of the spectrum. The reason for this decrease will be investigated in the following paragraphs; one might expect charge collection issues for thick solar cells due to the decreased electric field. However, this effect should be visible as a decrease of the EQE over the whole spectrum, which is not the case.

Figure 9.4 shows the EQE measurements for all substrate roughnesses and the two extreme absorber layer thicknesses, 120 and 1000 nm. In addition, we show the relative gain in EQE, if a reverse bias voltage of $-1\,\mathrm{V}$ is applied: $\Delta_{EQE} = \frac{EQE(-1\,\mathrm{V})-EQE(0\,\mathrm{V})}{EQE(0\,\mathrm{V})}$. For the thin absorber layer (Fig. 9.4a), applying a bias voltage has only a small effect, indicating satisfying charge collection for all substrates. The substrate-roughness dependence of the EQE is small too. Only for the smoothest substrate (Z2 10'), the EQE is reduced at long wavelengths due to poorer light-trapping. For the thick absorber layer (Fig. 9.4b), we observe—same as in Fig. 9.3—that the EQE is lower at short wavelengths. In addition, we note that this decrease depends on the substrate roughness: with increasing substrate roughness, the

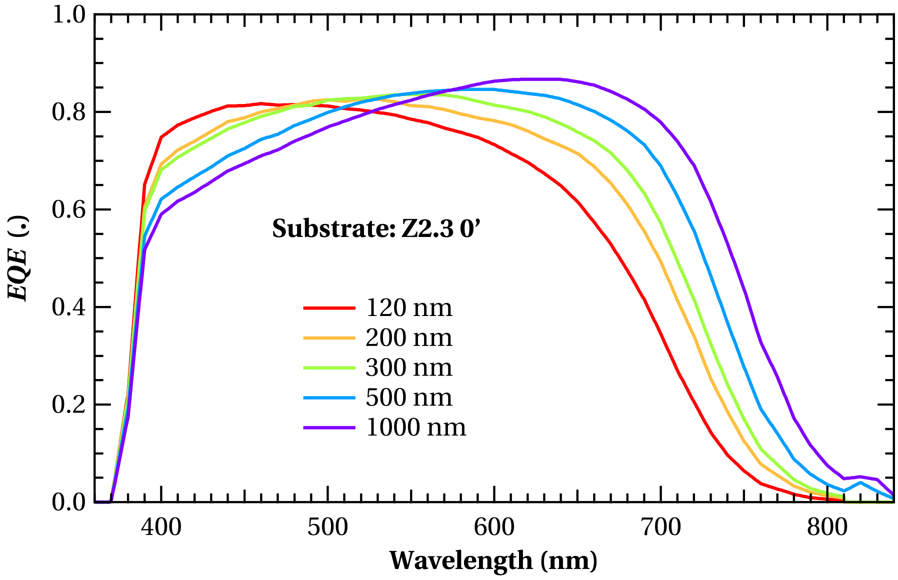

Figure 9.3: External quantum efficiency measurements, without anti-reflective coatings, for an absorber layer thickness series deposited on Z2.3 0’.

EQE drop in the short-wavelength range increases, and so does Δ_{EQE}. This means that it is not parasitic absorption but wavelength-specific charge collection issues that occur with increasing substrate roughness. In the V_{oc} and FF—shown in Fig. 9.5—this effect is visible as an increasing spread among different substrates with increasing thickness. (For other absorber layer thickness series covering thicknesses of less than 200 nm, we observed the contrary effect: thin solar cells grown on rough substrates suffered from a higher shunt probability than thicker cells, which manifested as lower V_{oc} and FF.)

In the following paragraphs, we present a mechanism that can explain the charge-collection issue observed for the combination of short wavelengths and rough substrates. Figure 9.6a shows a transmission electron microscopy image of an *a*-Si:H solar cell deposited in Octopus on Z2 0’. This serves as a template for the schematic representation of the electric field of an *a*-Si:H solar cell grown on rough substrates as shown in Fig. 9.6b.

Let us consider first a flat substrate: in this case, the nominal electric field, E_{nom}, decreases with increasing absorber layer thickness. However, for high-quality absorber layers, the defect concentration is typically low enough such that the charge collection is not seriously affected (this is not the case after light-induced degradation, see chapter 4).

For a rough substrate (in the p-i-n configuration, as in Fig. 9.6, this is the top electrode), E_{nom} is similar as for a flat substrate at places, where the two electrodes are parallel to each other. However, the electric field is enhanced at peaks of the electrodes and reduced in the valleys. This detrimental effect is shown in Fig. 9.6b where the incoming light is drawn: in the valley of the top electrode, the electric field is weak at the p-i interface, where short-wavelength light is predominantly absorbed. Therefore, weakening the electric field there reduces the charge collection, hence the EQE, specifically for short wavelengths. For the inverse geometry (peaks in the top electrode, valleys in the bottom electrode), this effect is less detrimental because of lower light intensity and the spectral distribution of the light there.

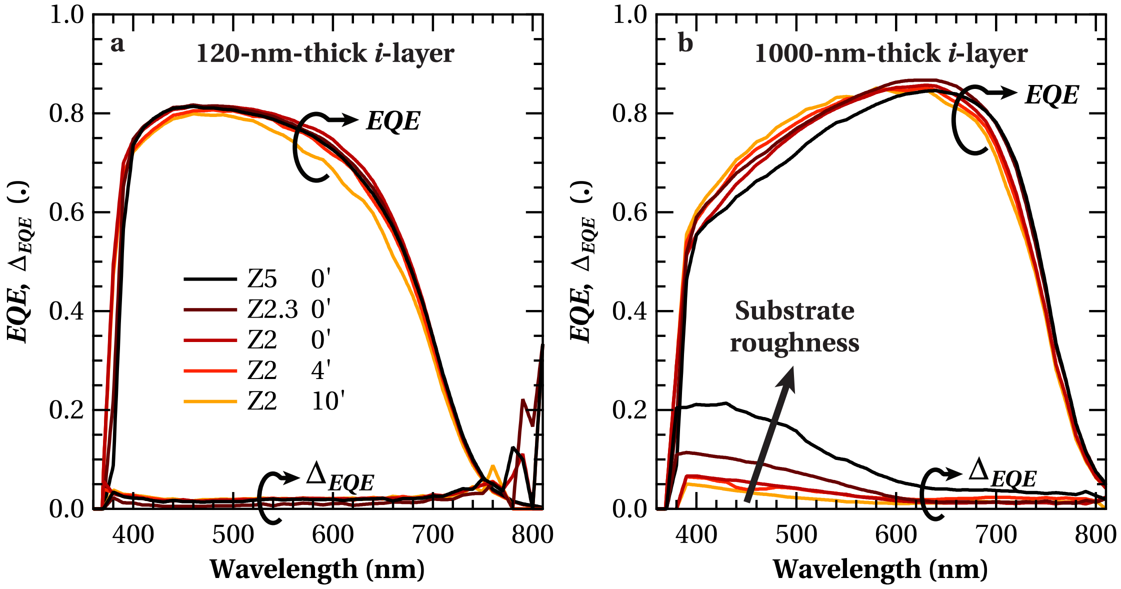

Figure 9.4: External quantum efficiency measurements and the relative gain by applying a reverse (negative) bias voltage $\left(\Delta_{EQE} = \frac{EQE(-1\,\mathrm{V})-EQE(0\,\mathrm{V})}{EQE(0\,\mathrm{V})}\right)$ for a substrate-roughness series with a 120-nm-thick (a) or a 1000-nm-thick (b) absorber layer.

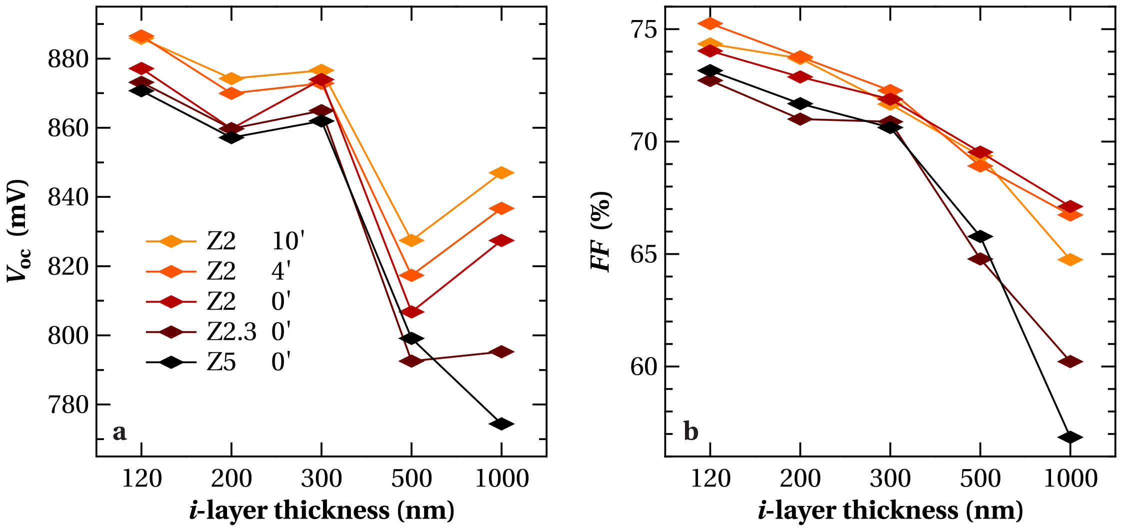

Figure 9.5: Open-circuit voltage (a) and fill factor (b) for an absorber layer thickness series. These solar cells were grown on substrates with increasing roughness from Z2 10’ to Z5. The marks represent the median values of the six best solar cells out of 12 on each substrate.

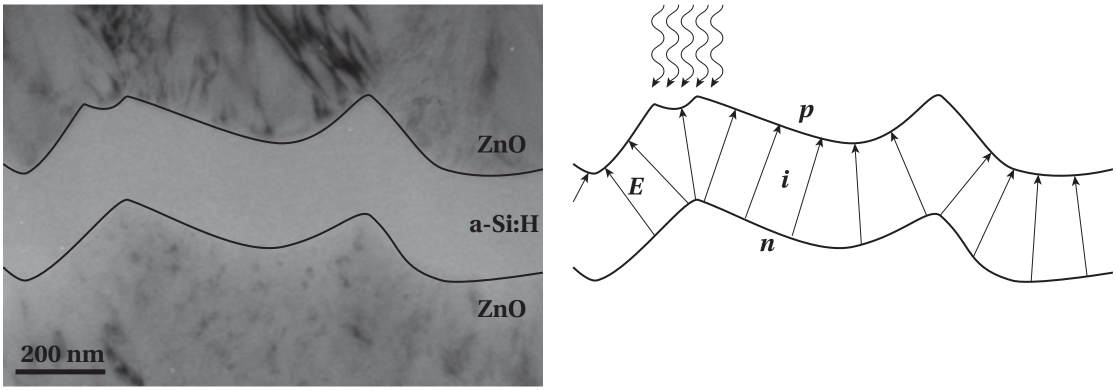

Figure 9.6: (a): Transmission electron microscopy image of a hydrogenated amorphous silicon solar cell grown on Z2 0' (taken by M. Duchamp) with emphasized interfaces ZnO/a-Si:H. (b): The interfaces ZnO/a-Si:H from (a) are drawn with a schematic representation of the electric field and the incoming light.

9.2 Wide-bandgap absorber layers for high voltages

9.2.1 Results from the Octopus system

Wide-bandgap a-Si:H absorber layers are used for the top cells in triple- or quadruple-junction solar cells, but could also be used in a-Si:H/a-Si:H tandem solar cells; for high-efficiency micromorph tandem cells, the current is too low.

Based on the developments shown in chapters 6 and 8, we optimized the solar cell performance with respect to the maximum $V_{oc} \times FF$ product in system B and Octopus. Two master's students under our supervision supported these developments: F. Maurizio investigated wide-bandgap absorber layers in the Octopus system [Maurizio 12], and N. Almat investigated boron- and gallium-doped hydrogenated amorphous silicon carbide (p-(a-SiC:H)) layers in system B [Almat 14].

In the Octopus system, this led to a top cell with the characteristics shown in Tab. 9.2; the deposition conditions are given in the caption.[3] These values of $V_{oc} \times FF$ up to 739 mV are among the highest reported in the literature, although they were obtained with non-optimized doped layers. In particular, the p-type and n-type doped layers were deposited in the same chamber (chamber D; chamber C was out of order at the time of these developments). This explains at least partially the light-induced degradation that is stronger than expected. Further, the p-type layers are rather thick and lead to significant parasitic absorption particularly in the short-wavelength part of the spectrum. This, the low thickness and the rather smooth substrate morphology (hence, low light scattering) led to the low current density that is too low even for high-efficiency triple-junction applications (note that these J_{sc} values were

---

[3] While the nominal temperature was 200 °C, the actual temperature dropped to 180 °C during deposition as in-situ temperature measurements showed. The reactor heater was replaced afterwards. Other nominal temperature values given in this thesis correspond to the measured temperatures.

measured in single-junction solar cells with a back reflector, which overestimates the J_{sc} in the configuration as a top cell incorporated in multi-junction solar cells).

With the optimization of doped layers and the implementation of high-pressure absorber layers, we expect that solar cells with V_{oc} above 1 V can be obtained in the Octopus system, while keeping the FF above 75% and enhancing simultaneously the current density.

Table 9.2: Performance of solar cells with a 100-nm-thick wide-bandgap absorber layer, deposited in the Octopus system. The absorber layer was deposited in chamber A with H_2 and SiH_4 flows of 80 and 5 sccm, respectively (dilution 16) at 13.56 MHz excitation frequency, 5 W power, 1 mbar pressure, and at 200 °C. “Ini” denotes the as-deposited state, and “deg” the degraded state after 550 h of light soaking under standard conditions (AM1.5g, 1000 $\frac{\mathrm{W}}{\mathrm{m}^2}$, 50 °C).

Substrate	State	V_{oc} (mV)	FF (%)	$V_{oc} \times FF$ (mV)	J_{sc} $\left(\frac{\mathrm{mA}}{\mathrm{cm}^2}\right)$	Efficiency (%)
Z2 40’	ini	975	75.8	739	9.43	7.00
Z2 40’	deg	932	65.2	652	8.74	5.69
Z2 15’	ini	969	73.1	731	10.50	7.67
Z2 15’	deg	933	69.6	649	9.79	6.36

9.2.2 Results from system B

In contrast to the Octopus system, where most wide-bandgap absorber layers were deposited at 13.56 MHz, absorber layers in system B were deposited at 70 MHz. We reproducibly obtained V_{oc} values above 1 V, deposited on LPCVD ZnO substrates of different roughness (still with decreasing V_{oc} for enhanced substrate roughness). Note that we did not use oxide or carbon in the absorber layer to increase the bandgap but varied only the deposition temperature and the H_2 dilution.

Figure 9.7 shows the $J(V)$ characteristics of a solar cell deposited in system B in the initial state.[4] This cell was deposited on smoothly grown LPCVD ZnO, treated for four minutes with an Ar plasma (smooth 4’). This cell provides V_{oc} of 1.0 V with 71% FF and 9.4 $\frac{\mathrm{mA}}{\mathrm{cm}^2}$ at a light intensity of 1000 $\frac{\mathrm{W}}{\mathrm{m}^2}$. The measurement temperature of this cell was above 30 °C,[5] hence the V_{oc} was underestimated compared to the standard measurement temperature of 25 °C. Still, the obtained V_{oc} values—our maximum V_{oc} was 1.04 V at 30 °C—are among the highest reported values for *a*-Si:H single-junction solar cells. The FF is limited in these solar cells by the series resistance of the front ZnO.

Under very low illumination $\left(4\,\frac{\mathrm{W}}{\mathrm{m}^2}\right)$, this cell still provides 760 mV, which makes it a good candidate for powering small electronic circuits, e.g. for indoor applications.

---

[4] This cell was deposited shortly before the laboratory moved to another building, where the light-soaking facilities were not yet running. Therefore, we can show only the initial values here.

[5] At the moment of the measurement, the air-conditioning was not yet installed.

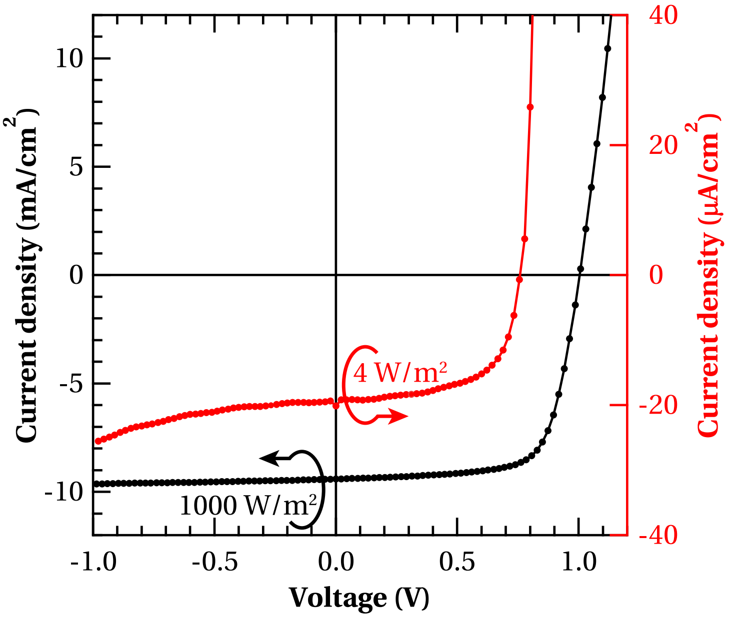

Figure 9.7: Current density–voltage curve of a hydrogenated amorphous silicon solar cell with an open-circuit voltage of 1.0 V under standard conditions and 760 mV at 4 W/m^2 light intensity, measured using a 0.4% grey transmission filter. The current densities are normalized to the result of an external quantum efficiency measurement.

All the layers except the absorber layer of this solar cell were optimized for narrow-bandgap absorber layers; the p-(a-SiC:H) was deposited using the recipe that performed best among all the layers investigated in [Almat 14] with the following deposition conditions: gas flows of 100 (H_2), 20 (SiH_4), 10 (CH_4), and 0.2 sccm ($B(CH_3)_3$), 70 MHz excitation frequency, 5 W power, 0.4 mbar pressure and 180 °C. The absorber layer was deposited at the same frequency and temperature, but using gas flows of 80 (H_2) and 3.6 sccm (SiH_4), 3 W power, and 0.5 mbar pressure. The optimization of the doped and buffer layers for cells with a wide-bandgap absorber layer would probably lead to a further V_{oc} increase.

This solar cell is part of a deposition temperature series for which the degradation kinetics and further trends are described in section 7.3.

9.3 Triode-deposited absorber layers for high stability

In triode reactors (see section 5.1.3), a-Si:H absorber layers can be deposited at a very low deposition rate and with predominantly SiH_3 as the precursor radical. Both aspects are reported to provide the most stable a-Si:H materials, and indeed, the lowest light-induced degradation and highest a-Si:H single-junction solar cell efficiencies are reported for triode-deposited absorber materials (see section 6.1.5 and the literature referenced therein). This motivated our collaboration with T. Matsui from AIST, who hosted us for two visits of three weeks and three months, respectively, for developing high-efficiency solar cells on LPCVD ZnO substrates. In the following sections, we show a few highlights of this development.

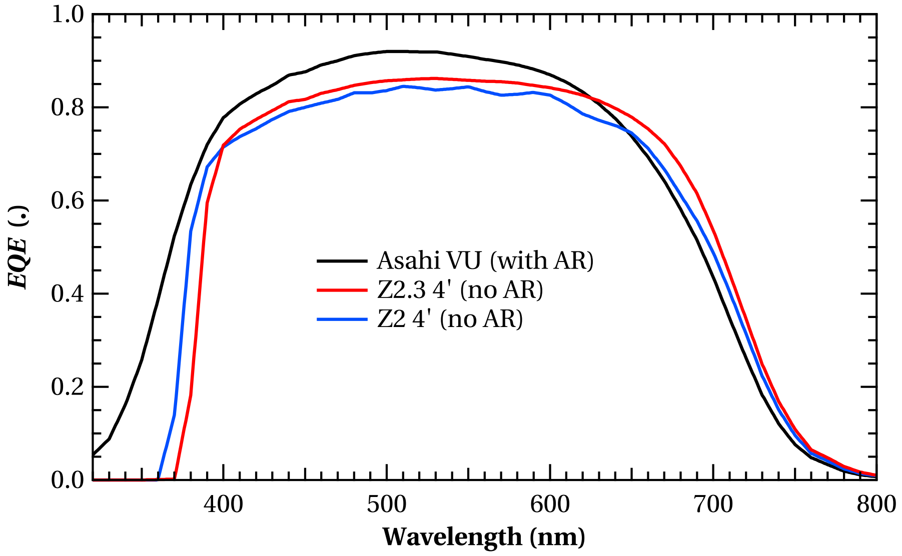

Figure 9.8: External quantum efficiency measurements of hydrogenated amorphous silicon single-junction solar cells, co-deposited on three standard substrates from AIST and PVLAB using a recipe providing high currents. The Asahi VU substrate (standard at AIST) includes anti-reflective coatings; the ZnO substrates Z2.3 4' and Z2 4' (grown by low-pressure chemical vapor deposition, standards at PVLAB) are without an anti-reflective coating.

9.3.1 Asahi vs. ZnO substrates using a high-current recipe

Figure 9.8 shows the comparison of *EQE* measurements of cells that were co-deposited on three standard substrates: Asahi VU [AGC 14] denotes here the stack of a TiO_2-based anti-reflective coating at the air/glass interface, a 1.1-mm-thick glass, a SnO_2-based transparent conductive oxide (TCO), and an anti-reflective coating based on TiO_2 protected with aluminum-doped ZnO at the TCO/silicon interface. Z2.3 4' and Z2 4' are standard LPCVD grown ZnO substrates deposited at PVLAB.

The need for high currents for micromorph tandem solar cells motivated the specific development of high-current devices on LPCVD ZnO. The development proceeded not only by trying to decrease the absorber-layer bandgap, but also by optimizing the doped layers that parasitically absorb light. Figure 9.8 shows the result of such a current-optimized recipe—in this case with a back electrode of LPCVD-grown Z2.3 for all substrates. With this design, we obtained 17.2 $\frac{\mathrm{mA}}{\mathrm{cm}^2}$ for the Asahi VU substrate, 16.3 $\frac{\mathrm{mA}}{\mathrm{cm}^2}$ for the Z2 4' substrate, and 16.8 $\frac{\mathrm{mA}}{\mathrm{cm}^2}$ for the Z2.3 4' substrate. These are among the highest initial current densities of *a*-Si:H single-junction solar cells deposited at AIST. Note that the Asahi VU substrate includes anti-reflective coatings in contrast to the ZnO substrates.

Further, these *EQE* measurements show exemplarily the difference between the substrates: SnO_2 has a wider bandgap than ZnO, and hence lets significantly more short-wavelength light pass to the silicon. In contrast, Asahi VU provides less light trapping, which leads to a lower

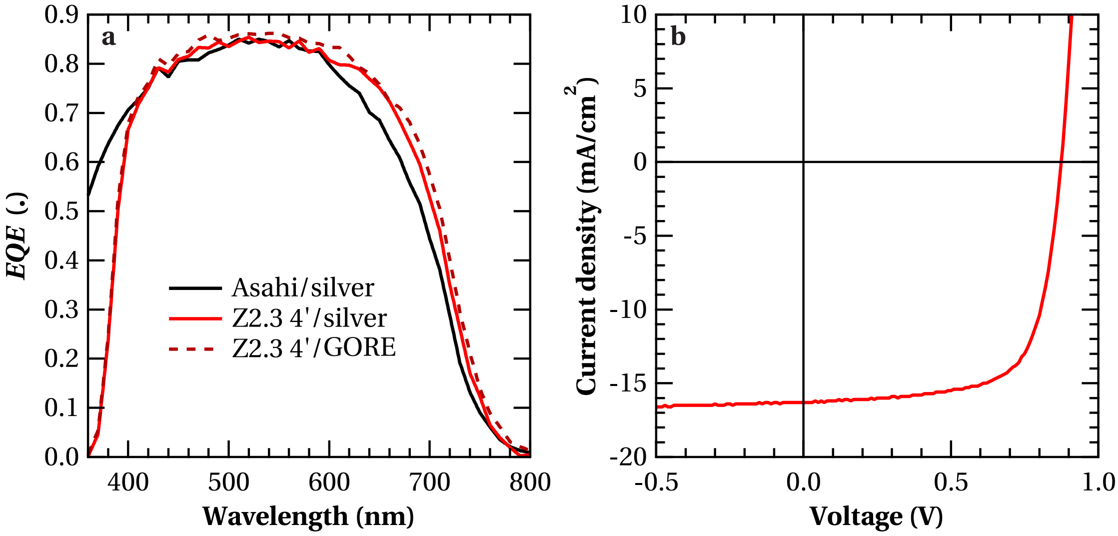

Figure 9.9: (a): External quantum efficiency of triode-deposited solar cells with different front electrodes (Asahi) and back reflectors (silver and GORE). (b): $J(V)$ curve of a light-soaked a-Si:H single-junction solar cell with 10.0% efficiency. Etched glass and LPCVD ZnO were used at the front and a silver reflector was used at the back.

response at long wavelengths. The wider bandgap of Z2 as compared to Z2.3 (a result of the stronger doping) is also the reason for the difference between the two corresponding EQE curves at short wavelengths. The appearance of slight interference fringes and the lower EQE of Z2 4' as compared to Z2.3 4' at long wavelengths indicate that this substrate has a lower surface roughness, hence, scatters less light. In contrast, the slightly lower EQE over the full spectrum is a consequence of parasitic absorption of that specific batch of ZnO which is not typical for Z2. The high maximum of Asahi VU is due to the anti-reflective coatings.

Subtracting the effect of the anti-reflective coatings (assessed by comparative tests with anti-reflective-coated ZnO substrates), cells on ZnO substrates showed mostly a higher current density. This is because there are more photons to collect at long than at short wavelengths within the spectrum relevant for a-Si:H solar cells.

9.3.2 Silver vs. GORE backreflectors in high-current recipe

We compare different back reflectors on triode-deposited cells in Fig. 9.9a. The first substrate is an Asahi type we used as our reference with the standard process flow that includes a thin aluminum-doped ZnO (ZnO:Al) layer at the interface with the n-layer and a silver back electrode serving as the back reflector simultaneously. The same process flow was used with a Z2.3 4' substrate. To compare the silver back reflector with the standard back reflector used at PVLAB, we deposited the ZnO:Al on the n-layer of a third substrate only, and measured the EQE using a quasi-Lambertian, 3-mm-thick back reflector from GORE [GORE 14] based on polytetrafluoroethylene (PTFE).

We can see that the GORE reflector performs slightly better in this experimental configuration. The measured current density of 17.0 $\frac{\text{mA}}{\text{cm}^2}$ (compared to 16.4 $\frac{\text{mA}}{\text{cm}^2}$ with a silver reflector) set the benchmark for solar cells fully processed at AIST without an anti-reflective coating.

The direct comparison of back-reflector stacks following the AIST standard (ZnO:Al & Ag) and the PVLAB standard (LPCVD ZnO & PTFE) on co-deposited solar cells revealed no significant difference.

9.3.3 Solar cell efficiency after light soaking

The highest solar cell efficiencies were not obtained with recipes optimized for high current density, as narrow-gap absorber layers deposited in the triode reactor suffered significantly more from light-induced degradation than medium-gap absorber layers. On some solar cells, we applied an anti-reflective coating with pyramids at the air/glass interface providing geometrical light trapping [Escarré 12] prior to light soaking, or performed a dry-etch of the front glass with a similar effect. Many solar cells with an anti-reflective coating showed a conversion efficiency between 9.7 and 10% after light soaking. The $J(V)$ curve of such a solar cell with 10.0% efficiency ($V_{\text{oc}} = 874\,\text{mV}$, FF=70.3%, J_{sc}=16.3 $\frac{\text{mA}}{\text{cm}^2}$) is shown in Fig. 9.9b. The light soaking was performed for 1000 h under AM1.5g spectrum at 50 °C. Unfortunately, the light intensity dropped during light soaking from 1000 to about 500 $\frac{\text{W}}{\text{m}^2}$.

9.4 Conclusions

While the focus of the previous chapter was on the systematic investigation of trends and the correlation of deposition conditions with layer and solar cell performance, we presented in this chapter highlights in terms of solar cell performance that followed from the optimization of deposition regimes that seemed promising in the systematic studies, mostly of the absorber layers, but also of the doped layers. In particular, we showed in this chapter results from

- *a*-Si:H single-junction solar cells with *narrow-bandgap* absorber layers, providing:
  - Short-circuit current densities of 18.2 $\frac{\text{mA}}{\text{cm}^2}$ with a 300-nm-thick absorber layer.
  - Short-circuit current densities of 19.5 $\frac{\text{mA}}{\text{cm}^2}$ with a 1000-nm-thick absorber layer.
  - Current densities above 20 $\frac{\text{mA}}{\text{cm}^2}$ at reverse bias voltage with a 1000-nm-thick absorber layer.

  For the combination of thick absorber layers and rough substrates, we found a decrease in the EQE specific to short-wavelength light. We explained this effect with a weaker electric field in valleys of the top-electrode.

- *a*-Si:H single-junction solar cells with *wide-bandgap* absorber layers, providing:
  - Open-circuit voltages up to 1.04 V under one-sun illumination.
  - Open-circuit voltages up to 760 mV under 0.4% of one-sun illumination.
  - $V_{\text{oc}} \times FF$ products of 739 mV under one-sun illumination.

- *a*-Si:H single-junction solar cells with absorber layers deposited in a *triode* reactor, providing:
  - Efficiencies of 10.0% after light soaking.
  - Short-circuit current densities of 17.2 $\frac{\text{mA}}{\text{cm}^2}$ on Asahi VU (with an anti-reflective coating and an LPCVD ZnO back electrode).
  - Short-circuit current densities of 16.8 $\frac{\text{mA}}{\text{cm}^2}$ on an LPCVD ZnO front electrode (no anti-reflective coating but with an LPCVD ZnO back electrode).
  - Short-circuit current densities of 17.0 $\frac{\text{mA}}{\text{cm}^2}$ on an LPCVD ZnO front electrode (no anti-reflective coating but with a silver back electrode).

An important advantage of *a*-Si:H is the tunability of the bandgap in a wide range. Together with variable (intermediate) reflectors, substrates and morphologies—from flat to pillars—this allows for applications of *a*-Si:H at different places in thin-film silicon solar cells:

- In single-junction solar cells, the low degradation and high current are most important. Therefore, the highest efficiency is obtained with materials with a low or medium bandgap on substrates with strong light scattering.
- In micromorph tandem solar cells, the low degradation and high current are at least as important as in single-junction solar cells—even more, as the device current should be bottom-limited for maximum performance due to the lower FF of the *a*-Si:H top cell after light soaking.
- In *a*-Si:H/*a*-Si:H tandem solar cells, the top cell and the bottom cell should absorb about the same amount of light. One possibility to match the currents is different thicknesses—but a wide-bandgap top-cell absorber and a narrow-bandgap bottom-cell absorber is another promising possibility, particularly as the top cell (deposited with conditions close to the amorphous-to-microcrystalline transition for a wide bandgap and enhanced stability, see chapter 6) would suffer less from light-induced degradation, and the narrow-bandgap absorber of the bottom cell, which is more sensitive to degradation, would absorb fewer high-energy photons.
- In triple-junction solar cells, the top cell should have a rather wide bandgap, but the current density needed in a matched device can still limit the bandgap of the top cell absorber layer.
- In quadruple-junction solar cells, the top cell as well as the second cell can be made from *a*-Si:H with similar requirements as in *a*-Si:H/*a*-Si:H tandem solar cells. However, the second cell must absorb more light in one pass due to the lack of a (full) back reflector.

These cases consider serially interconnected stacked solar cells; different criteria apply for the choice of the *a*-Si:H absorber type for four-terminal devices or devices for which criteria other than maximum efficiency under standard measurement conditions are critical. These can be low-illumination performance (e.g. for indoor applications), low temperature coefficients (e.g. for installations in warm climates), compatibility with rough substrates (e.g. for deposition on pillars), transparency at certain wavelengths (e.g. for architectural reasons), etc.

Hydrogenated amorphous silicon materials developed during this thesis found applications in many single- and multi-junction devices assembled by collaborators; some of the results are published—a list of co-authored articles can be found on page 242.

10 Conclusions

We conclude the thesis in this chapter: section 10.1 presents the general conclusions and achievements, summarizing major results chapter by chapter. In section 10.2, we relate this thesis to correlated fields of research and discuss general applications and perspectives.

10.1 Summary

10.1.1 Chapter 3: Class AAA LED-based solar simulator

We developed a solar simulator to test hydrogenated amorphous silicon (a-Si:H) solar cells under variable conditions and to measure in-situ degradation kinetics. The key characteristics of the simulator are:

- *Classification:* The solar simulator satisfies the highest classifications (class AAA) in the spectral range from 400 to 750 nm.
- *LED-based:* The light source is fully based on light-emitting diodes (LEDs) with inherently stable light intensity and long lifetime.
- *High intensity:* Up to five-sun-equivalent light intensity can be reached in continuous operation and, if the current electronics are replaced by faster electronics, also in flash mode.
- *Modularity:* The area with the mounted LEDs and the illuminated area are of equal size and parallel to each other; no concentrator optics is used in between. These aspects and modular LED arrangement (with corresponding electronic cards) allow for easy up- and down-scalability.
- *Low cost:* We designed electronic circuits for low-cost power supply.
- *Flexibility:* Spectral flexibility is provided by eleven types of individually controlled LEDs, the light intensity can be varied quasi-continuously, and the sample stage is temperature controlled.
- *Adaptability:* The LEDs can be changed to expand the spectrum into the ultraviolet or infrared (e.g. for crystalline silicon (c-Si), organic, or perovskite solar cell measurements).

The simulator is connected to a current-voltage measurement setup for tracking performance for up to 30 devices with a four-point probe during illumination. Within this thesis, the solar simulator was mainly used to measure the light-induced-degradation (LID) kinetics presented in chapter 7.

10.1.2 Chapter 4: Modeling and solar cell analysis

We evaluated and extended different approaches of modeling *a*-Si:H solar cells with respect to charge collection and compared the modeling approaches with experimental results, particularly from solar cell series with varied absorber layer thicknesses.

We developed a simple model with the goal of creating a tool that intuitively describes charge collection effects in thin-film solar cells, while providing experimental access to crucial parameters. We used the model to estimate the contributions of free charge carriers, charges trapped in valence and conduction band tails, and charged dangling bonds to the electric field deformation and hence to the charge collection.

This model was compared to other simulations and the experimentally determined collection voltage. The simulations indicate—in agreement with the experimental results—that free electrons and holes do not contribute significantly to the electric field deformation but that negative charges trapped in the band tail close to the i-n interface contribute most to the electric field deformation if a constant defect concentration distribution is assumed. Light soaking generates defects predominantly close to the p-i interface. Therefore, the positively charged defects are detrimental after light soaking, and *a*-Si:H solar cells are often limited by the p-i interface.

10.1.3 Chapter 5: Plasma physics of hydrogenated amorphous silicon deposition

To provide a solid basis for investigations of the performance of layers and solar cells grown by plasma-enhanced chemical vapor deposition (PECVD), we investigated the plasma properties with methods that are accessible in industrial reactors. First, we measured the optical emission spectra of the plasmas for all process gases typically used for thin-film silicon solar cells. Second, we measured the electrical power as a function of the pressure in analogy to Paschen measurements of the breakdown voltage as a function of the pressure–interelectrode-distance product. Here, we distinguished between the minimum power needed for plasma ignition with and without an external electron source, and the extinction power. For all process gases we measured the extinction power as a function of the pressure at different frequencies and showed that these curves follow an adapted formulation of Paschen's law.

For the deposition of intrinsic *a*-Si:H layers, the Paschen curves of SiH_4 and H_2 are of particular importance, and we explained how their crossing is responsible for the fact that the H_2 dilution can make it impossible to sustain a SiH_4 plasma at low pressures, while it is mandatory to sustain a plasma at higher pressures.

Further, we explored extensively the deposition parameter space including temperature, frequency, power, gas composition and pressure. We provided experimental evidence and possible explanations for observed trends, including a linear increase in the deposition rate with power and temperature. The dilution dependence of the deposition rate is more complex: the deposition rate is limited by powder production at low dilutions, and by hydrogen etching and power dissipation by H_2 molecules at high dilutions. To account for the latter, we introduced the concept of the partial power, ascribing the deposition rate decrease with increasing H_2 dilution to the increasing fraction of power that is used for the dissociation of H_2 molecules instead of SiH_4; this concept is in agreement with experimental data from our H_2 dilution series in ten different pressure and power regimes.

10.1.4 Chapter 6: Comparison of intrinsic hydrogenated amorphous silicon absorber layers

Mapping the two-dimensional deposition parameter space of the deposition pressure and H_2/SiH_4 ratio for excitation frequencies of 13.56 and 40.68 MHz, we covered the deposition regimes of low-pressure, protocrystalline, polymorphous, and high-pressure a-Si:H. We investigated the layer properties of these materials—particularly, with respect to their bandgaps and microstructure factor R^*—and inserted them into solar cells. For the comparison of absorber layers, we kept the cell design constant with dedicated buffer layers at the p-i and the i-n interfaces to reduce the effect of doped layers and interfaces. Comparing the initial and the degraded states and the relative LID of the solar cells using these intrinsic a-Si:H materials as absorber layers, and putting the results into relation with deposition conditions and layer properties, we established a catalog of intrinsic a-Si:H layers, resulting in a consistent picture of a-Si:H materials.

While optimum H_2 dilutions leading to relative LID below 15% were identified for all process pressures, the process windows leading to such results become narrower for increasing deposition pressure due to powdery plasmas at low dilutions. The best cells reached efficiencies of 8.7% and fill factors (FF) of 68% after light soaking without anti-reflective coatings.

Light-induced degradation was shown to correlate with the microstructure factor R^*, which has a sharp minimum for high pressures but depends only a little on the H_2 dilution for lower pressures. However, the comparison of R^* with the relative FF losses of the corresponding solar cells revealed a strong scattering, showing the limited predictive power of R^* for solar cell performance.

While the same trends of solar cell performance in terms of short-circuit current density (J_{sc}), open-circuit voltage (V_{oc}), FF, and efficiency were observed for cells co-deposited on four substrates with different roughnesses, their sensitivity changed considerably with the substrate roughness. In particular, the substrate dependence of V_{oc} increases from about 10 to 40 mV from low to high H_2 dilutions (narrow- to wide-bandgap material). In scanning electron transmission microscopy (STEM) images of solar cells with a very wide-bandgap absorber layer, chains of small voids or porous zones in the form of platelets were identified above peaks of the underlying ZnO. On rough substrates, these zones—represented by weak diodes—may lead to a decrease of V_{oc} and limit the use of wide-bandgap materials to rather smooth substrates. Further investigations will show whether this substrate dependence can be reduced using other wide-bandgap absorber materials deposited right at the transition between amorphous and microcrystalline silicon. However, we assume that this detrimental effect is intrinsically linked to high H_2 dilutions needed for the very wide bandgap, as we observed the trend of increased substrate-roughness dependence for deposition pressures ranging from 1 to 9 mbar.

10.1.5 Chapter 7: Kinetics of light-induced degradation

We studied the light-induced degradation of solar cell series under accelerated light soaking at three-sun-equivalent light intensity and found the following trends for relative performance changes:

- *H_2 dilution:* The higher the better. The upper limit is given by the amorphous-to-microcrystalline transition or acceptable current density.
- *Power:* The lower the better, if the deposition temperature is not too high. The lower limit is given by plasma extinction and economical considerations.
- *Absorber-layer thickness:* The thinner the better. The lower limit is given by the acceptable current density or shunt issues.
- *p-layer thickness:* The thinner the better. The lower limit is found when the V_{oc} drops strongly for thinner p-layers. This is around the critical p-layer thickness for which the V_{oc} is not affected by light soaking.
- *Excitation frequency:* No significant difference could be found, if the deposition pressure and dilution are adapted to the frequency. Eventually, higher frequencies lead to slightly more stable materials.
- *Temperature:* Only a weak deposition-temperature dependence of LID was found. The lower limit is given by too many defects, the upper limit by H_2 effusion.

In general, we did not observe a stabilization of the solar cell performance within the typical light-soaking time of 24 h, corresponding to more than 1000 h of light soaking under standard conditions. Instead, the solar cells continue to degrade with time. Often, the kinetics can be approximated by a logarithmic degradation, the slope (in semi-logarithmic scale) changing typically less with time than with deposition conditions. We cannot confirm the presence of faster degradation in the beginning due to void-related defects as reported in the literature.

10.1.6 Chapter 8: Light-induced changes of the open-circuit voltage

In several series of *a*-Si:H solar cells in which we varied the thickness of the boron-doped hydrogenated amorphous silicon carbide layers (*p*-(*a*-SiC:H)) and the substrate roughness, we observed a light-induced V_{oc} increase for thin, and a light-induced V_{oc} decrease for thicker, *p*-(*a*-SiC:H) layers. These effects were enhanced with increased substrate roughness.

Measurements of layer properties served as the input for the simulation of the solar cells with ASA (a layer-by-layer approach). Here, we reproduced all experimentally observed effects with a cell model that requires only changing the light-induced dangling-bond concentrations in *p*-(*a*-SiC:H) and absorber layers. We attributed the light-induced V_{oc} increase to creation of defects in the *p*-(*a*-SiC:H) layer that get charged and cause—via depletion of the adjacent boron-doped microcrystalline silicon-oxide layer—an increased negative space charge concentration in the *p*-(*a*-SiC:H) layer and thus an enhanced V_{oc}. In contrast, we attribute the light-induced V_{oc} decrease for thicker *p*-(*a*-SiC:H) layers to defect creation in the absorber layer, where the quasi-Fermi-level splitting is reduced.

We discussed observations of light-induced V_{oc} changes reported in the literature and found a general agreement with our experimental and simulated results. Particularly, we were able to explain the often reported V_{oc} increase for high-quality absorber layers and the V_{oc} decrease for low-quality absorbers within the same model.

For optimization of thin-film silicon solar cells, the fact that V_{oc} can be enhanced by light soaking with thin *p*-(*a*-SiC:H) layers is of great importance: despite the fact that V_{oc} stays in most cases below the V_{oc} for cells with thicker *p*-(*a*-SiC:H) layers, the efficiency can be higher (especially in multi-junction solar cells) due to less parasitic absorption.

One can imagine that similar effects as presented in this chapter are also beneficial for other types of solar cells, especially for heterojunction solar cells with similar interfaces. Further, it should be investigated whether similar effects can be observed at the *i*-*n* interface. Typically, that interface is optimized less than the *p*-*i* interface due to its lower impact on cell performance. However, more transparent, and hence thinner, *n*-layers get more important with the increasing number of junctions in a solar-cell stack.

10.1.7 Chapter 9: Tuning hydrogenated amorphous silicon to its extremes

We tuned the bandgap of *a*-Si:H to its extremes without the use of precursor gases other than SiH_4 and H_2, while keeping the overall solar cell performance high.

We showed that, with narrow-bandgap absorber layers, J_{sc} values of 18.2 $\frac{\mathrm{mA}}{\mathrm{cm}^2}$ can be reached for cells with a 300-nm-thick absorber layer; with a 1000-nm-thick absorber layer, we reached a J_{sc} of 19.5 $\frac{\mathrm{mA}}{\mathrm{cm}^2}$, and under reverse bias voltage we extracted more than 20 $\frac{\mathrm{mA}}{\mathrm{cm}^2}$, showing the potential of very high currents with improved light management or in tandem devices. Such narrow-bandgap absorber layers are most suited for single-junction *a*-Si:H devices, in the top cell in micromorph tandem devices, or in the second cell in tandem-, triple-, or quadruple-junction thin-film silicon devices.

Increasing the bandgap of *a*-Si:H materials (lowering the deposition temperature and enhancing the H_2 dilution), we achieved solar cells with more than 1 V V_{oc} using a wide-bandgap absorber layer, providing 760 mV V_{oc} under 0.4% of one-sun illumination. Further, we obtained solar cells with $V_{oc} \times FF$ products of up to 739 mV. The wide-bandgap absorber layers used for such solar cells are most suited for use in the top cell of triple- or quadruple-junction thin-film silicon devices, or for high-voltage applications as single-junction solar cells.

For the highest efficiencies, we combined the core competences of AIST[1] (absorber-layer depositions in triode reactors) and PVLAB (solar cell deposition on the comparably rough ZnO front electrodes grown by low-pressure chemical vapor deposition, LPCVD). This led to solar cell efficiencies of 10.0% after light soaking and set benchmarks for the current of triode-deposited solar cells with short-circuit current densities of 17.2 $\frac{\text{mA}}{\text{cm}^2}$ on Asahi VU (with an anti-reflective coating) and 16.8 $\frac{\text{mA}}{\text{cm}^2}$ on LPCVD ZnO (without an anti-reflective coating).

10.2 Conclusions and perspectives

10.2.1 The future of hydrogenated amorphous silicon for thin-film silicon solar cells

A personal motivation for the investigation of *a*-Si:H materials was the possibility of contributing to a cleaner energy supply. Thin-film silicon (TF-Si) solar cells were, and still are, a promising candidate for generating power on the scale of terawatts, although the economic environment has become more difficult for this technology which suffers from lower conversion efficiency as compared to *c*-Si and other thin-film solar cell technologies.

Nevertheless, the large improvements achieved in recent years in the field of TF-Si solar cells with new world records at both the research and industrial level show that the potential of further improvements is still there, and we are convinced that the findings of this thesis can contribute to them as they have done already. Particularly, the use of high-quality materials explored here with wide and narrow bandgaps for absorber layers in tandem-, triple-, and quadruple-junction solar cells is promising, and the systematic comparison of their properties including substrate-roughness dependence allow us to judge which absorber material is best for which application. Further applications arise from the variability of the appearance, allowing for the visually pleasant integration of TF-Si solar modules into roofs.

Apart from solar modules for mass production, solar cells based on *a*-Si:H materials show interesting properties. One aspect is the bandgap that is well adapted to visible light. Therefore, under a spectrum with a blueshift as compared to AM1.5g (e.g., such as used mostly indoors)

---

[1] National Institute of Advanced Industrial Science and Technology (Japan), [AIST 14]

a-Si:H solar cells show a significantly higher efficiency. Another aspect is the very high ratio of photoconductivity to dark conductivity. This leads to lower efficiency losses compared to *c*-Si under low illumination, which is another argument for indoor applications and low-illumination applications in general. Note also that the solar cell design can be adapted correspondingly: for instance, LID and light trapping are typically less important indoors, hence, one can allow for thicker cells on smoother substrates and further enhancing the low-illumination response. Further applications of *a*-Si:H solar cells profit from the high voltage of single-junction solar cells—many electronic circuits need a minimum voltage on the order of 0.5 V which can be provided by *a*-Si:H solar cells even under very low illumination (in contrast to *c*-Si-based solar cells), and higher voltages can be obtained by serial interconnection of cells to micro-modules (in [Wyrsch 08], the authors demonstrated 180 V from a 3 mm × 3 mm module). With the increased use of low-power circuits in sensors etc., this type of application may increase in the future. Other applications profit from the possibility of flexible TF-Si solar modules—be it for lightweight rooftop modules or integrated in electronic equipment.

10.2.2 Alternative applications of hydrogenated amorphous silicon

The properties of *a*-Si:H make it an interesting material not only for TF-Si solar cells but also for other applications.

First of all, *a*-Si:H is the material that makes the difference between standard *c*-Si solar cells and heterojunction solar cells, which hold the current world record for *c*-Si-based solar cells: in heterojunction solar cells, contacts are passivated by *a*-Si:H. We believe that they can be further improved by optimizing the *a*-Si:H layers—not only with respect to passivation, but also by enhancing the bandgap for reduced parasitic absorption, and we hope that this thesis can contribute to that.

Second, *a*-Si:H can be used for different types of detectors ranging from medical applications to particle detectors and others—e.g., *a*-Si:H solar cells produced within the framework of this thesis were explored as position detectors in satellites. Such applications have in common that they profit from the large ratio of photoconductivity to dark conductivity, which manifests in a wide range of linear response.

Third, the application of *a*-Si:H in opto-electronic devices has attracted attention in recent years. It is used there as waveguide in various forms (e.g. as ring resonators as presented in [Abel 13]), which takes advantage of the low absorption of *a*-Si:H in the infrared spectral range (in most cases, a wavelength of 1550 nm is used). Within this thesis, we provided different types of *a*-Si:H materials to three institutes for such applications. In addition to technical applications in opto-electronic devices, such waveguides could also be useful for the investigation of the absorber-layer quality. An important quality criterion for waveguides is losses (measured in db/cm)—if these are not limited by defects induced by the waveguide processing, this could be a very precise (though rather complicated) method to measure the absorption of *a*-Si:H by defect states at the laser wavelength.

10.2.3 Methodological achievements

Another motivation for this thesis was to improve the methodology in a field of research that is experimentally less accessible than others. Particularly, methods like X-ray-based techniques, transmission electron microscopy (TEM), or Raman spectroscopy that provide sharp signals allowing for a detailed analysis of microscopic crystalline structures, are more difficult to use for amorphous materials that often reveal broad signals with overlapping peaks. The demanding characterization of amorphous materials encouraged us to investigate techniques of experimental access to *a*-Si:H to make it disclose its variety of structures and properties.

We showed that ellipsometry, Fourier transform infrared spectroscopy (FTIR) or TEM can contribute to the understanding of specific material properties. However, we believe that the most important contributions evolved from the correlation of experimental results obtained on different levels: for a variety of *a*-Si:H materials, we were able to correlate growth conditions from plasma properties to properties of the resulting layers and to the performance of these layers in solar cells including their degradation behavior. From these correlations on multidimensional series we learned more about these materials than what had been possible investigating single materials by sophisticated methods.

Particularly successful was the use of functional devices to study properties of *a*-Si:H as absorber layers—on the one hand to access bulk absorber properties, on the other, to access properties that are inherently linked to the device. The study of light-induced V_{oc} increase and decrease as a function of *p*-layer thickness, substrate roughness, and absorber-layer quality is an example of this: none of the single methods (layer property measurements, simulations, and solar-cell-performance measurements) could have satisfactorily explained the experimental results, but a consistent picture of the mechanisms evolved from the combination of these methods, with explanatory power not only for the presented results but for a whole variety of observations reported in the literature. Here and in other examples—e.g. electric-field deformation or the concept of partial SiH_4 power—we showed that simple models with drastic simplifications can provide an intuitive understanding of physical effects.

A Solar cell efficiency limits

The upper limit of the maximum open-circuit voltage (V_{oc}) for a single-junction solar cell is given by the bandgap of the absorber layer, $V_{\text{oc}} = \frac{E_{\text{g}}}{q}$, with the elementary charge q. Closer to experimental results but without any physical background is the rule of thumb $V_{\text{oc}} = \frac{2}{3} \cdot \frac{E_{\text{g}}}{q}$. Often, calculations of V_{oc} limits start from $\frac{E_{\text{g}}}{q}$ and consider further terms reducing the maximum V_{oc}.

For the models considered here, the maximum V_{oc} depends logarithmically on the generated electron–hole pairs. The main assumption is that the short-circuit current density $J_{\text{sc}}^{\text{single-pair}}$ is maximal for a given bandgap, if exactly one electron–hole pair is created and collected per photon whose energy is larger than the bandgap. This is the current density limit shown in Fig. 1.5c, calculated with the solar spectrum AM1.5g [ASTM 14b] from [ASTM 14a] with $1000\,\frac{\text{W}}{\text{m}^2}$ via

$$J_{\text{sc}}^{\text{single-pair}} = q \cdot N_{E_{\text{g}}}^{\text{AM1.5g}} \quad \text{with} \quad N_{E_{\text{g}}}^{\text{AM1.5g}} = \int_0^{\lambda_{E_{\text{g}}}} \frac{S_{\text{AM1.5g}}}{\frac{hc}{\lambda}}\, \text{d}\lambda. \tag{A.1}$$

Here $N_{E_{\text{g}}}^{\text{AM1.5g}}$ denotes the number of photons with an energy above the bandgap per unit surface and wavelength, λ the wavelength, h the Planck constant, c the speed of light, $S_{\text{AM1.5g}}$ the solar spectrum (in units of $\text{W}/(\text{m}^2\,\text{nm})$), and $\lambda_{E_{\text{g}}} = \frac{hc}{E_{\text{g}}}$ the wavelength of photons with the energy E_{g}.

M.A. Green suggests in [Green 82b] a semi-empirical model for the V_{oc} maximum:

$$V_{\text{oc}}^{\text{green}} = \frac{k_{\text{B}} T}{q} \cdot \ln\left(\frac{J_{\text{ph}}}{J_0} + 1\right) \quad \text{with} \quad J_0 \equiv 1.5 \cdot 10^8\,\frac{\text{mA}}{\text{cm}^2} \cdot e^{-\frac{E_{\text{g}}}{k_{\text{B}} T}}. \tag{A.2}$$

Here k_{B} is the Boltzmann constant, T the solar cell temperature, and J_{ph} the photoinduced current density (see also the discussion in section 4.2), which is here $J_{\text{sc}}^{\text{single-pair}}$. He calculates the FF as detailed in [Green 81, Green 82a, Green 82b] based on the equation of ideal diodes[1]

---

[1] As we consider here the ideal case, the ideality factor is set $n = 1$.

via

$$FF^{\text{green}} = \frac{\tilde{v}_{\text{oc}} - \ln(\tilde{v}_{\text{oc}} + 0.72)}{\tilde{v}_{\text{oc}} + 1} \quad \text{with} \quad \tilde{v}_{\text{oc}} = \frac{qV_{\text{oc}}}{k_{\text{B}}T}, \tag{A.3}$$

shown in Fig. 1.5b.

More fundamentally, H. Kiess et al. and W. Shockley with H.J. Queisser determined the maximum solar cell efficiencies from thermodynamic considerations [Shockley 61, Kiess 95]. For the V_{oc}, H. Kiess et al. found

$$V_{\text{oc}}^{\text{kiess}} = \frac{E_{\text{g}}}{q} + \frac{k_{\text{B}}T}{q} \cdot \ln\left(\frac{h^3c^2}{2\pi k_{\text{B}}T} \cdot \frac{N_{E_{\text{g}}}^{\text{AM1.5g}}}{E_{\text{g}}^2}\right). \tag{A.4}$$

W. Shockley and H.J. Queisser used in their original paper blackbody radiation for the solar spectrum; here, we calculate the Shockley-Queisser limit for the AM1.5g spectrum. The minimum recombination rate of charge carriers (only thermodynamically limited radiative recombination is considered) is

$$R_{\text{rec}}^{\text{Sh-Qu}} = \frac{2\pi}{c^2h^3} \int_{E_{\text{g}}}^{\infty} \frac{E^2}{e^{\frac{E}{k_{\text{B}}T}} - 1}\, \mathrm{d}E. \tag{A.5}$$

For the current density as a function of the voltage V applied on the solar cell, this gives the following upper limit of a $J(V)$ curve:

$$J^{\text{Sh-Qu}}(V) = q \cdot \left(N_{E_{\text{g}}}^{\text{AM1.5g}} - R_{\text{rec}}^{\text{Sh-Qu}} \cdot e^{\frac{q\cdot V}{k_{\text{B}}T}}\right). \tag{A.6}$$

For $V = 0$, we get the maximum short-circuit current density $J_{\text{sc}}^{\text{Sh-Qu}}$, for $J = 0$ the maximum open-circuit voltage $V_{\text{oc}}^{\text{Sh-Qu}}$:

$$J_{\text{sc}}^{\text{Sh-Qu}} = q \cdot \left(N_{E_{\text{g}}}^{\text{AM1.5g}} - R_{\text{rec}}^{\text{Sh-Qu}}\right) \quad \text{and} \quad V_{\text{oc}}^{\text{Sh-Qu}} = \frac{k_{\text{B}}T}{q} \cdot \ln\left(\frac{N_{E_{\text{g}}}^{\text{AM1.5g}}}{R_{\text{rec}}^{\text{Sh-Qu}}}\right). \tag{A.7}$$

At low temperatures, i.e. when $k_{\text{B}}T \ll E_{\text{g}}$ holds, recombination is negligible and the Shockley-Queisser limit $J_{\text{sc}}^{\text{Sh-Qu}}$ equals the single-pair limit $J_{\text{sc}}^{\text{single-pair}}$ as shown in Fig. 1.5c. (The calculations were made with $T = 298.15\,\text{K}$; the Shockley-Queisser- and the Kiess-limits are very close to each other for V_{oc}.)

From the maximization of $J \times V$ from equation (A.6), we get the maximum power point MPP, and hence the fill factor FF (see Fig. 1.5b), and with J_{sc} and V_{oc} finally the Shockley-Queisser limit for the conversion efficiency as shown in Fig. 1.5d. The single-pair limit, also shown there, marks the very upper limit, even neglecting thermodynamic recombination, using $V_{\text{oc}} = \frac{E_{\text{g}}}{q}$, $FF = 1$, and $J_{\text{sc}}^{\text{single-pair}}$.

B Solar simulator details

B.1 Light-intensity measurements

Absolute light-intensity measurements are far from trivial, but essential for solar cell characterization. Light intensity is measured mostly by one of the two following methods: one, by measuring the spectral irradiance followed by integration over the full spectrum. In this case, a high-quality spectrometer is needed with a time-consuming calibration of the spectrometer with a calibrated light source. The second method is by measuring the photocurrent or voltage generated in reference solar cells, photodiodes, or thermopiles. While the first method is often more precise—which is why we selected this method for calibration of our solar simulator based on light-emitting diodes (LEDs)—the second is more convenient in most laboratories. Therefore, we focus on this second method and show how to correctly measure light intensities over a wide range correctly. However, there are limits—note that even high-quality reference solar cells as sold by calibration laboratories often have an absolute error of ±2%, which is then the lower limit for solar-cell efficiency measurement error. In the following, we assume the possibility to measure the light intensity at one intensity with a reference cell or using a spectrometer.

One way to measure light intensity over a wide range uses grey filters. Therefore, we measured first the transmittance of the grey filters commonly used in PVLAB for variable-illumination measurements (VIM). The results are presented in table B.1. To measure the filter transmittance (T) under the four-lamp (three halogen, one xenon) solar simulator from

Table B.1: Grey-filter transmittance calibration under a Wacom class AAA solar simulator with a thermopile.

Nominal T of filter (%)	0.4	1.6	16	26	50	no filter
Thermopile voltage (µV)	5.50	18.0	207	339	668	1300
Meas. T under Wacom (%)	0.442	1.38	15.8	26.0	51.3	100
Meas. T under LED (%)	–	0.841	–	23.3	46.2	100

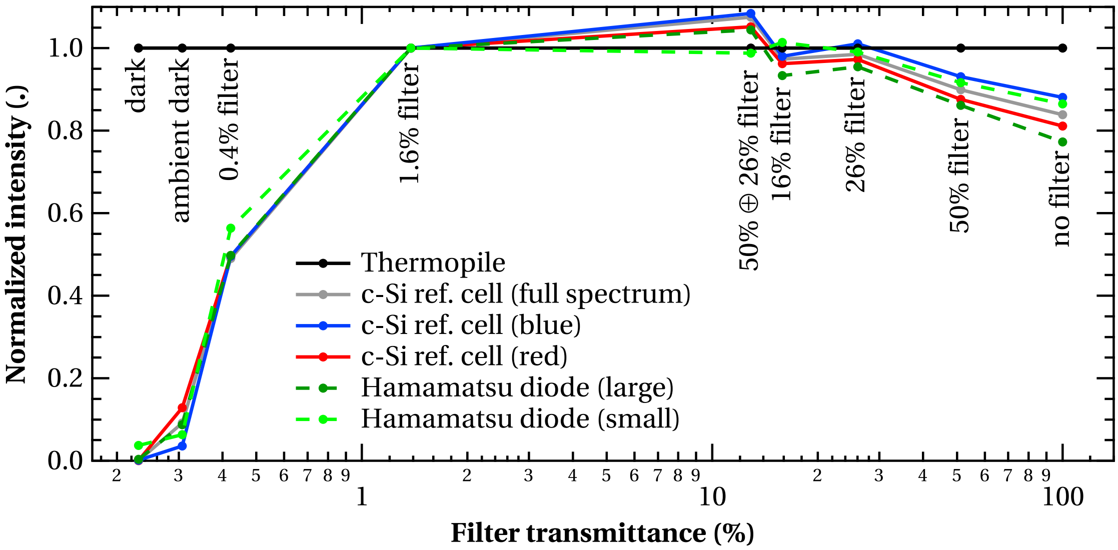

Figure B.1: Intensity measurements under the Wacom solar simulator by photocurrent or voltage of different reference cells and grey filters commonly used at PVLAB. All intensities were normalized to the light-intensity measurement using a 1.6% filter and a thermopile.

Wacom, we used a thermopile, whose intensity response was supposed to be linear (at least, much more linear than that of reference cells). Hence, the T values were obtained by dividing the thermopile voltage of the measurement with the filter by the voltage of the measurement without the filter.

Under the LED simulator, access to the sample holder is more difficult, and covering the thermopile between measurements was not possible. Therefore, the thermopile heated up, showing up in a hysteresis of more than 20% between intensity ramp-up and ramp-down. In this case, we determined the filter transmittance by comparing the current of a photodiode with and without the filter at 0.7 sun-equivalents, an intensity in the linear range of the photodiode.

Note the significant difference between the transmittance under the two solar simulators. Repeating these measurements we found the same trend. We explain it by the different angular distribution of the light: under the Wacom simulator, the light is parallel to a large extent. In contrast, the LEDs emit the light under a cone of typically 30%. With increasing angle, the filters appear stronger as the effective lightpath through them is longer. This is even more the case for these filters, which are made of stacks of metallic grids—this explains why the difference between the Wacom and LED solar simulators is enhanced for strong filters.

Figure B.1 shows the intensity measurements of the reference cells that are used for the calibration of the Wacom solar simulator and of two photodiodes. This graph shows exemplarily why one should not take directly the photocurrent as a measure of the light intensity: at low intensities, recombination is strong, and hence the collection efficiency of the crystalline silicon (c-Si) based detectors is weak. At medium-intensity illumination (filters

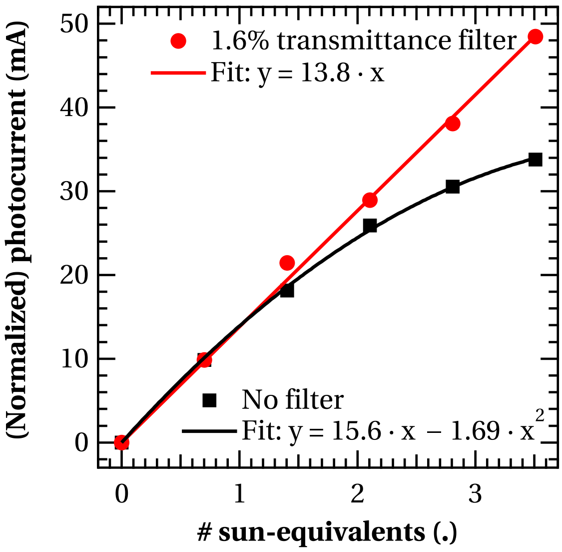

Figure B.2: Current measured by a photodiode at light intensities from 0 to 3.5 sun-equivalents measured with and without a 1.6% transmittance filter. The measurement with the filter is normalized to the measurement without the filter at 0.7 sun-equivalents.

with T between about 1 and 30%), the light-induced current is linear with the light intensity. At higher intensities, the series resistance, both of the detector and the current-measurement tool, reduces the current.

This effect is more severe when measuring high intensities such as under the LED solar simulator: Figure B.2 shows the current measurements of the large Hamamatsu photodiode at light intensities up to 3.5 sun-equivalents. If a filter is used, the photocurrent is linear with the light intensities; without a filter, it is sublinear—in the fit, we approximated this dependence with a second-degree polynomial. This fit was used for experiments with the solar simulator to determine the light intensity from the photocurrent.

B.2 Electronic circuit to power the LED solar simulator

Figures B.3, B.4, and B.5 show details of the electronic circuits used to power and control the LEDs in the solar simulator and serve as reference for future changes or issues. For further information, we refer to chapter 3.

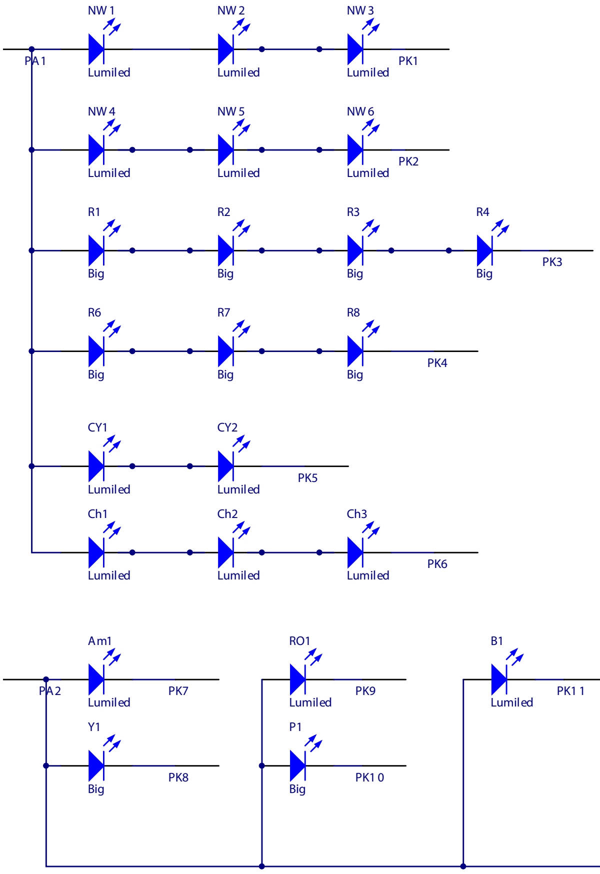

Figure B.3: Schema of the printed circuit board with light emitting diodes used in the solar simulator.

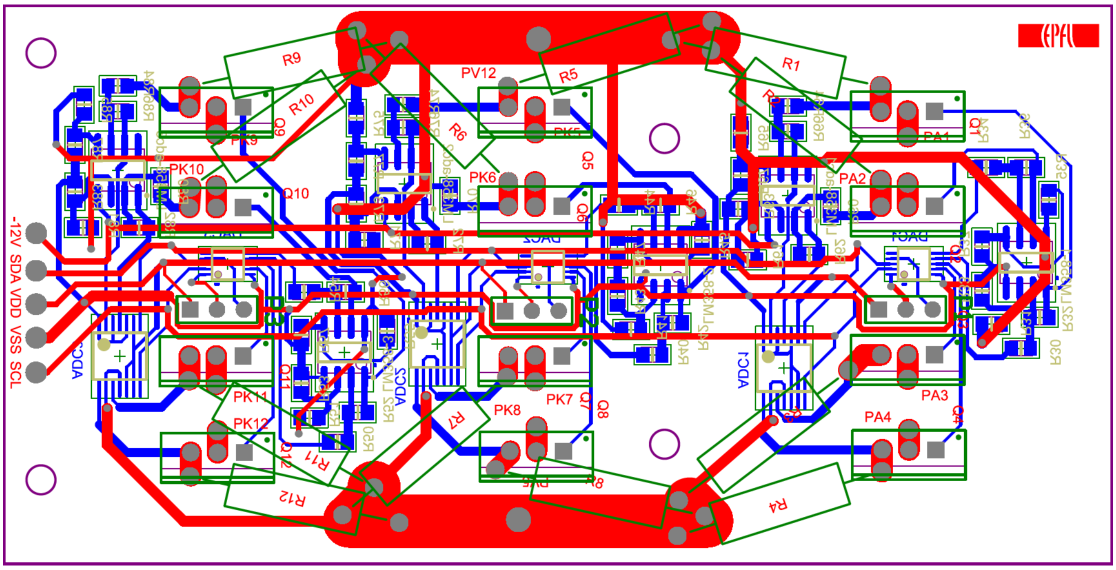

Figure B.4: Design of the electronic circuit of the printed circuit board (PCB) that powers and controls the light-emitting diodes on a second PCB with 12 channels at 5 and 12 V.

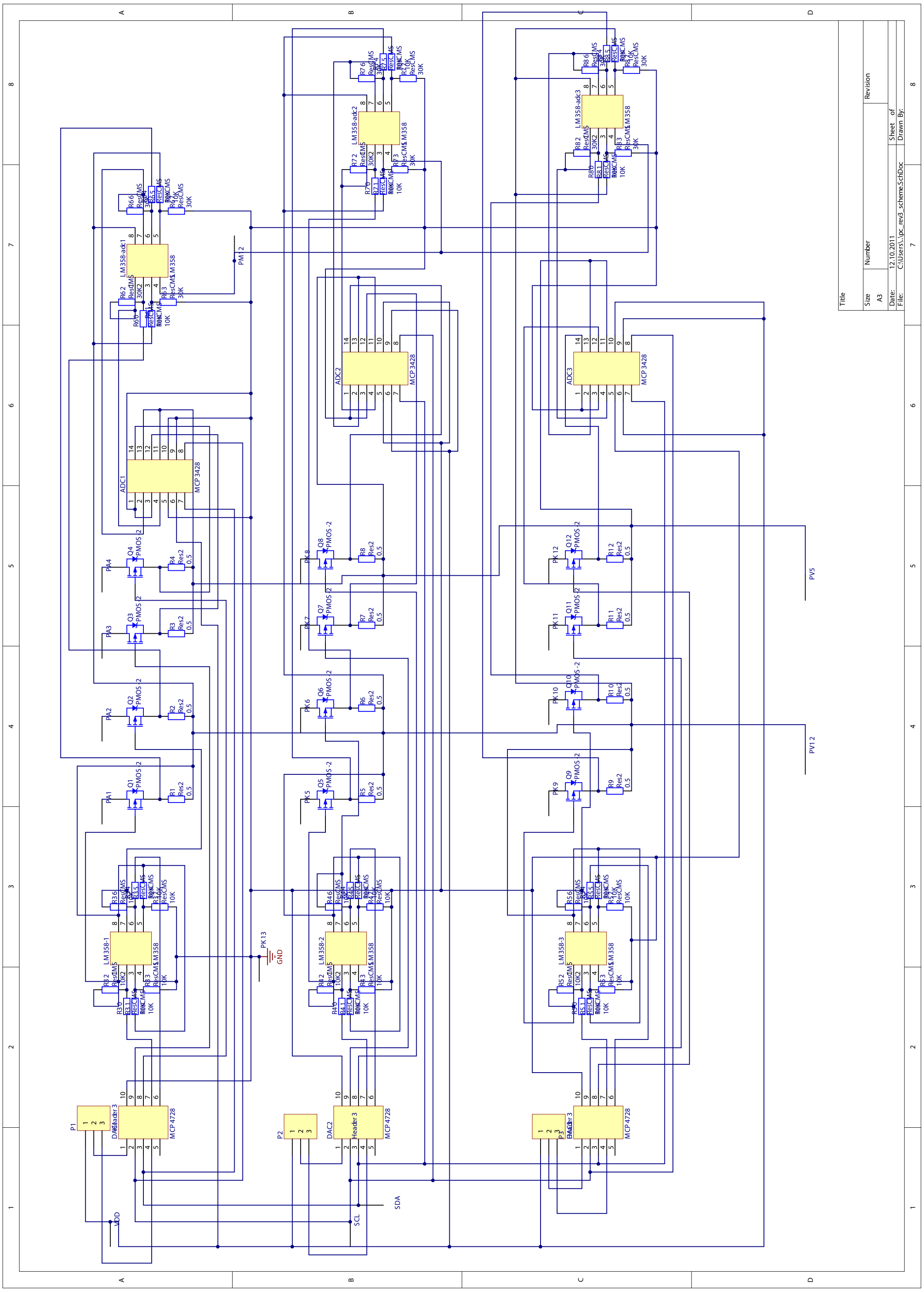

Figure B.5: Schema of the printed circuit board shown in Fig. B.4.

C Input parameters for ASA simulations

We present here the input parameters we used for the ASA simulations presented in chapter 8. Values indicated as `VARIABLE` are the crucial values that we varied and that are discussed in detail in section 8.4. For details on the parameters, we refer to the ASA manual [Zeman 13b].

```
C    Device structure;
layers electrical=6 front=2 back=1;
grid[1] d=5e-9 spaces=20;
grid[2] d=VARIABLE spaces=20;
grid[3] d=10.0e-9 spaces=20;
grid[4] d=220.0e-9 spaces=200;
grid[5] d=5.0e-9 spaces=20;
grid[6] d=30.0e-9 spaces=20;
grid[f.1] d=0.5e-3;
grid[f.2] d=2.00e-06;
grid[b.1] d=2.00e-6;
frontcon schottky e.bar=1.5;
backcon schottky e.bar=0.20;

C    Optical properties;
optical[1] lnk.file=Lj_p-ucSi.nk;
optical[2] lnk.file=tud_p-aSiC.nk;
optical[3] lnk.file=tud_i-aSi.nk;
optical[4] lnk.file=tud_i-aSi.nk;
optical[5] lnk.file=tud_n-aSi.nk;
optical[6] lnk.file=tud_n-aSi.nk;
optical[f.1] ext.coeff=0 ref.index=1.5 incoherent;
optical[f.2] lnk.file=ZnoOz2min0.nk;
optical[b.1] lnk.file=ZnoOz2min0.nk;

C    Semiconductor properties;
doping[1] e.act.acc=0.15;
doping[2] e.act.acc=0.4;
doping[5] e.act.don=0.15;
doping[6] e.act.don=0.05;
```

```
bands[1] e.mob=1.40 chi=4.0 nc=6.0E+26 nv=6.0E+26 epsilon=7.2;
bands[2] e.mob=1.95 chi=4.0 nc=6.0E+26 nv=6.0E+26 epsilon=7.2;
bands[3] e.mob=1.95 chi=4.0 nc=2.0E+26 nv=2.0E+26 epsilon=11.9;
bands[4] e.mob=1.76 chi=4.0 nc=2.0E+26 nv=2.0E+26 epsilon=11.9;
bands[5] e.mob=1.76 chi=4.0 nc=6.0E+26 nv=6.0E+26 epsilon=11.9;
bands[6] e.mob=1.40 chi=4.0 nc=6.0E+26 nv=6.0E+26 epsilon=11.9;

mobility[1] mu.e=10.0e-4 mu.h=1.0e-4;
mobility[2] mu.e=10.0e-4 mu.h=1.0e-4;
mobility[3] mu.e=20.0e-4 mu.h=5.0e-4;
mobility[4] mu.e=20.0e-4 mu.h=5.0e-4;
mobility[5] mu.e=10.0e-4 mu.h=1.0e-4;
mobility[6] mu.e=10.0e-4 mu.h=1.0e-4;

C    Description of DOS;
vbtail[all] e.range=0.5 levels=50 c.neut=0.7e-15 c.pos=0.7e-15;
vbtail[1] n.emob=1.0e28 e.char=0.090;
vbtail[2] n.emob=1.0e28 e.char=0.090;
vbtail[3] n.emob=1.0e27 n1.emob=1.0e27 e.char=0.043 e1.char=0.043;
vbtail[4] n.emob=1.0e27 n1.emob=1.0e27 e.char=0.043 e1.char=0.043;
vbtail[5] n.emob=1.0e28 e.char=0.090;
vbtail[6] n.emob=1.0e28 e.char=0.090;

cbtail[all] e.range=0.5 levels=50 c.neut=0.7e-15 c.neg=0.7e-15;
cbtail[1] n.emob=5.0e27 e.char=0.070;
cbtail[2] n.emob=5.0e27 e.char=0.070;
cbtail[3] n.emob=2.0e27 e.char=0.030;
cbtail[4] n.emob=2.0e27 e.char=0.030;
cbtail[5] n.emob=1.0e28 e.char=0.080;
cbtail[6] n.emob=1.0e28 e.char=0.080;

dbond[all]
levels=40 e.corr=0.2 ce.pos=200.0e-15 ce.neut=1.0e-15 ch.neg=100.0e-15 ch.neut=1.0e-15;
dbond[1] n=1e21 e.neut=-0.70;
dbond[2] n=VARIABLE e.neut=-0.70;
dbond[3] n=VARIABLE e.neut=-0.88;
dbond[4] n=VARIABLE e.neut=-0.88;
dbond[5] n=5e23 e.neut=-1.40;
dbond[6] n=1e21 e.neut=-1.40;

C    Numerical settings;
model[all] amorphous;
model[all] external;

settings newton gummel.starts=2;
settings damp=3 max.iter=50;
settings sr.flux=1.0e16;
settings Rs=1e-4;

opticgen spectrum=am15.dat genpro3 mult=1.0;
```

D Software code written during thesis

During the thesis, I wrote several software code packages, some of which are in daily use by other laboratory members now. The most important ones include:

- Together with M. Bonnet-Eymard and Y. Riesen, we wrote a program in LabVIEW [LabVIEW 14] that controls current–voltage ($I(V)$) measurements including automatic temperature corrections and sequential $I(V)$ measurements, analysis and reporting.
- During civil service prior to the thesis, I developed hardware and software for a maximum-power-point (MPP) tracker combined with variable resistors: 12 solar cells were consecutively measured and analyzed, and a variable resistance (independently for the 12 cells) was applied such that each solar cell could be set to short circuit, open circuit, maximum power point, or any other working point. This setup was finished and tested to compare light-induced degradation under different conditions in the beginning of the thesis.
- For the solar simulator described in chapter 3, the software controlling the LEDs and another package measuring the kinetics of $I(V)$ characteristics was written together with M. Bonnet-Eymard and Y. Riesen in LabVIEW.
- I wrote a software package in Igor [WaveMetrics 14] for automated analysis and comparison of different measurement techniques: external quantum efficiency, dark conductivity, ellipsometry, $I(V)$, Fourier transform infrared spectroscopy, photospectroscopy, degradation kinetics, and others.
- For educational purposes and to understand issues with real devices, we implemented several models for equivalent electronic circuits for solar cells in Igor. A screenprint of the graphic user interface for one of these models simulating a micromorph tandem device is shown in Fig. D.1.

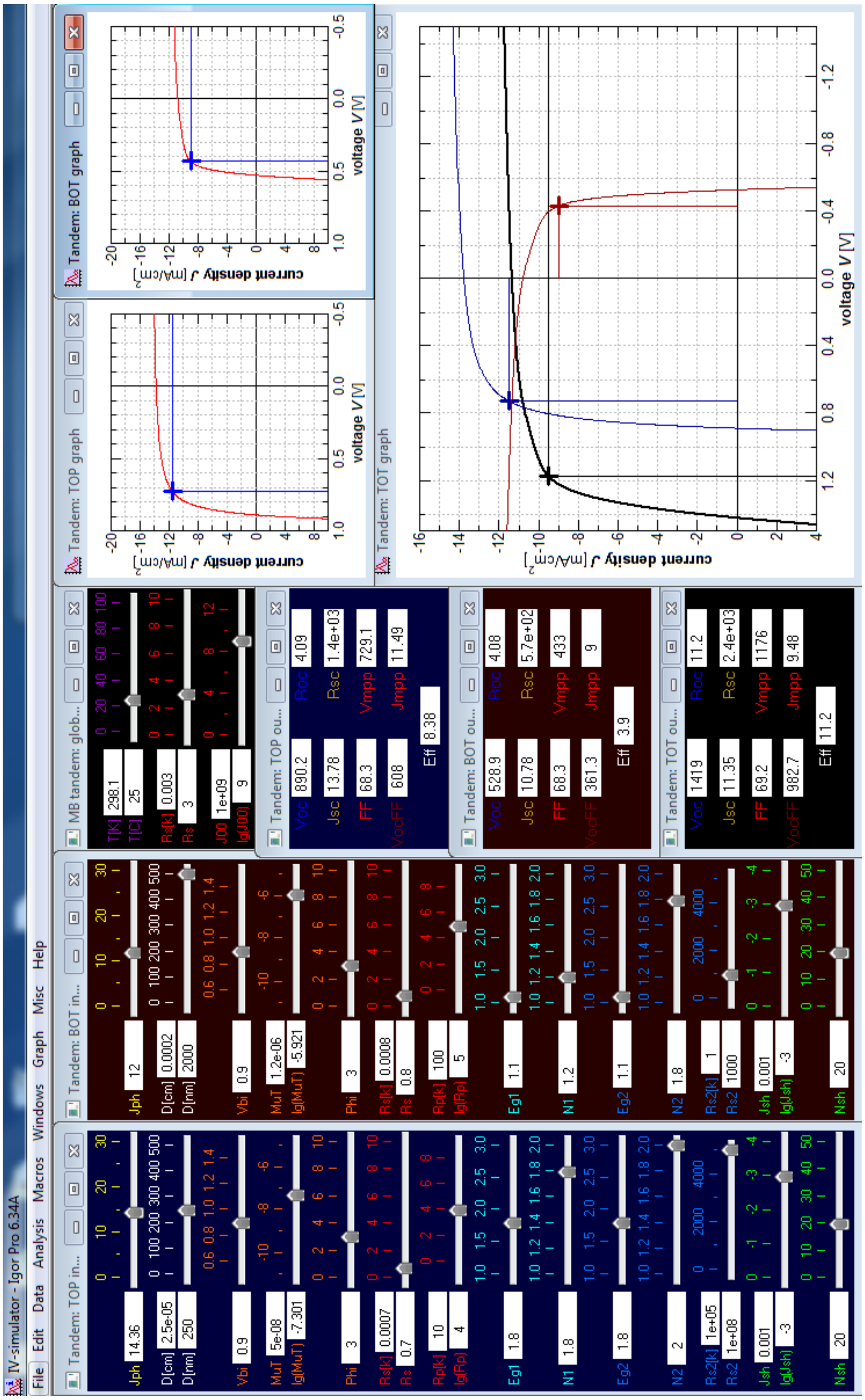

Tandem: TOP in...

Jph 14.36
D[cm] 2.5e-05
D[nm] 250
Vbi 0.9
MuT 5e-08
lg(MuT) -7.301
Phi 3
Rs[k] 0.0007
Rs 0.7
Rp[k] 10
lg(Rp) 4
Eg1 1.8
N1 1.8
Eg2 1.8
N2 2
Rs2[k] 1e+05
Rs2 1e+08
Jsh 0.001
lg(Jsh) -3
Nsh 20

Tandem: BOT in...

Jph 12
D[cm] 0.0002
D[nm] 2000
Vbi 0.9
MuT 1.2e-06
lg(MuT) -5.921
Phi 3
Rs[k] 0.0008
Rs 0.8
Rp[k] 100
lg(Rp) 5
Eg1 1.1
N1 1.2
Eg2 1.1
N2 1.8
Rs2[k] 1
Rs2 1000
Jsh 0.001
lg(Jsh) -3
Nsh 20

MB tandem: glob...

T[K] 298.1
T[C] 25
Rs[k] 0.003
Rs 3
J00 1e+09
lg(J00) 9

Tandem: TOP ou...

Voc 890.2
Jsc 13.78
FF 68.3
VocFF 608
Roc 4.09
Rsc 1.4e+03
Vmpp 729.1
Jmpp 11.49
Eff 8.38

Tandem: BOT ou...

Voc 528.9
Jsc 10.78
FF 68.3
VocFF 361.3
Roc 4.08
Rsc 5.7e+02
Vmpp 433
Jmpp 9
Eff 3.9

Tandem: TOT ou...

Voc 1419
Jsc 11.35
FF 69.2
VocFF 982.7
Roc 11.2
Rsc 2.4e+03
Vmpp 1176
Jmpp 9.48
Eff 11.2

Figure D.1: Screenprint of the graphic user interface of the program with different equivalent electronic circuits for single- and tandem-junction solar cells. Here: micromorph cell.

Bibliography

[3M 14] 3M, 2014. http://www.amsmaterials.com/products/Fluorinert-FC%252d72.html, last accessed July 20, 2014.

[Abdi 13] F. F. Abdi, L. Han, A. H. M. Smets, M. Zeman, B. Dam & R. van de Krol. *Efficient solar water splitting by enhanced charge separation in a bismuth vanadate-silicon tandem photoelectrode.* Nature Communications, vol. 4, 2013.

[Abel 13] S. Abel, T. Stöferle, C. Marchiori, D. Caimi, L. Czornomaz, C. Rossel, M. D. Rossell, R. Erni, M. Sousa, H. Siegwart, J. Hofrichter, M. Stuckelberger, A. Chelnokov, B. J. Offrein, & J. Fompeyrine. *Electro-optical active barium titanate thin films in silicon photonic devices.* Integrated Photonics Research, Silicon and Nanophotonics, Rio Grande, Puerto Rico (USA), 2013.

[AGC 14] AGC, 2014. Asahi Glass Company, http://www.agc-solar.com/glass-products/coated-glass/tco/tco-vu.html#uid_11_desc, last accessed August 14, 2014.

[AIST 14] AIST, 2014. National Institute of Advanced Industrial Science and Technology (Japan), http://www.aist.go.jp/index_en.html, last accessed July 20, 2014.

[Almat 14] N. Almat. *Gallium and boron doping of amorphous silicon for solar cells.* Master thesis at Ecole Polytechnique Fédérale de Lausanne, Switzerland, 2014.

[Alpuim 99] P. Alpuim, V. Chu & J. P. Conde. *Amorphous and microcrystalline silicon films grown at low temperatures by radio-frequency and hot-wire chemical vapor deposition.* Journal of Applied Physics, vol. 86, no. 7, pages 3812–3821, 1999.

[Andújar 91] J. L. Andújar, E. Bertran, A. Canillas, J. Campmany & J. L. Morenza. *Effect of substrate temperature on deposition rate of rf plasma-deposited hydrogenated amorphous silicon thin films.* Journal of Applied Physics, vol. 69, no. 6, pages 3757–3759, 1991.

[Arch 91] J. K. Arch, F. A. Rubinelli, J. Y. Hou & S. J. Fonash. *Computer analysis of the role of p-layer quality, thickness, transport mechanisms, and contact barrier height in the performance of hydrogenated amorphous silicon p-i-n solar cells.* Journal of Applied Physics, vol. 69, no. 10, pages 7057–7066, 1991.

[ASA 14] ASA, 2014. http://www.ewi.tudelft.nl/over-de-faculteit/afdelingen/electrical-sustainable-energy/photovoltaische-materialen-en-devices/asa-software, last accessed July 20, 2014.

[Aspnes 79] D. E. Aspnes, J. B. Theeten & F. Hottier. *Investigation of effective-medium models of microscopic surface roughness by spectroscopic ellipsometry.* Physical Review B, vol. 20, no. 8, pages 3292–3302, 1979.

[ASTM 14a] ASTM, 2014. http://rredc.nrel.gov/solar/spectra/am1.5, last accessed July 20, 2014.

[ASTM 14b] ASTM. *Standard tables for reference solar spectral irradiances: Direct normal and hemispherical on 37° tilted surface*, 2014. American Society for Testing and Materials, Designation: G173-03 (Reapproved 2012).

[Azuma 94] M. Azuma, T. Yokoi & I. Shimizu. *Fabrication of highly stable a-Si:H from chlorinated precursors.* Mat. Res. Soc. Symp. Proc., vol. 336, pages 239–244, 1994.

[Bailat 06] J. Bailat, D. Dominé, R. Schlüchter, J. Steinhauser, S. Faÿ, F. Freitas, C. Bücher, L. Feitknecht, X. Niquille, T. Tscharner, A. Shah & C. Ballif. *High-efficiency p-i-n microcrystalline and micromorph thin film silicon solar cells deposited on LPCVD ZnO coated glass substrates.* Conf. Rec. 4th WCPEC, pages 1533–1536, 2006.

[Bartlome 09] R. Bartlome, A. Feltrin & C. Ballif. *Infrared laser-based monitoring of the silane dissociation during deposition of silicon thin films.* Applied Physics Letters, vol. 94, no. 20, page 201501, 2009.

[Beck 96] N. Beck, N. Wyrsch, C. Hof & A. Shah. *Mobility lifetime product – A tool for correlating a-Si:H film properties and solar cell performances.* Journal of Applied Physics, vol. 79, no. 12, pages 9361–9368, 1996.

[Benagli 09] S. Benagli, D. Borrello, E. Vallat-Sauvain, J. Meier, U. Kroll, J. Hoetzel, J. Bailat, J. Steinhauser, M. Marmelo, G. Monteduro &

L. Castens. *High-efficiency amorphous silicon devices on LPCVD-ZnO TCO prepared in industrial Kai^{TM}-M R&D reactor.* 24th EU PVSEC Proc., pages 2293–2298, 2009.

[Beyer 89] W. Beyer, R. Hager, H. Schmidbaur & G. Winterling. *Improvement of the photoelectric properties of amorphous SiC_x:H by using disilylmethane as a feeding gas.* Applied Physics Letters, vol. 54, no. 17, pages 1666–1668, 1989.

[BFS 13] BFS, 2013. Bundesamt für Statistik: *Die Bevölkerung der Schweiz,* Nr. 348-1200.

[Bhattacharya 88] E. Bhattacharya & A. Mahan. *Microstructure and the light-induced metastability in hydrogenated amorphous silicon.* Applied Physics Letters, vol. 52, no. 19, pages 1587–1589, 1988.

[Bieberícher 02] A. C. W. Biebericher, v. d. W. W. F., W. J. Goedheer & J. K. Rath. *Mechanism of argon treatment on a growing surface in layer-by-layer deposition of hydrogenated amorphous silicon.* Journal of Non-Crystalline Solids, vol. 299–302, pages 74–78, 2002.

[Biron 13] R. Biron. *Layers with advanced optoelectronic properties for high-efficiency micromorph solar cells on opaque substrates.* PhD thesis, Ecole Polytechnique Fédérale de Lausanne, Switzerland, 2013.

[Bliss 09a] M. Bliss, T. Betts & R. Gottschalg. *An LED-based photovoltaic measurement system with variable spectrum and flash speed.* Solar Energy Materials & Solar Cells, vol. 93, pages 825–830, 2009.

[Bliss 09b] M. Bliss, S. Wendlandt, T. R. Betts & R. Gottschalg. *Towards a high power, all LED solar simulator closely matching realistic solar spectra.* 24th EU PVSEC Proc., pages 3321–3326, 2009.

[Boccara 80] A. C. Boccara, D. Fournier & J. Badoz. *Thermo-optical spectroscopy: Detection by the "mirage effect".* Applied Physics Letters, vol. 36, no. 2, pages 130–132, 1980.

[Boccard 11] M. Boccard, P. Cuony, M. Despeisse, D. Dominé, A. Feltrin, N. Wyrsch & C. Ballif. *Substrate dependent stability and interplay between optical and electrical properties in µc-Si:H single junction solar cells.* Solar Energy Materials & Solar Cells, vol. 95, pages 195–198, 2011.

[Boccard 12a] M. Boccard, T. Söderström, P. Cuony, C. Battaglia, S. Hänni, S. Nicolay, L. Ding, M. Benkhaira, G. Bugnon, A. Billet, M. Charrière, F. Meillaud, M. Despeisse & C. Ballif. *Optimization* *of ZnO front electrodes for high-efficiency micromorph thin-film Si solar cells.* IEEE Journal of Photovoltaics, vol. 2, no. 3, pages 229–235, 2012.

[Boccard 12b] M. Boccard. *Novel micromorph solar cell structures for efficient light trapping and high-quality absorber layers.* PhD thesis, Ecole Polytechnique Fédérale de Lausanne, Switzerland, 2012.

[Boccard 14] M. Boccard. *Low-refractive index silicon-oxide interlayers for high-stable-efficiency multi-junction thin-film silicon solar cells*, 2014. Presented at IEEE PVSC in Denver.

[Böhm 93] C. Böhm, J. Perrin & P. Roca i Cabarrocas. *Ion-induced secondary electron emission in SiH_4 glow discharge, and temperature dependence of hydrogenated amorphous silicon deposition rate.* Journal of Applied Physics, vol. 73, no. 5, pages 2578–2580, 1993.

[Bonnet-Eymard 13] M. Bonnet-Eymard, M. Boccard, G. Bugnon, F. Sculati-Meillaud, M. Despeisse & C. Ballif. *Optimized short-circuit current mismatch in multi-junction solar cells.* Solar Energy Materials & Solar Cells, vol. 117, pages 120–125, 2013.

[Branz 99] H. M. Branz. *Hydrogen collision model: Quantitative description of metastability in amorphous silicon.* Physical Review B, vol. 59, no. 8, pages 5098–5512, 1999.

[Brodsky 77] M. H. Brodsky, M. Cardona & J. J. Cuomo. *Infrared and Raman spectra of the silicon-hydrogen bonds in amorphous silicon prepared by glow discharge and sputtering.* Physical Review B, vol. 16, no. 8, pages 3556–3571, 1977.

[Bronneberg 11] A. C. Bronneberg, A. H. M. Smets, M. Creatore & M. C. M. van den Sanden. *On the oxidation mechanism of microcrystalline silicon thin films studied by Fourier transform infrared spectroscopy.* Journal of Non-Crystalline Solids, vol. 357, pages 884–887, 2011.

[Bronneberg 12] A. C. Bronneberg. *Plasma processing of microcrystalline silicon films: filling hin the gaps.* PhD thesis, Technische Universiteit Eindhoven, 2012.

[Bronsveld 06] P. C. P. Bronsveld, J. K. Rath, R. E. I. Schropp, T. Mates, A. Fejfar, B. Rezek & J. Kočka. *Internal structure of mixed phase hydrogenated silicon thin films made at 39 C.* Applied Physics Letters, vol. 89, page 051922, 2006.

[Bronsveld 10] P. C. P. Bronsveld, T. Mates, A. Fejfar, J. Kočka, J. K. Rath & R. E. I. Schropp. *High hydrogen dilution and low substrate* *temperature cause columnar growth of hydrogenated amorphous silicon.* Physica Status Solidi A, vol. 207, no. 3, pages 525–529, 2010.

[Bruggeman 35] D. A. G. Bruggeman. *Berechnung verschiedener physikalischer Konstanten von heterogenen Substanzen.* Annalen der Physik, vol. 24, pages 636–664, 1935.

[Buehlmann 07] P. Buehlmann, J. Bailat, D. Dominé, A. Billet, F. Meillaud, A. Feltrin & C. Ballif. *In situ silicon oxide based intermediate reflector for thin-film silicon micromorph solar cells.* Applied Physics Letters, vol. 91, page 143505, 2007.

[Bugnon 13] G. Bugnon. *High-quality microcrystalline silicon for efficient thin-film solar cells: insights into plasma and material properties.* PhD thesis, Ecole Polytechnique Fédérale de Lausanne, Switzerland, 2013.

[Bugnon 14] G. Bugnon, G. Parascandolo, S. Hänni, M. Stuckelberger, M. Charrière, M. Despeisse, F. Meillaud & C. Ballif. *Silicon oxide buffer layer at the p–i interface in amorphous and microcrystalline silicon solar cells.* Solar Energy Materials & Solar Cells, vol. 120, pages 143–150, 2014.

[Bullock 94] J. N. Bullock & S. Wagner. *Amourphous silicon films from dichlorosilane and hydrogen.* Mat. Res. Soc. Symp. Proc., vol. 336, pages 97–102, 1994.

[Bundesrat 02] Bundesrat, 2002. Bericht des Bundesrates: Strategie Nachhaltige Entwicklung.

[Burgelman 04] M. Burgelman, J. Verschraegen, S. Degrave & P. Nollet. *Modeling Thin-film PV Devices.* Prog. Photovolt: Res. Appl., vol. 12, pages 143–153, 2004.

[Calvet 14] W. Calvet, E. Murugasen, J. Klett, B. Kaiser, W. Jaegermann, F. Finger, S. Hoch, M. Blug & J. Busse. *Silicon based tandem cells: novel photocathodes for hydrogen production.* Phys. Chem. Chem. Phys., vol. 16, no. 12043, 2014.

[Carlson 76] D. E. Carlson & C. R. Wronski. *Amorphous silicon solar cell.* Applied Physics Letters, vol. 28, no. 11, pages 671–673, 1976.

[Chatham 89] H. Chatham, P. Bhat, A. Benson & C. Matovich. *High-efficiency amorphous silicon p-i-n solar cells deposited from disilane at rates up to 2 nm/s using VHF discharges.* Journal of Non-Crystalline Solids, vol. 115, pages 201–203, 1989.

[Chesaux 13] M. Chesaux. *A grid reactor with low ion bombardement energy for large area PECVD of thin film silicon soloar cells.* PhD thesis, Ecole Polytechnique Fédérale de Lausanne, Switzerland, 2013.

[Cody 81] G. D. Cody, T. Tiedje, B. Abeles, B. Brooks & Y. Goldstein. *Disorder and the optical-absorption edge of hydrogenated amorphous silicon.* Physical Review Letters, vol. 47, no. 20, pages 1480–1483, 1981.

[Collins 00] R. W. Collins, J. Koh, A. S. Ferlauto, P. I. Rovira, Y. Lee, R. J. Koval & C. R. Wronski. *Real time analysis of amorphous and microcrystalline silicon film growth by multichannel ellipsometry.* Thin Solid Films, vol. 364, pages 129–137, 2000.

[Collins 02] R. W. Collins & A. S. Ferlauto. *Advances in plasma-enhanced chemical vapor deposition of silicon films at low temperatures.* Curr. Opin. Solid-State Mater. Sci., vol. 6, pages 425–437, 2002.

[Collins 03] R. W. Collins, A. S. Ferlauto, G. M. Ferreira, C. Chen, J. Koh, R. J. Koval, Y. Lee, J. M. Pearce & C. R. Wronski. *Evolution of microstructure and phase in amorphous, protocrystalline, and microcrystalline silicon studied by real time spectroscopic ellipsometry.* Solar Energy Materials & Solar Cells, vol. 78, pages 143–180, 2003.

[Comber 72] P. G. L. Comber, A. Madan & W. E. Spear. *Electronic transport and state distribution in amorphous Si films.* Journal of Non-Crystalline Solids, vol. 11, pages 219–234, 1972.

[Comber 79] P. G. L. Comber, W. E. Spear & A. Ghaith. *Amorphous-silicon field-effect device and possible application.* Electronics Letters, vol. 15, no. 6, pages 179–181, 1979.

[Crandall 83] R. S. Crandall. *Modeling of thin film solar cells: Uniform field approximation.* Journal of Applied Physics, vol. 54, pages 7176–7186, 1983.

[CrysTec 14] CrysTec, 2014. http://www.crystec.de, last accessed July 20, 2014.

[Cuony 10] P. Cuony, M. Marending, D. T. L. Alexander, M. Boccard, G. Bugnon, M. Despeisse & C. Ballif. *Mixed-phase p-type silicon oxide containing silicon nanocrystals and its role in thin-film silicon solar cells.* Applied Physics Letters, vol. 97, page 213502, 2010.

[Cuony 11] P. Cuony. *Optical layers for thin-film silicon solar cells.* PhD thesis, Ecole Polytechnique Fédérale de Lausanne, Switzerland, 2011.

[Cuony 12] P. Cuony, D. T. L. Alexander, I. Perez-Wurfl, M. Despeisse, G. Bugnon, M. Boccard, T. Söderström, A. Hessler-Wyser, C. Hébert & C. Ballif. *Silicon filaments in silicon oxide for next-generation photovoltaics.* Adv. Mater., vol. 24, pages 1182–1186, 2012.

[Davis 70] E. A. Davis & N. F. Mott. *Conduction in non-crystalline systems V. Conductivity, optical absorption and photoconductivity in amorphous semiconductors.* Philosophical Magazine, vol. 22, no. 179, pages 0903–0922, 1970.

[de Jong 10] M. M. de Jong, J. de Koning, J. K. Rath & R. E. I. Schropp. *Identification of various plasma regimes in very high frequency PECVD of amorphous and nanocrystalline silicon near the phase transition.* 25th EU PVSEC/WCPEC-5 Proc., pages 3149–3151, 2010.

[De Wolf 12] S. De Wolf, A. Descoeudres, Z. C. Holman & C. Ballif. *High-efficiency silicon heterojunction solar cells: A review.* Green, vol. 2, no. 1, pages 7–24, 2012.

[De Wolf 14] S. De Wolf, J. Holovsky, S.-J. Moon, P. Löper, B. Niesen, M. Ledinsky, F.-J. Haug, J.-H. Yum & C. Ballif. *Organometallic halide perovskites: sharp optical absorption edge and its relation to photovoltaic performance.* J. Phys. Chem. Lett., vol. 5, no. 6, pages 1035–1039, 2014.

[Deane 93] S. C. Deane & M. J. Powell. *Defect chemical potential and the density of states in amorphous silicon.* Physical Review Letters, vol. 70, no. 11, pages 1654–1657, 1993.

[Demaurex 14] B. Demaurex, R. Bartlome, J. P. Seif, J. Geissbühler, D. T. L. Alexander, Q. Jeangros, C. Ballif & S. De Wolf. *Low-temperature plasma-deposited silicon epitaxial films: Growth and properties.* Journal of Applied Physics, vol. 116, no. 5, page 053519, 2014.

[Deng 06] J. Deng, B. Rross, M. Albert, R. Collins & C. Wronski. *Characterization of the evolution in metastable defects created by recombination of carriers generated by photo-generation and injection in pin a-Si:H solar cells.* Mat. Res. Soc. Symp. Proc., vol. 910, pages A02–02, 2006.

[Descoeudres 11] A. Descoeudres, L. Barraud, S. De Wolf, B. Strahm, D. Lachenal, C. Guérin, Z. Holman, F. Zicarelli, B. Demaurex, J. Seif, J. Holovsky & C. Ballif. *Improved amorphous/crystalline silicon interface* *passivation by hydrogen plasma treatment.* Applied Physics Letters, vol. 99, no. 12, page 123506, 2011.

[Despeisse 10a] M. Despeisse, M. Boccard, G. Bugnon, P. Cuony, T. Söderström, G. Parascandolo, M. Stueckelberger, M. Charrière, L. Löfgren, C. Battaglia, S. Hänni, A. Billet, L. Ding, S. Nicolay, F. Meillaud, N. Wyrsch & C. Ballif. *Low-conductivity doped layers for improved performance of thin film silicon solar cells on highly textured substrates.* 25th EU PVSEC Proc., pages 2793–2797, 2010.

[Despeisse 10b] M. Despeisse, G. Bugnon, A. Feltrin, M. Stueckelberger, P. Cuony, F. Meillaud, A. Billet & C. Ballif. *Resistive interlayer for improved performance of thin film silicon solar cells on highly textured substrate.* Applied Physics Letters, vol. 96, page 073507, 2010.

[Ding 13] L. Ding. *Low-pressure chemical vapor deposited zinc oxide films: toward decoupled opto-electrical and morphological properties for more efficient electrodes.* PhD thesis, Ecole Polytechnique Fédérale de Lausanne, Switzerland, 2013.

[Ding 14] L. Ding, M. Stuckelberger, M. Morales Masis, S. Nicolay & C. Ballif. *Stability of the opto-electrical properties of Zinc Oxide electrodes in thin-film silicon solar cells under light soaking.* Manuscript in preparation, 2014.

[Dominé 09] D. Dominé. *The role of front electrodes and intermediate reflectors in the optoelectronic propterties of high-efficiency micromorph solar cells.* PhD thesis, Université de Neuchâtel, Switzerland, 2009.

[Dongaonkar 10] S. Dongaonkar, J. D. Servaites, G. M. Ford, S. Loser, J. Moore, R. M. Gelfand, H. Mohseni, H. W. Hillhouse, R. Agrawal, M. A. Ratner, T. J. Marks, M. S. Lundstrom & M. A. Alam. *Universality of non-Ohmic shunt leakage in thin-film solar cells.* Journal of Applied Physics, vol. 108, page 124509, 2010.

[Dorier 92] J. Dorier, C. Hollenstein, A. A. Howling & U. Kroll. *Powder dynamics in very high frequency silane plasmas.* Journal of Vacuum Science and Technology A, vol. 10, pages 1048–1052, 1992.

[Dornstetter 13] J.-C. Dornstetter, S. Kasouit & P. Roca i Cabarrocas. *Deposition of High-Efficiency Microcrystalline Silicon Solar Cells Using SiF/H/Ar Mixtures.* IEEE Journal of Photovoltaics, vol. 3, no. 1, pages 581–586, 2013.

[Droz 03] C. Droz. *Thin film microcrystalline silicon layers and solar cells: microstructure and electrical performances.* PhD thesis, Université de Neuchâtel, Switzerland, 2003.

[Droz 04] C. Droz, E. Vallat-Sauvain, J. Bailat, L. Feitknecht, J. Meier & A. Shah. *Relationship between Raman crystallinity and open-circuit voltage in microcrystalline silicon solar cells.* Solar Energy Materials & Solar Cells, vol. 81, pages 61–71, 2004.

[EIA 13] EIA, 2013. eia, U.S. Energy information administration: *International energy outlook 2013*, DOE/EIA-0484(2013).

[El Mhamdi 14] E. M. El Mhamdi, J. Holovsky, B. Demaurex, C. Ballif & S. De Wolf. *Is light-induced degradation of a-Si:H/c-Si interfaces reversible?* Applied Physics Letters, vol. 104, page 252108, 2014.

[EPIA 14] EPIA. *Global market outlook for photovoltaics 2014–2018*, 2014.

[Escarré 12] J. Escarré, K. Söderström, M. Despeisse, S. Nicolay, C. Battaglia, G. Bugnon, L. Ding, F. Meillaud, F.-J. Haug & C. Ballif. *Geometric light trapping for high efficiency thin film silicon solar cells.* Solar Energy Materials & Solar Cells, vol. 98, no. 185–190, 2012.

[EWZ 14] EWZ, 2014. https://www.stadt-zuerich.ch/content/ewz/de/index/energie/stromprodukte-zuerich/stromprodukte_zuerich_20131/energie_privat/ewz_atommixpower_2013/preiskomponenten_privat.html, last accessed August 11, 2014.

[Fanni 14] L. Fanni, B. A. Aebersold, D. T. L. Alexander, L. Ding, M. Morales Masis, S. Nicolay & C. Ballif. *c-texture versus a-texture low pressure metalorganic chemical vapor deposition ZnO films: lower resistivity despite smaller grain size.* Thin Solid Films, vol. 565, no. 0, pages 1–6, 2014.

[Fantz 98] U. Fantz. *Spectroscopic diagnostics and modelling of silane microwave plasmas.* Plasma Phys. Control. Fusion, vol. 40, pages 1035–1056, 1998.

[Fathi 09] E. Fathi & A. Sazonov. *Thin Film Silicon Solar Cells on Transparent Plastic Substrates.* Mater. Res. Soc. Symp. Proc., vol. 1153, no. 1153-A20-03, 2009.

[Faÿ 03] S. Faÿ. *L’oxyde de zinc par dépot chimique en phase vapeur comme contact ’electrique transparent et diffuseur de lumi‘ere pour les cellules solaires.* PhD thesis, Ecole Polytechnique Fédérale de Lausanne, Switzerland, 2003.

[Fecioru-Morariu 10] M. Fecioru-Morariu, B. Mereu, J. Kalas, J. Hoetzel, P. A. Losio, M. Kupich, O. Kluth & T. Eisenhammer. *High quality amorphous silicon layers for large area thin film PV applications.* 25th EU PVSEC/WCPEC-5 Proc., pages 2947–2950, 2010.

[Fehr 14] M. Fehr, A. Schnegg, B. Rech, O. Astakhov, F. Finger, R. Bittl, C. Teutloff, & K. Lips. *Metastable defect formation at microvoids identified as a source of light-induced degradation in a-Si:H.* Physical Review Letters, vol. 112, page 066403, 2014.

[Filonovich 08] S. A. Filonovich, P. Alpuim, L. Rebouta, J.-E. Bourée & Y. M. Soro. *Hydrogenated amorphous and nanocrystalline silicon solar cells deposited by HWCVD and RF-PECVD on plastic substrates at 150C.* Journal of Non-Crystalline Solids, vol. 354, pages 2376–2380, 2008.

[Fischer 93] D. Fischer, N. Wyrsch, C. M. Fortmann & A. V. Shah. *Amorphous silicon solar cells with graded low-level doped i-layers characterized by bifacial measurements.* IEEE Photovoltaic Specialists Conf. Proc., Louisville, KY, pages 878–884, 1993.

[Fischer 13] M. Fischer, R. J. V. Quax, M. Zeman & A. H. M. Smets. *Degradation kinetics of amorphous silicon solar cells processed at high pressure and its relation to the nanostructure.* IEEE Photovoltaic Specialists Conf. Proc., Tampa, FL, 2013.

[Fölsch 92] J. Fölsch, H. RübeI & H. Schade. *Change in bonding properties of amorphous hydrogenated silicon-carbide layers prepared with different gases as carbon sources.* Applied Physics Letters, vol. 61, no. 25, pages 3029–3031, 1992.

[Fontcuberta i Morral 01a] A. Fontcuberta i Morral & P. Roca i Cabarrocas. *Shedding light on the growth of amorphous, polymorphous, protocrystalline and microcrystalline silicon thin films.* Thin Solid Films, vol. 383, pages 161–164, 2001.

[Fontcuberta i Morral 01b] A. Fontcuberta i Morral. *Croissance, propriétés structurales et optiques du silicium polymorphe.* PhD thesis, Ecole Polytechnique, 2001.

[Fontcuberta i Morral 02] A. Fontcuberta i Morral, H. Hofmeister & P. Roca i Cabarrocas. *Structure of plasma-deposited polymorphous silicon.* Journal of Non-Crystalline Solids, vol. 299–302, pages 284–289, 2002.

[Fontcuberta i Morral 04] A. Fontcuberta i Morral & P. Roca i Cabarrocas. *Structure and hydrogen content of polymorphous silicon thin films studied by spectroscopic ellipsometry and nuclear measurements.* Physical Review B, vol. 69, no. 125307, 2004.

[Francombe 02] M. H. Francombe, editor. Thin films and nanostructures. Academic Press, 2002.

[Fridman 08] A. Fridman. Plasma chemistry. Cambridge university press, 2008.

[Fujiwara 02] H. Fujiwara, M. Kondo & A. Matsuda. *Microcrystalline silicon nucleation sites in the sub-surface of hydrogenated amorphous silicon.* Surface Science, vol. 497, pages 333–340, 2002.

[Fujiwara 03] H. Fujiwara, M. Kondo & A. Matsuda. *Interface-layer formation in microcrystalline Si:H growth on ZnO substrates studied by real-time spectroscopic ellipsometry and infrared spectroscopy.* Journal of Applied Physics, vol. 93, no. 5, pages 2400–2409, 2003.

[Fujiwara 04] H. Fujiwara, M. Kondo & A. Matsuda. *Nucleation mechanism of microcrystalline silicon from the amorphous phase.* Journal of Non-Crystalline Solids, vol. 338–340, pages 97–101, 2004.

[Fujiwara 07] H. Fujiwara. Spectroscopic ellipsometry: principles and applications. John Wiley & Sons, 2007.

[Funde 09] A. M. Funde, N. A. Bakr, T. S. Salve, K. D. Diwate, D. K. Kamblea, R. R. Hawaldarb, D. P. Amalnerkarb & S. R. Jadkarc. *Influence of Argon Flow on Deposition of Hydrogenated Nanocrystalline Silicon (nc-Si:H) Films by Plasma Chemical Vapor Deposition.* Journal of Nano Research, vol. 5, pages 185–191, 2009.

[Gibson 98] J. M. Gibson, M. M. J. Treacy, P. M. Voyles, H.-C. Jin & J. R. Abelson. *Structural disorder induced in hydrogenated amorphous silicon by light soaking.* Applied Physics Letters, vol. 73, no. 21, pages 3093–3095, 1998.

[Gogoi 07] P. Gogoi, P. N. Dixit & P. Agarwal. *Amorphous silicon films with high deposition rate prepared using argon and hydrogen diluted silane for stable solar cells.* Solar Energy Materials & Solar Cells, vol. 91, pages 1253–1257, 2007.

[Goldemberg 85] J. Goldemberg, T. B. Johansson, A. K. N. Reddy & R. H. Williams. *Basic needs and much more with one kilowatt per capita.* Ambio, vol. 14, no. 4–5, pages 190–200, 1985.

[GORE 14] GORE, 2014. https://www.gore.com/MungoBlobs/349/632/DRPdatasheet_e.pdf, last accessed August 12, 2014.

[Green 81] M. A. Green. *Solar cell fill factors: General graph and empirical expressions.* Solid-State Electronics, vol. 24, no. 8, pages 788–789, 1981.

[Green 82a] M. A. Green. *Accuracy of analytical expressions for solar cell fill factors.* Solar Cells, vol. 7, no. 3, pages 337–340, 1982.

[Green 82b] M. A. Green, editor. Solar cells: Operating principles, technology, and system applications. Englewood Cliffs, NJ, Prentice-Hall, Inc., 1982.

[Green 14] M. A. Green, K. Emery, Y. Hishikawa, W. Warta & E. D. Dunlop. *Solar cell efficiency tables (version 44).* Prog. Photovolt: Res. Appl., vol. 22, pages 701–710, 2014.

[Guha 86] S. Guha, J. Yang, P. Nath & M. Hack. *Enhancement of open circuit voltage in high efficiency amorphous silicon alloy solar cells.* Applied Physics Letters, vol. 49, no. 4, pages 218–219, 1986.

[Guizot 91] J.-L. Guizot, K. Nomoto & A. Matsuda. *Surface reactions during the a-Si: H growth in the diode and triode glow-discharge reactors.* Surface science, vol. 244, no. 1, pages 22–38, 1991.

[Hall 52] R. N. Hall. *Electron-Hole Recombination in Germanium.* Phys. Rev., vol. 87, pages 387–387, Jul 1952.

[Hänni 13] S. Hänni, G. Bugnon, G. Parascandolo, M. Boccard, J. Escarré, M. Despeisse, F. Meillaud & C. Ballif. *High-efficiency microcrystalline silicon single-junction solar cells.* Prog. Photovolt: Res. Appl., vol. 921, pages 821–826, 2013.

[Hänni 14] S. Hänni. *Microcrystalline silicon for high-efficiency thin-film photovoltaic devices*. PhD thesis, Ecole Polytechnique Fédérale de Lausanne, Switzerland, 2014.

[Hazra 99] S. Hazra & S. Ray. *Nanocrystalline silicon as intrinsic layer in thin film solar cells.* Solid State Communications, vol. 109, pages 125–129, 1999.

[Heath 02] J. T. Heath, J. D. Cohen, W. N. Shafarman, D. X. Liao & A. A. Rockett. *Effect of Ga content on defect states in* $CuIn_{1-x}Ga_xSe_2$. Applied Physics Letters, vol. 80, no. 24, pages 4540–4542, 2002.

[Hecht 32] K. Hecht. *Zum Mechanismus des lichtelektrischen Primärstromes in isolierenden Kristallen.* Zeitschrift für Physik, vol. 66, pages 235–245, 1932.

[Heinstein 13] P. Heinstein, C. Ballif & L.-E. Perret-Aebi. *Building integrated photovoltaics (BIPV): review, potentials, barriers and myths.* Green, vol. 3, no. 2, pages 125–156, 2013.

[Herrmann 12] W. Herrmann & L. Rimmelspacher. *Uncertainty of solar simulator spectral irradiance data and problems with spectral match classification.* 27^{th} EU PVSEC Proc., pages 3017–3021, 2012.

[Hilfiker 12]	J. N. Hilfiker, N. Singh, T. Tiwald, D. Convey, S. M. Smith, J. H. Baker & H. G. Tompkins. *Survey of methods to characterize thin absorbing films with spectroscopic ellipsometry.* Thin Solid Films, vol. 516, pages 7979–7989, 2012.
[Hof 99]	C. Hof. *Thin Film Solar Cells of Amorphous Silicon: Influence of i-Layer Material on Cell Efficiency.* PhD thesis, Université de Neuchâtel, IMT, 1999.
[Hof 00]	C. Hof, N. Wyrsch & A. Shah. *Influence of electric field distortion and i-layer quality on the collection function of drift-driven a-Si:H solar cells.* Journal of Non-Crystalline Solids, vol. 266–269, no. 1114-1118, 2000.
[Hollenstein 94]	C. Hollenstein, J.-L. Dorier, J. Dutta, L. Sansonnens & A. Howling. *Diagnostics of particle genesis and growth in RF silane plasmas by ion mass spectrometry and light scattering.* Plasma Sources Science and Technology, vol. 3, no. 3, pages 278–285, 1994.
[Holovský 12]	J. Holovský, M. Schmid, M. Stuckelberger, M. Despeisse, C. Ballif, A. Poruba & M. Vaněček. *Time evolution of surface defect states in hydrogenated amorphous silicon studied by photothermal and photocurrent spectroscopy and optical simulation.* Journal of Non-Crystalline Solids, vol. 358, no. 2035–2038, 2012.
[Horcas 07]	I. Horcas, R. Fernández, J. M. Gómez-Rodrígez, J. Colchero, J. Gómez-Herrero & A. M. Baro. *WSXM: A software for scanning probe microscopy and a tool for nanotechnology.* Ref. Sci. Instrum., vol. 78, page 013705, 2007.
[Horiba 06]	Horiba. *Spectroscopic ellipsometry: Tauc-Lorentz dispersion formula.* Technical Note 11, 2006. http://www.horiba.com/fileadmin/uploads/Scientific/Downloads/OpticalSchool_CN/TN/ellipsometer/Tauc-Lorentz_Dispersion_Formula.pdf, last accessed July 20, 2014.
[Horiba 08]	Horiba. *Spectroscopic ellipsometry user guide.* Horiba Jobin Yvon, P/N 31 087 134, 2008.
[Horiba 11]	Horiba. *DeltaPsi2 software reference manual.* Horiba Jobin Yvon, P/N 31 087 091, 2011.
[Horiba 14]	Horiba, 2014. http://www.horiba.com/scientific/products/ellipsometers, last accessed July 20, 2014.
[Hou 11]	G. Hou, Q. Fan, X. Liao, C. Chen, X. Xiang & X. Deng. *High-efficiency and highly stable a-Si:H solar cells deposited at high rate*

(8 Å/s) with disilane grading process. Journal of Vacuum Science and Technology A, vol. 29, no. 6, page 061201, 2011.

[Howling 92] A. A. Howling, J. L. Dorier, C. Hollenstein, U. Kroll & F. Finger. *Frequency effects in silane plasmas for plasma enhanced chemical vapor deposition.* Journal of Vacuum Science and Technology A, vol. 10, pages 1080–1085, 1992.

[Howling 07] A. A. Howling, B. Strahm, P. Colsters, L. Sansonnens & C. Hollenstein. *Fast equilibration of silane/hydrogen plasmas in large area RF capacitive reactors monitored by optical emission spectroscopy.* Plasma Sources Science and Technology, vol. 16, pages 679–696, 2007.

[Howling 09] A. A. Howling, B. Strahm & C. Hollenstein. *Non-intrusive plasma diagnostics for the deposition of large area thin film silicon.* Thin Solid Films, vol. 517, no. 23, pages 6218–6224, 2009.

[Hubin 92] J. Hubin, A. V. Shah & E. Sauvain. *Effects of dangling bonds on the recombination function in amorphous semiconductors.* Philosophical Magazine Letters, vol. 66, no. 3, pages 115–125, 1992.

[Hubin 94] J. Hubin. *Effets des etats localisés du silicium amorphe hydrogéné sur le transport électronique.* PhD thesis, Université de Neuchâtel, 1994.

[Hubin 95] J. Hubin & A. V. Shah. *Effect of the recombination function on the collection in a p-i-n solar cell.* Philosophical Magazine, vol. 72, pages 589–599, 1995.

[IEC 06] IEC. *IEC (International Electrotechnical Commission) 60904-3 Ed.2: Photovoltaic devices - Part 3: Measurement principles for terrestrial photovoltaic (PV) solar devices with reference spectral irradiance data*, 2006.

[IEC 07] IEC. *IEC (International Electrotechnical Commission) 60904-9 Ed.2: Photovoltaic devices - Part 9: Solar simulator performance requirements*, 2007.

[IEC 08] IEC. *IEC (International Electrotechnical Commission) 61646 Ed.2: Thin-film terrestrial photovoltaic (PV) modules - Design qualification and type approval*, 2008.

[INDEOtec 14] INDEOtec, 2014. http://www.indeotec.com (Switzerland), last accessed July 20, 2014.

[Inthisang 09] S. Inthisang, K. Sripapha, S. Miyajima, A. Yamada & M. Konagai. *Hydrogenated amorphous silicon oxide solar cells fabricated near the phase transition between amorphous and microcrystalline structures.* Japanese Journal of Applied Physics, vol. 48, page 122402, 2009.

[Isomura 98] M. Isomura, H. Yamamoto, M. Kondo & A. Matsuda. *The light-induced increase in open circuit voltage of amorphous silicon solar cells.* 2^{nd} world conference and exhibition on photovoltaic solar energy conversion, pages 925–928, 1998.

[Ivashchenko 09] V. I. Ivashchenko, A. V. Vasin, L. A. Ivashchenko & P. L. Skrynskyy. *Blue/white emission from hydrogenated amorphous silicon carbide films prepared by PECVD.* Mat. Res. Soc. Symp. Proc., vol. 1153, no. 1153-A16-01, 2009.

[Jackson 85] W. B. Jackson, S. M. Kelso, C. C. Tsai, J. W. Allen & S.-J. Oh. *Energy dependence of the optical matrix element in hydrogenated amorphous and crystalline silicon.* Physical Review B, vol. 31, no. 8, pages 5187–5198, 1985.

[Jellison 96a] G. E. Jellison & F. A. Modine. *Erratum: "Parameterization of the optical functions of amorphous materials in the interband region" [Appl. Phys. Lett. 69, 371 (1996)].* Applied Physics Letters, vol. 69, page 2137, 1996.

[Jellison 96b] G. E. Jellison & F. A. Modine. *Parameterization of the optical functions of amorphous materials in the interband region.* Applied Physics Letters, vol. 69, pages 371–373, 1996.

[Jiang 09] C.-S. Jiang, Y. Yan, H. R. Moutinho, M. M. Al-Jassim, B. Yan, L. Sivec, J. Yang & S. Guha. *Phosphorus and Boron Doping Effects on Nanocrystalline Formation in Hydrogenated Amorphous and Nanocrystalline Mixed-Phase Silicon Thin Films.* Mater. Res. Soc. Symp. Proc., vol. 1153, no. 1153-A17-07, 2009.

[Johnson 08] E. V. Johnson, A. Abramov, Y. Soro, M. Gueunier-Farret, J. Méot & P. Roca i Cabarrocas. *Application of high deposition rate (9A/s) pm-Si:H to photovoltaic modules.* 23rd EU PVSEC Proc., pages 2339–2342, 2008.

[Johnson 10] E. V. Johnson, F. Dadouche, M. E. Gueunier-Farret, J. P. Kleider & P. Roca i Cabarrocas. *Open-circuit voltage increase dynamics in high and low deposition rate polymorphous silicon solar cells.* Physica Status Solidi A, vol. 207, no. 691–694, 2010.

[Kageyama 11] S. Kageyama, M. Akagawa & H. Fujiwara. *Dielectric function of a-Si:H based on local network structures.* Physical Review B, vol. 83, page 195205, 2011.

[Kageyama 12] S. Kageyama, M. Akagawa & H. Fujiwara. *Ellipsometry characterization of a-Si:H layers for thin-film solar cells.* Journal of Non-Crystalline Solids, vol. 358, pages 2257–2259, 2012.

[Kalache 03] B. Kalache, A. I. Kosarev, R. Vanderhaghen & P. Roca i Cabarrocas. *Ion bombardment effects on microcrystalline silicon growth mechanisms and on the film properties.* Journal of Applied Physics, vol. 93, pages 1262–1273, 2003.

[Kasouit 10] S. Kasouit, K. Hirata, L. Kroely & P. Roca i Cabarrocas. *MDECR plasma deposition of microcrystalline silicon as an alternative to rf capacitive methods.* 25th EU PVSEC/WCPEC-5 Proc., pages 3138–3140, 2010.

[Kharchenko 03] A. V. Kharchenko, V. Suendo & P. Roca i Cabarrocas. *Plasma studies under polymorphous silicon deposition conditions.* Thin Solid Films, vol. 427, no. 1, pages 236–240, 2003.

[Kiess 95] H. Kiess & W. Rehwald. *On the ultimate efficiency of solar cells.* Solar Energy Materials & Solar Cells, vol. 38, pages 45–55, 1995.

[Kim 12a] K. H. Kim, E. V. Johnson, A. Abramov & P. Roca i Cabarrocas. *Light induced electrical and macroscopic changes in hydrogenated polymorphous silicon solar cells.* EPJ Photovoltaics, vol. 3, page 30301, 2012.

[Kim 12b] K.-H. Kim, E. V. Johnson & P. Roca i Cabarrocas. *Irreversible light-induced degradation and stabilization of hydrogenated polymorphous silicon solar cells.* Solar Energy Materials & Solar Cells, vol. 105, pages 208–2012, 2012.

[Kim 13a] K.-H. Kim, S. Kasouit, E. V. Johnson & P. Roca i Cabarrocas. *Substrate versus superstrate configuration for stable thin film silicon solar cells.* Solar Energy Materials & Solar Cells, vol. 119, pages 124–128, 2013.

[Kim 13b] S. Kim, J.-W. Chung, H. Lee, J. Park, Y. Heo & H.-M. Lee. *Remarkable progress in thin-film silicon solar cells using high-efficiency triple-junction technology.* Solar Energy Materials & Solar Cells, vol. 119, pages 26–35, 2013.

[Knights 78] J. C. Knights, G. Lucovsky & R. J. Nemanich. *Hydrogen bonding in silicon-hydrogen alloys.* Philosophical Magazine B, vol. 37, no. 4, pages 467–475, 1978.

[Knights 79] J. C. Knights. *Characterization of plasma-deposited amorphous Si:H thin films.* Japanese Journal of Applied Physics, vol. 18, pages 101–108, 1979.

[Kondo 04] M. Kondo & A. Matsuda. *Novel aspects in thin film silicon solar cells – amorphous, microcrystalline and nanocrystalline silicon.* Thin Solid Films, vol. 457, pages 97–102, 2004.

[Konuma 91] M. Konuma. Film deposition by plasma techniques. Springer-Verlag, 1991.

[Kopecki 10] J. Kopecki, A. Schulz, M. Walker, J. Glatz-Reichenbach, K. Peter, S. Laure & U. Stroth. *Plasma spraying technique for the deposition of* α*-Si/*μ*c-Si.* 25th EU PVSEC/WCPEC-5 Proc., pages 3087–3089, 2010.

[Korevaar 02] B. A. Korevaar, A. M. H. N. Petit, C. Smit, R. A. C. M. M. van Swaaij & M. C. M. van de Sanden. *Effect of buffer layers on p-i-n a-Si:H solar cells deposited at high rate utilising an expanding thermal plasma.* IEEE Photovoltaic Specialists Conference, pages 1230–1233, 2002.

[Krc 03] J. Krc, F. Smole & M. Topic. *Analysis of light scattering in amorphous Si:H solar cells by a one-dimensional semi-coherent optical model.* Prog. Photovolt: Res. Appl., vol. 11, pages 15–26, 2003.

[Kroll 98] U. Kroll, J. Meier, P. Torres, J. Pohl & A. Shah. *From amorphous to microcrystalline silicon films prepared by hydrogen dilution using the VHF (70 MHz) GD technique.* Journal of Non-Crystalline Solids, vol. 227–230, pages 68–72, 1998.

[LabVIEW 14] LabVIEW, 2014. http://www.ni.com/labview, last accessed July 20, 2014.

[Lanz 13] T. Lanz, M. Bonmarin, M. Stuckelberger, C. Schlumpf, C. Ballif & B. Ruhstaller. *Electrothermal finite-element modeling for defect characterization in thin-film silicon solar modules.* IEEE journal of selected topics in quantum electronics, vol. 19, no. 5, page 4000308, 2013.

[Layadi 95] N. Layadi, P. Roca i Cabarrocas, B. Drévillon & I. Solomon. *Real-time spectroscopic ellipsometry study of the growth of amorphous* *and microcrystalline silicon thin films prepared by alternating silicon deposition and hydrogen plasma treatment.* Physical Review B, vol. 52, no. 7, pages 5136–5143, 1995.

[Lebib 05] S. Lebib & P. Roca i Cabarrocas. *Effects of ion energy on the crystal size and hydrogen bonding in plasma-deposited nanocrystalline silicon thin films.* Journal of Applied Physics, vol. 97, page 104334, 2005.

[Lechner 10] P. Lechner, R. Geyer, A. Haslauer & T. Roehrl. *Long-term performance of ASI tandem junction thin film solar modules.* 25th EU PVSEC Proc., pages 3283–3287, 2010.

[Lieberman 05] M. A. Lieberman & A. J. Lichtenberg. Principles of Plasma Discharges and Materials Processing. John Wiley & Sons, Inc., 2005.

[Lin 87] W.-L. Lin, H.-K. Tsai, S.-C. Lee, W.-J. Sah & W.-J. Tzeng. *Identification of infrared absorption peaks of amorphous siliconcarbon alloy by thermal annealing.* Applied Physics Letters, vol. 51, no. 25, pages 2112–2114, 1987.

[Lisovskiy 98] V. A. Lisovskiy & V. D. Yegorenkov. *Rf breakdown of low-pressure gas and a novel method for determination of electron-drift velocities in gases.* J. Phys. D: Appl. Phys., vol. 31, pages 3349–3357, 1998.

[Lisovskiy 05] V. Lisovskiy, J.-P. Booth, S. Martins, K. Landry, D. Douai & V. Cassagne. *Extinction of RF capacitive low-pressure discharges.* Europhys. Lett., vol. 71, no. 3, pages 407–411, 2005.

[Lisovskiy 06] V. Lisovskiy, J.-P. Booth, K. Landry, D. Douai, V. Cassagne & V. Yegorenkov. *Electron drift velocity in argon, nitrogen, hydrogen, oxygen and ammonia in strong electric fields determined from rf breakdown curves.* J. Phys. D: Appl. Phys., vol. 39, pages 660–665, 2006.

[Lisovskiy 07] V. Lisovskiy, J.-P. Booth, K. Landry, D. Douai, V. Cassagne & V. Yegorenkov. *Electron drift velocity in silane in strong electric fields determined from rf breakdown curves.* J. Phys. D: Appl. Phys., vol. 40, pages 3408–3410, 2007.

[Lisovskiy 08] V. Lisovskiy, J.-P. Booth, K. Landry, D. Douai, V. Cassagne & V. Yegorenkov. *Similarity law for rf breakdown.* Europhysics Letters, vol. 82, page 15001, 2008.

[Lo 10] A. Lo, M. Despeisse, R. Théron & C. Ballif. *An hybrid LED/halogen large-area solar simulator allowing for variable spectrum and* *variable illumination pulse shape.* 25th EU PVSEC Proc., pages 4232–4235, 2010.

[Lord 01] K. Lord, B. Yan, J. Yang, & S. Guha. *Light-induced increase in the open-circuit voltage of thin-film heterogeneous silicon solar cells.* Applied Physics Letters, vol. 79, no. 23, pages 3800–3802, 2001.

[Lucovsky 79] G. Lucovsky, R. J. Nemanich & J. C. Knights. *Structural interpretation o fthe vibrational spectra of a-Si:H alloys.* Physical Review B, vol. 19, no. 4, pages 2064–2073, 1979.

[Matsuda 83] A. Matsuda. *Formation kinetics and control of microcrystallite in μc-Si:H from glow discharge plasma.* Journal of Non-Crystalline Solids, vol. 59–60, pages 767–774, 1983.

[Matsuda 90] A. Matsuda, K. Nomoto, Y. Takeuchi, A. Suzuki, A. Yuuki & J. Perrin. *Temperature dependence of the sticking and loss probabilities of silyl radicals on hydrogenated amorphous silicon.* Surface Science, vol. 227, pages 50–56, 1990.

[Matsuda 98] A. Matsuda. *Plasma and surface reactions for obtaining low defect density amorphous silicon at high growth rates.* Journal of Vacuum Science and Technology A, vol. 16, pages 365–368, 1998.

[Matsuda 03] A. Matsuda, M. Takai, T. Nishimoto & M. Kondo. *Control of plasma chemistry for preparing highly stabilized amorphous silicon at high growth rate.* Solar Energy Materials & Solar Cells, vol. 78, pages 3–26, 2003.

[Matsuda 04] A. Matsuda. *Thin-Film Silicon - Growth Process and Solar Cell Application.* Japanese Journal of Applied Physics, vol. 43, no. 12, pages 7909–7920, 2004.

[Matsui 12] T. Matsui, H. Sai, K. Saito & M. Kondo. *Amorphous-silicon-based thin-film solar cells exhibiting low light-induced degradation.* Japanese Journal of Applied Physics, vol. 51, page 10NB04, 2012.

[Matsui 13a] T. Matsui, H. Sai, K. Saito & M. Kondo. *High-efficiency thin-film silicon solar cells with improved light-soaking stability.* Prog. Photovolt: Res. Appl., vol. 21, no. 2, pages 1363–1369, 2013.

[Matsui 13b] T. Matsui, H. Sai, T. Suezaki, M. Matsumoto, K. Saito, I. Yoshida & M. Kondo. *Development of highly stable and efficient amorphous silicon based solar cells.* 28th EU PVSEC Proc., pages 2213–2217, 2013.

[Matsui 14a] T. Matsui, 2014. Private communication.

[Matsui 14b] T. Matsui, 2014. MRS spring conference 2014, presentation A1.01.

[Maurizio 12] F. Maurizio. *Development of high band gap protocrystalline material for p-i-n thin film silicon solar cells.* Master thesis at Ecole Polytechnique Fédérale de Lausanne, Switzerland, 2012.

[Meillaud 12] F. Meillaud, A. Billet, C. Battaglia, M. Boccard, G. Bugnon, P. Cuony, M. Charrière, M. Despeisse, L. Ding, J. Escarre-Palou, S. Hänni, L. Löfgren, S. Nicolay, G. Parascandolo, M. Stuckelberger & C. Ballif. *Latest developments of high-efficiency micromorph tandem silicon solar cells implementing innovative substrate materials and improved cell design.* IEEE Journal of Photovoltaics, vol. 2, no. 3, pages 236–240, 2012.

[Melskens 14] J. Melskens, M. Schouten, R. Santbergen, M. Fischer, R. Vasudevan, D. J. van der Vlies, R. J. V. Quax, S. G. M. Heirman, K. Jäger, V. Demontis, M. Zeman & A. H. M. Smets. *In situ manipulation of the sub gap states in hydrogenated amorphous silicon monitored by advanced application of Fourier transform photocurrent spectroscopy.* Solar Energy Materials & Solar Cells, 2014. in press.

[Merten 98] J. Merten, J. M. Asensi, C. Voz, A. V. Shah, R. Platz & J. Andreu. *Improved Equivalent Circuit and Analytical Model for Amorphous Silicon Solar Cells and Modules.* IEEE Transactions on Electron Devices, vol. 45, no. 2, 1998.

[Middya 01] A. R. Middya, S. Hamma, S. Hazra, S. Ray & C. Longeaud. *Stability and nanostructure of heterogeneous amorphous silicon thin-film synthesized under chamber pressure (500 to 2200 mTorr) regime of RF PECVD.* Mat. Res. Soc. Symp. Proc., vol. 664, no. A9.5, 2001.

[Minowa 09] A. Minowa & M. Kondo. *Low temperature Si homoepitaxy by a reactive CVD with a* SiH_4/F_2 *mixture.* Mater. Res. Soc. Symp. Proc., vol. 1153, no. 1153-A09-02, 2009.

[Mott 69] N. F. Mott. *Conduction in non-crystalline materials: III. Localized states in a pseudogap and near extremities of conduction and valence bands.* Philosophical Magazine, vol. 19, no. 160, pages 835–852, 1969.

[Moustakas 82] T. D. Moustakas & R. Friedman. *Amorphous silicon p-i-n solar cells fabricated by reactive sputtering.* Applied Physics Letters, vol. 40, no. 6, pages 515–517, 1982.

[Murphy 80] J. C. Murphy & L. C. Aamodt. *Photothermal spectrosopy using optical beam probing: mirage effect.* Journal of Applied Physics, vol. 51, pages 4580–4588, 1980.

[Muthmann 11] S. Muthmann & A. Gordijn. *Amorphous silicon solar cells deposited with non-constant silane concentration.* Solar Energy Materials & Solar Cells, vol. 95, pages 573–578, 2011.

[Newport 14] Newport, 2014. http://www.newport.com/Oriel, last accessed July 20, 2014.

[Nicolay 12] S. Nicolay, M. Benkhaira, L. Ding, J. Escarre, G. Bugnon, F. Meillaud & C. Ballif. *Control of CVD-deposited ZnO films properties through water/DEZ ratio: Decoupling of electrode morphology and electrical characteristics.* Solar Energy Materials & Solar Cells, vol. 105, pages 46–52, 2012.

[Niikura 07] C. Niikura, N. Itagaki & A. Matsuda. *Guiding Principles for Obtaining High-Quality Microcrystalline Silicon at High Growth Rates Using SiH4/H2 Glow-Discharge Plasma.* Japanese Journal of Applied Physics, vol. 46, no. 5A, pages 3052–3058, 2007.

[Ouwens 24] J. D. Ouwens & R. E. I. Schropp. *Hydrogen microstructure in hydrogenated amorphous silicon.* Physical Review B, vol. 54, pages 17759–17762, 24.

[Palik 98] E. D. Palik, editor. Handbook of optical constants of solids. Academic press, 1998.

[Pan 04] B. C. Pan & R. Biswas. *Structure and simulation of hydrogenated nanocrystalline silicon.* Journal of Applied Physics, vol. 96, no. 11, pages 6247–6252, 2004.

[Panasonic 14] Panasonic, 2014. *Panasonic HIT solar cell achieves world's highest energy conversion efficiency of 25.6% at research level*, press release of April 10, 2014, http://panasonic.co.jp/corp/news/official.data/data.dir/2014/04/en140410-4/en140410-4.html, last accessed August 6, 2014.

[Paschen 89] F. Paschen. *Ueber die zum Funkenübergang in Luft, Wasserstoff und Kohlensäure bei verschiedenen Drucken erforderliche Potentialdifferenz.* Annalen der Physik, vol. 273, no. 5, pages 69–96, 1889.

[Pearce 07] J. M. Pearce, N. Podraza, R. W. Collins, M. M. Al-Jassim, K. M. Jones, J. Deng & C. R. Wronski. *Optimization of open circuit voltage in amorphous silicon solar cells with mixed-phase (amorphous+nanocrystalline) p-type contacts of low nanocrystalline content.* Journal of Applied Physics, vol. 101, page 114301, 2007.

[Perret-Aebi 14] L.-E. Perret-Aebi, P. Heinstein, M. Despeisse, C. Ballif & M. Stückelberger, 2014. *Solar module and its production process*, Patent application WO2014044620 (A1).

[Perrin 93] J. Perrin. *Modelling of the power dissipation and rovibrational heating and cooling in SiH4-H2 RF glow discharges.* J. Phys. D: Appl. Phys., vol. 26, pages 1662–1679, 1993.

[Pieters 06] B. E. Pieters, J. Krc & M. Zeman. *Advanced numerical simulation tool for solar cells - ASA5.* Conf. Rec. 4th WCPEC, vol. 2, pages 1513–1516, 2006.

[Poissant 03] Y. Poissant, P. Chatterjee & P. Roca i Cabarrocas. *Analysis and optimization of the performance of polymorphous silicon solar cells: Experimental characterization and computer modeling.* Journal of Applied Physics, vol. 94, no. 11, pages 7305–7316, 2003.

[Pollard 6] W. B. Pollard & G. Lucovsky. *Phonons in polysilane alloys.* Physical Review B, vol. 26, pages 3172–3180, 6.

[Powell 92] M. J. Powell, C. van Berkel & A. R. Franklin. *Defect pool in amorphous-silicon thin-film transistors.* Physical Review B, vol. 45, no. 8, pages 4160–4170, 1992.

[Python 08] M. Python, E. Vallat-Sauvain, J. Bailat, D. Dominé, L. Fesquet, A. Shah & C. Ballif. *Relation between substrate surface morphology and microcrystalline silicon solar cell performance.* Journal of Non-Crystalline Solids, vol. 354, pages 2258–2262, 2008.

[Python 09] M. Python, O. Madani, D. Dominé, F. Meillaud, E. Vallat-Sauvain & C. Ballif. *Influence of the substrate geometrical parameters on microcrystalline silicon growth for thin-film solar cells.* Solar Energy Materials & Solar Cells, vol. 93, pages 1714–1720, 2009.

[Raizer 91] Y. P. Raizer. Gas discharge physics. Springer-Verlag, 1991.

[Rath 09] J. K. Rath, M. M. de Jong, A. Verkerk, M. Brinza & R. E. I. Schropp. *Gas phase conditions for obtaining device quality amorphous silicon at low temperature and high deposition rate.* Mater. Res. Soc. Symp. Proc., vol. 1153, no. 1153-A22-04, 2009.

[Raugei 12] M. Raugei, P. F. i Palmer & V. Fthenakis. *The energy return on energy investment (EROI) of photovoltaics: Methodology and comparisons with fossil fuel life cycles.* Energy Policy, vol. 45, pages 576–582, 2012.

[Rech 97a] B. Rech, C. Beneking, S. Wieder & H. Wagner. *Initial and stabilized open-circuit voltage of a-Si:H solar cells: a discussion on the basis of dark I-V curves.* 14th EU PVSEC Proc., pages 574–577, 1997.

[Rech 97b] B. Rech. *Solarzellen aus amorphem Silizium mit hohem stabilem Wirkungsgrad.* PhD thesis, Forschungszentrum Jülich, 1997.

[Rech 01] B. Rech, T. Roschek, J. Müller, S. Wieder & H. Wagner. *Amorphous and microcrystalline silicon solar cells prepared at high deposition rates using RF (13.56MHz) plasma excitation frequencies.* Solar Energy Materials & Solar Cells, vol. 66, pages 267–273, 2001.

[Repmann 03] T. Repmann, J. Kirchhoff, W. Reetz, F. Birmans, J. Müller & B. Rech. *Investigations on the current matching of highly efficient tandem solar cells based on amorphous and microcrystalline silicon.* Proc. 3rd World Conference on Photovoltaic Energy Conversion, no. 5P-D4-32, 2003.

[Rinnert 98] H. Rinnert, M. Vergnat, G. Marchal & A. Burneau. *Improvement of the stability under illumination of a-Si:H films elaborated by ion-beam-assisted evaporation using a hydrogen-argon plasma.* Journal of Applied Physics, vol. 83, no. 2, pages 1103–1106, 1998.

[Roca i Cabarrocas 91] P. Roca i Cabarrocas, J. B. Chévrier, J. Huc, A. Lloret, J. Y. Parey & J. P. M. Schmitt. *A fully automated hot-wall multiplasma-monochamber reactor for thin film deposition.* Journal of Vacuum Science and Technology A, vol. 9, no. 4, pages 2331–2341, 1991.

[Roca i Cabarrocas 98] P. Roca i Cabarrocas, P. Stáhel, S. Hamma & Y. Poissant. *Stable single junction p-i-n solar cells with efficiencies approaching 10%.* 2nd world conference and exhibition on photovoltaic solar energy conversion, pages 355–358, 1998.

[Roca i Cabarrocas 00] P. Roca i Cabarrocas. *Plasma enhanced chemical vapor deposition of amorphous, polymorphous and microcrystalline silicon films.* Journal of Non-Crystalline Solids, vol. 266–269, pages 31–37, 2000.

[Roca i Cabarrocas 02] P. Roca i Cabarrocas, A. Fontcuberta i Morral & Y. Poissant. *Growth and optoelectronic properties of polymorphous silicon thin films.* Thin Solid Films, vol. 403–404, pages 39–46, 2002.

[Sah 57] C.-T. Sah, R. N. Noyce & W. Shockley. *Carrier generation and recombination in p-n junctions and p-n junction characteristics.* Proceedings of the IRE, vol. 45, no. 9, pages 1228–1243, Sept 1957.

[Sai 13] H. Sai, T. Koida, T. Matsui, I. Yoshida, K. Saito, & M. Kondo. *Microcrystalline silicon solar cells with 10.5% efficiency realized* *by improved photon absorption via periodic textures and highly transparent conductive oxide.* Applied physics express, vol. 6, page 104101, 2013.

[Sakai 90] H. Sakai, T. Yoshida, T. Hama & Y. Ichikawa. *Effects of surface morphology of transparent electrode on the open-circuit voltage in a-Si:H solar cells.* Japanese Journal of Applied Physics, vol. 29, no. 4, pages 630–635, 1990.

[Schiff 03] E. A. Schiff. *Low-mobility solar cells: a device physics primer with application to amorphous silicon.* Solar Energy Materials & Solar Cells, vol. 78, pages 567–595, 2003.

[Schott 14] Schott. *Data sheet AF 32 thin glass*, 2014. http://www.us.schott.com/advanced_optics/english/download/schott-af-32-eco-thin-glass-may-2013-us.pdf, last accessed July 20, 2014.

[Schouten 13] M. Schouten. *The nanostructure of hydrogenated amorphous silicon, examined by means of thermal annealing and light soaking.* Master thesis at TU Delft, 2013.

[Schroeder 01] B. Schroeder, U. Weber, H. Seitz, A. Ledermann & C. Mukherjee. *Current status of the thermo-catalytic (hot-wire) CVD of thin silicon films for photovoltaic applications.* Thin Solid Films, vol. 395, pages 298–304, 2001.

[Schropp 09] R. E. I. Schropp, J. K. Rath & H. Li. *Growth mechanism of nanocrystalline silicon at the phase transition and its application in thin film solar cells.* Journal of Crystal Growth, vol. 311, pages 760–764, 2009.

[Schülke 81] W. Schülke. *Structural investigation of hydrogenated amorphous silicon by X-ray diffraction.* Philosophical Magazine B, vol. 43, no. 3, pages 451–468, 1981.

[Schüttauf 14a] J.-W. Schüttauf, G. Bugnon, M. Stuckelberger, S. Hänni, M. Boccard, M. Despeisse, F.-J. Haug, F. Meillaud & C. Ballif. *Thin-film silicon triple-junction solar cells on highly transparent front electrodes with stabilized efficiencies up to 12.8 %.* IEEE Journal of Photovoltaics, vol. 4, no. 3, pages 757–762, 2014.

[Schüttauf 14b] J. W. Schüttauf, B. Niesen, M. Boccard, G. Bugnon, S. Hänni, X. Niquille, M. Stuckelberger, F. Sculati-Meillaud, F.-J. Haug & C. Ballif. *High-efficiency thin-film silicon triple and quadruple junction solar cells.* Manuscript in preparation, 2014.

[Sculati-Meillaud 06] F. Sculati-Meillaud. *Microcrystalline silicon solar cells: Theory, diagnosis and stability.* PhD thesis, Université de Neuchâtel, Switzerland, 2006.

[SFOE 13] SFOE, 2013. Swiss Federal Office of Energy: *Energy consuption in Switzerland 2013*, Nr. 805.006.13.

[Shah 10] A. Shah, editor. Thin-film silicon solar cells. CRC Press, 2010.

[Shah 11] A. V. Shah, F. Sculati-Meillaud, Z. J. Berenyi, O. M. Ghahfarokhi & R. Kumar. *Diagnostics of thin-film silicon solar cells and solar panels/modules with variable intensity measurements (VIM).* Solar Energy Materials & Solar Cells, vol. 95, pages 398–403, 2011.

[Shanks 80] H. Shanks, C. J. Fang, L. Ley, M. Cardona, F. J. Demond & S. Kalbitzer. *Infrared spectrum and structure of hydrogenated amorphous silicon.* Physica Status Solidi B, vol. 100, no. 1, pages 43–56, 1980.

[Shimizu 04] T. Shimizu. *Staebler-Wronski effect in hydrogenated amorphous silicon and related alloy films.* Japanese Journal of Applied Physics, vol. 43, no. 6A, pages 3257–3268, 2004.

[Shimizu 05] S. Shimizu, M. Kondo & A. Matsuda. *A highly stabilized hydrogenated amorphous silicon film having very low hydrogen concentration and an improved Si bond network.* Journal of Applied Physics, vol. 97, page 033522, 2005.

[Shockley 49] W. Shockley. *The theory of p-n junctions in semiconductors and p-n junction transistors.* Bell system technical journal, vol. 28, no. 3, pages 435–489, 1949.

[Shockley 52] W. Shockley & W. T. Read. *Statistics of the recombinations of holes and electrons.* Physical Review, vol. 87, no. 5, pages 835–842, 1952.

[Shockley 61] W. Shockley & H. J. Queisser. *Detailed balance limit of efficiency of p-n junction solar cells.* Journal of Applied Physics, vol. 32, no. 3, pages 510–519, 1961.

[Smets 02] A. H. M. Smets. *Growth Related Material Properties of Hydrogenated Amorphous Silicon.* PhD thesis, Technische Universiteit Eindhoven, 2002.

[Smets 03] A. H. M. Smets, W. M. M. Kessels & M. C. M. van de Sanden. *Vacancies and voids in hydrogenated amorphous silicon.* Applied Physics Letters, vol. 82, no. 10, pages 1547–1549, 2003.

[Smets 07a] A. H. M. Smets, W. M. M. Kessels & M. C. M. van de Sanden. *The effect of ion-surface and ion-bulk interactions during hydrogenated amorphous silicon deposition.* Journal of Applied Physics, vol. 102, page 073523, 2007.

[Smets 07b] A. H. M. Smets & M. C. M. van de Sanden. *Relation of the Si-H stretching frequency to the nanostructural Si-H bulk environment.* Physical Review B, vol. 76, page 073202, 2007.

[Smets 08] A. H. M. Smets, T. Matsui & M. Kondo. *High-rate deposition of microcrystalline silicon p-i-n solar cells in the high pressure depletion regime.* Journal of Applied Physics, vol. 104, page 034508, 2008.

[Smets 09] A. H. M. Smets, T. Matsui, M. Kondo & M. C. M. van de Sanden. *The hydride stretching modes of hydrogentated vacancies in amorphous and nanocrystalline silicon: A helpful tool for material characterization.* Proc. 34th IEEE Photovoltaic Specialists Conference, 2009.

[Smets 10] A. H. M. Smets, C. R. Wronski, M. Zeman & M. C. M. van de Sanden. *The Staebler-Wronski effect: new physical approaches and insights as a route to reveal its origin.* Mat. Res. Soc. Symp. Proc., vol. 1245, pages 1245–A14–02, 2010.

[Smets 12] A. H. M. Smets, M. A. Wank, B. Vet, M. Fischer, R. A. C. M. M. van Swaaij, M. Zeman, D. C. Bobela, C. R. Wronski & R. M. C. M. van de Sanden. *The relation between the bandgap and the anisotropic nature of hydrogenated amorphous silicon.* IEEE Journal of Photovoltaics, vol. 2, no. 2, pages 94–98, 2012.

[Smits 58] F. M. Smits. *Measurement of sheet resistivities with the four-point probe.* Bell system technical journal, vol. 37, no. 3, pages 711–718, 1958.

[Söderström 11] K. Söderström, J. Escarré, O. Cubero, F.-J. Haug, S. Perregaux & C. Ballif. *UV-nano-imprint lithography technique for the replication of back reflectors for n-i-p thin film silicon solar cells.* Prog. Photovolt: Res. Appl., vol. 19, no. 2, pages 202–210, 2011.

[Söderström 13] K. Söderström. *Coupling light into thin silicon layers for high-efficiency solar cells.* PhD thesis, Ecole Polytechnique Fédérale de Lausanne, Switzerland, 2013.

[Solaronix 14] Solaronix, 2014. http://www.solaronix.com, last accessed July 20, 2014.

[SolidWorks 14] SolidWorks, 2014. http://www.solidworks.com, last accessed July 20, 2014.

[Soro 08] Y. M. Soro, A. Abramov, M. E. Gueunier-Farret, E. V. Johnson, Longeaud, P. Roca i Cabarrocas & J. P. Kleider. *Device grade hydrogenated polymorphous silicon deposited at high rates*. Journal of Non-Crystalline Solids, vol. 354, pages 2092–2095, 2008.

[Spear 75] W. E. Spear & P. G. L. Comber. *Substitutional doping of amorphous silicon*. Solid State Communications, vol. 17, pages 1193–1196, 1975.

[Sriraman 02] S. Sriraman, S. Agarwal, E. S. Aydil & D. Maroudas. *Mechanism of hydrogen-induced crystallization of amorphous silicon*. Nature, vol. 418, pages 62–65, 2002.

[Staebler 77] D. L. Staebler & C. R. Wronski. *Reversible conductivity changes in discharge-produced amorphous Si*. Applied Physics Letters, vol. 31, no. 4, pages 292–294, 1977.

[St'ahel 97] P. St'ahel, A. Hadjadj, P. Sládek & P. Roca i Cabarrocas. *Metastability in boron doped a-Si:H and a-SiC:H materials: correlation with solar cell parameters*. 14th EU PVSEC Proc., pages 640–643, 1997.

[St'ahel 98] P. St'ahel, P. Roca i Cabarrocas, P. Sladek & M. L. Theye. *Metastability of phosphorus- or boron doped a-Si:H films*. MRS Symp. Proc. Series, vol. 507, page 649, 1998.

[Stavola 88] M. Stavola, S. J. Pearton, J. Lopata & W. C. Dautremont-Smith. *Vibrational spectroscopy of acceptor-hydrogen complexes in silicon: Evidence for low-frequency excitations*. Physical Review B, vol. 37, no. 14, pages 8313–8318, 1988.

[Steinhauser 08] J. Steinhauser. *Low pressure chemical vapor deposited zinc oxide for thin film silicon solar cells: optical and electrical properties*. PhD thesis, Université de Neuchâtel, Switzerland, 2008.

[Strahm 07] B. Strahm, A. A. Howling, L. Sansonnens & C. Hollenstein. *Plasma silane concentration as a determining factor for the transition from amorphous to microcrystalline silicon in* SiH_4/H_2 *discharges*. Plasma Sources Science and Technology, vol. 16, pages 80–89, 2007.

[Street 91] R. A. Street. Hydrogenated amorphous silicon. Cambridge university press, 1991.

[Stuckelberger 10] M. Stuckelberger, A. Shah, J. Krc, M. Despeisse, F. Meillaud & C. Ballif. *Internal electric field and fill factor of amorphous silicon solar cells.* 35th IEEE Photovoltaic Specialists Conference Proc., pages 001569–001574, 2010.

[Stuckelberger 12] M. Stuckelberger, Y. Riesen, B. Perruche, M. Despeisse, N. Wyrsch & C. Ballif. *Charge collection in amorphous silicon solar cells: cell analysis and simulation of high-efficiency pin devices.* Journal of Non-Crystalline Solids, vol. 358, pages 2187–2189, 2012.

[Stuckelberger 13] M. Stuckelberger, M. Despeisse, G. Bugnon, J.-W. Schüttauf, F.-J. Haug & C. Ballif. *Comparison of amorphous silicon absorber materials: Light-induced degradation and solar cell efficiency.* Journal of Applied Physics, vol. 114, page 154509, 2013.

[Stuckelberger 14a] M. Stuckelberger, 2014. MRS spring conference 2014, presentation A1.02.

[Stuckelberger 14b] M. Stuckelberger, A. Billet, Y. Riesen, M. Boccard, M. Despeisse, J.-W. Schüttauf, F.-J. Haug & C. Ballif. *Comparison of amorphous silicon absorber materials: kinetics of light-induced degradation*, 2014. Accepted for publication in Prog. Photovolt: Res. Appl.

[Stuckelberger 14c] M. Stuckelberger, B. Perruche, M. Bonnet-Eymard, Y. Riesen, M. Despeisse, F.-J. Haug & C. Ballif. *Class AAA LED-based solar simulator for steady-state measurements and light soaking.* IEEE Journal of Photovoltaics, vol. 4, no. 5, pages 1282–1287, 2014.

[Stuckelberger 14d] M. Stuckelberger, Y. Riesen, M. Despeisse, J.-W. Schüttauf, F.-J. Haug & C. Ballif. *Light-induced* V_{oc} *increase and decrease in high-efficiency amorphous silicon solar cells.* Journal of Applied Physics, page 094503, 2014.

[Stutzmann 84] M. Stutzmann, W. B. Jackson & C. C. Tsai. *Kinetics of the Staebler-Wronski effect in hydrogenated amorphous silicon.* Applied Physics Letters, vol. 45, no. 10, pages 1075–1077, 1984.

[Stutzmann 85] M. Stutzmann, W. B. Jackson & C. C. Tsai. *Light-induced metastable defects in hydrogenated amorphous silicon: A systematic study.* Physical Review B, vol. 32, no. 1, pages 23–47, 1985.

[Stutzmann 89] M. Stutzmann. *The defect density in amorphous silicon.* Philosiphical Magazine B, vol. 60, no. 4, pages 531–546, 1989.

[Sze 07] S. M. Sze & K. K. Ng. Physics of semiconductor devices. Wiley, 2007.

[t-global 14] t-global, 2014. http://www.tglobaltechnology.com/thermal-management-products/tg2030-ultra-soft-thermal-conductive-pad.php, last accessed August 10, 2014.

[Tauc 66] J. Tauc, R. Grigorovici & A. Vancu. *Optical properties and electronic structure of amorphous germanium.* Physica Status Solidi B, vol. 15, no. 2, pages 627–637, 1966.

[TEL solar 14a] TEL solar, 2014. *New record-breaking PV module efficiency has been achieved*, press release of July 9, 2014, http://www.solar.tel.com, last accessed July 28, 2014.

[TEL solar 14b] TEL solar, 2014. http://www.solar.tel.com, last accessed July 20, 2014.

[Tiedje 81] T. Tiedje, J. M. Cebulka, D. L. Morel & B. Abeles. *Evidence for exponential band tails in amorphous silicon hydride.* Physical Review Letters, vol. 46, no. 15, pages 1425–0428, 1981.

[Tompkins 05] H. G. Tompkins & E. A. Irene, editors. Handbook of ellipsometry. William Andrew, Inc., 2005.

[Townsend 10] J. S. Townsend. The theory of ionization of gases by collision. Constable & Company LTD, 1910.

[Tsuda 89] M. Tsuda, S. Oikawa & K. Sato. *On the primary process in the plasmachemical and photochemical vapor deposition from silane. III. Mechanism of the radiative species Si(1P0) formation.* Journal of Chemical Physics, vol. 91, no. 11, pages 6822–6829, 1989.

[Urbach 56] F. Urbach. *The long-wavelength edge of photographic sensitivity and the electronic absorption of solics.* Physical Review Letters, vol. 92, page 1324, 1956.

[Valdes 54] L. B. Valdes. *Resistivity measurements on germanium for transistors.* Proceedings of the IRE, vol. 42, no. 2, pages 420–427, 1954.

[van Elzakker 07] G. van Elzakker, F. D. Tichelaar & M. Zeman. *Suppression of crystalline growth in silicon films deposited from hydrogen diluted silane using a layer-by-layer approach.* Thin Solid Films, vol. 515, pages 7460–7464, 2007.

[van Elzakker 09] G. van Elzakker, P. Sutta & M. Zeman. *Structural Properties of a-Si:H Films With Improved Stability Against Light Induced Degradation.* Mater. Res. Soc. Symp. Proc., vol. 1153, no. 1153-A18-02, 2009.

[van Elzakker 10]	G. van Elzakker. *Hydrogenated Amorphous Silicon Solar Cells Deposited from Silane Diluted with Hydrogen.* PhD thesis, TU Delft, 2010.
[Vaněček 83]	M. Vaněček, J. Kočka, J. Stuchlík, Z. Kožíšek, O. Štika & A. Tříska. *Density of the gap states in undoped and doped glow discharge a-Si:H.* Solar Energy Materials, vol. 8, pages 411–423, 1983.
[Vignoli 03]	S. Vignoli, R. Butté, R. Meaudre, M. Meaudre & R. Brenier. *Links between hydrogen bonding, residual stress, structural properties and metastability in hydrogenated nanostructured silicon thin films.* J. Phys.: Condens. Matter, vol. 15, pages 7185–7200, 2003.
[von Roedern 77]	B. von Roedern, L. Ley & M. Cardona. *Photoelectron spectra of hydrogenated amorphous silicon.* Physical Review Letters, vol. 39, no. 24, pages 1576–1580, 1977.
[Voyles 03]	P. M. Voyles & J. R. Abelson. *Medium-range order in amorphous silicon measured by fluctuation electron microscopy.* Solar Energy Materials & Solar Cells, vol. 78, pages 85–113, 2003.
[WaveMetrics 14]	WaveMetrics, 2014. http://www.wavemetrics.com/products/igorpro/igorpro.htm, last accessed July 20, 2014.
[Winer 89]	K. Winer. *Chemical-equilibrium description of the gap-state distribution in a-Si:H.* Physical Review Letters, vol. 63, no. 14, pages 1487–1490, 1989.
[Winer 91]	K. Winer. *Defect pool model of defect formation in a-Si:H.* Journal of Non-Crystalline Solids, vol. 137&138, pages 157–162, 1991.
[Woollam 14]	J. A. Woollam, 2014. http://www.jawoollam.com, last accessed July 20, 2014.
[Würfel 05]	P. Würfel. Physics of solar cells: From principles to new concepts. Wiley-VCH, 2005.
[www.2000watt.ch 14]	www.2000watt.ch, 2014. http://www.2000watt.ch/fileadmin/user_upload/2000Watt-Gesellschaft/de/Dateien/2000-Watt-Gesellschaft/Weg/Bilanzierungskonzept_2kW_Experten2012.pdf, last accessed August 11, 2014.
[Wyrsch 91]	N. Wyrsch, F. Finger, T. J. McMahon & M. Vanecek. *How to reach more precise interpretation of subgap absorption spectra in terms of deep defect density in a-Si:H.* Journal of Non-Crystalline Solids, vol. 137&138, pages 347–350, 1991.

[Wyrsch 92] N. Wyrsch. *La technique de temps de vol et la détermination des proprietés électroniques du silicium amorphe hydrogéné.* PhD thesis, Université de Neuchâtel, Switzerland, 1992.

[Wyrsch 08] N. Wyrsch, S. Dunand & C. Ballif. *Micro photovoltaic modules for micro systems.* Mat. Res. Soc. Symp. Proc., vol. 1066, pages A10–4, 2008.

[Xin 11] J. Xin, K. H. M. van der Werf & R. E. I. Schropp. *Thinner silicon-based tandem solar cell with high efficiency made by hot wire CVD.* Physica Status Solidi C, vol. 8, no. 10, pages 3002–3004, 2011.

[Xu 96] X. Xu, J. Yang & S. Guha. *Hydrogen dilution effects on a-Si:H and a-SiGe:H materials properties and solar cell performance.* Journal of Non-Crystalline Solids, vol. 198–200, pages 60–64, 1996.

[Yablonovitch 87] E. Yablonovitch. *Inhibited spontaneous emission in solid-state physics and electronics.* Physical Review Letters, vol. 58, no. 20, pages 2059–2062, 1987.

[Yan 03a] B. Yan, J. Yang & S. Guha. *Effect of hydrogen dilution on the open-circuit voltage of hydrogenated amorphous silicon solar cells.* Applied Physics Letters, vol. 83, no. 4, pages 782–784, 2003.

[Yan 03b] B. Yan, J. Yang, G. Yue & S. Guha. *Correlation of material properties and open-circuit voltage of amorphous silicon based solar cells.* Mat. Res. Soc. Symp. Proc., vol. 762, page A7.4.1, 2003.

[Yan 03c] B. Yan, J. Yang, G. Yue, K. Lord & S. Guha. *On the mechanism of light-induced open-circuit voltage increase in mixed-phase hydrogenated silicon solar cells.* 3rd world conference on photovoltaic solar energy conversion, pages 5P–A9–06, 2003.

[Yan 04] B. Yan, G. Yue, J. M. Owens, J. Yang & S. Guha. *Light-induced metastability in hydrogenated nanocrystalline silicon solar cells.* Applied Physics Letters, vol. 85, no. 11, pages 1925–1927, 2004.

[Yan 10] B. Yan, C.-S. Jiang, Y. Yan, L. Sivec, J. Yang, S. Guha & M. M. Al-Jassim. *Effect of hydrogen dilution profiling on the microscopic structure of amorphous and nanocrystalline silicon mixed-phase solar cells.* Physica Status Solidi C, vol. 7, no. 3–4, pages 513–516, 2010.

[Yan 12] B. Yan, J. Yang & S. Guha. *Amorphous and nanocrystalline silicon thin film photovoltaic technology on flexible substrates.* Journal of Vacuum Science and Technology A, vol. 30, no. 4, page 04D108, 2012.

[Yang 02]	J. Yang, K. Lord, B. Yan, A. Banerjee & S. Guha. *Correlation of the open-circuit voltage enhancement of heterogeneous silicon solar cells and the Staebler-Wronski effect.* 29th IEEE PVSC Proc., pages 1094–1097, 2002.
[Yang 03]	J. Yang, A. Banerjee & S. Guha. *Amorphous silicon based photovoltaics—from earth to the "final frontier".* Solar Energy Materials & Solar Cells, pages 597–612, 2003.
[Yue 03]	G. Yue, B. Yan, J. Yang, K. Lord & S. Guha. *Kinetics of light-induced effects in mixed-phase hydrogenated silicon solar cells.* Mater. Res. Soc. Symp. Proc., vol. 762, page A12.2, 2003.
[Yunaz 09]	I. A. Yunaz, K. Hashizume, S. Miyajima, A. Yamada & M. Konagai. *Fabrication of amorphous silicon carbide films using VHF-PECVD for triple-junction thin-film solar cell applications.* Solar Energy Materials & Solar Cells, vol. 93, pages 1056–1061, 2009.
[Zanzucchi 77]	P. J. Zanzucchi, C. R. Wronski & D. E. Carlson. *Optical and photoconductive properties of discharge-produced amorphous silicon.* Journal of Applied Physics, vol. 48, no. 12, pages 5227–5236, 1977.
[Zeman 97]	M. Zeman, J. A. Willemen, L. L. A. Vosteen, G. Tao & J. W. Metselaar. *Computer modelling of current matching in a-Si:H/a-Si:H tandem solar cells on textured TCO substrates.* Solar Energy Materials & Solar Cells, vol. 46, pages 81–99, 1997.
[Zeman 13a]	M. Zeman, O. Isabella, S. Solntsev & K. Jäger. *Modelling of thin-film silicon solar cells.* Solar Energy Materials & Solar Cells, vol. 119, pages 94–111, 2013.
[Zeman 13b]	M. Zeman, J. van den Heuvel, M. Kroon, J. Willemen, B. Pieters, J. Krc & S. Solntsev. *Advanced Semiconductor Analysis (ASA), user's manual, version 6.0*, 2013.
[Zhang 01]	S. B. Zhang & H. M. Branz. *Hydrogen above saturation at silicon vacancies: H-pair reservoirs and metastability sites.* Physical Review Letters, vol. 87, no. 10, page 105503, 2001.

Publication list

Last update: October 20, 2014

Publications as first author

[1] Michael Stuckelberger, Arvind Shah, Janez Krc, Matthieu Despeisse, Fanny Meillaud, and Christophe Ballif, *Internal electric field and fill factor of amorphous silicon solar cells*, 35th IEEE Photovoltaic Specialists Conference Proc., pages 001569–001574, 2010.

[2] Michael Stuckelberger, Yannick Riesen, Brice Perruche, Matthieu Despeisse, Nicolas Wyrsch, and Christophe Ballif, *Charge collection in amorphous silicon solar cells: cell analysis and simulation of high-efficiency pin devices*, Journal of Non-Crystalline Solids, vol. 358, pages 2187–2189, 2012.

[3] Michael Stuckelberger, Matthieu Despeisse, Grégory Bugnon, Jan-Willem Schüttauf, Franz-Josef Haug, and Christophe Ballif. *Comparison of amorphous silicon absorber materials: Light-induced degradation and solar cell efficiency*, Journal of Applied Physics, vol. 114, no. 154509, 2013.

[4] Michael Stuckelberger, Brice Perruche, Maximilien Bonnet-Eymard, Yannick Riesen, Matthieu Despeisse, Franz-Josef Haug, and Christophe Ballif, *Class AAA LED-based solar simulator for steady-state measurements and light soaking*, IEEE Journal of Photovoltaics, vol. 4, no. 5, pages 1282–1287, 2014.

[5] Michael Stuckelberger, Yannick Riesen, Matthieu Despeisse Jan-Willem Schüttauf, Franz-Josef Haug, and Christophe Ballif, *Light-induced V_{oc} increase and decrease in high-efficiency amorphous silicon solar cells*, Journal of Applied Physics, vol. 116, no. 094503, 2014.

[6] Michael Stuckelberger, Adrian Billet, Yannick Riesen, Mathieu Boccard, Matthieu Despeisse, Jan-Willem Schüttauf, Franz-Josef Haug, and Christophe Ballif, *Comparison of amorphous silicon absorber materials: kinetics of light-induced degradation*, accepted for publication in Progress in Photovoltaics: Research and Applications, 2014.

[7] Michael Stuckelberger, Nil Almat, Adrian Billet, Yannick Riesen, Léo Egger, Arnaud Walter, Jan-Willem Schüttauf, Franz-Josef Haug, and Christophe Ballif. *Properties*

and light-induced degradation of optimized p-type amorphous silicon-carbide layers, manuscript in preparation, 2014.

[8] Michael Stuckelberger, Adrian Billet, Arnaud Walter, Jan-Willem Schüttauf, Franz-Josef Haug, and Christophe Ballif, *Impact of substrate roughness on charge collection in amorphous silicon solar cells*, manuscript in preparation, 2014.

[9] Michael Stuckelberger, Matthieu Despeisse, Byoung-Suk Park, Franz-Josef Haug, and Christophe Ballif, *Hydrogenated amorphous silicon solar cells: the boron tailing story*, manuscript in preparation, 2014.

[10] Michael Stuckelberger, Laura Ding, Adrian Billet, Franz-Josef Haug, and Christophe Ballif, *Light-induced degradation kinetics of boron-doped zinc oxide*, manuscript in preparation, 2014.

[11] Michael Stuckelberger, Gizem Nogay, Franz-Josef Haug, and Christophe Ballif, *Plasma conditions for the growth of thin-film silicon solar cells*, manuscript in preparation, 2014.

Publications as co-author

[12] Matthieu Despeisse, Grégory Bugnon, Andrea Feltrin, Michael Stueckelberger, Peter Cuony, Fanny Meillaud, Adrian Billet, and Christophe Ballif, *Resistive interlayer for improved performance of thin film silicon solar cells on highly textured substrate*, Applied Physics Letters, no. 073507, 2010.

[13] Matthieu Despeisse, Mathieu Boccard, Grégory Bugnon, Peter Cuony, Thomas Söderström, Gaetano Parascandolo, Michael Stueckelberger, Mathieu Charrière, Linus Löfgren, Corsin Battaglia, Simon Hänni, Adrian Billet, Laura Ding, Sylvain Nicolay, Fanny Meillaud, Nicolas Wyrsch, and Christophe Ballif, *Low-conductivity doped layers for improved performance of thin film silicon solar cells on highly textured substrates*, 25th EU PVSEC Proc., pages 2793–2797, 2010.

[14] Corsin Battaglia, Loris Barraud, Adrian Billet, Mathieu Boccard, Grégory Bugnon, Mathieu Charrière, Peter Cuony, Matthieu Despeisse, Stefaan de Wolf, Laura Ding, Lukas Erni, Jordi Escarré, Simon Hänni, Franz-Josef Haug, Linus Löfgren, Fanny Meillaud, Sylvain Nicolay, Gaetano Parascandolo, Karin Söderström, Michael Stückelberger, and Christophe Ballif, *Advanced nanostructured materials for pushing light trapping towards the Yablonovitch limit*, Optical Nanostructures and Advanced Materials for Photovoltaics, Austin TX (USA), 2011.

[15] Jakub Holovský, Martin Schmid, Michael Stuckelberger, Matthieu Despeisse, Christophe Ballif, Aleš Poruba, and Milan Vaněček, *Time evolution of surface defect states in hydrogenated amorphous silicon studied by photothermal and photocurrent spectroscopy and optical simulation*, Journal of Non-Crystalline Solids, vol. 358, pages 2035–2038, 2012.

[16] Matthieu Despeisse, Mathieu Boccard, Corsin Battaglia, Gregory Bugnon, Mathieu Charrière, Loïc Garcia, Maximilien Bonnet-Eymard, Jordi Escarre, Peter Cuony, Michael Stuckelberger, Gaetano Parascandolo, Simon Hanni, Linus Löfgren, Jan-Willem Schüttauf, Laura Ding, Sylvain Nicolay, Fanny Meillaud, and Christophe Ballif, *Light harvesting schemes for high efficiency thin film silicon solar cells*, 38th IEEE PVSC Proc., pages 003015–003019, 2012.

[17] Fanny Meillaud, Adrian Billet, Corsin Battaglia, Mathieu Boccard, Grégory Bugnon, Peter Cuony, Mathieu Charrière, Matthieu Despeisse, Laura Ding, Jordi Escarré-Palou, Simon Hänni, Linus Löfgren, Sylvain Nicolay, Gaetano Parascandolo, Michael Stuckelberger, and Christophe Ballif, *Latest developments of high-efficiency micromorph tandem silicon solar cells implementing innovative substrate materials and improved cell design*, IEEE Journal of Photovoltaics, vol. 2, no. 3, pages 236–240, 2012.

[18] Thomas Lanz, Mathias Bonmarin, Michael Stuckelberger, Christian Schlumpf, Christophe Ballif, and Beat Ruhstaller, *Electrothermal finite-element modeling for defect characterization in thin-film silicon solar modules*, IEEE journal of selected topics in quantum electronics, vol. 19, no. 5, pages 4000308, 2013.

[19] Stefan Abel, Thilo Stöferle, Chiara Marchiori, Daniele Caimi, Lukas Czornomaz, Christophe Rossel, Marta D. Rossell, Rolf Erni, Marilyne Sousa, Heinz Siegwart, Jens Hofrichter, Michael Stuckelberger, Alexei Chelnokov, Bert J. Offrein, and Jean Fompeyrine, *Electro-optical active barium titanate thin films in silicon photonic devices*, Integrated Photonics Research, Silicon and Nanophotonics, Rio Grande, Puerto Rico (USA), 2013.

[20] Jan-Willem Schüttauf, Grégory Bugnon, Michael Stuckelberger, Simon Hänni, Mathieu Boccard, Matthieu Despeisse, Franz-Josef Haug, Fanny Meillaud, and Christophe Ballif, *Thin-film silicon triple-junction solar cells on highly transparent front electrodes with stabilized efficiencies up to* 12.8 %, IEEE Journal of Photovoltaics, vol. 4, no. 3, pages 757–762, 2014.

[21] Grégory Bugnon, Gaetano Parascandolo, Simon Hänni, Michael Stuckelberger, Mathieu Charrière, Matthieu Despeisse, Fanny Meillaud, and Christophe Ballif, *Silicon oxide buffer layer at the p–i interface in amorphous and microcrystalline silicon solar cells*, Solar Energy Materials & Solar Cells, vol. 120, pages 143–150, 2014.

[22] Mathieu Boccard, Peter Cuony, Simon Hänni, Michael Stuckelberger, Franz-Joseph Haug, Fanny Meillaud, Matthieu Despeisse, and Christophe Ballif, *The role of front and back electrodes in parasitic absorption in thin-film solar cells*, EPJ Photovoltaics, vol. 5, no. 50601, 2014.

[23] Bjoern Niesen, Nicolas Blondiaux, Mathieu Boccard, Michael Stuckelberger, Raphaël Pugin, Emmanuel Scolan, Fanny Meillaud, Franz-Josef Haug, Aïcha Hessler-Wyser, and Christophe Ballif, *Self-patterned nanoparticle layers for vertical interconnects: application in tandem solar cells*, Nano Letters, vol. 14, pages 5085–5091, 2014.

[24] Etienne Moulin, Mark Steltenpool, Mathieu Boccard, Loïc Garcia, Grégory Bugnon, Michael Stuckelberger, Elmar Feuser, Björn Niesen, Rob van Erven, Jan-Willem Schüttauf, Franz-Josef Haug, and Christophe Ballif, *2-D periodic and random-on-periodic front textures for tandem thin-film silicon solar cells*, IEEE Journal of Photovoltaics, vol. 4, no. 5, pages 1177–1184, 2014.

[25] Jan-Willem Schuttauf, Björn Niesen, Linus Löfgren, Maximilien Bonnet-Eymard, Michael Stuckelberger, Simon Hänni, Mathieu Boccard, Grégory Bugnon, Matthieu Despeisse, Franz-Josef Haug, Fanny Meillaud, and Christophe Ballif, *Amorphous silicon-germanium for triple and quadruple junction thin-film silicon based solar cells*, submitted for publication, 2014.

[26] Neda Neykova, Etienne Moulin, Andrej Campa, Karel Hruska, Michael Stuckelberger, Franz-Josef Haug, Marko Topic, Milan Vanecek, and Christophe Ballif, *3-dimensional amorphous silicon solar cells on periodically ordered ZnO nanocolumns*, manuscript in preparation, 2014.

Oral conference contributions

[27] Michael Stuckelberger, Yannick Riesen, Brice Perruche, Matthieu Despeisse, Nicolas Wyrsch, and Christophe Ballif, *Charge collection in amorphous silicon solar cells: cell analysis and simulation of high-efficiency pin devices*, 24th ICANS (Nara, Japan), August 22, 2011.

[28] Michael Stuckelberger, Matthieu Despeisse, Grégory Bugnon, Jan-Willem Schüttauf, Franz-Josef Haug, and Christophe Ballif, *Comparison of different absorber layers fabricated by PECVD for high-efficiency solar cells*, 25th ICANS (Toronto, Canada), August 22, 2013.

[29] Michael Stuckelberger, Yannick Riesen, Matthieu Despeisse, Jan-Willem Schüttauf, Franz-Josef Haug, and Christophe Ballif, *High efficiency amorphous silicon solar cells: impact of the p-doped silicon-carbide layer on light induced degradation*, MRS spring meeting (San Francisco CA, USA), presentation A1.02, April 22, 2014.

[30] Michael Stuckelberger, Matthieu Despeisse, Byoung-Suk Park, Franz-Josef Haug, and Christophe Ballif, *Amorphous silicon solar cells: annealing effects of the window layers during subsequent deposition steps*, MRS spring meeting (San Francisco CA, USA), presentation H3.06, April 23, 2014.

[31] Michael Stuckelberger, Mathieu Boccard, Jan-Willem Schüttauf, Matthieu Despeisse, Franz-Josef Haug, and Christophe Ballif, *Comparison of amorphous silicon absorber materials: kinetics of light-induced degradation*, 29th EU-PVSEC (Amsterdam, The Netherlands), presentation 3CO.6.6, September 24, 2014.

Visual conference contributions

[32] Michael Stückelberger, Arvind Shah, Janez Krc, Matthieu Despeisse, Fanny Meillaud, and Christophe Ballif, *Internal electric field and fill factor of amorphous silicon (a-Si:H) solar cells*, 35th IEEE PVSC (Honolulu HI, USA), presentation 360-O2, June 22, 2010.

[33] Michael Stuckelberger, Brice Perruche, Maximilien Bonnet-Eymard, Yannick Riesen, Matthieu Despeisse, Franz-Josef Haug, and Christophe Ballif, *Fully LED-based solar simulator for steady state measurements and light soaking*, 29th EU-PVSEC (Amsterdam, The Netherlands), presentation 1BV.6.16, September 23, 2014 (poster award).

Patents

[34] Laure-Emmanuelle Perret-Aebit, Patrick Heinstein, Matthieu Despeisse, Christophe Ballif, and Michael Stückelberger, *Solar module and its production process*, Patent application WO2014044620 (A1), 2014.

Acknowledgements

This thesis would not have been possible without the tremendous support of many people. In particular, I sincerely acknowledge:

- My supervisors. You offered me the opportunity to conduct this research, guided me, challenged me, fought with me, and prevented me from succumbing to the temptation to resolve all the world's problems within a thesis.
- My thesis jury for your careful reading, positive feedback and stimulating discussions.
- The students under my supervision during internships, civil service, and master theses. Thank you for your efforts and contributions to the work presented in this thesis—it was a pleasure to work with you!
- My office mates. Here a question, there a joke or moaning about equipment on strike … what else do you need for the lab to feel like home?
- All my current and former colleagues for discussions and practical support, but even more for the great atmosphere in the lab and outside. All the pirate depositions with you late in the evenings, never-ending aperos, and philosophical discussions with beer and smoke turned colleagues into friends.
- My colleagues from AIST/PVTEC in Tsukuba, Japan, for hosting me twice and teaching me not only about triode reactors but also about Japanese culture. I had a great time with you!
- The teams from EPFL, CSEM (Switzerland), IndeoTec (Switzerland), Ecole Polytechnique (Palaiseau, France), FZ Jülich (Germany), TU Delft (Netherlands), IPP (Prague), SUPSI (Switzerland), EMPA (Switzerland), and other institutes for the exchange of samples and knowledge and for unforgettable evenings.
- Octopus, system B, the three-sun solar simulator and my other babies: I will miss you!
- The technical staff. Not only do you maintain a large technical park at a high level, but you were also very willing to find solutions to any new challenge.
- The administrative staff for all your work in the background.
- Governmental and industrial partners for financial support.
- Lara for your endurance in correcting hundreds of pages of publications, not only eliminating mistakes but also making the texts read more smoothly.
- My family and Michèle for your continuous support and love.

Neuchâtel, October 2014 Michael Stückelberger

Michael Elias STÜCKELBERGER

Allenmoosstrasse 66
CH-8057 Zurich
Switzerland

michael.stuckelberger@epfl.ch
michael.stuckelberger.epfl@gmail.com
Birthday: January 17, 1982
Nationality: Swiss

Education

03/2010 – present	EPFL (Lausanne, Switzerland): PhD candidate in material science
10/2005 – 02/2009	ETHZ (Zurich, Switzerland): student of physics, specialization in particle physics and detector physics
07/2004 – 08/2005	TPU (Tomsk, Russia): student of nuclear physics and Russian
10/2001 – 06/2004	ETHZ (Zurich, Switzerland): student of interdisciplinary sciences (physics and chemistry)
08/1995 – 01/2001	Kantonsschule Zurich Oerlikon : specialization in new languages

Language skills:	German (mother tongue), English, and French (proficient), Spanish and Russian (basic)
Software skills:	Good knowledge of MS Office suite, LaTeX, Igor, LabVIEW; basic knowledge of Matlab, Mathematica, C++/root, Illustrator, SolidWorks, ASA, and others

Internships

05/2012 – 08/2012	Exchange student at AIST (Tsukuba, Japan): *« Development of a-Si:H solar cells on ZnO substrates in a triode reactor »*
03/2009 – 11/2009	Civil service at EPFL (Lausanne, Switzerland): *« Fabrication, characterization, and degradation of a-Si:H solar cells »*
09/2008 – 02/2009	Diploma thesis at CERN/PSI/ETHZ (Switzerland): *« Threshold calibration of the CMS pixel detector »*
07/2007 – 09/2007	Summer school at DESY (Hamburg, Germany): *« On the inclusion of the forward and backward silicon tracker to the H1 track reconstruction and its application with charged current »*
02/2006 – 07/2006	Internship at PSI (Villigen, Switzerland): *« VIA-XAFS model and its Excel application for the study of zirconia films »*
02/2004 – 03/2004	Internship at CERN (Geneva, Switzerland): *« Recovery of light yield and transmission of* $PbWO_4$ *crystals after* γ*-irradiation »*
08/1999 – 03/2000	Project: *« Planning and construction of a pilot-biogas-production plant »*

Professional activities

03/2010 – 06/2011	Teaching assistant for *« Opto- and macroelectronic materials »* at EPFL (Lausanne, Switzerland)
10/2007 – 12/2007	Physics teacher at the high school SAMD (Davos, Switzerland)
10/2006 – 07/2007	Teaching assistant for *« Analysis I and II »* at ETHZ (Zurich, Switzerland)
1999 – 2008	Tutor for the YMCA and private clients

Scientific contributions

I co-authored 19 scientific journal contributions, including 6 as first author; further articles are in the publication process. I took part in four international conferences, gave five oral presentations and presented two posters (poster award at the 27th EU-PVSEC, 2014). A publication list is available on http://scholar.google.ch/citations?user=ClCMSZAAAAAJ&hl=en.

Private interests

Since childhood, I have been fascinated by nature and concerned about the environment, which resulted in voluntary service for different organizations, but also in the construction of my own solar power plants. Further, I love tailoring and travelling, especially by bicycle, and working as stage manager or light engineer for dance performance groups and theaters.